

# Iron-bearing Oxides, Silicate Glasses and Carbonates at Lower Mantle Pressures

Thesis by

Natalia V. Solomatova

In Partial Fulfillment of the Requirements

for the Degree of

Doctor of Philosophy

The Caltech logo, featuring the word "Caltech" in a bold, orange, sans-serif font, centered within a light orange rectangular background.

CALIFORNIA INSTITUTE OF TECHNOLOGY

Pasadena, California

2017

Defended May 23, 2017

© 2017

Natalia V. Solomatova

ORCID: 0000-0002-2331-3427

# Acknowledgements

I would first like to thank my advisors, Jennifer Jackson and Paul Asimow. Under Jennifer's mentorship, I learned how to conduct high-quality experiments and effectively present my results in papers and at conferences. Jennifer inspired me to continuously improve and become a better scientist, and I greatly appreciate her encouragement and support throughout my graduate studies. While performing *ab initio* calculations, Paul showed great patience while I searched for the best approaches and strategies, discussing the various options and implications. His optimism helped motivate me when aspects of the calculations were particularly difficult. I am extremely fortunate to have gotten the opportunity to work under the supervision of such incredible advisors.

I am thankful to George Rossman for discussions on the spectroscopy of minerals, for teaching me how to use the UV/VIS/NIR and Raman spectrometers, and for sharing with me the many exciting stories from his life. I am grateful to Wolfgang Sturhahn, developer of the MINUTI and CONUSS softwares, for advising me in data processing and for the valuable discussions during group meetings. I am thankful to Chi Ma for teaching me how to use the SEM, giving me the opportunity to become the analytical laboratory assistant and teaching me troubleshooting tricks to solve problems users commonly experience. I would also like to thank Mike Baker for his continual assistance with sample synthesis and valuable discussions. I greatly appreciate the time Naveed Near-Ansari has spent on helping me compile the various softwares I use on FRAM, the high-performance computing cluster at Caltech.

I thank Rachel Morrison and Greg Finkelstein for their care and dedication in helping me conduct experiments at the synchrotron. Likewise, the beamline scientists at Sector 3 of the Advanced Photon Source (APS) have been a tremendous help in collecting time-domain Mössbauer spectra: Tom Toellner, Ercan Alp, Wenli Bi and Jiyong Zhao. Ambient X-ray diffraction experiments at 11-BM of the APS were made possible by Saul Lapidus and Lynn Ribaud. At Sector 12.2.2 of the Advanced Light Source (ALS), Bora Kalkan, Martin Kunz and Christine Beavers were extremely helpful and supportive during our X-ray diffraction experiments. I would also like to thank Mathieu Roskosz and William Steinhardt for their contributions to our study of silicate glasses and ferropericlaase, respectively. I am grateful to June Wicks who helped me collect high-fidelity X-ray diffraction data on (Mg,Fe)O at my first beamtime at ALS. June has also provided me with friendship and guidance throughout my graduate studies. And I am extremely thankful to my office mate, Jennifer Buz, who has been a constant source of encouraging words, friendship and enjoyment.

The research on ferropicicase was funded by NSF-EAR-CAREER-0956166 and NSF-CSEDI-EAR-1161046. Caltech microprobe analyses of ferropicicase were partially funded by the MRSEX Program of the NSF (DMR-0080065). The research on silicate glasses was funded by NSF-CSEDI-EAR-1600956, NSF-EAR-1322082, the Keck Institute for Space Studies, the French ANR Program (2011JS56 004 01, FrIHIDDA), and Region Nord-Pas de Calais. The research on high-pressure carbonates was supported by NSF-EAR-1551433. Ruby fluorescence measurements were conducted at GSECARS and HPCAT at the APS. COMPRES and the U.S. DOE Office of Science support operations at the APS and ALS.

# Abstract

Iron is the fourth most abundant element in Earth's mantle and it affects geophysically observable properties, such as the density, sound velocities, viscosity and transport properties of mantle phases. Additionally, the concentration of iron in minerals and melts of the lower mantle dictates their structure and stability. Thus, understanding the effect of iron is important to interpret seismically observable complexities and understand their effect on processes in the deep Earth. In this thesis, I use experimental and theoretical methods to improve our understanding of the high-pressure behavior of iron-bearing periclase ("ferropericlase"), silicate glasses and carbonates.

Ferropericlase is thought to represent a significant fraction of Earth's lower mantle, and may explain the slow compressional and shear sound velocities of ultra-low velocity zones at the core-mantle boundary. To understand the effect of iron concentration on the (Mg,Fe)O solid solution, the equation of state and hyperfine parameters of (Mg,Fe)O with 48 mol% FeO were measured using X-ray powder diffraction and time-domain Mössbauer spectroscopy, respectively, and the spin crossover behavior was compared to that of (Mg,Fe)O with 10 to 60 mol% FeO. I find that iron-rich ferropericlase at core-mantle boundary pressures likely contains a significant fraction of high-spin iron, contributing a positive buoyancy to promote topographic relief of ultra-low velocity zones in the lowermost mantle.

Some ultra-low velocity zones, particularly those at the base of the central parts of large low shear velocity provinces, may be best explained by the presence of iron-bearing silicate melts. The behavior of iron in silicate melts is poorly understood, but may be approximated by iron-bearing silicate glasses. I measured the hyperfine parameters of iron-bearing rhyolitic glass up to ~120 GPa and basaltic glasses up to ~90 GPa using time-domain Mössbauer spectroscopy. Iron within these glasses experiences changes in coordination environment with increasing pressure without undergoing a high-spin to low-spin transition. Thus, ferrous iron in chemically-complex silicate melts likely exists in a high-spin state throughout most of Earth's mantle.

Decomposition of carbonates may be responsible for creating silicate melts within the lower mantle by lowering the melting temperature of surrounding rock. Identifying and characterizing the stability of carbonate phases is therefore a necessary step towards understanding the transport and storage of carbon in Earth's interior. Dolomite is one of the major mineral forms in which carbon is subducted into the Earth's mantle. Although iron-free dolomite is expected to break down upon compression into single-cation carbonates, high-pressure polymorphs of iron-bearing dolomite may resist decomposition. Using a genetic algorithm that predicts crystal structures (USPEX), I

have found a monoclinic phase with space group  $C2/c$  that has a lower energy than all previously reported dolomite structures at pressures above 15 GPa, and the substitution of iron for magnesium stabilizes monoclinic dolomite with respect to decomposition at certain pressures of the lower mantle.

In this thesis, I demonstrate that iron undergoes a spin transition in  $(\text{Mg,Fe})\text{O}$ ,  $(\text{Mg,Fe})\text{CO}_3$  and  $\text{Ca}(\text{Mg,Fe})(\text{CO}_3)_2$ , while iron in basaltic and silicate glasses likely does not experience a spin transition up to lowermost mantle pressures. Additionally, I find that the amount of iron in  $(\text{Mg,Fe})\text{O}$  and  $\text{Ca}(\text{Mg,Fe})(\text{CO}_3)_2$  dictates the dynamic and thermodynamic stabilities of those phases within Earth's lower mantle.

# Contents

Acknowledgements.....	ii
Abstract.....	iv
List of Figures.....	ix
List of Tables.....	xi
Acronyms.....	xii
Published Content and Contributions.....	xiv
1. Introduction.....	1
1.1 Earth's Structure.....	1
1.2 Complexities of Earth's Lower Mantle.....	1
1.3 Thesis Overview.....	5
2. Experiments.....	9
2.1 Diamond Anvil Cell.....	9
2.2 X-ray Diffraction.....	14
2.3 Mössbauer Spectroscopy.....	16
2.4 Optical Spectroscopy.....	21
3. Equation of State and Spin Crossover of (Mg,Fe)O.....	24
3.1 Introduction.....	24
3.2 Experiments and Data Evaluation.....	25
3.2.1 Sample Synthesis.....	25
3.2.2 X-ray Diffraction.....	26
3.2.3 Synchrotron Mössbauer Spectroscopy.....	26
3.3 Results.....	27
3.3.1 Equation of State.....	27
3.3.2 Synchrotron Mössbauer Spectroscopy.....	32
3.3.3 Hyperfine Parameters.....	34
3.4 Effect of Iron Concentration.....	39
3.5 Implications.....	42
4. Electronic Structure of Iron in Rhyolitic and Basaltic Glasses.....	47

4.1 Introduction.....	47
4.2 Methods .....	48
4.2.1 Sample Preparation .....	48
4.2.2 Experimental Methods .....	50
4.2.2 Fitting Procedure of Mössbauer Spectra .....	52
4.3 Results.....	53
4.3.1 Optical Absorption Spectroscopy .....	53
4.3.2 Mössbauer Spectroscopy .....	55
4.4 Discussion.....	61
4.4.1 Coordination Environments at Room Pressure .....	61
4.4.2 Coordination Environments at High Pressure .....	65
4.4.3 Comparison with Previous Studies .....	66
4.4.4 Trends with Composition .....	68
4.5 Conclusions.....	72
5. Theory.....	73
5.1 Introduction.....	73
5.2 Density Functional Formalism.....	74
5.3 Periodicity and Plane Waves .....	75
5.4 Implementation of Density Functional Theory.....	77
5.4 The Hubbard $U$ Method.....	80
5.5 Crystal Structure Prediction.....	84
6. <i>Ab initio</i> Study of the Structure and Stability of $\text{CaMg}(\text{CO}_3)_2$ .....	86
6.1 Introduction.....	86
6.2 Computational Methods.....	88
6.3 High-Pressure Dolomite Structures .....	90
6.4 Discussion.....	96
6.5 Implications .....	98
7. <i>Ab initio</i> Study of Iron-bearing Carbonates .....	99
7.1 Introduction.....	99
7.2 Computational Methods.....	100
7.3 Results.....	105

7.3.1 Spin Transition.....	105
7.3.2 Monoclinic Dolomite.....	107
7.4 Discussion.....	108
7.4.1 Spin Transition.....	108
7.4.2 Monoclinic Dolomite.....	111
7.5 Concluding Remarks.....	112
8. Conclusions.....	114
Bibliography.....	116

# List of Figures

1.1 Earth's structure .....	2
1.2 Core-mantle boundary .....	4
2.1 Symmetric diamond anvil cell .....	10
2.2 Mounting diamonds .....	11
2.3 Diamond alignment.....	12
2.4 Indenting a metal gasket .....	13
2.5 Shift of ruby fluorescence spectra with pressure .....	14
2.6 Setup of Beamline 12.2.2 at the Advanced Light Source .....	15
2.7 Ambient X-ray diffraction pattern .....	16
2.8 Electronic configurations of high-spin and low-spin ferrous and ferric iron.....	18
2.9 Setup of Sector 3-ID-B at the Advanced Photon Source .....	21
2.10 Setup of a FT-IR UV/VIS/NIR spectrometer .....	22
3.1 X-ray diffraction patterns for (Mg,Fe)O with 48 mol% FeO.....	28
3.2 FWHM of the 200 and 220 reflections for (Mg,Fe)O with 48 mol% FeO.....	29
3.3 Pressure-volume relationship and equations of state for (Mg,Fe)O .....	30
3.4 Representative synchrotron Mössbauer spectra for (Mg,Fe)O with 48 mol% FeO.....	35
3.5 Quadrupole splitting and isomer shift for (Mg,Fe)O with 48 mol% FeO.....	36
3.6 Volume and bulk modulus as a function of iron concentration for (Mg,Fe)O.....	41
3.7 Spin transition pressure of (Mg,Fe)O as a function of iron concentration.....	42
3.8 Isothermal bulk modulus of (Mg,Fe)O as a function of iron concentration .....	43
3.9 Density of (Mg,Fe)O as a function of iron concentration.....	43
3.9 Bulk sound velocity of (Mg,Fe)O as a function of iron concentration .....	43
4.1 Composition of silicate glasses in mole percent .....	50
4.2 UV/VIS/NIR absorption spectra of rhyolitic and basaltic glasses .....	54
4.3 Conventional Mössbauer spectra for rhyolitic and basaltic glasses.....	56
4.4 Synchrotron Mössbauer spectra of rhyolitic and basaltic glasses at high pressure.....	57
4.5 Modeled energy spectra of rhyolitic and basaltic glasses .....	58
4.6 Quadrupole splitting and isomer shift of rhyolitic and basaltic glasses.....	59

4.7	Quadrupole splitting versus isomer shift at 0 and 60 GPa.....	67
4.8	Quadrupole splitting as a function of FeO concentration at 0 GPa.....	69
4.9	Quadrupole splitting as a function of the oxide mole ratios at 0 GPa.....	70
4.10	Quadrupole splitting as a function of the oxide mole ratios at 60 GPa.....	71
5.1	Schematic of the total energy as a function of electronic occupations .....	80
5.2	Occupations as a function of the strength of the applied potential shift .....	82
5.3	$U_{out}$ as a function of $U_{in}$ .....	83
6.1	High-pressure dolomite polymorphs.....	92
6.2	Synthetic X-ray diffraction patterns of high-pressure dolomite polymorphs .....	93
6.3	Enthalpies of candidate dolomite structures .....	95
6.4	Pressure-volume data and equations of state for candidate dolomite structures.....	96
6.5	Enthalpy differences between dolomite polymorphs and aragonite + magnesite .....	98
7.1	$U_{in}$ vs. $U_{out}$ for high-spin and low-spin ferromagnesite.....	101
7.2	Calculated Hubbard $U$ as a function of pressure.....	103
7.3	Partial density of states for iron's 3d electrons in high-spin ferromagnesite .....	104
7.4	Spin transition in ferromagnesite and monoclinic dolomite .....	106
7.5	Enthalpy difference between Fe-free dolomite and single-cation carbonates.....	107
7.6	Enthalpy difference between ferrodolomite and single-cation carbonates .....	109

# List of Tables

1.1 Summary of synchrotron experiments presented in this thesis.....	7
1.2 Summary of fitting and graphing softwares used in this thesis .....	8
1.3 Summary of software packages used for the <i>ab initio</i> calculations in this thesis .....	8
3.1 Compression data from X-ray diffraction experiments on (Mg,Fe) with 48 mol% FeO.....	31
3.2 Error correlation matrix for the EOS parameters for (Mg,Fe) with 48 mol% FeO.....	32
3.3 Equation of state parameters as a function of pressure for (Mg,Fe) with 48 mol% FeO.....	33
3.4 Best fit hyperfine parameters for (Mg,Fe) with 48 mol% FeO, compression pathway .....	37
3.5 Best fit hyperfine parameters for (Mg,Fe) with 48 mol% FeO, decompression pathway .....	38
3.6 Error correlation matrix for fitted hyperfine parameters for (Mg,Fe) with 48 mol% FeO .....	38
3.7 Spin crossover equation of state parameters for (Mg,Fe)O .....	44
3.8 Experimental studies on the reported spin transition pressure.....	45
4.1 Oxide weight percents of silicate glasses.....	49
4.2 Best-fit hyperfine parameters for silicate glasses at 0 GPa.....	56
4.3 Best-fit hyperfine parameters for rhyolitic glass at high pressure .....	62
4.4 Error correlation matrix for the fitted hyperfine parameters for rhyolitic glass.....	63
4.5 Best-fit hyperfine parameters for basaltic glass at high pressure.....	64
4.6 Error correlation matrix for the fitted hyperfine parameters for basaltic glass.....	65
5.1 A comparison of the units used in VASP and Quantum Espresso.....	77
6.1 Fractional coordinates and lattice parameters of high-pressure dolomite polymorphs.....	91
6.2 Equation of state parameters for calculated and experimental dolomite polymorphs .....	94

# Acronyms

AFM	AntiFerroMagnetic
ALS	Advanced Light Source
APD	Avalanche PhotoDiode
APS	Advanced Photon Source
APW	Augmented Plane Waves
CMB	Core-Mantle Boundary
CONUSS	COherent NUclear resonant Scattering by Single crystals
DAC	Diamond Anvil Cell
DFT	Density Functional Theory
EOS	Equation Of State
FM	FerroMagnetic
Fp	Ferropericlase
FT-IR	Fourier-Transform Infra-Red
FWHM	Full Width at Half Maximum
GGA	Generalized Gradient Approximation
HS	High Spin
IR	Infra-Red
IS	Isomer Shift
KS	Kohn-Sham
LAPW	Linear Augmented Plane Wave
LDA	Local Density Approximation
LLSVP	Large Low Shear Velocity Province
LS	Low Spin
MINUTI	MINeral physics UTILities
MORB	Mid-Ocean Ridge Basalt
Mw	Magnesiowüstite
NIR	Near Infra-Red
PAW	Projector-Augmented Waves
PBE	Perdew-Burke-Ernzerhof

PP	PseudoPotentials
PREM	Preliminary Reference Earth Model
PW	Perdew–Wang
PWscf	Plane-Wave self-consistent field
QE	Quantum ESPRESSO (opEn-Source Package for Research in Electronic Structure, Simulation and Optimization)
QS	Quadrupole Splitting
SMS	Synchrotron Mössbauer Spectroscopy
SS	Stainless Steel
ULVZ	Ultra-Low Velocity Zone
USPEX	Universal Structure Predictor: Evolutionary Xtallography
UV	UltraViolet
VASP	Vienna <i>Ab initio</i> Simulation Package
VESTA	Visualization for Electronical and Structural Analysis
VIS	VISible light
XRD	X-Ray Diffraction

# Published Content and Contributions

Solomatova, N. V., and Asimow, P. D. (2017), First-principles calculations of high-pressure iron-bearing monoclinic dolomite and single-cation carbonates with internally consistent Hubbard  $U$ , *Physics and Chemistry of Minerals* (in review). N.V.S. performed the calculations and wrote the manuscript.

Solomatova, N. V., Jackson, J. M., Sturhahn, W., Rossman, G. R., Roskocz, M. (2017), Electronic environments of ferrous iron in rhyolitic and basaltic glasses at high pressure, *Journal of Geophysical Research: Solid Earth* (in review). N.V.S. conducted the synchrotron experiments, conducted the optical spectroscopy experiments, performed the data analysis and wrote the manuscript.

Solomatova, N. V. and Asimow, P. D. (2017): *Ab initio* study of the structure and stability of  $\text{CaMg}(\text{CO}_3)_2$  at high pressure, *American Mineralogist*, 102, 201-215, doi:10.2138/am-2017-5830. N.V.S. performed the calculations and wrote the manuscript.

Solomatova, N. V., Jackson, J. M., Sturhahn, W., Wicks, J. K., Zhao, J., Toellner, T. S., Kalkan, B., Steinhardt, W. M. (2016): Equation of state and spin crossover of (Mg,Fe)O at high pressure, with implications for explaining topographic relief at the core-mantle boundary, *American Mineralogist*, 101, 1084-1093, doi:10.2138/am-2016-5510. N.V.S. conducted the synchrotron experiments, performed the data analysis and wrote the manuscript.

# Chapter 1

## Introduction

### 1.1 Earth's Structure

Most of Earth's interior is physically inaccessible to humans. It took 24 years to drill the Kola Superdeep Borehole, which at 12 km deep is about 0.2% of the Earth's radius. Despite this obstacle, the combination of seismology, mineral physics, geology, geochemistry and cosmochemistry has provided significant insight into the structure, composition and evolution of our planet.

To first order, Earth's interior is differentiated into four distinct layers: the crust, mantle, outer core and inner core (Figure 1.1). The crust is composed of two chemically and dynamically distinct types: a thin oceanic crust (~5-10 km thick) and relatively thicker continental crust (~25-70 km thick). Oceanic crust consists of basaltic and gabbroic rock, formed at mid-ocean ridges and recycled through subduction within tens of millions of years. Continental crust is more buoyant than oceanic crust and is thought to form mostly at subduction zones. Resisting subduction, continental crust is billions of years in age and is more complex in its structure and composition than basaltic crust. Beneath the crust lies about 2,900 km of mantle, which may be subdivided into the upper mantle, lower mantle and a transition zone between the two. The upper mantle is composed primarily of olivine, garnets and pyroxenes. At about 410 km, olivine undergoes a phase transition to wadsleyite, marking the onset of the mantle's transition zone. At about 520 km, wadsleyite transitions to ringwoodite, which decomposes into bridgmanite and ferropericlase above 660 km. The lower mantle is composed of iron-bearing bridgmanite, calcium perovskite and ferropericlase while the liquid outer-core and solid inner-core are made up of an iron-nickel alloy with small amounts of lighter elements.

### 1.2 Complexities of Earth's Lower Mantle

Carbon is subducted into Earth's interior primarily in the form of carbonate minerals in the form of metasomatically calcium-enriched basaltic rock (rodingite), calcified serpentinites (ophicarbonates) and sedimentary carbonaceous ooze [*Brenker et al.*, 2006]. The survival of carbonates during subduction depends on the temperature and

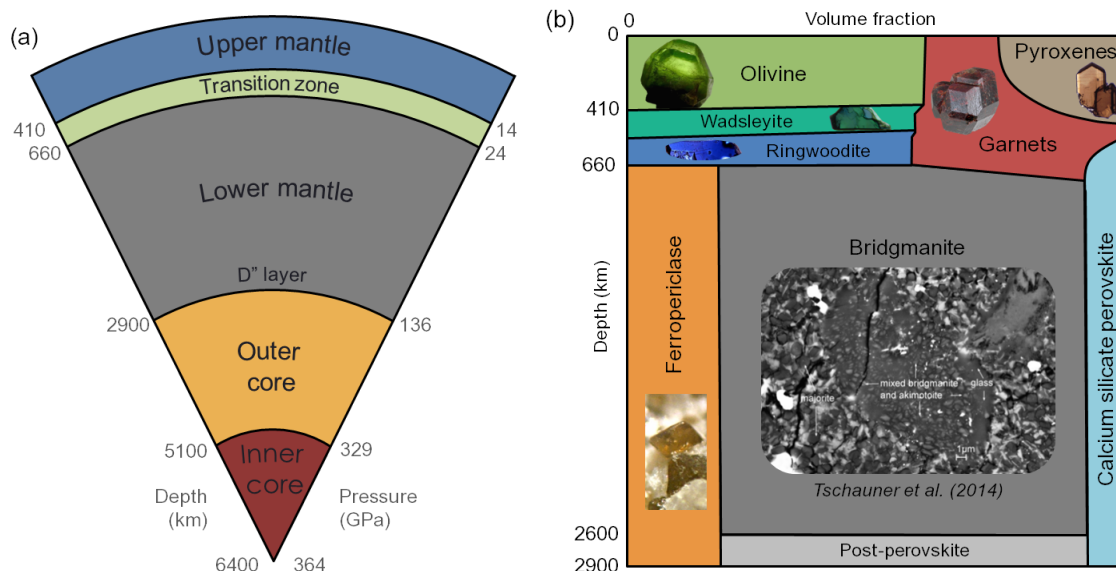


Figure 1.1: (a) Concentric layers of the Earth. Depth (km) is indicated on the left and the corresponding pressure (GPa) is indicated on the right. (b) Approximate mineralogy of a pyrolite mantle. Vertical axis is the depth (km) and horizontal axis is the volumetric fraction of the different phases. Figure after *Akaogi et al.* [2007]. Data sources from *Irifune and Ringwood* [1993], *Hirose et al.* [1999], *Ono et al.* [2001], *Aoki and Takahashi* [2004] and *Murakami et al.*, [2014]. Photographs of orthopyroxene from G. Rossman; olivine from R. Lavinsky; wadsleyite from T. Kawazoe; and ringwoodite from J. Smyth. A scanning-electron microscope image of natural bridgmanite is shown from *Tschauner et al.* [2014].

rate of subduction, as well as the location of carbonates within the slab [*Hammouda, 2003; Dasgupta and Hirschmann, 2010*]. Within the mantle, carbon is most likely stored in the form of carbon-rich phases due to carbon's low solubility in mantle silicates [*Shcheka et al., 2006*]. The combined uncertainties on the percentage of carbon that is subducted into the mantle and the unknown quantity of primordial carbon that survived the lunar-forming impact makes it difficult to estimate the quantity of carbon that exists within Earth's mantle, and so this number is highly debated [e.g., *Sano and Williams, 1996; Dasgupta and Hirschmann, 2010; Kelemen and Manning, 2015*].

Evidence of carbon-bearing phases in the Earth's mantle includes: the release of  $\text{CO}_2$  in volcanic eruptions, dissolved  $\text{CO}_2$  in magmatic glasses and glass inclusions [*Mörner and Etiope, 2002*], diamonds and carbonate minerals in mantle xenoliths [*Egger 1978; Sobolev and Shatsky, 1990*], and the existence of carbonatite and kimberlite magmas [*Wyllie et al., 1990*]. The oxygen fugacity of the mantle is heterogeneous, and depends on the local tectonic environment and depth within the mantle [*Wood et al., 1990; McCammon, 2005*]. Near oceanic ridges and continental rift zones the mantle is more reduced, while near subduction zones the mantle is more oxidized. Most carbonates will likely be stored as diamonds or metal carbides within the average mantle due to the

reducing environment [Kesson and Ringwood; 1989; Frost *et al.*, 2004; McCammon, 2005]. However, within subducted slabs, carbonates are expected to be the dominant carrier of carbon up to pressures of about 50 GPa [Oganov *et al.*, 2008]. It has been hypothesized that magnesite,  $\text{MgCO}_3$ , may be stable at the base of the lower mantle, as the carbonate stability field is expected to approach the IW buffer [Stagno *et al.*, 2011]. End-member  $\text{CaMg}(\text{CO}_3)_2$  dolomite typically breaks down upon compression into  $\text{MgCO}_3$  and  $\text{CaCO}_3$  at 5-6 GPa in the temperature range of 800-1200 K [Shirasaka *et al.*, 2002]. However, high-pressure X-ray diffraction experiments have shown that dense high-pressure polymorphs of iron-bearing dolomite may be favored over single-cation carbonates [Santillan *et al.*, 2003; Mao *et al.*, 2011; Merlini *et al.*, 2012]. It has been suggested that Ca-Mg-Fe carbonates play a leading role in transporting and storing carbon in the deep earth [Brenker *et al.*, 2007; Boulard *et al.*, 2012]. The identification of a new, more stable carbonate phase that is able to host carbon under conditions where known carbonates may decompose has the potential to substantially change estimates of the geochemical fluxes of carbon.

Decomposition of carbonates can produce free  $\text{CO}_2$ , which lowers the viscosity and melting temperature of the surrounding mantle [Eggler *et al.*, 1976]. The possibility of transporting small amounts of carbonates to the base of the lower mantle, where decarbonation reactions might take place, may explain the existence of partial melts at the core-mantle boundary [Isshiki *et al.*, 2004; Presnall and Gudfinnsson, 2005].

The core-mantle boundary (CMB) region is characterized by the existence of two large-scale structures, referred to as large low shear velocity provinces (LLSVPs), and smaller features, referred to as ultra-low velocity zones (ULVZs) (Figure 1.2). Located beneath the African continent and the Pacific Ocean, the two largest LLSVPs are approximately 1000 km tall and are attributed to a chemical and/or thermal anomaly, characterized by slow sound velocities, a relatively higher density and a sharp boundary. Often located at the edges of LLSVPs, ULVZs are about 5-70 km thick patches that are characterized by a further reduction in sound velocities by about 5-30% [Garnero *et al.*, 1998; McNamara *et al.*, 2010; Sun *et al.*, 2013]. ULVZs have been suggested to be composed of mantle-core reaction products ( $\text{FeO}$  and  $\text{FeSi}$ ) [Manga and Jeanloz, 1996], iron-rich  $(\text{Mg,Fe})\text{O}$  [Wicks *et al.* 2010, 2015, 2017; Bower *et al.*, 2011], iron-rich  $(\text{Mg,Fe})\text{SiO}_3$  post-perovskite [Mao *et al.*, 2004], subducted banded iron formations [Dobson and Brodholt, 2005], and/or partial melt [Williams and Garnero, 1996; Mosenfelder *et al.*, 2009].

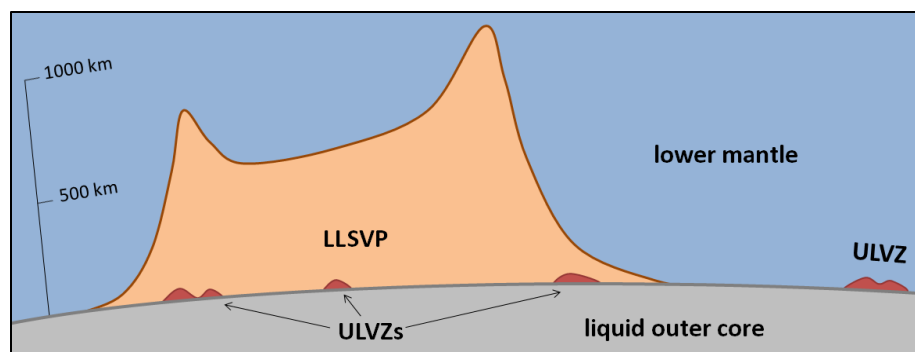


Figure 1.2: Schematic illustration of a large low shear velocity province (LLSVP) and ultra-low velocity zones (ULVZs) at the boundary between the solid lower mantle and liquid outer core.

Although many ULVZs are associated with LLSVPs and are thought to contain partial melt [Williams *et al.*, 1998], some appear uncorrelated with LLSVPs and hotspots on Earth's surface [Sun *et al.*, 2013]. These particular patches might be best explained by an enrichment of iron-rich ferropericlase, (Mg,Fe)O [Labrosse *et al.*, 2007; Wicks *et al.*, 2010; Bower *et al.*, 2011; Rost *et al.*, 2013; Wicks *et al.*, 2017]. An enhanced iron content might be the result of melting events in Earth's history and/or reactions with the iron-dominated liquid outer core. At lower mantle conditions, iron is expected to be preferentially incorporated into ferropericlase in the presence of bridgmanite or magnesium silicate post-perovskite [Kobayashi *et al.*, 2005; Auzende *et al.*, 2008; Sinmyo *et al.*, 2008; Sakai *et al.*, 2009; Tange *et al.*, 2009] and undergo a high-spin to low-spin transition. In a spin transition, the electrons pair up, which results in a smaller atomic size and, thus, a denser phase. At temperatures of the lower mantle, spin transitions occur over a range of pressures, resulting in a spin crossover region where high-spin and low-spin states coexist. The proportion of high-spin to low-spin atoms affects the density and, in turn, the buoyancy and sound velocities of ferropericlase. In order to explain ULVZs by the presence of ferropericlase, the resulting mixture must have topographic relief and wave speed reductions that match seismic observations. Numerical convection models have explored permissible compositions of ULVZs using a range of chemical density anomalies, where the buoyancy number of such a layer is determined in part by its thermal equation of state and controls its evolved topography [Bower *et al.*, 2011].

In regions of the mantle where silicate melts are thought to exist, it is important to understand the physical properties and dynamic behavior of the melts. The physical properties of silicate melts within Earth's mantle affect the chemical and thermal evolution of its interior. Composition, degree of polymerization, and iron's spin state affect such properties. The behavior of iron in silicate melts is poorly understood but, in some cases, may be approximated by iron-bearing glasses. Previous studies reached

conflicting conclusions on the coordination of iron in silicate glasses [Alberto *et al.*, 1996; Rossano *et al.*, 1999; Wilke *et al.*, 2005; Cottrell and Kelley, 2011]. There are also conflicting predictions as to whether iron in lower mantle silicate melts and glasses goes through a high-spin to low-spin transition [Nomura *et al.*, 2011; Gu *et al.*, 2012; Murakami *et al.*, 2014]. Thus, additional studies are necessary to help constrain the bonding environment and electronic state of iron in silicate melts at high pressure.

### 1.3 Thesis Overview

To improve our understanding of the complexities of the lower mantle described above, I have investigated the spin crossover behavior of iron in ferroperricite, the behavior of iron in silicate melt analogues (glasses), and the relative stability of carbonates. In Chapter 2, I discuss the experimental techniques used in this thesis: a description of diamond anvil cell preparation, X-ray powder diffraction, Mössbauer spectroscopy and UV/VIS/NIR absorption spectroscopy. The synchrotron experiments that were conducted for this thesis are summarized in Table 1.1 and the software used to fit the data are described in Table 1.2.

In Chapter 3, I discuss the results of my experiments on (Mg,Fe)O with 48 mol% FeO using synchrotron Mössbauer spectroscopy and X-ray diffraction. A spin-crossover equation of state was fitted to the pressure-volume data acquired from the X-ray diffraction patterns, revealing a gradual volume drop between about 45 and 83 GPa due to a high-spin to low-spin transition in iron. To confirm that the observed volume drop was due to a spin transition, the quadrupole splitting and isomer shift were determined from the synchrotron Mössbauer spectra. At low pressures the spectra were well explained with two high-spin ferrous sites, whereas at pressures between 44 and 84 GPa, a low-spin ferrous site with a quadrupole splitting of 0 and an increasing weight fraction with increasing pressure is required, confirming a spin crossover in iron. To systematically compare the effect of iron on the spin transition pressure, a spin-crossover equation of state was systematically fitted to the pressure-volume data from previous experiments. The spin transition pressure increases from about 50 to 80 GPa and the width of the spin transition increases from 2 to 25 GPa as the FeO content of (Mg,Fe)O increases from 10 to 60 mol%. A key implication of my experiments is that iron-rich (Mg,Fe)O at the core-mantle boundary would likely contain a significant fraction of high-spin (less dense) iron, contributing a positive buoyancy to promote topographic relief of ultra-low velocity zones in the lowermost mantle.

In Chapter 4, I present my results on silicate glasses using synchrotron Mössbauer spectroscopy, and I examine the effect of composition on the local structure of iron. The physical properties of silicate melts within Earth's mantle affect the chemical and thermal

evolution of its interior. Chemistry and coordination environments affect such properties. I measured the hyperfine parameters of iron-bearing rhyolitic and basaltic glasses up to  $\sim 120$  GPa and  $\sim 90$  GPa, respectively, in a neon pressure medium using time-domain synchrotron Mössbauer spectroscopy. The spectra for rhyolitic and basaltic glasses are well explained by three high-spin  $\text{Fe}^{2+}$ -like sites with distinct quadrupole splittings. This study is complemented by optical absorption spectroscopy measurements at room pressure and temperature. The ferrous site with a relatively low quadrupole splitting and isomer shift at low pressures may be related to a fourfold or a second fivefold ferrous iron site, which transitions to higher coordination in basaltic glass, but likely remains in low coordination in rhyolitic glass. These results indicate that iron experiences changes in its coordination environment with increasing pressure without undergoing a high-spin to low-spin transition. With the assumption that coordination environments in silicate glasses may serve as a good indicator for those in a melt, this study suggests that ferrous iron in chemically-complex silicate melts likely exists in a high-spin state throughout most of Earth's mantle.

In Chapter 5, I give a brief overview of the theoretical methods that I have implemented in this thesis. The results of my calculations on iron-free and iron-bearing carbonates are described in Chapters 6 and 7, respectively, and the type of calculations that were performed for this thesis are summarized in Table 1.3. Dolomite is one of the major mineral forms in which carbon is subducted into the Earth's mantle. End-member  $\text{CaMg}(\text{CO}_3)_2$  dolomite typically breaks down upon compression into two carbonates at 5–6 GPa in the temperature range of 800–1200 K. However, high-pressure X-ray diffraction experiments have shown that dense high-pressure polymorphs of iron-bearing dolomite may be favored over single-cation carbonates. Using density functional theory interfaced with a genetic algorithm that predicts crystal structures (USPEX), a monoclinic phase with space group  $C2/c$  was found to have lower energy at pressures above 15 GPa than all previously reported dolomite structures. I calculated the equation of state of a set of lowest-energy dolomite polymorphs with space groups  $P\bar{1}$ ,  $P2/c$ , and  $C2/c$  up to 80 GPa. Iron-free dolomite, however, has a higher enthalpy than single-cation carbonates at all pressures of the lower mantle. To investigate the effect of iron on the stability of dolomite, it is important to accurately describe the strongly correlated nature of iron's  $d$  electrons, which is poorly treated by the conventional approximations to the electron correlation (LDA or GGA) alone. Thus, an internally consistent Hubbard  $U$  was calculated with linear response theory as a function of pressure, phase and spin state. The calculated spin transition pressure in ferromagnesite and ferrodolomite is insensitive to iron concentration and depends strongly on the choice of  $U$ . My calculations demonstrate that ferrodolomite  $C2/c$  is more stable with respect to single-cation carbonate

assemblages at pressures corresponding to the upper portion of the lower mantle. Thus, high-pressure polymorphs of iron-bearing dolomite could represent an important reservoir for carbon storage within oxidized sections of Earth's mantle.

Dates	Beamline	Method	Material	Description
6/2013	ALS 12.2.2	XRD	(Mg,Fe)O	Powder XRD patterns were collected on Fp48 at 7.5- 82.9 GPa in pressure steps of 1-2 GPa
11/2013	APS 3-ID-B	SMS	(Mg,Fe)O	Time-domain SMS spectra were collected on Fp48 at 4-107 GPa with an average pressure step of ~5 GPa
11/2013	APS 3-ID-B	SMS	(Mg,Fe)O	Time-domain SMS spectra were collected on the Fp48 DAC from the ALS XRD experiments at 84-61 GPa with an average pressure step of ~6 GPa
11/2013	APS 3-ID-B	SMS	Basaltic glass	Time-domain SMS spectra were collected on basaltic glass at 2-92 GPa with an average pressure step of ~6 GPa
2/2014	APS 3-ID-B	SMS	Rhyolitic glass	Time-domain SMS spectra were collected on rhyolitic glass at 3- 81 GPa with an average pressure step of ~5 GPa
11/2014	APS 11-BM	XRD	(Mg,Fe)O	A high-quality ambient XRD pattern was collected on a finely powdered Fp48 sample to constrain the zero-pressure volume
4/2015	APS 3-ID-B	SMS	Rhyolitic glass	Time-domain SMS spectra were collected on rhyolitic glass at 94-119 GPa with an average pressure step of ~8 GPa

Table 1.1: Summary of synchrotron experiments presented in this thesis. High-pressure X-ray powder diffraction (XRD) experiments were conducted at the Advanced Light Source (ALS) at Lawrence Berkeley National Laboratory while high-pressure synchrotron Mössbauer spectroscopy (SMS) experiments were conducted at the Advanced Photon Source (APS) at Argonne National Laboratory near Chicago. Detailed compositional analyses of (Mg,Fe)O with 48 mol% FeO (“Fp48”) and silicate glasses are described in Chapter 3 and Chapter 4, respectively. A neon pressure-transmitting medium was used for all high-pressure experiments. Ruby was used as a pressure gauge with the *Mao et al.* [1987] and *Jacobsen et al.* [2008] scales for Fp48 and silicate glasses, respectively.

Software acronym	Software full name	Use of software	Reference
Fit2D	Two-dimensional detector software	Integrated powder X-ray diffraction patterns	<i>Hammersley et al.</i> [1996]
Fityk	General-purpose peak fitting program	Fitted integrated powder X-ray diffraction patterns	<i>Wojdyr</i> [2010]
MINUTI	MINeral physics UTILities	Fitted equations of state to pressure-volume data	<i>Sturhahn</i> [2015]
CONUSS	COherent NUClear resonant Scattering by Single crystals	Fitted time-domain and energy-domain Mössbauer spectra	<i>Sturhahn</i> [2000]
VESTA	Visualization for Electronical and Structural Analysis	Visualized crystal structures	<i>Momma and Izumi</i> [2008]

Table 1.2: Summary of fitting and graphing softwares used in this thesis.

Software acronym	Software full name	Description of calculations	Reference
USPEX	Universal Structure Predictor: Evolutionary Xtallography	Predicted the crystal structure of iron-free dolomite at high pressure, interfaced with VASP	<i>Oganov and Glass</i> [2006]
VASP	Vienna <i>Ab initio</i> Simulation Package	Relaxed carbonate structures as a function of pressure using density functional theory	<i>Kresse and Furthmüller</i> [1996]
QE	Quantum ESPRESSO: opEn-Source Package for Research in Electronic Structure, Simulation and Optimization	Relaxed Fe-free and Fe-bearing carbonates using density functional theory; used linear response theory to calculate the Hubbard $U$	<i>Giannozzi et al.</i> [2009]

Table 1.3: Summary of software packages used for the *ab initio* calculations in this thesis.

## Chapter 2

# Experiments

High-pressure experiments were conducted at the Advanced Photon Source (APS) at Argonne National Laboratory and the Advanced Light Source (ALS) at Lawrence Berkeley National Laboratory. Diamond anvil cells were prepared at the Diamond Anvil Cell Laboratory at Caltech prior to synchrotron experiments. Optical spectroscopy experiments were conducted at the Caltech mineral spectroscopy laboratory. In this chapter, I describe the details involved in preparing a diamond anvil cell and conducting X-ray diffraction, Mössbauer spectroscopy and optical absorption spectroscopy experiments.

### 2.1 Diamond Anvil Cell

A symmetric diamond anvil cell (DAC) is used to replicate the pressures of the Earth's interior (Figure 2.1). The apparatus that is used for the experiments in my thesis consists of a stainless steel piston and cylinder, each part holding a cylindrical seat (also known as a backing plate) with an epoxy-mounted diamond. Diamonds are gem-quality type-IA single crystals that are approximately 2 mm thick with 8 or 16 sides and a flat tip (culet) that is typically 100-600  $\mu\text{m}$  in diameter. The small surface area of the culets requires the application of a relatively small amount of force to the DAC to achieve megabar pressures.

The diamonds are mounted onto cubic boron-nitride (cBN) or tungsten carbide (WC) seats in a mounting jig where two sets of two perpendicular screws are used to align the diamond on the seat, such that the culet is centered on the aperture in the seat. Vertical screws are then tightened to close the jig and tightly secure the diamond on the surface of the seat. Epoxy is prepared by mixing Stycast 2651 resin with a catalyst in a 100:7 ratio by weight, after which it is carefully applied to the junction between the base of the diamond and seat using a needle or toothpick using a microscope (Figure 2.2). The epoxy has a low enough viscosity to adhere to the diamond and jig simultaneously, and so the needle or toothpick itself should not touch the diamond or alignment jig surface. The mounting jigs with the seated diamonds are placed on a heating plate for 6-8 hours at about 100°C.

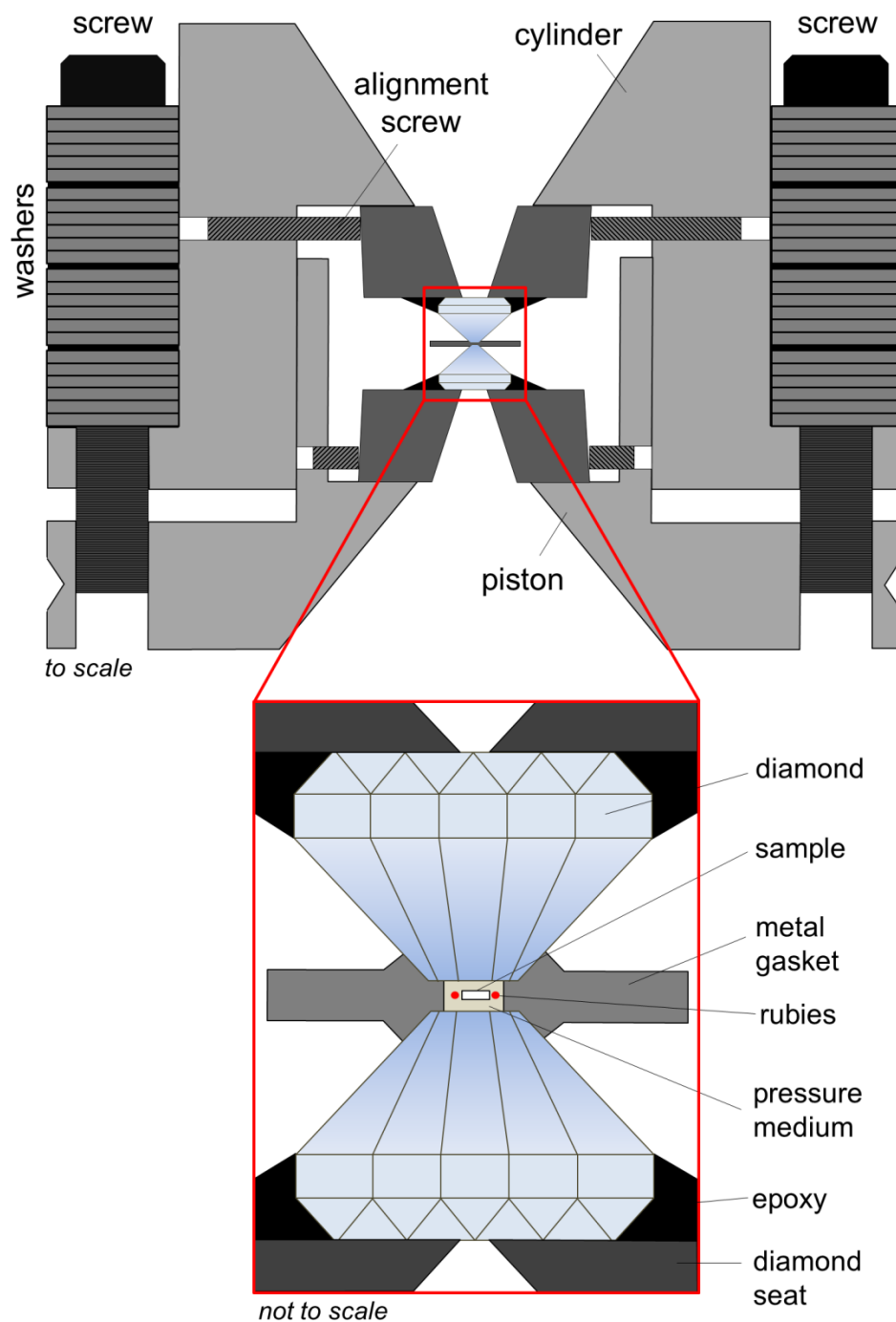


Figure 2.1: Cross section of the diamond anvil cell (DAC), from one compression screw to the opposing compression screw. Magnification shows the details of a standard sample chamber setup.

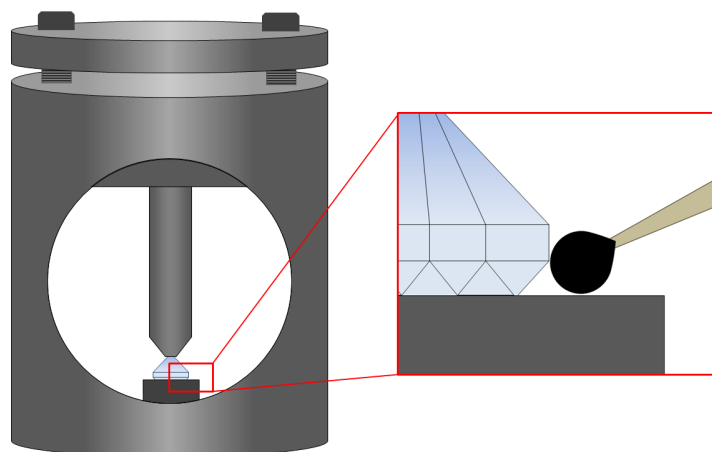


Figure 2.2: Alignment jig with a centered diamond on a CBN or WC seat. Inset shows how to apply epoxy to the base of the diamond with a toothpick while the diamond is firmly positioned on the center of the seat aperture.

After the epoxy is hardened, the seats are placed into the piston and cylinder parts of the DAC where the diamonds are shifted via alignment screws until they are translationally and rotationally aligned with respect to each other (Figure 2.3). To determine if the culets are parallel relative to each other, the diamonds are slowly brought together, aligning the diamonds translationally at various increments until the diamonds touch; this is done with an optical microscope using the on-axis setting to remove parallax effects. When touching, small refinements to the translational alignment are made. The absence of interference fringes within the small gap between the diamonds indicates that the diamonds are parallel. If the diamonds are not parallel to each other, fringes will appear where the diamonds are touching; when a small pressure is applied to the diamonds, the fringes will move towards the edge where the diamonds are further apart. To make the diamonds parallel, one may try to align them with different rotational orientations of the diamonds with respect to each other. An additional cleaning of the base of the seats and all surfaces in contact with one another may further improve alignment.

Two right-handed and two left-handed screws penetrate the length of the DAC (henceforth referred to as the compression screws) to compress the diamonds together. The screws are dressed with a column of conical spring washers that alternate in the up/down orientation in packets of three to six washers. A metal gasket (e.g., rhenium, stainless steel or beryllium) serves as a containment for the pressure medium and supports the diamonds at the edges of the culets where stresses are concentrated. Beveled diamond tips further reduce the stress gradient at the edges, allowing the diamonds to reach higher pressures. Force is applied by tightening the compression screws.

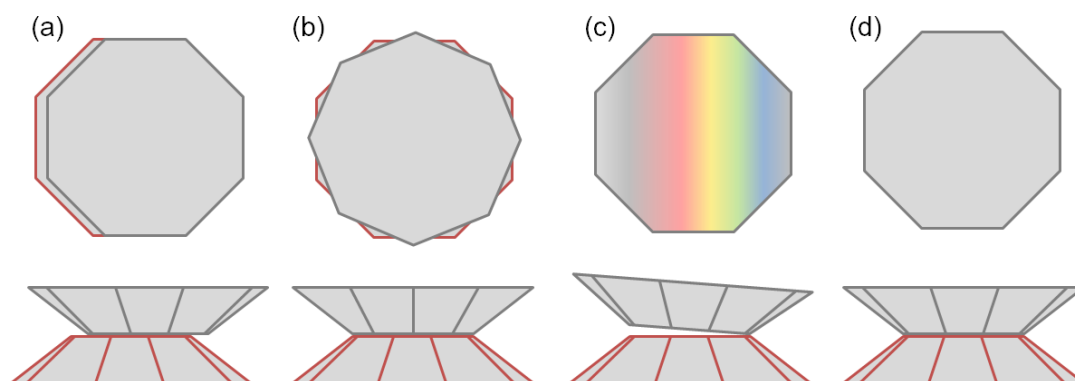


Figure 2.3: Schematic illustration of (a) translationally unaligned diamonds, (b) rotationally unaligned diamonds, (c) non-parallel diamonds and (d) aligned diamonds. The top diamond is outlined in grey and the bottom diamond is outlined in red. The first row is a view perpendicular to the culet face and the second row is parallel to the culet face. The tilt of the diamonds in (c) is exaggerated. The number of fringes observed is proportional to the tilt angle.

The metal gasket is created by drilling a hole into a pre-indented piece of metal. For the X-ray diffraction and SMS experiments presented in this thesis, a rhenium gasket was used. A 5 by 5 mm piece of rhenium metal with an initial thickness of about 200  $\mu\text{m}$  is placed between the diamonds, often aligned with the cross-hairs in the microscope to easily replicate its position in the future. It is secured in a horizontal orientation with putty or wax. After measuring the initial height of the DAC, the compression screws are turned to compress the rhenium metal between the diamonds. The height ( $h$ ) of the DAC is measured every 45-90° turn until the desired  $\Delta h$  is achieved. One should overshoot the indentation by about 10  $\mu\text{m}$  to account for the elasticity of the metal. A final thickness of 30-60  $\mu\text{m}$  is typically desired. The pre-indented metal is then drilled using an electrical, mechanical or laser drilling system to about  $\sim 1/3$  of the culet diameter for Ne loading. The gasket and diamonds are thoroughly cleaned before placing the gasket on one of the diamond culets, secured with putty or wax. The DAC is briefly closed to ensure that the gasket is situated securely on the culet.

The sample, typically on the order of 10-100  $\mu\text{m}$  in size, is loaded either into the gasket or on the opposing diamond culet. The sample should be well-centered to avoid pinching the sample and to decrease the contribution of Re peaks in X-ray diffraction experiments, as the gasket hole shrinks upon gas-loading and increasing pressure. A pressure marker is placed near the sample, avoiding the edges of the gasket. Ruby spheres

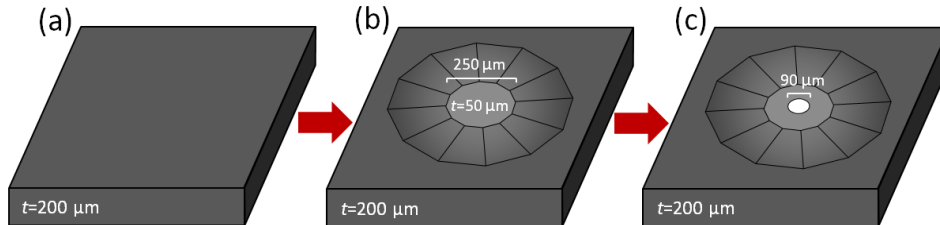


Figure 2.4: Schematic illustration of a 200- $\mu\text{m}$  metal gasket prior to indentation (a), after indentation to 50  $\mu\text{m}$  (b) and after drilling a 90- $\mu\text{m}$  hole (c).

were used as pressure gauges in the experiments presented in this thesis. Rubies ( $\text{Al}_2\text{O}_3$ ) naturally fluoresce upon stimulation by visible and ultraviolet light due to the presence of trace amounts of  $\text{Cr}^{3+}$  substituting for  $\text{Al}^{3+}$ . Ruby fluorescence spectroscopic systems typically use a green 532 nm laser to excite the  $\text{Cr}^{3+}$  ions. After the  $\text{Cr}^{3+}$  ion is excited from the  ${}^4A_2$  ground state to the  ${}^4F_2$  and  ${}^4F_1$  states, it immediately transitions to the metastable  ${}^2E$  state until a photon having the right energy can de-excite it. The  ${}^2E$  state is split into the  $\bar{E}$  and  $2\bar{A}$  states with a separation of  $29\text{ cm}^{-1}$ . The transitions,  $\bar{E} \rightarrow {}^4A_2$  and  $2\bar{A} \rightarrow {}^4A_2$  are the  $R_1$  and  $R_2$  lines at 694.3 and 692.9 nm, respectively, at room temperature and pressure. The  $R_1$  and  $R_2$  peaks shift to higher wavelengths with decreasing volume (i.e., increasing pressure and/or decreasing temperature) (Figure 2.5). The shift of the  $R_1$  and  $R_2$  peaks have been calibrated in various pressure mediums against materials with known equations of state, such as against Cu and Ag in an Ar pressure medium [Mao *et al.*, 1986], against MgO in a He pressure medium [Jacobsen *et al.*, 2008], and against transition metals in a He pressure medium [Dewaele *et al.*, 2008]. In our high-pressure experiments, the fluorescence spectra of the ruby spheres are measured before and after each experiment, such that each compression point typically has four measurements.

After loading the ruby sphere(s) next to the sample, the DAC is closed and the compression screws are inserted to prepare for gas-loading. To ensure that the sample chamber is not sealed completely, the gasket is checked for interference fringes, which indicate that the diamonds are touching the gasket without the force required to seal the chamber. The sample chamber is then loaded with a pressure-transmitting medium (Ne in the experiments presented in this thesis) using the gas-loading system at Caltech [see Rivers *et al.*, 2008]. The diamond anvil cell is placed into a specially-designed holder with hex screws that fit into the compression screws of the DAC. The holder is then placed into the gas-loading system, aligning the hex socket screws of the holder with the remotely-controlled hex screws in the gas-loading system. After closing the gas-loading system, an EPICS control screen is used to turn the motors and open/close the valves.

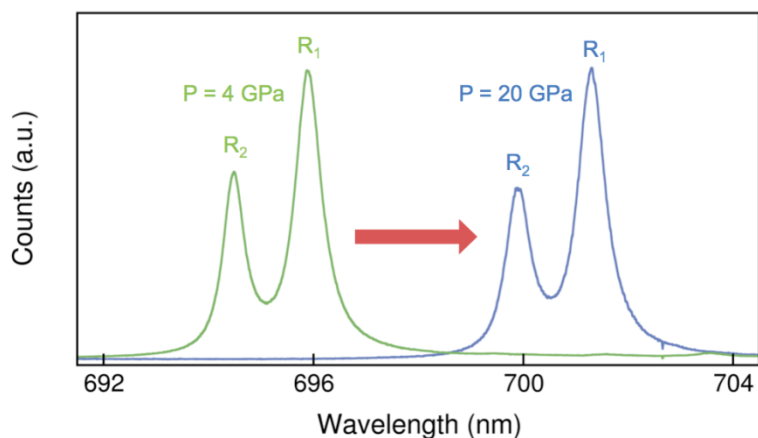


Figure 2.5: Ruby fluorescence spectra at 4 and 20 GPa, demonstrating the shift of the  $R_1$  and  $R_2$  peaks to higher wavelengths with increasing pressure [ruby scale from *Mao et al.*, 1986].

First, the pressure vessel is filled from the lecture bottle. Then, the compressor pumps the high-pressure system to >25,000 PSI. The compressor pressurizes the vessel for 10-15 min, after which the cell is sealed by turning the compression screws with the remotely-controlled hex ends. A ruby fluorescence system is used to determine when the sample chamber is at the desired pressure (typically  $\sim 1$  GPa). Finally, the pressure vessel is vented, the Ne gas is recaptured into the lecture bottle and the DAC is carefully removed from the gas-loading system.

## 2.2 X-ray Diffraction

Powder X-ray diffraction is frequently used to determine the unit-cell volume of a crystal as a function of pressure and/or temperature. Beamline 12.2.2 at the Advanced Light Source in the Berkeley National Lab provides enough photons, which are subsequently filtered with a Si(111) monochromator to eV bandwidth and focused to a spot size of about 10 by 10  $\mu\text{m}^2$  (with wider tails), required for the small sample size used in diamond anvil cells. When the X-rays reach the sample, they are diffracted from the planes of atoms of the crystallites according to Bragg's Law:

$$n\lambda = 2d\sin\theta, \quad (2.1)$$

where  $\lambda$  is the wavelength of the X-ray beam,  $d$  is the interplanar spacing of the crystal and  $\theta$  is the diffraction angle. In other words, X-rays diffracted from equivalent planes will interfere constructively when the angle between the incoming X-ray and the plane results in a path-length difference that is an integer multiple of the wavelength of the X-ray. A diffraction pattern is collected on a MAR345 image plate. A beamstop blocks the

unscattered photons from damaging the image plate (Figure 2.6). The sample-to-detector distance is determined every 12-24 hours using a calibrated  $\text{LaB}_6$  or  $\text{Ce}_2\text{O}_3$  standard.

The DAC is situated on the sample stage via a magnetic base such that the diamonds are oriented along the beam path, after which the sample chamber is roughly centered on the beam path with the camera view. Moving the sample stage in the vertical and horizontal directions while the shutters are open (i.e., X-ray beam is enabled), allows us to center the sample chamber on the X-ray due to the fact that the rhenium gasket has a stronger absorption contrast of X-rays than the sample and sample chamber, due to its relatively high atomic number. Trial XRD patterns may be collected on several spots on the sample to find the optimal diffraction pattern. It is desirable to have multiple sample diffraction rings or reflections with minimal overlap with reflections from other materials in the sample chamber (gasket material, pressure medium, pressure gauges, etc.) and it is best to avoid bright diamond peaks and secondary diamond rings. If the diamond Bragg reflections are strong, the DAC may be rotated by  $1\text{-}2^\circ$ .

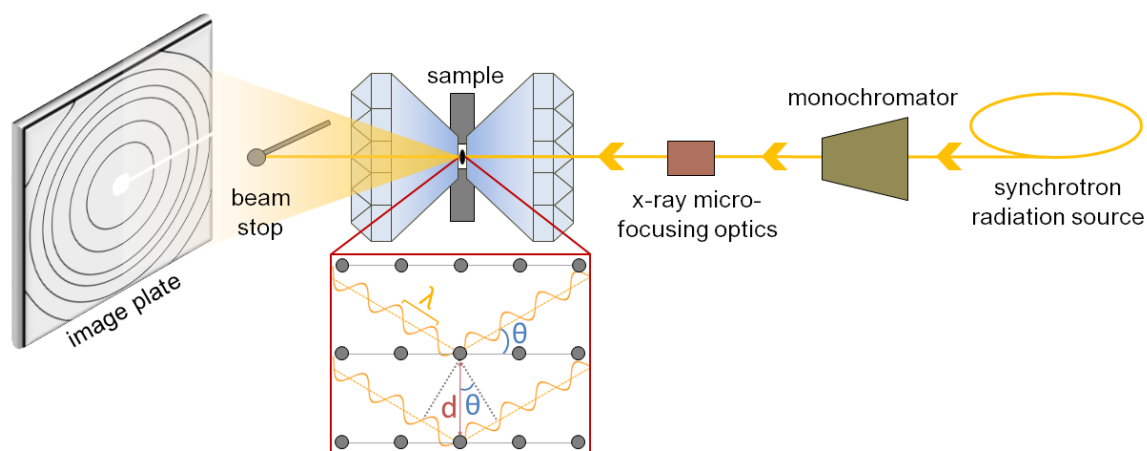


Figure 2.6: Synchrotron X-ray diffraction setup at beamline 12.2.2 at the Advanced Light Source. A Si(111) monochromator filters the synchrotron radiation source to eV bandwidth after which it is focused to a spot size of about  $10$  by  $10 \mu\text{m}^2$  with microfocusing mirrors. A high-resolution image plate (MAR345) is inserted in the forward direction to collect a diffraction pattern. The beamstop blocks the direct (unscattered) photons from damaging the image plate. Below the sample is a schematic magnification of the X-rays scattering at angle  $\theta$  off of two equivalent planes of atoms separated by distance  $d$ .

X-ray diffraction patterns were integrated with the Fit2D software [Hammersley *et al.*, 1996]. The calibrant diffraction pattern is imported to refine the sample-to-detector distance and angle, after which the diffraction pattern of the sample is imported. Bright diamond reflections, oversaturated sample reflections (e.g., from larger crystallites) and the beamstop may be removed from the final pattern by using the masking feature. After integrating the diffraction pattern, relatively simple diffraction patterns such as those

presented here can be fitted with the Fityk software [Wojdyr 2010] using a Gaussian or Voigt peak shape.

For a crystal with cubic symmetry the volume of the unit cell is simply:

$$V = d^3(h^2 + k^2 + l^2)^{3/2}, \quad (2.2)$$

where  $h$ ,  $k$  and  $l$  correspond to Miller indices of a plane and  $d$  is the interplanar spacing between the corresponding planes. The structure factor,

$$F = \sum_{j=1}^N f_j e^{[-2\pi i(hx_j + ky_j + lz_j)]} \quad (2.3)$$

determines which reflections are allowed and the intensity of those reflections where  $x_j$ ,  $y_j$  and  $z_j$  are the fractional coordinates of the  $j^{\text{th}}$  atom and  $f_j$  is the atomic scattering factor of the  $j^{\text{th}}$  atom. For face-centered cubic unit cells (e.g., ferropericlase with space group  $Fm\bar{3}m$ ), Miller indices that are all odd or even result in  $F=4f$  while Miller indices that are mixed result in  $F=0$ . Thus, we observe the reflections corresponding to the (111), (200), (220), (311), ... planes in ferropericlase (Figure 2.7).

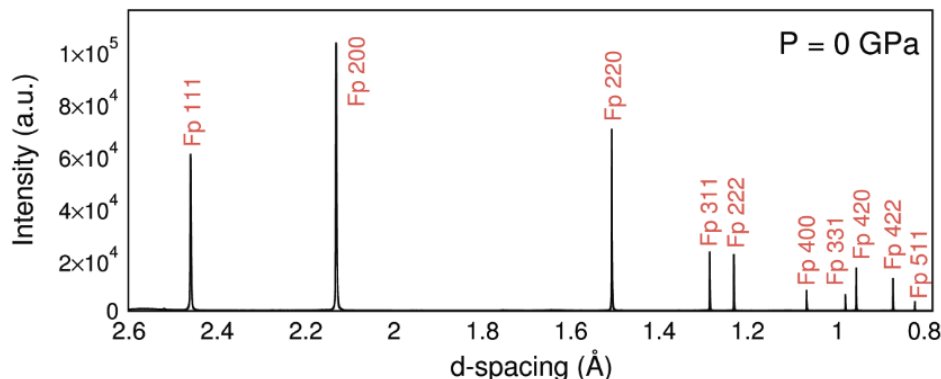


Figure 2.7: Ambient X-ray diffraction pattern for (Mg,Fe)O with 48 mol% FeO, collected at Sector 11-BM at the Advanced Photon Source ( $\lambda = 0.45900 \text{ \AA}$ ), demonstrating the Bragg reflections in face-centered cubic (Mg,Fe)O in this range of  $d$ -spacings.

## 2.3 Mössbauer Spectroscopy

Any particle or molecule that emits or absorbs radiation must recoil to conserve energy and momentum. However, in 1957 Rudolph Mössbauer discovered that if an atom is bound in a solid, a fraction of the nuclei will emit or absorb radiation without individually recoiling. Instead, the whole lattice recoils and the energy of the emitted gamma ray is essentially equal to the resonant energy of that nucleus because the recoil energy is inversely related to the mass of the recoiling system, and so the recoil energy of

the lattice becomes negligible. This phenomenon is known as the Mössbauer effect, and is the basis for Mössbauer spectroscopy.

Mössbauer spectroscopy probes the electronic, nuclear and structural environment of elements with certain resonant nuclei, such as  $^{57}\text{Fe}$ ,  $^{119}\text{Sn}$ ,  $^{151}\text{Eu}$ ,  $^{121}\text{Sb}$  and  $^{161}\text{Dy}$ . Iron is geologically relevant, often substituting for magnesium in minerals, such as oxides, silicates and carbonates. In this thesis, I use the  $^{57}\text{Fe}$  isotope to study the behavior of iron in ferropericlase and iron-bearing silicate glasses, which have been enriched in  $^{57}\text{Fe}$ .

In conventional Mössbauer spectroscopy, a radioactive  $^{57}\text{Co}$  source decays to  $^{57}\text{Fe}$  in a resonant state 14.4125 keV above its ground state. When the excited  $^{57}\text{Fe}$  nucleus decays, it emits a 14.4125 keV gamma ray. A sample containing  $^{57}\text{Fe}$  is placed next to the source to absorb the 14.4125 keV gamma ray. However, the nuclear resonant energy in the sample is very slightly affected by the electronic, magnetic and local structural environment of the atom, and the  $^{57}\text{Fe}$  atoms in the sample will only absorb and emit the gamma ray if the energy is equal to the resonant energy in that particular lattice. To provide the energy needed to excite the  $^{57}\text{Fe}$  atoms in the sample, very small changes to the energy of the gamma ray are created by moving the source relative to the sample, exploiting the Doppler effect.

The difference between the energy required to excite the  $^{57}\text{Fe}$  in the sample and the resonant energy of  $\alpha$ -iron (or a reference material containing  $^{57}\text{Fe}$ ) is the isomer shift (sometimes referred to as the chemical or center shift). An isomer shift arises from a difference in the  $s$  electron density at the nucleus in the sample relative to the reference material. The  $s$  electron density at the nucleus is affected by shielding effects from outer orbital electrons. Ferrous iron has a lower  $s$  electron density than ferric iron due to greater screening from the  $d$  electrons (ferrous iron has six  $d$  electrons while ferric iron has five  $d$  electrons), resulting in a larger isomer shift. Thus, the isomer shift is useful for determining the valence state of iron. It is most frequently reported in units of mm/s, the Doppler velocity (also referred to as the source velocity).

Nuclei with an angular quantum number greater than  $I=1/2$  have a non-spherical charge distribution, which creates a nuclear quadrupole moment. The isotope  $^{57}\text{Fe}$  has an excited state quantum number of  $I=3/2$  that splits into two substates  $m_I=\pm 1/2$  and  $m_I=\pm 3/2$ . In an electric field gradient, the resonant energy level is split into two by a separation width referred to as the quadrupole splitting. The electric field gradient is created by an asymmetric electronic charge distribution in incompletely filled outer shells of the atom itself or by charges from neighboring atoms. If the electron cloud is symmetric, then there is no electric field gradient or quadrupole splitting. The quadrupole splitting is influenced by the valence state, spin state, magnetic field at the nucleus, site distortion and coordination number.



a high-spin to low-spin transition, resulting in a symmetric valence charge distribution and the collapse of the quadrupole splitting to  $\sim 0$  mm/s. Sixfold  $\text{Fe}^{3+}$  has a smaller quadrupole splitting than  $\text{Fe}^{2+}$ , typically between 0.2 and 1.5 mm/s, mostly due to the lack of a Jahn-Teller distortion and a more symmetric valence charge distribution. Sixfold  $\text{Fe}^{3+}$  experiences an increase in the quadrupole splitting upon transition to the low-spin state due to the increase in asymmetry of the valence charge distribution.

The development of the synchrotron branch of nuclear resonant scattering was initiated by the pioneering experimental work of *Gerdau et al.* [1985]. In time-domain nuclear forward scattering, also known as synchrotron Mössbauer spectroscopy [*van Bürck et al.*, 1992; *Alp et al.*, 1994; *Sturhahn et al.*, 1996], the synchrotron X-ray source, in the form of electron bunches, is pulsed, tuned to 14.4125 keV with a high-resolution monochromator, and focused on the sample with microfocusing optics. The X-rays with 14.4125 keV energy excite all resonant nuclei in the beam path. As the nuclei decay, they emit photons with energies ( $\sim \mu\text{eV}$ ) corresponding to their hyperfine fields. An avalanche photodiode detector with a large dynamic range and ns time resolution, placed in the forward direction, collects the elastically and coherently scattered photons (Figure 2.9). The number of delayed photons is recorded as a function of time. For a thin sample without a quadrupole or magnetic splitting, the spectrum, when plotted as the logarithm of photon counts versus time, appears as a negative linear function corresponding to an exponential decay with the natural lifetime of the excited  $^{57}\text{Fe}$  atoms. The short X-ray pulses excite the different nuclear transitions simultaneously. This process is analogous to a set of oscillators with small energy differences that are excited in phase. After the X-ray pulse passes, de-excitation of each oscillator occurs with slightly different lifetimes, leading to accumulating phase shifts and destructive and constructive interference phenomena at specific delay times. This process describes well the oscillations in the decay of forward-scattered radiation [e.g., *Sturhahn*, 2004]. Due to self-absorption effects, a thick sample produces aperiodic oscillations, known as dynamical beats, and must be carefully treated during the fitting procedure. The time-domain spectrum can be Fourier transformed to the energy domain. The effect of source broadening does not exist in time-domain SMS, and so the “distributions” observed in SMS are only a result of the distribution of hyperfine parameters of a particular site, allowing one to detect sites with small abundances that may be hidden beneath broad peaks in energy-domain Mössbauer spectra.

Mössbauer spectra are analyzed with the CONUSS (COherent NUclear resonant Scattering by Single crystals) software [*Sturhahn*, 2000]. CONUSS uses a least-square algorithm to fit iron's hyperfine parameters (e.g., isomer shift, magnetic field, quadrupole splitting and distribution of the quadrupole splitting expressed as the full width at half

maximum) and material properties (e.g., effective thickness, thickness distribution and relative weights of the sites). The effective thickness ( $\eta$ ) is the product of the volume density of the resonant nuclei ( $\rho$ ), nuclear resonant cross section ( $\sigma$ ), Lamb-Mössbauer factor ( $f_{LM}$ ) and the sample thickness ( $D$ ). Prior to experiments, the effective thickness is calculated to determine the optimal physical thickness for sample loading. Version 2.1.1 of CONUSS has the added capabilities of (1) performing a simultaneous (or dual) fit of the spectrum with and without the reference foil and (2) fitting a correlation strength for the quadrupole splitting and isomer shift distributions, which is particularly useful for fitting spectra of silicate glasses. Mössbauer spectra of silicate glasses are characteristically asymmetric, with the low-velocity peak more intense and narrow than the high-velocity peak (in the energy domain), and require correlated distributions to fit the spectral asymmetry (see Chapter 4 for more details). The dual-fit method is particularly useful in constraining the most likely model in situations where more than one model fits the individual spectra of the sample or sample with a reference absorber, and is also more time-efficient and more physically accurate compared to fitting the spectra individually.

A correlation matrix is output after fitting the spectrum, giving the normalized covariance between each pair of fitted parameters, where perfect correlation corresponds to  $\pm 1$  and a lack of correlation corresponds to 0. The degree of correlation between parameters is incorporated into the fitting error of each parameter. When the sample contains multiple iron sites, the number of unknown parameters may be larger than can be fitted with a least-square algorithm due to parameter correlations. In this case, it is useful to perform a Monte Carlo search to find the optimal parameters and to keep fixed parameters that are highly correlated. Chapters 3 and 4 discuss these situations for the cases of the (Mg,Fe)O and silicate glass spectra.

Once the spectrum or spectra at the first pressure are fitted with a satisfactory model, those parameters serve as starting values for the next compression point. Generally, the quadrupole splitting values and distributions gradually increase with increasing pressure due to an increase in the degree of distortion of iron's local site environment while the isomer shift gradually decreases with increasing pressure due to an increase in the  $s$  electron density at the nucleus relative to the reference absorber. Discontinuous changes in the spectra as a function of pressure typically indicate the onset of a phase or spin transition, at which point the introduction of additional sites may be required.

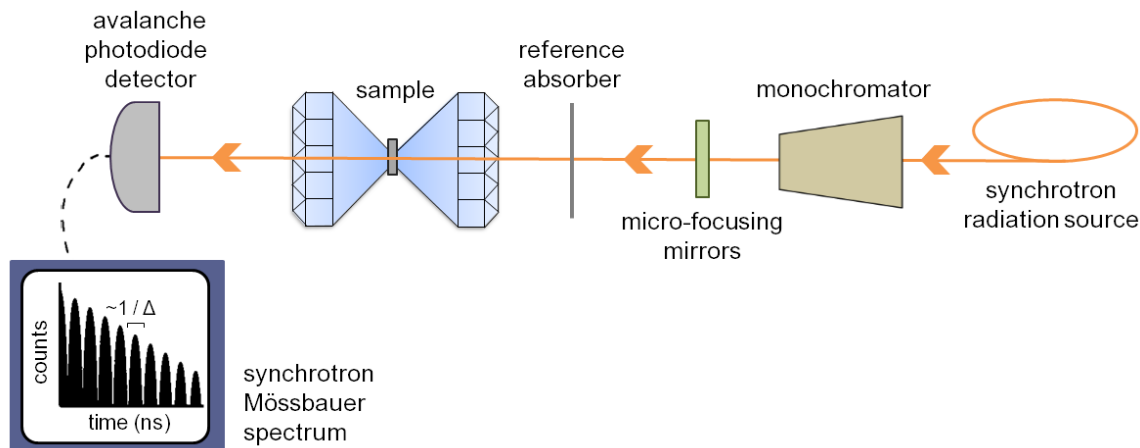


Figure 2.9: A typical time-domain synchrotron Mössbauer spectroscopy (SMS) experimental setup at Sector 3-ID-B of the Advanced Photon Source (APS) at Argonne National Laboratory. The synchrotron X-ray source passes through the high-resolution monochromator at 14.4125 keV, the energy required to excite a  $^{57}\text{Fe}$  nucleus. The avalanche photodiode detector is situated in the forward scattering direction to measure the elastic and coherently scattered photons. A reference absorber, typically a well-characterized stainless steel foil, may be placed in the beam path for isomer shift measurements.

## 2.4 Optical Spectroscopy

Ultraviolet/visible/near-infrared (UV/VIS/NIR) absorption spectroscopy experiments [Rossman, 1988; Langer *et al.*, 1996] were conducted at the Caltech mineral spectroscopy laboratory. A Nicolet iS50 Fourier-Transform-Infrared (FT-IR) spectrometer with  $\text{CaF}_2$ , KBr and  $\text{SiO}_2$  beamsplitters and InGaAs and deuterated triglycine sulfate detectors is used for wavenumbers below about  $10000\text{ cm}^{-1}$ . Above about  $10000\text{ cm}^{-1}$ , a Si diode array spectrometer is used. The setup for FT-IR absorption experiments is schematically illustrated in Figure 2.10. In this setup, radiation from a source, typically a silicon-nitride element or a tungsten-halogen lamp, is passed through a beamsplitter. Half of the radiation is reflected from a fixed mirror while the other half is reflected from a moving mirror. When the two beams recombine at the detector, an interference pattern is produced, and a He-Ne laser is directed through the interferometer as a frequency reference.

To prepare for an optical absorption experiment, the sample must be polished to achieve flat and horizontal surfaces and uniform thickness, while being optically translucent or transparent (see below). The sample is typically placed on a metal plate with the largest aperture possible to achieve the best signal-to-noise ratio. The sample chamber of the FT-IR spectrometer is purged with dry gas to reduce absorption bands associated with atmospheric  $\text{H}_2\text{O}$  and  $\text{CO}_2$  in the infrared region. Absorption spectra are collected with and without the sample in the beam path, the latter serving as the

background. Spectra should be averaged over a sufficient number of scans to resolve the desired absorption features.

The absorption of the light that passes through a sample varies linearly with the concentration of the absorbing species, the thickness of the sample and the probability of the absorption. This relationship is known as the Beer-Lambert law:

$$A = \log\left(\frac{I_0}{I}\right) = \epsilon lc, \quad (2.4)$$

where  $A$  is the absorbance,  $I_0$  is the intensity of light entering the sample,  $I$  is the intensity of light leaving the sample,  $\epsilon$  is the extinction coefficient (a measure of the probability of absorption),  $l$  is the sample thickness and  $c$  is the concentration of the absorbing species.

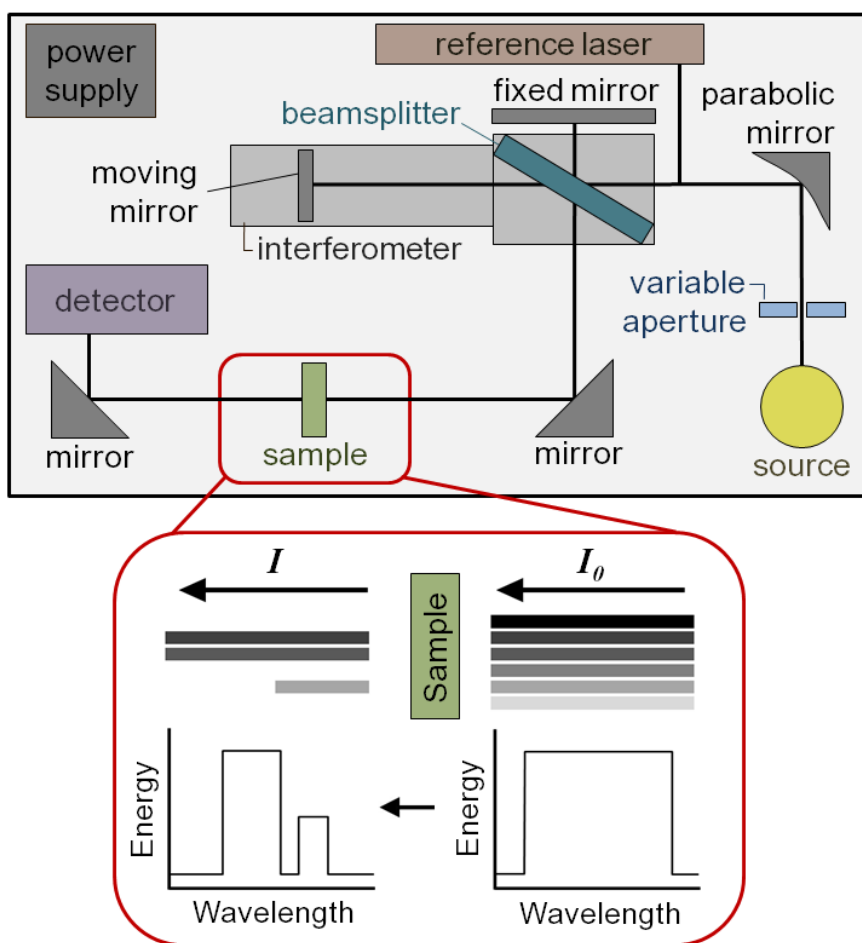


Figure 2.10: Schematic illustration of a FT-IR UV/VIS/NIR spectrometer. Radiation from a source passes through a beamsplitter. Half of the radiation is reflected from a fixed mirror while the other half is reflected from a moving mirror. When the two beams recombine, an interference pattern is produced. A Ne-He reference laser ( $\lambda=632.8$  nm) is directed through the interferometer as a frequency reference. Inset shows the absorption of certain wavelengths of light by a sample.

Radiation is absorbed through rotational, vibrational and electronic transitions within the sample. The exact wavenumbers associated with absorption depend on selection rules, which are governed by the types of atoms present, their oxidation states and their local coordination environments. Rotational transitions typically require lower energies, occurring at wavenumbers of  $400 - 10 \text{ cm}^{-1}$  (far-IR and microwave regions). Overtone and harmonic vibrations occur at  $14000 - 4000 \text{ cm}^{-1}$  (near-IR region). Electronic transitions due to the rearrangement of  $d$  electrons in transition row elements typically occur in the range of  $25000 - 5000 \text{ cm}^{-1}$  (VIS and near-IR regions) while electronic transitions due to charge transfer between cations and anions require larger energies and occur at  $50000 - 30000 \text{ cm}^{-1}$  (UV region). Particularly relevant to this thesis are the absorption bands associated with iron cations. Electronic transitions in ferrous iron in sixfold and fourfold coordination typically occur in the near-IR region at around  $10000 \text{ cm}^{-1}$  and  $5000 \text{ cm}^{-1}$ , respectively [Goldman and Rossman, 1977; Burns, 1985; Rossman and Taran, 2001], while ferric iron absorption bands occur in the visible region near  $20000 \text{ cm}^{-1}$  [Waychunas and Rossman, 1983; Mattson and Rossman, 1984]. Additional absorption features will not be discussed here, but have been summarized in detail in Rossman [2014].

## Chapter 3

# Equation of State and Spin Crossover of (Mg,Fe)O\*

\* This chapter has been reformatted from what was previously published as: Solomatova, N. V., Jackson, J. M., Sturhahn, W., Wicks, J. K., Zhao, J., Toellner, T. S., Kalkan, B., Steinhardt, W. M. (2016): Equation of state and spin crossover of (Mg,Fe)O at high pressure, with implications for explaining topographic relief at the core-mantle boundary, *American Mineralogist*, 101, 1084-1093, doi:10.2138/am-2016-5510.

### 3.1 Introduction

Earth's lower mantle occupies more than half of Earth's volume, and is expected to be composed primarily of bridgmanite, calcium silicate perovskite and iron-bearing periclase. Although it is suggested that (Mg,Fe)O (“ferropericlase”) represents a significant volume fraction of Earth's interior, the concentration of iron in (Mg,Fe)O at conditions considered to be present in the lower mantle is largely uncertain and not very well constrained by known data. Just above the core-mantle boundary, an enhanced iron content may be found due to melting events in Earth's history and/or reactions with the iron-dominated liquid outer core. In this region, seismologists have observed 5-40 km thick patches of ultra-low velocity zones (ULVZs), often located at the edges of large low shear velocity provinces [Garnero and Helmberger, 1996; McNamara et al., 2010; Rost, 2013]. These zones are thought to be composed of an iron-bearing layer of FeO and FeSi [Manga and Jeanloz, 1996], iron-rich (Mg,Fe)O [Wicks et al., 2010; Bower et al., 2011; Wicks et al., 2015], iron-rich (Mg,Fe)SiO<sub>3</sub> post-perovskite [Mao et al., 2004], subducted banded iron formations [Dobson and Brodholt, 2005], and/or partial melt [Williams and Garnero, 1996; Mosenfelder et al., 2009].

Periclase and wüstite are two end-members of the MgO-FeO solid solution with magnesiowüstite describing the iron-rich compositions and ferropericlase the magnesium-rich compositions. Under lower mantle conditions, iron is expected to be preferentially incorporated into ferropericlase when in the presence of bridgmanite and magnesium silicate post-perovskite [Auzende et al., 2008; Kobayashi et al., 2005; Sinmyo et al., 2008; Sakai et al., 2009]. However, there is disagreement in the experimental and computational data for the (Mg,Fe)O solid solution regarding magnetic ordering, spin crossovers, and phase transitions [Badro et al., 2003; Lin et al., 2005; Kantor et al., 2006;

*Lin et al.*, 2007]. At ambient conditions, (Mg,Fe)O exhibits the space group  $Fm\bar{3}m$  with  $Mg^{2+}$  and high-spin  $Fe^{2+}$  atoms located in octahedral coordination environments. Periclase (MgO) remains cubic (B1) throughout the Earth's mantle pressures and temperatures [*Duffy and Ahrens*, 1993], while wüstite (FeO) experiences a rhombohedral distortion at upper mantle pressures and transforms to the B8 structure at pressures of the lower mantle [*Yagi et al.*, 1985; *Fei and Mao*, 1994; *Mao et al.*, 2002; *Fischer et al.*, 2011]. For iron-rich (Mg,Fe)O, the rhombohedral distortion may be coupled to a magnetic-ordering transition from a paramagnetic (disordered) to antiferromagnetic (oppositely ordered) state [*Mao et al.*, 1996; *Speziale et al.*, 2005; *Fujii et al.*, 2011; *Zhang et al.*, 2012]. However, it is uncertain if (Mg,Fe)O with 48 mol% FeO experiences a rhombohedral and/or magnetic-ordering transition.

At higher pressures, it is known that iron in iron-poor (Mg,Fe)O undergoes a spin crossover, resulting in a ~10% decrease in iron's ionic radius [*Tsuchiya et al.*, 2006]. A reduction in volume for iron-poor (Mg,Fe)O has been shown to affect seismically-relevant properties, such as sound velocities and density [*Antonangeli et al.*, 2011; *Jackson et al.*, 2006; *Lin et al.*, 2006b; *Marquardt et al.*, 2009a, 2009b]. The spin crossover pressure is a function of iron concentration in ferropericlase [*Sturhahn et al.*, 2005; *Tsuchiya et al.*, 2006; *Persson et al.*, 2006; *Fei et al.*, 2007]; however, scatter in reported transition pressures is large. Additionally, there is uncertainty about the effect of temperature on the spin transition pressure and broadness of the crossover. Probing the entire solid solution of (Mg,Fe)O is essential for our understanding of the behavior of iron within the ferropericlase lattice. In this study, we use X-ray diffraction and time-domain synchrotron Mössbauer spectroscopy to determine the high-pressure equation of state and hyperfine parameters for (Mg,Fe)O containing 48 mol% FeO.

## 3.2 Experiments and Data Evaluation

### 3.2.1 Sample Synthesis

The polycrystalline (Mg,Fe)O sample was synthesized by grinding together  $^{57}Fe_2O_3$  and MgO and then firing the powder in an  $H_2/CO_2$  gas-mixing furnace for about 20 hours at 1400 °C, after which it was reground and reheated for an additional 20 hours at the same temperature with the same  $H_2/CO_2$ . The measured oxygen fugacity,  $\log(fO_2)$  was about -0.9. Electron microprobe analysis identifies the composition as  $(Mg_{0.490(3)}Fe_{0.483(2)}Ti_{0.027(5)})O$ , hereafter referred to as Fp48. Titanium originated from the  $^{57}Fe_2O_3$  starting material purchased from AMT Ventures Pte, Ltd.

### 3.2.2 X-ray Diffraction

The isothermal equation of state for (Mg,Fe)O with 48 mol% FeO was determined using X-ray diffraction at 300 K. A symmetric diamond-anvil cell was prepared with two beveled anvils, each with 300- $\mu\text{m}$  culet diameters, mounted with epoxy on WC backing plates. A 130- $\mu\text{m}$  hole with a pre-indented thickness of 43  $\mu\text{m}$  was drilled in a rhenium gasket. Polycrystalline Fp48 was ground to a fine powder, pressed into a 10- $\mu\text{m}$  thick pellet ( $\sim 40 \times 40 \mu\text{m}^2$ ), then loaded on the diamond culet and two 11- $\mu\text{m}$  ruby spheres were loaded on the opposing diamond anvil. Neon was loaded into the sample chamber using a newly designed gas-loading system at Caltech. After the sample chamber was loaded with neon, the gasket hole diameter decreased to 90- $\mu\text{m}$ .

High-pressure X-ray diffraction experiments were conducted at Beamline 12.2.2 at the Advanced Light Source (ALS) of Lawrence Berkeley National Laboratory. The incident energy was set to 30 keV ( $\lambda=0.41328 \text{ \AA}$ ) with a beam full width at half maximum of about 10  $\mu\text{m}$  by 10  $\mu\text{m}$ . A high-resolution image plate (MAR345) was used to collect diffraction patterns. The calibration standard used was LaB<sub>6</sub>. A fine grid was sampled throughout the sample chamber until the optimal XRD pattern was collected. X-ray diffraction patterns were collected at 44 different pressures, in intervals of 1-2 GPa from 7.5 to 82.9 GPa with an average pressure drift of 0.4 GPa. *Ex situ* pressure determinations were collected on the two rubies before and after each set of XRD measurements, using the ruby fluorescence pressure scale reported in *Jacobsen et al.* [2008]. XRD patterns were integrated with Fit2D [*Hammersley et al.*, 1996] and analyzed with the curve-fitting program, Fityk [*Wojdyr*, 2010]. Pressure errors for the ALS XRD experiments were determined from the standard deviation between the four ruby measurements. The 111 reflection was not resolvable at all pressures, either due to peak overlap or oversaturation on the image plate and was thus not included in this analysis. An ambient diffraction pattern was collected at Sector 11-BM of the Advanced Photon Source at Argonne National Laboratory, using a calibrated incident energy of 27 keV (0.45900  $\text{\AA}$ ). Powdered Fp48 was loaded into a Kapton capillary tube between amorphous silica such that only the Fp48 sample was in the beam path.

### 3.2.3 Synchrotron Mössbauer Spectroscopy

The hyperfine interactions, namely the quadrupole splitting and isomer shift, of Fp48 were determined with time-domain synchrotron Mössbauer spectroscopy (SMS). The isomer shift is proportional to the *s* electron density at the nucleus, and hence is indirectly influenced, via shielding effects, by the *d* electron population in the valence shell. The isomer shift thus provides information that helps determine the valence (i.e., oxidation) state. A quadrupole splitting is observed when an inhomogeneous electric field

at the Mössbauer nucleus is present. In general, two factors can contribute to the electric field gradient, an electron distribution in the valence shell and/or a nearby lattice environment with non-cubic symmetry. Thus, the quadrupole splitting yields information on local structure and, complementary to the isomer shift, the oxidation state and spin state.

A diamond anvil cell was assembled with two beveled 250- $\mu\text{m}$  diamonds on WC seats for the SMS measurements. A rhenium gasket was prepared by drilling a hole with a 50- $\mu\text{m}$  thickness and 80- $\mu\text{m}$  diameter, which was then loaded with a powdered Fp48 sample (with a 10-20  $\mu\text{m}$  grain size). A 10- $\mu\text{m}$  ruby sphere was placed on the other diamond culet as a pressure gauge. Upon gas-loading the sample chamber with neon at Caltech, the gasket hole diameter decreased to  $\sim 65$   $\mu\text{m}$ .

The SMS measurements were conducted at Sector 3-ID-B of the Advanced Photon Source (APS). The storage ring was operated in top-up mode with 24 bunches separated by 153 ns. A high-resolution monochromator was tuned around the nuclear resonance energy of  $^{57}\text{Fe}$  with a FWHM of 1 meV [Toellner *et al.*, 2000]. An APD detector was positioned downstream in the forward direction to measure the time spectra. X-ray energy was tuned to 14.4125 keV (the  $^{57}\text{Fe}$  nuclear transition energy). The beam was focused to an area of 10 by 11  $\mu\text{m}^2$  using a Kirkpatrick-Baez mirror system [Zhang *et al.*, 2015]. A time window of 20 to  $\sim 130$  ns after excitation was used to observe nuclear resonant scattering and fit the data. At each compression point, an SMS spectrum was collected for the sample with and without  $^{57}\text{Fe}$ -enriched stainless steel (SS) foil with a physical thickness of 2  $\mu\text{m}$ . The stainless steel foil is placed in the downstream direction as a reference absorber for isomer shift measurements. The isomer shift between the SS foil and  $\alpha$ -iron metal was measured to be  $-0.1225(9)$  mm/s. To achieve high-statistical quality spectra, collection time ranged from about 30 min with the SS foil to 45 min without the SS foil. Pressure was measured before and after the SMS data collection with ruby fluorescence at GSE-CARS of the APS. The average pressure drift was 0.5 GPa. Decompression SMS data were collected for the DAC from our ALS XRD experiments. The sample was decompressed from  $\sim 84$  GPa to 61 GPa with an average pressure interval of 5.8 GPa.

### 3.3 Results

#### 3.3.1 Equation of State

Representative integrated XRD patterns for Fp48 are shown in Figure 3.1, and calculated volumes and densities are reported in Table 3.1. Although the FWHM values are scattered at low pressures and display a shallow slope at high pressure (Figure 3.2), we did not observe the splitting of any ferropicriase reflection peaks, suggesting that

there was no structural transition. In the studied pressure range, the XRD patterns included a couple of saturated reflections, which we unsuccessfully attempted to analyze as peak broadening due to a rhombohedral distortion. Thus, Fp48 likely remains in the *B1* structure up to at least 83 GPa. Above about 45 GPa, a gradual change in the trend of volume compression is observed, suggesting the onset of an electronic spin crossover from high-spin (HS) to low-spin (LS) octahedrally-coordinated Fe<sup>2+</sup> (Figure 3.3).

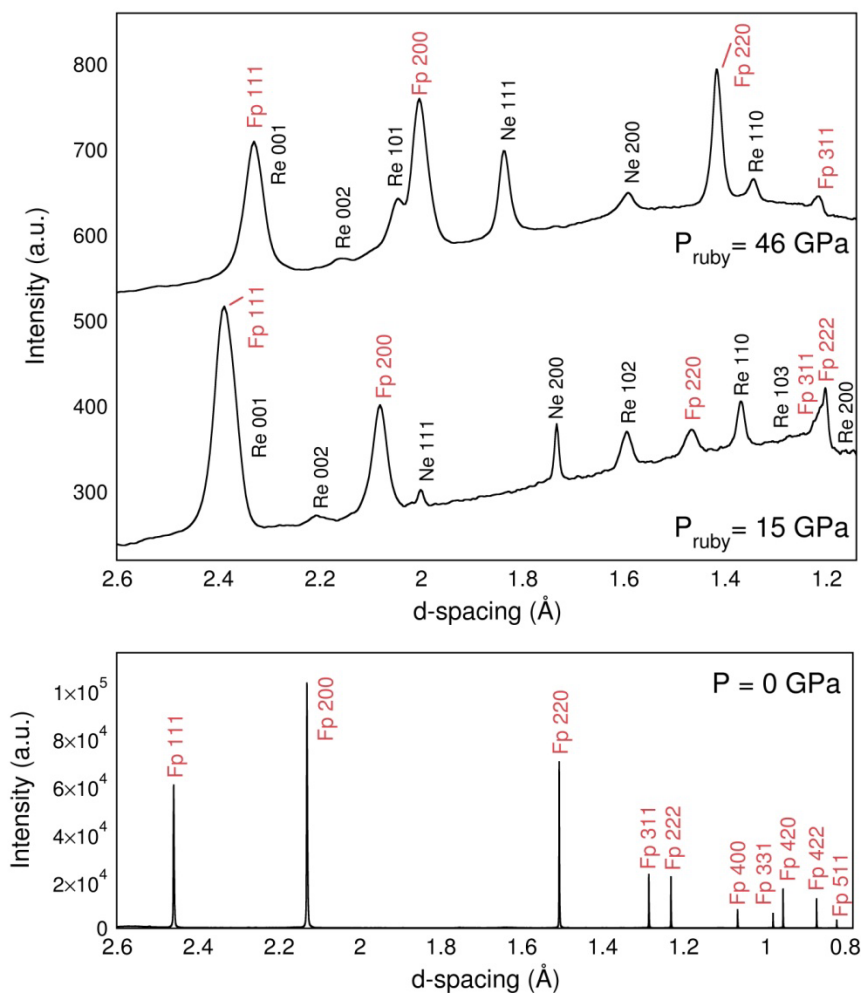


Figure 3.1: Integrated X-ray diffraction patterns for Fp48 at 0, 15 and 46 GPa at room temperature before background subtraction, where patterns are shifted vertically for clarity. Fp48, neon and rhenium peaks are labeled. The ambient pattern was collected at APS ( $\lambda=0.45900 \text{ \AA}$ ) while patterns at pressure were collected at ALS ( $\lambda=0.41328 \text{ \AA}$ ).

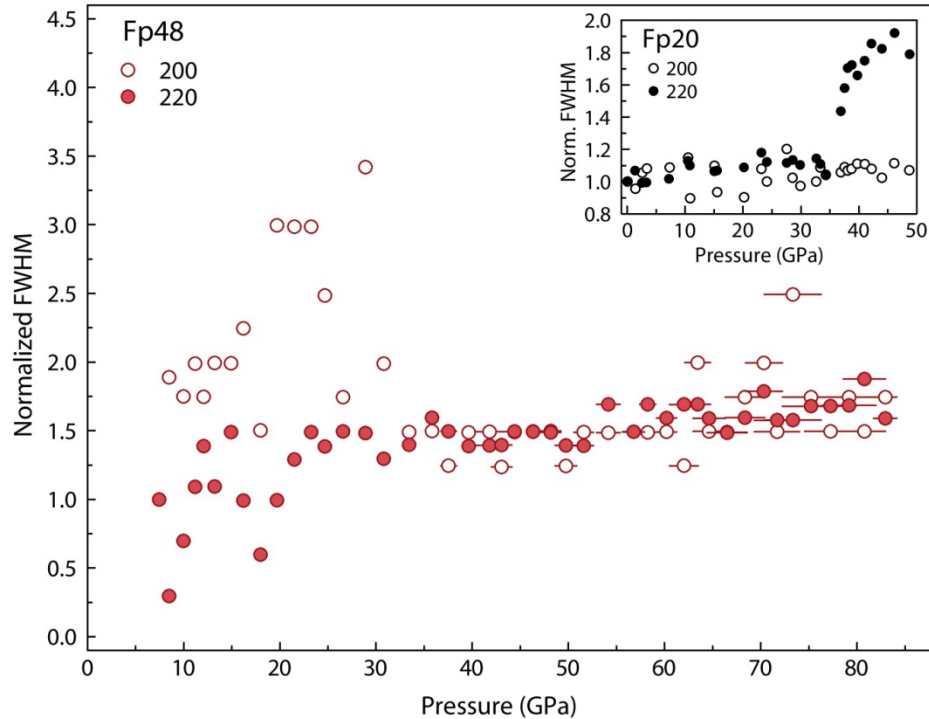


Figure 3.2: The full-width at half-maximum (FWHM) of the 200 and 220 reflections for Fp48 from ALS XRD experiments, normalized to the lowest pressure value collected at ALS (7.46 GPa). Although the FWHM values are scattered at low pressures, no steep broadening that would be associated with a rhombohedral distortion is observed for the 220 reflections. Inset shows 220 peak broadening for Fp20 compressed without a pressure medium [Kantor *et al.*, 2006].

A Birch-Murnaghan spin crossover equation of state (EOS) was fitted to our data with MINUTI 1.1.2 [Chen *et al.*, 2012; Sturhahn, 2015]. We fitted the HS zero-pressure volume ( $V_{0,HS}$ ), HS zero-pressure isothermal bulk modulus ( $K_{0T,HS}$ ), HS zero-pressure bulk modulus derivative ( $K'_{0T,HS}$ ), LS zero-pressure volume ( $V_{0,LS}$ ), LS zero-pressure isothermal bulk modulus ( $K_{0T,LS}$ ) and the transition pressure ( $P_{tr}$ ). A 1.85% volume drop is calculated at 68.8(2.7) GPa, the spin transition pressure where the volume change due to the HS to LS transition is 50% complete. The zero-pressure bulk modulus  $K_{0T,HS}$  for the HS state is 160(2) GPa with a  $K'_{0T,HS}$  of 4.12(14) and a unit-cell  $V_{0,HS}$  of 77.29(0)  $\text{\AA}^3$ . For the LS state, the fit parameters,  $K_{0T,LS}$  and  $V_{0,LS}$  are 173(13) GPa and 73.64(94)  $\text{\AA}^3$ , respectively. Fit parameter  $K'_{0T,LS}$  was fixed at 4. Parameter correlations and fit procedure are described in Table 3.2. The volume, isothermal bulk modulus, bulk sound velocity and density are reported as a function of pressure up to 140 GPa in Table 3.3 with associated errors that consider parameter correlations. A plot of normalized pressure (F) versus Eulerian strain (f) illustrates the change in compression behavior that occurs through the spin crossover (Figure 3.3 inset).

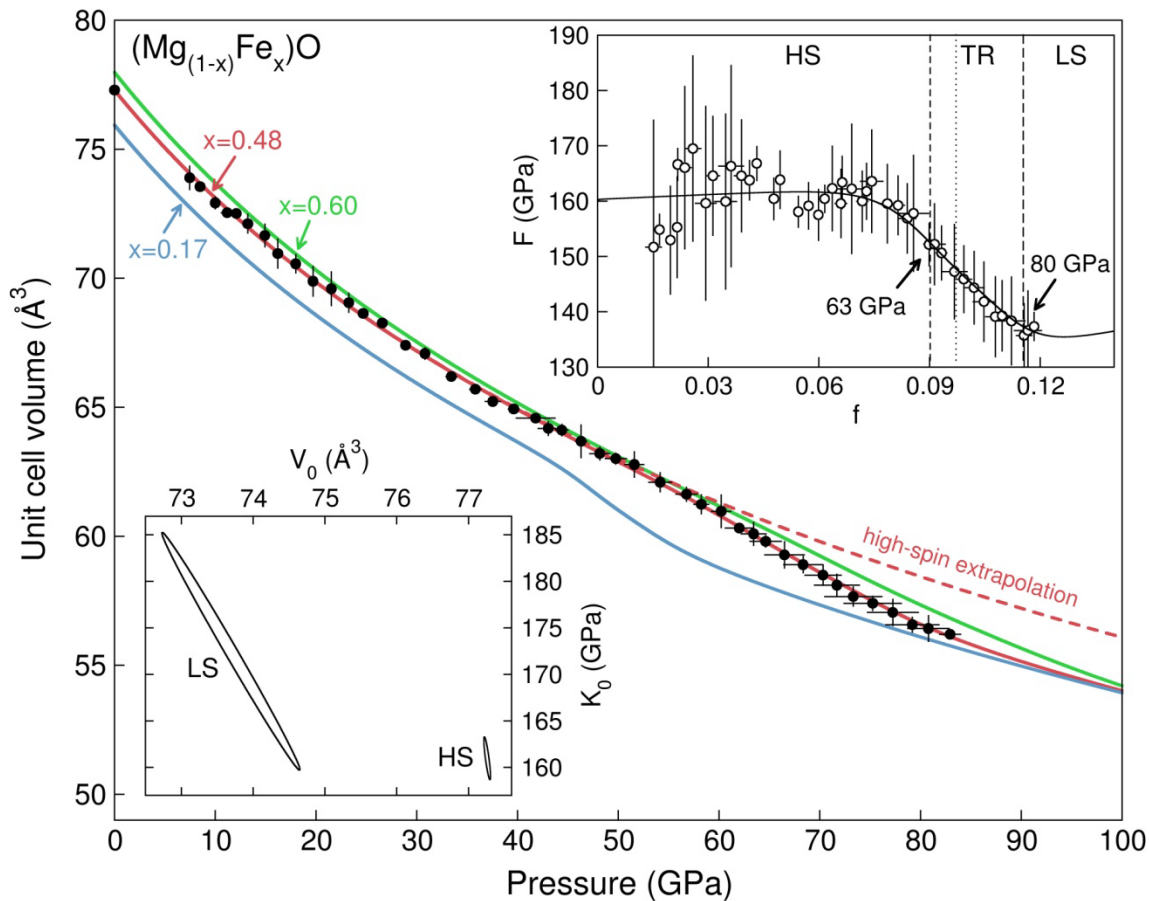


Figure 3.3: Pressure-volume relationship of Fp48 at 300 K, determined from the 200 and 220 reflections (solid black circles). The pressure standard is ruby [Jacobsen *et al.*, 2008]. The solid and dashed red curves are the fitted spin crossover and high-spin equations of state for Fp48, respectively. The blue and green are the spin crossover equations of state fitted with MINUTI to (Mg,Fe)O data with 17 mol% and 60 mol% FeO [Lin *et al.*, 2005], respectively. The upper right inset is the normalized pressure ( $F$ ) versus Eulerian strain ( $f$ ) for Fp48. The resulting spin crossover region (TR) from the SMS fitting procedure is indicated by the vertical dashed lines, corresponding to the point at which 35% (63 GPa) and 65% (80 GPa) of the  $\text{Fe}^{2+}$  atoms are in the LS state, respectively. The black dotted line corresponds to the spin transition pressure of 68.8 GPa, determined from the spin crossover EOS [Sturhahn, 2015]. The bottom left inset shows the covariance ellipses (68% confidence regions) for the HS and LS states for the parameters,  $K_{0T}$  and  $V_0$ , where  $K_{0T,LS}^2$  was fixed to 4.

P (GPa)	V ( $\text{\AA}^3$ )	$\rho$ (g/cm <sup>3</sup> )	P (GPa)	V ( $\text{\AA}^3$ )	$\rho$ (g/cm <sup>3</sup> )	P (GPa)	V ( $\text{\AA}^3$ )	$\rho$ (g/cm <sup>3</sup> )
0.0(0)	77.29(1)	4.862(10)	28.9(5)	67.40(12)	5.575(15)	58.2(0.7)	61.24(37)	6.136(39)
7.5(2)	73.89(45)	5.085(33)	30.8(3)	67.08(22)	5.601(22)	60.2(1.0)	60.97(63)	6.163(65)
8.5(1)	73.55(2)	5.109(10)	33.4(5)	66.19(6)	5.677(13)	62.0(1.4)	60.32(12)	6.230(17)
10.0(2)	72.92(23)	5.153(19)	35.8(6)	65.70(17)	5.720(19)	63.4(1.2)	60.09(44)	6.253(48)
11.2(6)	72.54(11)	5.180(13)	37.5(8)	65.23(18)	5.761(19)	64.6(1.6)	59.80(22)	6.284(26)
12.1(2)	72.51(2)	5.182(10)	39.6(5)	64.93(6)	5.787(13)	66.5(2.0)	59.28(51)	6.339(56)
13.2(4)	72.11(36)	5.211(28)	41.8(1.9)	64.58(9)	5.819(14)	68.3(1.9)	58.90(31)	6.380(36)
14.9(5)	71.66(44)	5.244(34)	43.1(1.0)	64.18(27)	5.855(27)	70.3(1.8)	58.49(39)	6.424(45)
16.2(3)	70.95(56)	5.296(43)	44.4(6)	64.11(22)	5.861(23)	71.7(2.2)	58.11(42)	6.467(49)
18.0(2)	70.56(35)	5.325(28)	46.3(6)	63.68(63)	5.900(59)	73.3(2.8)	57.66(37)	6.516(44)
19.7(1)	69.88(58)	5.377(46)	48.2(1.0)	63.20(25)	5.945(26)	75.2(2.8)	57.40(27)	6.546(34)
21.5(3)	69.59(65)	5.399(52)	49.8(1.0)	63.01(21)	5.963(23)	77.2(2.5)	57.05(51)	6.587(60)
23.3(5)	69.05(37)	5.442(31)	51.6(9)	62.78(49)	5.985(48)	79.2(2.6)	56.57(29)	6.642(36)
24.7(3)	68.63(12)	5.475(14)	54.2(1.1)	62.09(37)	6.051(38)	80.8(2.0)	56.43(50)	6.659(60)
26.6(4)	68.26(7)	5.505(12)	56.8(1.0)	61.63(27)	6.097(29)	82.9(1.0)	56.20(15)	6.686(22)

Table 3.1: Compression data from XRD measurements of Fp48 at 300 K. Ambient measurement was collected at Sector 11-BM of the Advanced Photon Source while measurements at pressure were collected at Beamline 12.2.2 at the Advanced Light Source. Note that density is calculated for a 95% <sup>57</sup>Fe enriched Fp48.

The normalized pressure decreases with increasing Eulerian strain in the spin crossover region. The onset of the spin crossover of Fp48 in this study is similar to the crossover pressures of previous studies of ferropicicase with iron concentrations of 35-50 mol% [Speziale *et al.*, 2005; Fei *et al.*, 2007; Zhuravlev *et al.*, 2010; Chen *et al.*, 2012], but higher than that of (Mg,Fe)O containing less iron [Marquardt *et al.*, 2009b; Lin *et al.*, 2005; Fei *et al.*, 2007; Mao *et al.*, 2011]. The crossover pressure is sensitive to hydrostatic conditions and is very likely a function of iron concentration, revealed by comparison to pressure-volume data for (Mg,Fe)O with 17 mol% and 60 mol%, as discussed below (Figure 3.3).

	$V_{0,HS}$	$K_{0T,HS}$	$K'_{0T,HS}$	$V_{0,LS}$	$K_{0T,LS}$	$P_{tr}$
$V_{0,HS}$	1.000	-0.091	0.038	0.008	-0.007	-0.010
$K_{0T,HS}$	-0.091	1.000	-0.903	-0.143	0.064	0.414
$K'_{0T,HS}$	0.038	-0.903	1.000	0.264	-0.151	-0.627
$V_{0,LS}$	0.008	-0.143	0.264	1.000	-0.984	-0.514
$K_{0T,LS}$	-0.007	0.064	-0.151	-0.984	1.000	0.376
$P_{tr}$	-0.010	0.414	-0.627	-0.514	0.376	1.000

Table 3.2: Error correlation matrix for the EOS parameters fitted with MINUTI for Fp48. Perfect correlation corresponds to  $\pm 1$  and a lack of correlation corresponds to 0. Priors (and prior windows) of 160 ( $\pm 5$ ) GPa, 170 ( $\pm 20$ ) GPa and 4 ( $\pm 0.5$ ) were used for  $K_{0T,HS}$ ,  $K_{0T,LS}$  and  $K'_{0T,HS}$ , respectively. No priors were used for  $V_{0,LS}$  and  $P_{tr}$ , and  $K'_{0T,LS}$  was fixed to 4.

### 3.3.2 Synchrotron Mössbauer Spectroscopy

Synchrotron Mössbauer spectroscopy (SMS) spectra were fitted with version 2.1 of the CONUSS software [Sturhahn, 2000], which uses a least-square algorithm to fit iron's hyperfine parameters (e.g., isomer shift, quadrupole splitting and distribution of the quadrupole splitting expressed as the full width at half maximum) and material properties (e.g., effective thickness, thickness distribution and relative weights of the sites). Typical spectra with their best-fit models are shown in Figure 3.4. Analysis of the SMS spectra suggests the existence of two  $Fe^{2+}$  environments with distinguishable quadrupole splittings (QS) and similar isomer shifts (IS). One  $Fe^{2+}$ -like site was not sufficient in describing the spectra. Attempts were made to introduce a  $Fe^{3+}$ -like site with starting values of the QS ranging from 0 to 0.8 mm/s and IS values with respect to  $Fe^{2+}$  of 0.4 to 0.8 mm/s. However, its weight converged to 0, suggesting the near absence of  $Fe^{3+}$  or a quantity below the detection limit.

P (GPa)	V ( $\text{\AA}^3$ )	$K_T$ (GPa)	$v_\Phi$ (km/s)	$\rho$ (g/cm <sup>3</sup> )
0	77.29(0)	160.3(1.5)	5.885(27)	4.829(9)
4	75.47(1)	176.6(1.0)	6.100(18)	4.945(10)
8	73.86(2)	192.6(0.7)	6.298(12)	5.054(10)
12	72.40(2)	208.2(0.7)	6.482(11)	5.155(10)
16	71.07(2)	223.6(0.9)	6.653(14)	5.252(10)
20	69.85(2)	238.8(1.3)	6.813(19)	5.344(11)
24	68.72(3)	253.7(1.7)	6.963(24)	5.431(11)
28	67.68(3)	268.1(2.0)	7.102(28)	5.515(11)
32	66.70(3)	282.1(2.3)	7.229(30)	5.596(11)
36	65.78(4)	295.0(2.5)	7.339(32)	5.674(11)
40	64.91(4)	306.3(2.9)	7.425(36)	5.750(12)
44	64.08(4)	314.7(4.0)	7.474(48)	5.824(12)
48	63.28(5)	317.9(6.5)	7.464(77)	5.898(12)
52	62.48(5)	312.8(10.4)	7.360(124)	5.973(13)
56	61.67(7)	297.0(13.6)	7.127(166)	6.052(14)
60	60.81(10)	275.3(11.3)	6.810(143)	6.137(15)
64	59.92(10)	266.1(12.3)	6.675(153)	6.229(16)
68	59.03(9)	272.6(12.0)	6.813(150)	6.323(16)
72	58.18(10)	273.8(13.9)	6.969(180)	6.416(17)
76	57.34(12)	283.4(16.7)	7.231(213)	6.509(18)
80	56.59(11)	327.0(25.3)	7.631(295)	6.596(18)
84	55.95(11)	381.9(24.4)	7.992(257)	6.671(19)
88	55.40(12)	427.8(19.5)	8.270(191)	6.737(20)
92	54.91(13)	462.6(15.6)	8.479(148)	6.798(20)
96	54.45(13)	489.2(13.8)	8.640(127)	6.855(21)
100	54.01(14)	510.6(13.2)	8.770(120)	6.910(22)
104	53.60(14)	528.6(13.2)	8.878(118)	6.964(23)
108	53.20(15)	544.6(13.5)	8.971(118)	7.016(24)
112	52.82(15)	559.4(13.8)	9.056(120)	7.067(24)
116	52.44(15)	573.4(14.1)	9.134(121)	7.117(25)
120	52.08(16)	586.9(14.3)	9.208(122)	7.166(26)
124	51.73(16)	600.1(14.4)	9.279(122)	7.214(27)
128	51.39(17)	613.1(14.6)	9.348(123)	7.262(28)
132	51.06(17)	626.0(14.6)	9.415(122)	7.309(29)
136	50.74(18)	638.8(14.7)	9.480(122)	7.356(29)
140	50.43(18)	651.6(15.1)	9.544(124)	7.401(30)

Table 3.3: Volume (V), isothermal bulk modulus ( $K_T$ ), bulk sound velocity ( $v_\Phi$ ) and density ( $\rho$ ) as a function of pressure, obtained from fitting a spin crossover EOS to the compression data for Fp48. Cited uncertainties include parameter correlations given in Table 3.2. The bulk sound velocity and density were corrected for natural <sup>57</sup>Fe abundance.

At pressures below 44 GPa, our spectra were fitted with two high-spin  $\text{Fe}^{2+}$ -like sites, distinguishable by their hyperfine fields (hereafter referred to as  $\text{Fe}_A^{2+}$  and  $\text{Fe}_B^{2+}$ ) with a relative weight of 40% and 60%, respectively (Figure 3.5; Table 3.4). At pressures between 44 and 84, we introduce an additional  $\text{Fe}^{2+}$ -like site with a QS of 0 mm/s, indicative of low-spin iron. The weight of LS  $\text{Fe}^{2+}$  increases with increasing pressure while the weight ratio of the two HS sites is preserved. This model was successfully applied to decompression measurements, which span the spin crossover pressure range (Table 3.5). Above 84 GPa, the spectra are best fit with two low-spin  $\text{Fe}^{2+}$ -like sites (with a relative weight of 40% and 60%) with identical IS values, but different IS distributions. For example, at 98 GPa, the two low spin  $\text{Fe}^{2+}$ -like sites have an IS of 0.434(8) mm/s and a full width at half maximum (FWHM) of 1.13 and 0.40 mm/s. The negative slope of the IS with pressure for the  $\text{Fe}^{2+}$  sites is consistent with previous studies on (Mg,Fe)O approaching a spin crossover [Kantor *et al.*, 2006; Lin *et al.*, 2006a] and is a result of an increase in electron density at the nucleus with increasing pressure. The CONUSS fits reveal that 50% of the  $\text{Fe}^{2+}$  atoms are in the LS state at 72 and 69 GPa in the compression and decompression pathways, respectively. These results compare well with the transition pressure of 68.8(2.7) GPa obtained from the spin crossover EOS fit with MINUTI to the pressure-volume data set of Fp48.

### 3.3.2 Hyperfine Parameters

The SMS spectra display quantum beats originating from the QS of HS  $\text{Fe}^{2+}$  and dynamic beats due to sample thickness. Flattening of the SMS spectra is a result of the gradual disappearance of the HS  $\text{Fe}^{2+}$  sites (QS $\approx$ 1.2 and  $\sim$ 1.7 mm/s) and the appearance of LS  $\text{Fe}^{2+}$  (QS=0 mm/s). The quadrupole splitting is related to the amount of distortion of the coordination polyhedron. Defects within a crystal lattice can result in variations of octahedral  $\text{Fe}^{2+}$  environments [Jacobsen *et al.*, 2002]. It is possible that the presence of Ti, high Fe concentration and/or clustering yields two dominant and unique hyperfine fields for  $\text{Fe}^{2+}$  rather than one  $\text{Fe}^{2+}$  site; however, further studies would be required to confirm this explanation. The measured values of QS and IS are consistent with high-spin  $\text{Fe}^{2+}$  in octahedral coordination environments and we interpret the two distinct QS values to represent relatively low and high distortion, respectively, while not breaking cubic symmetry of the long-range order. No evidence of magnetic ordering was observed.

The lack of complexity in the spectra without a stainless steel reference absorber resulted in a variety of possible solutions with nearly identical reduced  $\chi^2$ . Thus, those parameters were constrained with priors derived from the fit of the sample with SS, demonstrating the necessity of performing SMS measurements with a reference absorber and the benefit of using priors. For example, during the fit of Fp48 at 12.8 GPa without

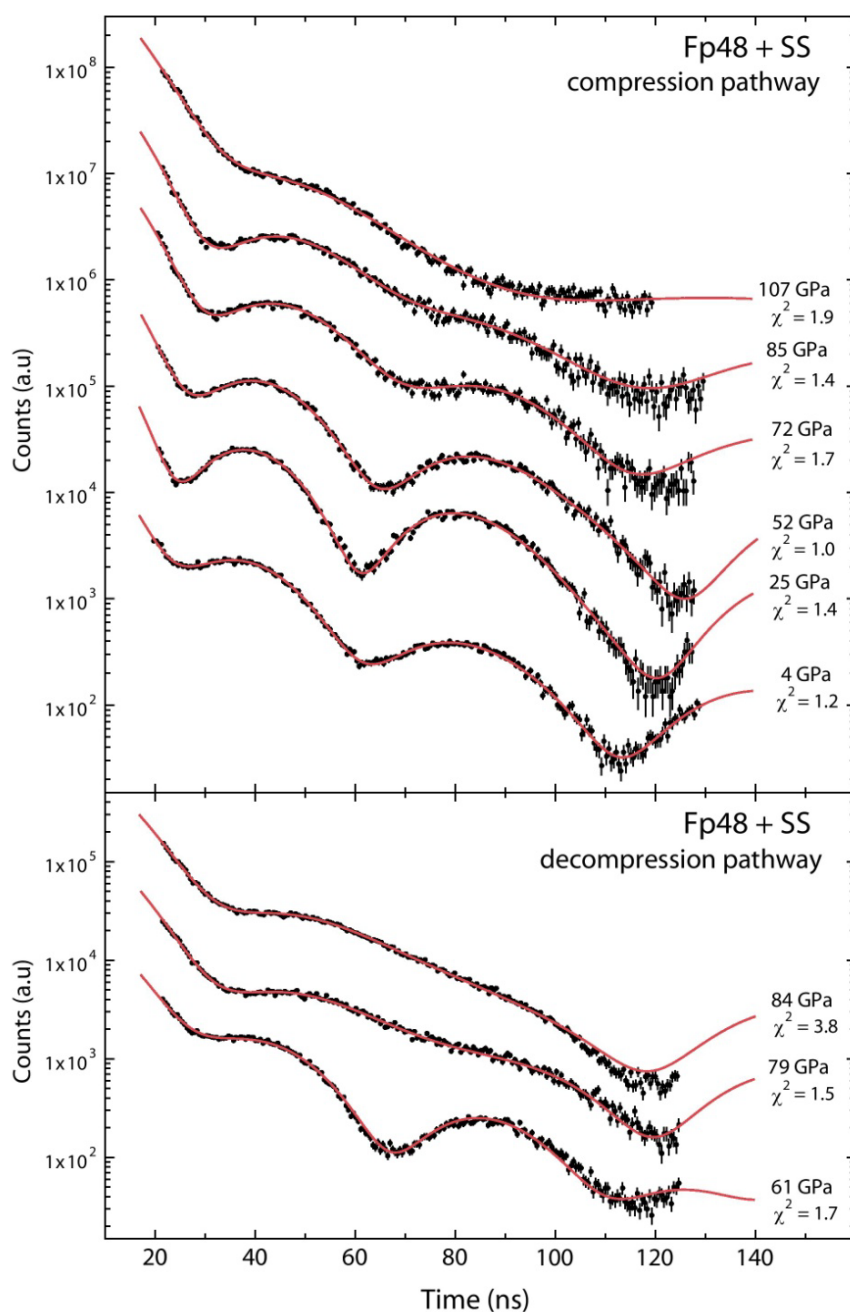


Figure 3.4: Representative SMS spectra and their best-fit models using CONUSS, collected at 3-ID-B of the APS (compression pathway on top; decompression pathway on bottom). The influence of pressure on the spectral features is evident through the decrease of the quantum beat amplitudes with increasing pressure. The corresponding pressure and reduced  $\chi^2$  of each fit is noted to the right of each spectrum. Note that these data sets are from two different DAC preparations, each with powdered Fp48 in a Ne pressure medium (see Experimental Methods).

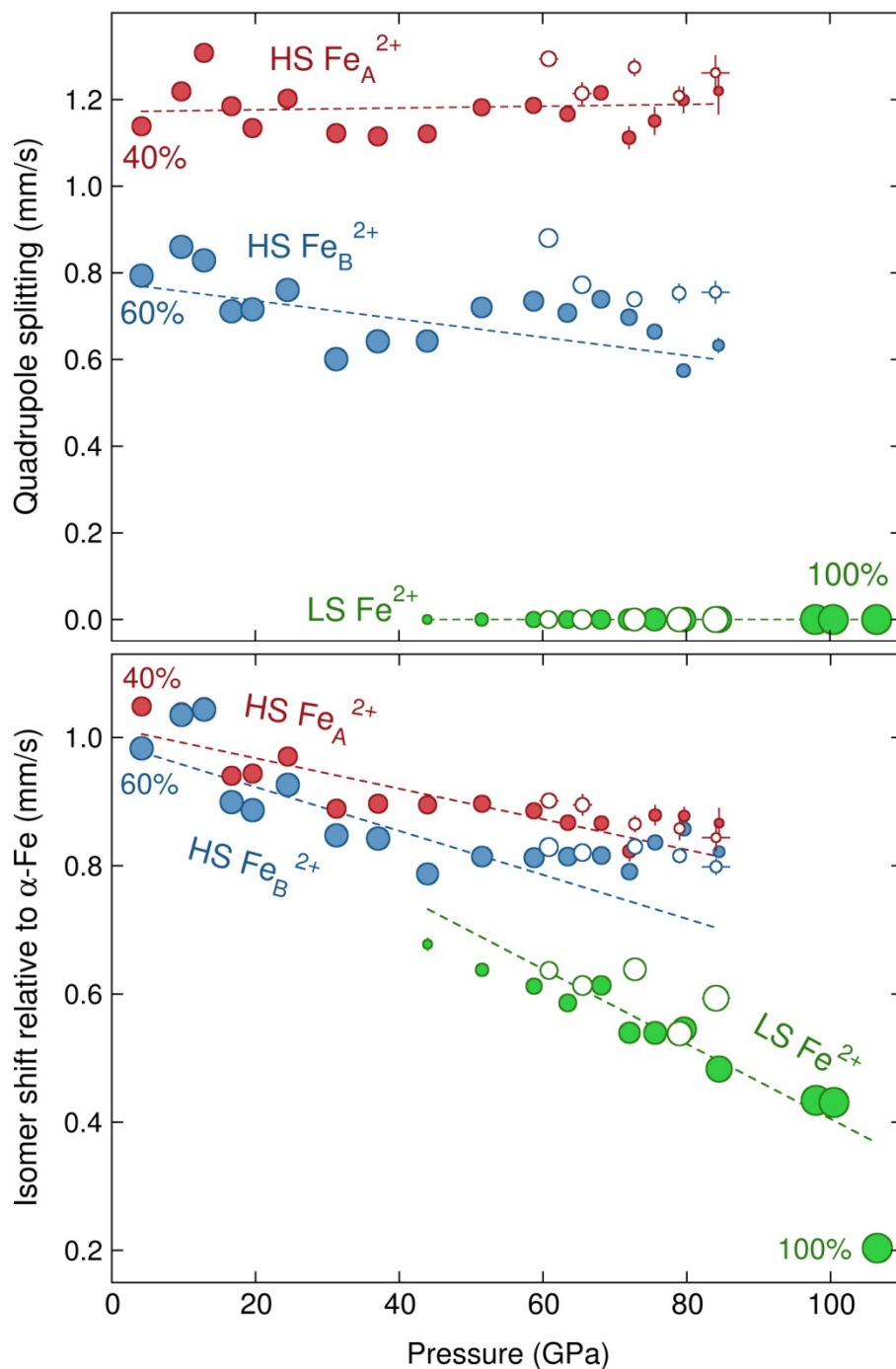


Figure 3.5: Quadrupole splitting and isomer shift (relative to  $\alpha$ -Fe) of Fp48. Red, blue and green circles correspond to the  $HS Fe_A^{2+}$ ,  $HS Fe_B^{2+}$  and  $LS Fe^{2+}$  sites, respectively. Filled symbols denote hyperfine parameters acquired during compression and open symbols denote hyperfine parameters acquired during decompression. The relative areas of the symbols are proportional to their weight fractions. Dashed lines are guides for the eyes.

Pressure (GPa)	Fe <sub>A</sub> <sup>2+</sup> QS (mm/s)	Fe <sub>A</sub> <sup>2+</sup> FWHM (mm/s)	Fe <sub>A</sub> <sup>2+</sup> IS (mm/s)	Fe <sub>B</sub> <sup>2+</sup> QS (mm/s)	Fe <sub>B</sub> <sup>2+</sup> FWHM (mm/s)	Fe <sub>B</sub> <sup>2+</sup> IS (mm/s)	Fe <sub>LS</sub> <sup>2+</sup> weight	Fe <sub>LS</sub> <sup>2+</sup> IS (mm/s)	Fe <sub>LS</sub> <sup>2+</sup> FWHM (mm/s)	reduced $\chi^2$
4.1(1)	1.138(11)	0.58	1.049(7)	0.793(4)	0.33	0.983(3)	-	-	-	1.23
9.7(3)	1.219(11)	0.67	1.040(8)	0.859(6)	0.38	1.035(3)	-	-	-	1.67
12.8(0)	1.308(7)	0.50	1.048(5)	0.828(6)	0.38	1.044(3)	-	-	-	1.53
16.7(1)	1.185(8)	0.40	0.940(6)	0.709(5)	0.30	0.899(3)	-	-	-	1.17
19.6(7)	1.134(6)	0.45	0.944(4)	0.714(3)	0.30	0.887(2)	-	-	-	1.65
24.5(0)	1.202(8)	0.40	0.970(9)	0.758(7)	0.35	0.926(4)	-	-	-	1.36
31.2(9)	1.122(7)	0.30	0.889(5)	0.600(4)	0.20	0.847(3)	-	-	-	1.89
37.0(1)	1.115(10)	0.30	0.897(8)	0.640(6)	0.30	0.842(4)	-	-	-	1.67
43.9(3)	1.121(6)	0.40	0.895(3)	0.641(3)	0.30	0.787(1)	0.10	0.678(9)	0.60	1.62
51.5(6)	1.182(9)	0.45	0.897(5)	0.717(5)	0.32	0.814(2)	0.19	0.638(8)	0.66	0.99
58.7(6)	1.186(7)	0.38	0.886(4)	0.735(6)	0.30	0.813(2)	0.28	0.612(6)	0.86	1.34
63.4(2)	1.166(14)	0.38	0.867(9)	0.707(9)	0.35	0.814(5)	0.35	0.586(10)	0.86	1.68
68.1(1)	1.215(15)	0.30	0.867(11)	0.689(16)	0.42	0.816(11)	0.42	0.613(13)	0.86	2.08
72.0(0)	1.112(25)	0.60	0.823(15)	0.689(15)	0.43	0.791(8)	0.50	0.540(7)	0.75	1.67
75.6(2)	1.151(31)	0.65	0.879(15)	0.664(11)	0.44	0.836(7)	0.58	0.539(7)	0.91	1.50
79.6(8)	1.199(29)	0.50	0.878(13)	0.571(12)	0.35	0.857(8)	0.66	0.545(7)	0.90	1.91
84.5(6)	1.220(53)	0.50	0.866(23)	0.627(16)	0.28	0.822(8)	0.76	0.483(5)	0.80	1.43
98.0(4)	-	-	-	-	-	-	1	0.434(8)	1.13, 0.40	1.82
100.5(3)	-	-	-	-	-	-	1	0.431(11)	1.24, 0.58	1.48
106.5(7)	-	-	-	-	-	-	1	0.203(11)	1.35, 0.65	1.92

Table 3.4: Best-fit hyperfine parameters for Fp48 with a stainless steel reference absorber and their corresponding reduced  $\chi^2$  for the compression pathway. The relative weight of the Fe<sub>A</sub><sup>2+</sup> and Fe<sub>B</sub><sup>2+</sup> sites are fixed to 40% and 60%, respectively. Values in parantheses indicate the 68% uncertainty in the last digit(s). The spectra with their best-fit models at 4.1(1), 24.5(0), 51.5(6), 72.0(0), 84.5(6) and 106.5(7) GPa are shown in Figure 3.4. IS values are with respect to  $\alpha$ -iron metal.

Pressure (GPa)	Fe <sub>A</sub> <sup>2+</sup> QS (mm/s)	Fe <sub>A</sub> <sup>2+</sup> FWHM (mm/s)	Fe <sub>A</sub> <sup>2+</sup> IS (mm/s)	Fe <sub>B</sub> <sup>2+</sup> QS (mm/s)	Fe <sub>B</sub> <sup>2+</sup> FWHM (mm/s)	Fe <sub>B</sub> <sup>2+</sup> IS (mm/s)	Fe <sub>LS</sub> <sup>2+</sup> weight	Fe <sub>LS</sub> <sup>2+</sup> IS (mm/s)	Fe <sub>LS</sub> <sup>2+</sup> FWHM (mm/s)	reduced $\chi^2$
84.1(1.9)	1.262(39)	0.63	0.844(21)	0.755(25)	0.18	0.798(12)	0.74	0.593(4)	0.52	3.85
79.0(3)	1.208(21)	0.73	0.858(17)	0.753(21)	0.04	0.816(11)	0.67	0.538(3)	0.50	1.48
72.8(8)	1.274(19)	0.63	0.865(12)	0.739(15)	0.18	0.830(8)	0.58	0.638(4)	0.52	2.34
65.5(1.2)	1.214(24)	0.57	0.895(16)	0.772(17)	0.10	0.821(9)	0.43	0.613(4)	0.53	1.41
60.8(1.3)	1.294(8)	0.19	0.901(7)	0.880(13)	0.28	0.829(5)	0.35	0.637(9)	0.98	1.74

Table 3.5: Best-fit hyperfine parameters for Fp48 with a stainless steel reference absorber and their corresponding reduced  $\chi^2$  for the decompression pathway. The spectra with their best-fit models at 60.8(1.3), 79.0(3) and 84.1(1.9) are shown in Figure 3.4.

	Fe <sub>A</sub> <sup>2+</sup> QS	Fe <sub>B</sub> <sup>2+</sup> QS	Fe <sub>A</sub> <sup>2+</sup> IS	Fe <sub>B</sub> <sup>2+</sup> IS	Fe <sub>LS</sub> <sup>2+</sup> IS
Fe <sub>A</sub> <sup>2+</sup> QS	1.000	-0.144	-0.756	0.024	0.433
Fe <sub>B</sub> <sup>2+</sup> QS	-0.144	1.000	0.276	-0.693	0.543
Fe <sub>A</sub> <sup>2+</sup> IS	-0.756	0.276	1.000	-0.146	-0.094
Fe <sub>B</sub> <sup>2+</sup> IS	0.024	-0.693	-0.146	1.000	-0.503
Fe <sub>LS</sub> <sup>2+</sup> IS	0.433	0.543	-0.094	-0.503	1.000

Table 3.6: Error correlation matrix for the fitted hyperfine parameters at 75.6 GPa (where high-spin and low-spin states coexist), acquired with CONUSS. Thickness, thickness distribution, the QS distribution and weight fractions of the different sites were fixed. The QS of Fe<sub>LS</sub><sup>2+</sup> was fixed to 0.

SS, the priors for the  $\text{Fe}_A^{2+}$  QS and  $\text{Fe}_B^{2+}$  QS were set to 1.308 mm/s and 0.828 mm/s, respectively, with a window of  $\pm 0.01$  mm/s. The prior for the isomer shift between the two  $\text{Fe}^{2+}$  sites ( $\text{IS}^{A-B}$ ) was set to 0.004 mm/s with a window of  $\pm 0.001$  mm/s. The resulting fitted values for the sample without the reference absorber were  $\text{Fe}_A^{2+}$  QS = 1.301(12) mm/s,  $\text{Fe}_B^{2+}$  QS = 0.8115(39) mm/s and  $\text{IS}^{A-B}$  = 0.0041(12) mm/s with a reduced  $\chi^2$  of 1.46. Thus, with this prior information, there was good agreement between parameters derived from fitting the sample with and without the SS reference absorber. Although individual spectra may have multiple satisfactory fits at a given pressure, the model presented here is the only self-consistent solution (i.e., a reasonable physical model that explains the data through the entire pressure range with and without a SS reference absorber). Due to the large number of parameters, the FWHM of the quadrupole splitting and the weight ratio of the  $\text{Fe}^{2+}$ -like sites were fixed at all pressures while the effective thickness (effective thickness ( $\eta$ ) is the product of the volume density of the resonant nuclei ( $\rho$ ), nuclear resonant cross section ( $\sigma$ ), Lamb-Mössbauer factor ( $f_{\text{LM}}$ ) and the sample thickness ( $D$ )) and its distribution was fixed when three sites were used (i.e., in the spin crossover region). Fixed values were determined from Monte Carlo searches. The error correlation matrix of a typical fit within the crossover region is reported in Table 3.6. No strong correlations occur in this fitting procedure, as reported by CONUSS. However, fitting either the thickness and thickness distribution or the FWHM of the QS in addition to the parameters in Table 3.6 within the crossover region results in nine strong correlations, emphasizing the need to fix highly correlated parameters to physically meaningful values.

### 3.4 Effect of Iron Concentration

To examine a systematic effect of iron concentration on the HS and LS volumes, bulk modulus and spin transition pressure, we fit a spin crossover equation of state to previously reported pressure-volume data of  $(\text{Mg}_{1-x}\text{Fe}_x)\text{O}$  ranging from  $x=0.10$  to  $x=0.60$  [Lin *et al.*, 2005; Fei *et al.*, 2007; Marquadt *et al.*, 2009; Zhuravlev *et al.*, 2010; Mao *et al.*, 2011; Chen *et al.*, 2012] using MINUTI. Fitted spin crossover EOS parameters from X-ray diffraction data are listed in Table 3.7 and plotted in Figure 3.6.  $V_{0,\text{HS}}$  generally increases with increasing iron content while the percent difference between the HS and LS  $V_0$  appears to be roughly constant between 17 and 60 mol% FeO. The fit parameter  $K_{0T,\text{HS}}$  appears to be insensitive to iron content within this range of compositions [Jacobsen *et al.*, 2002; Jackson *et al.*, 2006]. However, the percent difference between HS and LS  $K_{0T}$  is notably different for  $(\text{Mg}_{0.83}\text{Fe}_{0.17})\text{O}$ . Fitted spin transition pressures ( $P_{\text{tr}}^*$ ) show an increase from about 50 GPa at  $x=0.10$  to about 80 GPa for  $x=0.60$  (Figure 3.7).

Energy-domain Mössbauer experiments for  $(\text{Mg}_{0.50}\text{Fe}_{0.50})\text{O}$  with an Ar and alcohol mixture as a pressure medium reported a transition pressure at 60 GPa [Speziale *et al.*, 2005] while X-ray diffraction experiments for laser-annealed  $(\text{Mg,Fe})\text{O}$  with 20, 39 and 58 mol% FeO with an NaCl pressure medium report a spin crossover at about 40, 60 and 80 GPa, respectively [Fei *et al.*, 2007]. It is important to note that Fei *et al.* [2007] reported a cubic-rhombohedral phase transition at 44 GPa in  $(\text{Mg,Fe})\text{O}$  with 58 mol% FeO. However, also using a NaCl pressure medium with laser-heating, Lin *et al.* [2002] find that  $(\text{Mg,Fe})\text{O}$  with 61 mol% FeO remains cubic up to 102 GPa at 300 K and up to 2550 K. Furthermore, using a Ne pressure medium, Lin *et al.* [2005] observe no phase transition in  $(\text{Mg,Fe})\text{O}$  with 60 mol% FeO at 300 K.

Future Mössbauer experiments combined with X-ray diffraction measurements using a Ne pressure medium could help clarify the relationship between the rhombohedral phase transition and spin crossover. Reported spin transition pressures strongly depend on the pressure medium, pressure scale, other environmental conditions and the criteria for assigning a particular pressure to the transition (Table 3.8). In the pressure range investigated, our use of Ne as a pressure medium creates a more hydrostatic environment compared to the absence of a pressure medium, NaCl, Ar or alcohol mixtures [Klotz *et al.*, 2009], and allows us to directly compare our results to those that used Ne [Marquardt *et al.*, 2009b; Lin *et al.*, 2005; Zhuravlev *et al.*, 2010; Chen *et al.*, 2012]. Additionally, high-quality SMS measurements collected in fine ( $\sim 5$  GPa) pressure steps on grains of Fp48 from the same synthesis run charge allows us to resolve the presence of small low-spin weight fractions.

Computational studies have used density functional theory to predict the spin transition pressure and spin transition width for  $(\text{Mg,Fe})\text{O}$ . When HS and LS states coexist, the mixture of states can be treated as an ideal or non-ideal solution, having additive or non-additive volumes, respectively. Although most materials are non-ideal solutions, it is often convenient to treat them as ideal solutions to simplify the calculations. Tsuchiya *et al.* [2006] used the LDA+U method assuming an ideal solution of HS and LS Fe atoms to calculate the spin transition pressure range for  $(\text{Mg}_{0.8125}\text{Fe}_{0.1875})\text{O}$ . At 300 K, they predicted a spin transition pressure of 36 GPa and a narrow spin transition width of  $\sim 4$  GPa (20% and 80% LS population at 34 and 38 GPa, respectively). For  $(\text{Mg}_{0.75}\text{Fe}_{0.25})\text{O}$ , Holmström and Stixrude [2015] performed molecular dynamics simulations within density functional theory, using the GGA+U method. Assuming a non-ideal solution of HS and LS Fe atoms, the mixed spin phase is stabilized even at low temperatures. At 300 K, they predict a spin transition pressure of 65 GPa with a broad spin transition width of  $\sim 50$  GPa (20% and 80% LS population at approximately 45 and 95 GPa). Using the same percentage range of LS population, the

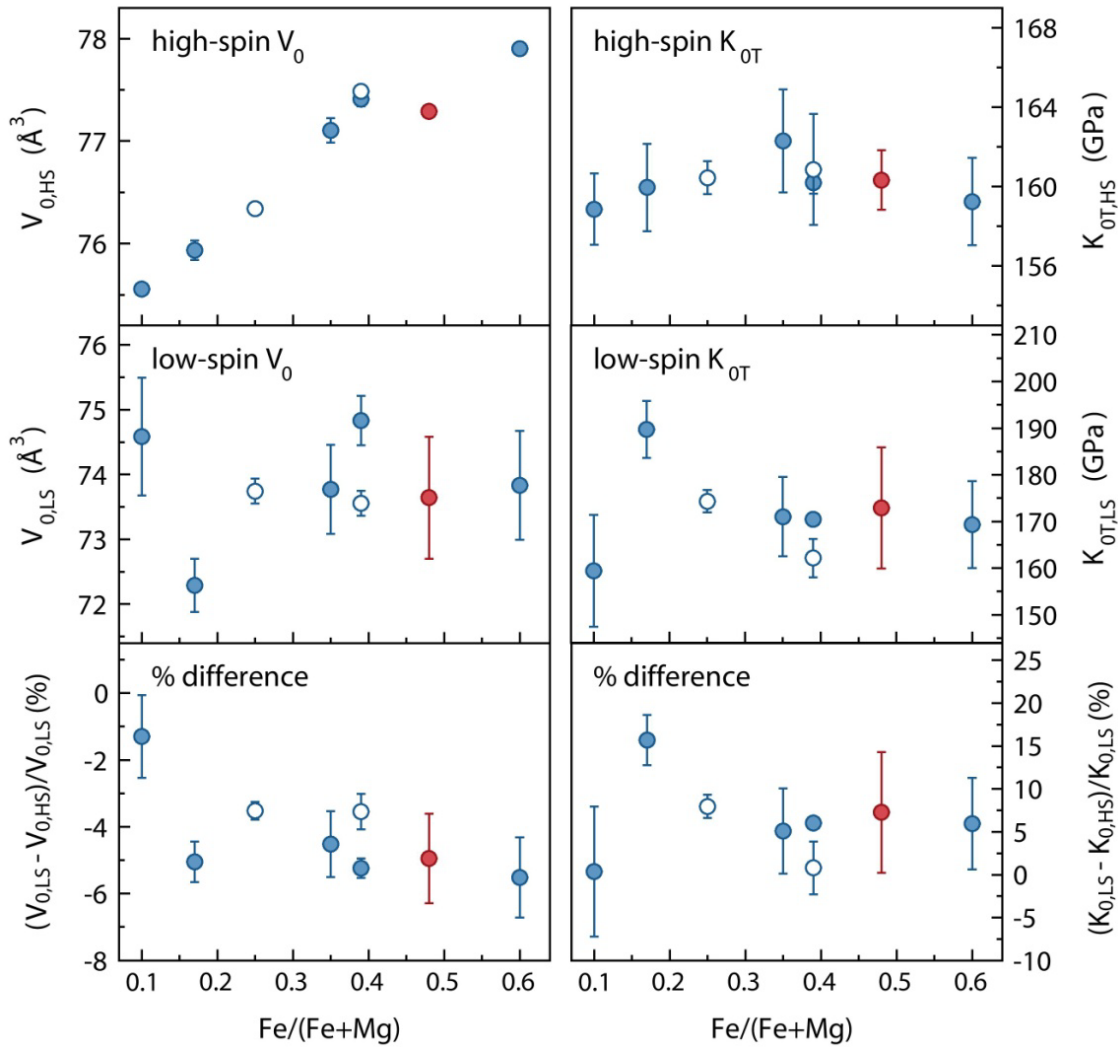


Figure 3.6: High-spin and low-spin zero-pressure volume and bulk modulus as a function of iron concentration, derived from a spin crossover EOS. Fp48 is denoted by a red circle and is compared to  $(Mg_{(1-x)}Fe_x)O$  with  $x=0.10$  [Marquardt *et al.*, 2009b],  $x=0.17$  [Lin *et al.*, 2005],  $x=0.25$  [Mao *et al.*, 2011],  $x=0.35$  [Chen *et al.*, 2012],  $x=0.39$  [Zhuravlev *et al.*, 2010; Fei *et al.*, 2007] and  $x=0.60$  [Lin *et al.*, 2005]. Solid blue symbols indicate studies that used Ne as a pressure medium [Marquardt *et al.*, 2009b; Lin *et al.*, 2005; Chen *et al.*, 2012; Zhuravlev *et al.*, 2010] while open blue symbols indicate studies that used NaCl or KCl as a pressure medium [Mao *et al.*, 2011; Fei *et al.*, 2007]. A larger concentration of iron likely results in a larger difference in volume between HS and LS  $(Mg,Fe)O$ , whereas  $K_0$  for the HS state appears to be insensitive to iron concentration in  $(Mg,Fe)O$  for these compositions.

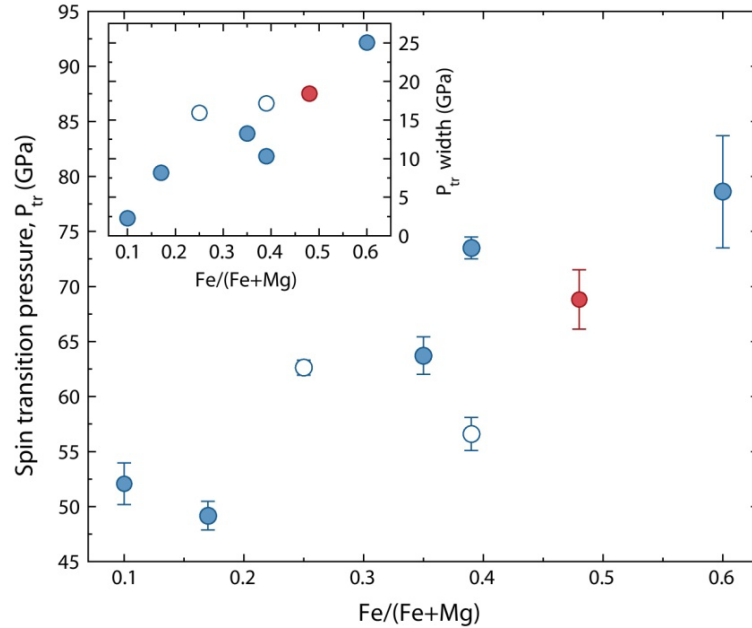


Figure 3.7: Spin transition pressure of  $(Mg_{(1-x)}Fe_x)O$  as a function of iron concentration, fitted with MINUTI. The inset shows the spin transition widths, determined from the 20/80% volume drop. References for symbols are the same as in Figure 3.6.

spin transition widths determined from XRD measurements using MINUTI are 8.2 GPa for  $(Mg_{0.83}Fe_{0.17})O$  and 15.9 GPa for  $(Mg_{0.75}Fe_{0.25})O$  (Figure 3.7 inset). Thus, it appears that using an ideal or non-ideal solution of HS and LS states either underestimates or overestimates the spin transition width observed experimentally at 300 K.

### 3.5 Implications

An understanding of the effect of iron on the density, crystal structure and magnetic behavior of ferropericlase is important for understanding the implications for the presence of  $(Mg,Fe)O$  in lower-mantle phase assemblages. Thus, to examine the effect of iron concentration in  $(Mg,Fe)O$  on geophysically relevant properties, we have calculated the bulk modulus, density and bulk sound velocities up to 140 GPa at 300 K for  $(Mg,Fe)O$  with 17 mol%, 48 mol% and 60 mol% FeO, with uncertainties that reflect the equations of state parameter correlations (Figure 3.8; Figure 3.9; Figure 3.10). The significant softening of the bulk modulus and bulk sound velocities in the spin crossover region is a direct result of the compression behavior at 300 K, but is unlikely to persist with the same magnitude at high temperatures [Sturhahn *et al.*, 2005, Tsuchiya *et al.*, 2006; Komabayashi *et al.*, 2010; Mao *et al.*, 2011; Holmström and Stixrude, 2015]. As shown previously, the effect of the gradual density crossover along a typical geotherm

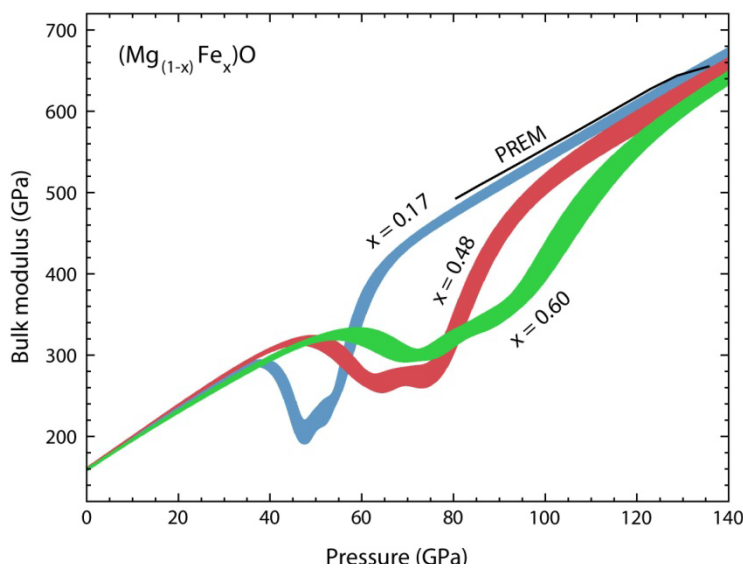


Figure 3.8: Isothermal bulk modulus as a function of pressure for  $(\text{Mg}_{(1-x)}\text{Fe}_x)\text{O}$  at 300 K where blue is  $x=0.17$  [Lin *et al.*, 2005], red is  $x=0.48$  (this study) and green is  $x=0.60$  [Lin *et al.*, 2005], fitted with MINUTI. The preliminary reference model (PREM) [Dziewonski and Anderson, 1981] is shown in black.

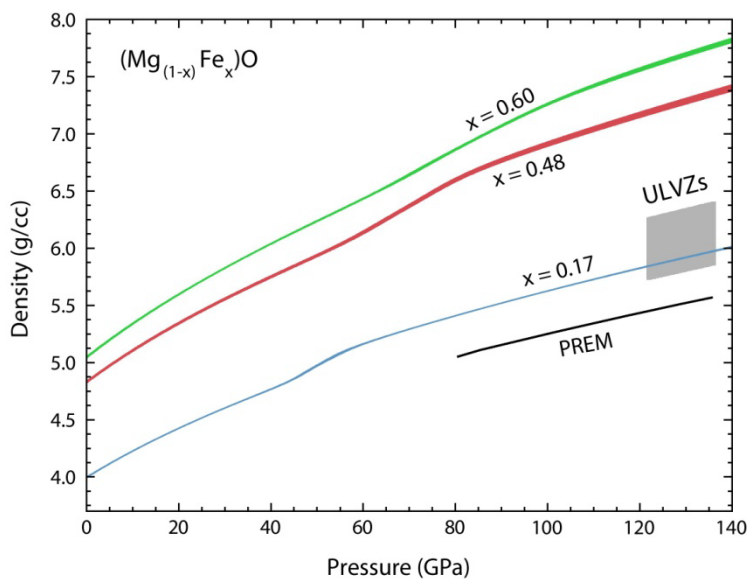


Figure 3.9: Density as a function of pressure for  $(\text{Mg}_{(1-x)}\text{Fe}_x)\text{O}$  at 300 K. An estimate for ULVZs is shown in grey [Rost *et al.*, 2005]. The density of Fp48 was corrected for natural  $^{57}\text{Fe}$  abundance. Color scheme same as Figure 3.8.

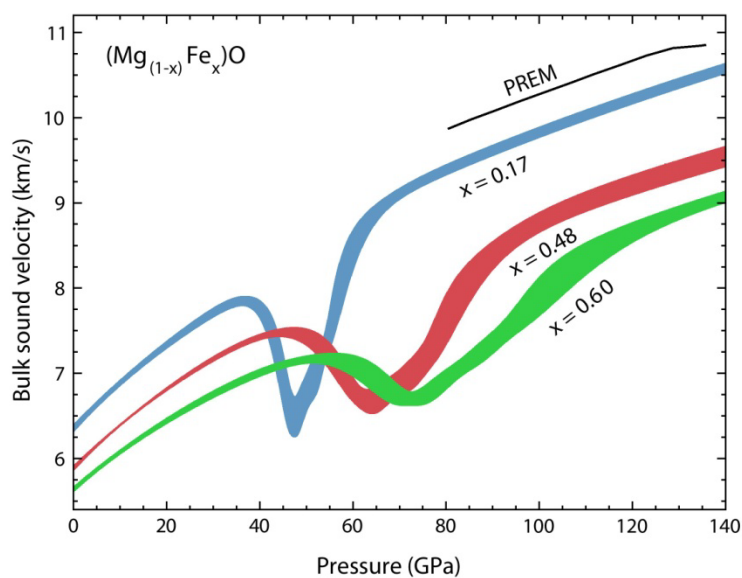


Figure 3.10: Bulk sound velocity as a function of pressure for  $(\text{Mg}_{(1-x)}\text{Fe}_x)\text{O}$  at 300 K. The bulk sound velocity for Fp48 was corrected for natural  $^{57}\text{Fe}$  abundance. Color scheme same as Figure 3.8.

Table 3.7: Spin crossover equation of state parameters determined from MINUTI using a third-order Birch Murnaghan equation of state and fixing  $K'_{0T,LS}$  to 4. For  $x=0.17$  to  $x=0.60$ , the data was fitted with the procedure described in Table 3.2. For  $x=0.10$ , where  $K_{0S,HS}$  was directly measured with Brillouin scattering [Marquardt *et al.*, 2009b], a prior of 161.4 GPa (the measured  $K_{0S,HS}$ ) with a prior window of  $\pm 3$  was used, accounting for a difference between the isothermal and adiabatic bulk modulus. The spin transition width ( $P_{tr}$  width) was determined from the 20/80% completion of the volume change due to the HS to LS transition, fitted with MINUTI.

Composition	$V_{0,HS}$ ( $\text{\AA}^3$ )	$V_{0,LS}$ ( $\text{\AA}^3$ )	$K_{0T,HS}$ (GPa)	$K_{0T,LS}$ (GPa)	$K'_{0T,HS}$	$P_{tr}$ (GPa)	$P_{tr}$ width (GPa)	References
(Mg <sub>0.90</sub> Fe <sub>0.10</sub> )O	75.55(4)	74.59(91)	159(2)	159(12)	3.96(14)	52.1(1.9)	2.3	Marquardt <i>et al.</i> [2009b]
(Mg <sub>0.83</sub> Fe <sub>0.17</sub> )O	75.94(10)	72.29(41)	160(2)	190(6)	4.04(16)	49.2(1.3)	8.2	Lin <i>et al.</i> [2005]
(Mg <sub>0.75</sub> Fe <sub>0.25</sub> )O	76.34(0)	73.74(19)	160(1)	174(2)	4.28(6)	62.6(7)	15.9	Mao <i>et al.</i> [2011]
(Mg <sub>0.65</sub> Fe <sub>0.35</sub> )O	77.10(12)	73.77(69)	162(3)	171(9)	3.99(15)	63.7(1.7)	13.3	Chen <i>et al.</i> [2012]
(Mg <sub>0.61</sub> Fe <sub>0.39</sub> )O	77.49(3)	74.83(38)	161(3)	162(4)	4.25(24)	56.6(1.5)	17.2	Fei <i>et al.</i> [2007]
(Mg <sub>0.61</sub> Fe <sub>0.39</sub> )O	77.41(7)	73.56(19)	160(1)	170(2)	4.07(5)	73.5(1.0)	10.3	Zhuravlev <i>et al.</i> [2010]
(Mg <sub>0.49</sub> Fe <sub>0.48</sub> )O*	77.29(0)	73.64(94)	160(2)	173(13)	4.12(14)	68.8(2.7)	18.4	This study
(Mg <sub>0.40</sub> Fe <sub>0.60</sub> )O	77.90(4)	73.83(84)	159(2)	169(9)	3.82(14)	78.6(5.1)	25.1	Lin <i>et al.</i> [2005]

\*See Experimental Methods for chemical analysis. The full composition as determined from microprobe analysis is (Mg<sub>0.490(3)</sub>Fe<sub>0.483(2)</sub>Ti<sub>0.027(5)</sub>)O.

Table 3.8: Experimental studies on the reported spin transition pressure ( $P_{tr}$ ) range of iron in (Mg,Fe)O at 300 K. The pressure mediums, pressure scales and definition of  $P_{tr}$  and  $P_{tr}$  range differ between these studies. Some of these studies did not use a pressure medium [Pasternak *et al.*, 1997; Badro *et al.*, 2003; Kantor *et al.*, 2006; Speziale *et al.*, 2005; Lin *et al.*, 2007].  $P_{tr}$  is a function of iron concentration and is likely sensitive to hydrostatic conditions.

Composition	$P_{tr}$ range (GPa)	Method	Pressure medium	Pressure scale	References
(Mg <sub>0.95</sub> Fe <sub>0.05</sub> )O	46-55	X-ray emission	none	ruby	Lin <i>et al.</i> [2007]
(Mg <sub>0.90</sub> Fe <sub>0.10</sub> )O	45-63	X-ray diffraction	Ne	ruby	Marquardt <i>et al.</i> [2009b]
(Mg <sub>0.88</sub> Fe <sub>0.12</sub> )O	51-60	Optical absorption	Ar	ruby	Keppler <i>et al.</i> [2007]
(Mg <sub>0.83</sub> Fe <sub>0.17</sub> )O	60-70	X-ray emission	none	ruby	Badro <i>et al.</i> [2003]
(Mg <sub>0.83</sub> Fe <sub>0.17</sub> )O	57-75	X-ray diffraction	Ne	Pt	Lin <i>et al.</i> [2005]
(Mg <sub>0.80</sub> Fe <sub>0.20</sub> )O	40-70 <sup>a</sup>	Energy-domain Mössbauer	none	ruby	Speziale <i>et al.</i> [2005]
(Mg <sub>0.80</sub> Fe <sub>0.20</sub> )O	55-105	Energy-domain Mössbauer	none	ruby	Kantor <i>et al.</i> [2006]
(Mg <sub>0.80</sub> Fe <sub>0.20</sub> )O	35-45	X-ray diffraction	NaCl	NaCl	Fei <i>et al.</i> [2007]
(Mg <sub>0.75</sub> Fe <sub>0.25</sub> )O	54-67	X-ray emission	NaCl	ruby	Lin <i>et al.</i> [2005]
(Mg <sub>0.75</sub> Fe <sub>0.25</sub> )O	55-65	Optical absorption	Ar, Ne	ruby	Goncharov <i>et al.</i> [2006]
(Mg <sub>0.75</sub> Fe <sub>0.25</sub> )O	52-70	Time-domain Mössbauer	KCl	ruby	Lin <i>et al.</i> [2006a]
(Mg <sub>0.75</sub> Fe <sub>0.25</sub> )O	52-78 <sup>b</sup>	X-ray diffraction	KCl, NaCl	Au	Mao <i>et al.</i> [2011]
(Mg <sub>0.65</sub> Fe <sub>0.35</sub> )O	49-79	X-ray diffraction	Ne	ruby	Chen <i>et al.</i> [2012]
(Mg <sub>0.61</sub> Fe <sub>0.39</sub> )O	60-66	X-ray diffraction	NaCl	NaCl	Fei <i>et al.</i> [2007]
(Mg <sub>0.61</sub> Fe <sub>0.39</sub> )O	65-77	X-ray diffraction	Ne	ruby	Zhuravlev <i>et al.</i> [2010]
(Mg <sub>0.49</sub> Fe <sub>0.48</sub> )O	59-78 <sup>c</sup>	X-ray diffraction	Ne	ruby	This study
(Mg <sub>0.49</sub> Fe <sub>0.48</sub> )O	52-85 <sup>d</sup>	Time-domain Mössbauer	Ne	ruby	This study
(Mg <sub>0.50</sub> Fe <sub>0.50</sub> )O	60-75 <sup>e</sup>	Energy-domain Mössbauer	none	ruby	Speziale <i>et al.</i> [2005]
(Mg <sub>0.42</sub> Fe <sub>0.58</sub> )O	75-85	X-ray diffraction	NaCl	NaCl	Fei <i>et al.</i> [2007]
(Mg <sub>0.40</sub> Fe <sub>0.60</sub> )O	84-102	X-ray emission	NaCl	ruby	Lin <i>et al.</i> [2005]
(Mg <sub>0.20</sub> Fe <sub>0.80</sub> )O	80-100	Energy-domain Mössbauer	none	ruby	Speziale <i>et al.</i> [2005]
(Mg <sub>0.16</sub> Fe <sub>0.84</sub> )O	100-121	Time-domain Mössbauer	boron epoxy	ruby	Wicks <i>et al.</i> [2010]
Fe <sub>0.94</sub> O	90-140	Energy-domain Mössbauer	none	ruby	Pasternak <i>et al.</i> [1997]

<sup>a</sup>Transition pressure at 6 K.

<sup>b</sup>A KCl pressure medium was used below 60 GPa, whereas NaCl was used above 60 GPa.

<sup>c</sup>Range from 20/80% volume change, as discussed in the text.

<sup>d</sup>Range from 19/76% LS population.

<sup>e</sup>Transition pressure at 10 K.

contributes an additional “spin buoyancy” to mantle materials containing ferropericlase [Bower *et al.*, 2009].

At the base of the mantle, 5-40 km thick patches of ultra-low velocity zones (ULVZs) have been detected, often located at the edges of large low shear velocity provinces (LLSVPs) [Garnero and Helmberger, 1996; McNamara *et al.*, 2010; Rost, 2013; Brown *et al.*, 2015]. Although many ULVZs are associated with LLSVPs and are thought to contain partial melt [Williams *et al.*, 1998], some appear uncorrelated with LLSVPs and hotspots on Earth's surface [Sun *et al.*, 2013]. These particular patches might be best explained by an enrichment of iron-rich (Mg,Fe)O [Labrosse *et al.*, 2007; Wicks *et al.*, 2010; Bower *et al.*, 2011; Rost *et al.*, 2013]. In order to explain ULVZs by the presence of (Mg,Fe)O, the resulting mixture must have topographic relief and wave speed reductions that match seismic observations. Distinct ULVZs at the base of the mantle have been explored in numerical convection models using a range of chemical density anomalies, where the buoyancy number of such a layer is determined in part by its thermal equation of state and controls its evolved topography [Bower *et al.*, 2011]. The systematic analysis presented here demonstrates that the enrichment of iron in (Mg,Fe)O increases the pressure and width of the spin crossover (see Figure 3.7 and Table 3.8). Therefore, iron-rich (Mg,Fe)O at the core-mantle boundary would likely contain a significant fraction of high-spin (less dense) iron, contributing a positive buoyancy to promote observable topographic relief. The combination of the results presented here and additional constraints on the phase equilibria, wave velocities and thermoelasticity of candidate phase assemblages will further narrow the range of plausible explanations of multi-scale structures in the deep mantle.

## Chapter 4

# Rhyolitic and basaltic glasses at high pressure\*

\* This chapter has been reformatted from what was submitted to the *Journal of Geophysical Research: Solomatova, N. V., Jackson, J. M., Sturhahn, W., Rossman, G. R., Roskocz, M. (2017), Electronic environments of ferrous iron in rhyolitic and basaltic glasses at high pressure, Journal of Geophysical Research: Solid Earth.*

### 4.1 Introduction

Iron-bearing silicate melts may exist in the lower mantle, particularly near the core-mantle boundary [Williams and Garnero, 1996; Vidale and Hedlin, 1998; Maruyama et al., 2007; Thomas et al., 2012]. The behavior of iron in melts derived from mantle rocks is poorly understood, but in some cases may be approximated by iron-bearing glasses. The local structure environment around iron in a glass can be taken as a good approximation for the melt structure, provided the quench rates are fast enough through the temperature interval of the glass transition,  $T_g$  [e.g., Rossano et al., 2008; Wilke et al., 2007]. Using X-ray absorption spectroscopy at the iron K-edge, Wilke et al. [2007] use the integrated pre-edge intensity and centroid position to determine iron's average coordination in Na, K and Al-bearing silicate melts and glasses. The average coordination of  $Fe^{2+}$  is found to be close to five, with a slightly higher concentration of fourfold coordinated  $Fe^{2+}$  in the melts compared to glasses. There is most likely a distribution of site geometries in the glasses. When compared to the liquid, the short-range metal-anion interatomic distances of quenched glasses have been shown to be similar or slightly shorter and the next-nearest neighbor distances longer, while the average coordination numbers of cations are smaller in the liquid (glass) than the crystalline aggregate. During crystallization, partitioning of the cations likely takes place between fourfold, fivefold and sixfold coordination sites in the magma and the octahedral sites in a crystal [Burns, 1993].

Nevertheless, previous studies have conflicting conclusions on the coordination of iron in silicate glasses, especially at high pressures. Experiments using X-ray absorption near edge spectroscopy on mid-oceanic ridge basalt (MORB) glasses have revealed that the average coordination of iron is about five regardless of oxidation state, and may potentially be a mixture of fourfold, fivefold and sixfold coordinated iron [Wilke et al.,

2005]. Nevertheless, it is still challenging to correlate spectral features to coordination environments in glasses, in part due to the range and distribution of available coordination environments. In Mössbauer experiments conducted in the energy-domain, the spectra are often fit using correlated distributions to capture these phenomena in glasses, yet challenges still remain. Conventional Mössbauer experiments have reported fivefold coordinated  $\text{Fe}^{2+}$  with small amounts of fourfold and sixfold coordinated  $\text{Fe}^{2+}$  for a suite of natural MORB glasses [Cottrell and Kelley, 2011], as well as predominantly sixfold  $\text{Fe}^{2+}$  with small amounts of fourfold  $\text{Fe}^{2+}$  in natural tektites and synthetic CaO-SiO<sub>2</sub>-FeO glasses [Alberto et al., 1996; Rossano et al., 1999]. Spectra from time-domain synchrotron Mössbauer experiments at high pressures have been fit with one to three  $\text{Fe}^{2+}$  sites with a wide range of quadrupole splitting and isomer shift values, but without the use of correlated distributions. These datasets have been used to interpret a range of spin, and in some cases oxidation states for the iron cations, leading to conflicting predictions on whether iron in lower mantle silicate melts goes through a high-spin to low-spin transition [Nomura et al., 2011; Gu et al., 2012; Murakami et al., 2014]. Thus, additional studies are necessary to help constrain the geometric and electronic state of iron in silicate glasses at high pressure.

## 4.2 Methods

### 4.2.1 Sample Preparation

The silicate glasses were synthesized at the University of Lille, France from powdered mixtures of SiO<sub>2</sub>, Al<sub>2</sub>O<sub>3</sub>, CaCO<sub>3</sub>, MgO, Na<sub>2</sub>CO<sub>3</sub>, K<sub>2</sub>CO<sub>3</sub>, TiO<sub>2</sub>, and Fe<sub>2</sub>O<sub>3</sub>, which were melted at 1550° C and quenched in air after 2-3 hours in the furnace. The oxidation state of iron was equilibrated with the imposed oxygen fugacity,  $\log(f\text{O}_2)$  of -8 (iron-wüstite buffer, IW + 0.3) using CO/CO<sub>2</sub> gas mixtures. For more synthesis details, we refer the reader to *Dauphas et al.* [2014]. The compositions of the glasses were determined with an electron microprobe at the UMET laboratory in the University of Lille 1. The oxide weight percents for the rhyolitic and basaltic glasses are listed in Table 4.1, and the oxide mole percents are illustrated in Figure 4.1.

Two diamond anvil cells with beveled 250- $\mu\text{m}$  diamonds on tungsten-carbide seats were assembled for the high-pressure measurements. For each experiment, a rhenium gasket of  $\sim 50\text{-}\mu\text{m}$  thickness was prepared by drilling a hole with a  $\sim 90\text{-}\mu\text{m}$  diameter. In one diamond anvil cell, a 60 by 50  $\mu\text{m}$  chip of rhyolitic glass with a thickness of about 11  $\mu\text{m}$  was loaded onto the center of the diamond culet and two ruby spheres with diameters of 6 and 7.5  $\mu\text{m}$ , respectively, were loaded next to the sample as a pressure gauge. In the second diamond anvil cell, a  $\sim 40\text{-}\mu\text{m}$  chip of basaltic glass with a

	MgO %	FeO %	Fe <sub>2</sub> O <sub>3</sub> %	CaO %	Na <sub>2</sub> O %	K <sub>2</sub> O %	TiO <sub>2</sub> %	Al <sub>2</sub> O <sub>3</sub> %	SiO <sub>2</sub> %
Basaltic glass	18.33	7.61	-	11.40	1.03	0.09	0.86	14.46	46.26
Rhyolitic glass	0.05	4.10	-	0.03	4.54	4.49	0.00	10.44	75.71
Andesitic glass	8.30	7.04	-	7.22	2.98	1.44	0.81	16.30	55.80
Dacitic glass	4.23	4.47	-	4.68	3.93	2.50	0.71	14.90	64.10
<i>Murakami et al.</i> [2014]	30.16	13.63	-	0.00	0.00	0.00	0.00	0.00	56.20
<i>Gu et al.</i> [2012], Al <sup>3+</sup> -free	30.16	13.63	-	0.00	0.00	0.00	0.00	0.00	56.20
<i>Gu et al.</i> [2012], Al <sup>3+</sup> -bearing	28.26	13.62	-	0.00	0.00	0.00	0.00	4.77	53.35
<i>Mao et al.</i> [2014]	31.05	1.56	6.15	0.00	0.00	0.00	0.00	4.97	56.26
<i>Prescher et al.</i> [2014], Fe <sup>3+</sup> -free	31.62	9.38	-	0.00	0.00	0.00	0.00	2.77	56.24
<i>Prescher et al.</i> [2014], Fe <sup>3+</sup> -bearing	0.00	9.29	25.44	0.00	12.91	0.00	0.00	0.00	52.36
<i>Alberto et al.</i> [1995], sample A	0.00	5.00	-	34.1	0.00	0.00	0.00	0.00	60.9
<i>Rossano et al.</i> [1999], Thailand tektite	2.02	4.91	0.29	2.23	1.21	2.16	0.77	12.73	73.27
<i>Dorfman et al.</i> [2016]	0.00	33.56	7.63	0.00	0.00	0.00	0.00	22.50	36.31
<i>Jackson et al.</i> [2005], BAS	0.00	13.74	-	9.96	3.07	0.00	0.00	15.85	50.08
<i>Jackson et al.</i> [2005], NC2	0.00	17.22	-	9.52	11.25	0.00	0.00	0.00	62.01
<i>Jackson et al.</i> [2005], NA1	0.00	27.51	-	0.00	10.95	0.00	0.00	0.00	61.54

Table 4.1: Oxide weight percents of silicate glasses considered in this study. The Fe<sub>2</sub>O<sub>3</sub> % is estimated as 0 for reduced glasses with Fe<sup>3+</sup> content below the detection level of the fit, except for *Rossano et al.* [1999] where coulometric titration was used to determine the exact Fe<sup>3+</sup> content. The rhyolitic and basaltic glasses contain about 0.02-0.04 wt% and 0.005-0.008 wt% of OH<sup>-</sup>, respectively (see text for details). The tektite in *Rossano et al.* [1999] has 0.03 wt% P<sub>2</sub>O<sub>5</sub>.

thickness of about 12  $\mu\text{m}$  was loaded with a 10  $\mu\text{m}$  ruby sphere. Both cells were loaded with neon at 25000 psi using the gas-loading system at Caltech.

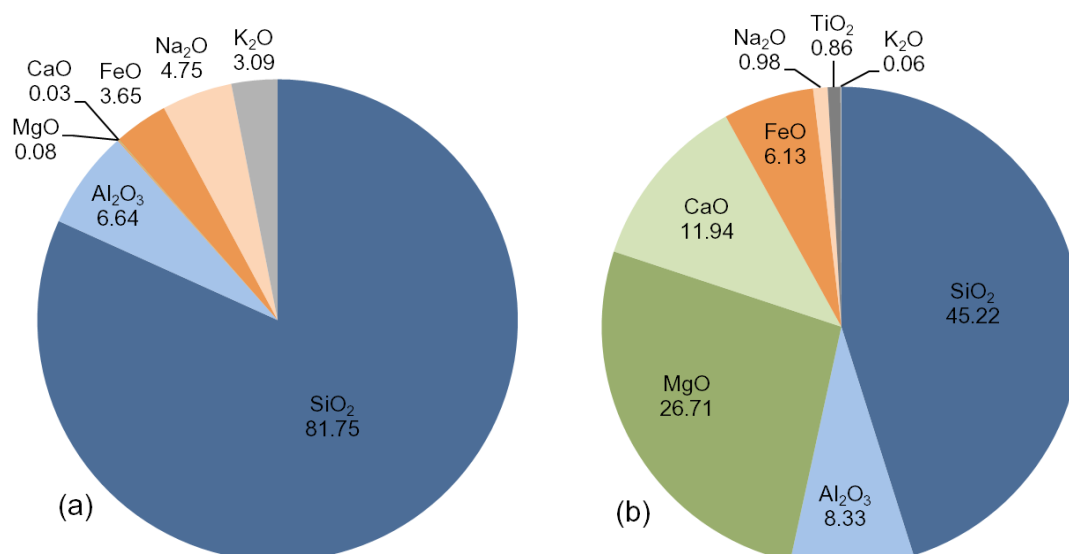


Figure 4.1: Composition in oxide mole percents for (a) rhyolitic glass and (b) basaltic glass. The rhyolitic and basaltic glasses contain about 0.1-0.2 mol% and 0.03-0.05 mol% of OH<sup>-</sup>, respectively (see text for details).

#### 4.2.2 Experimental Methods

Optical absorption spectroscopic measurements were conducted on polished samples of the rhyolitic and basaltic glasses with thicknesses of 95 and 300  $\mu\text{m}$ , respectively, at room temperature. Room-temperature ultraviolet/visible/near-infrared (UV/VIS/NIR) absorption spectra were collected at the Caltech mineral spectroscopy laboratory in the wavenumber range of  $\sim 27100\text{ cm}^{-1}$  and  $2000\text{ cm}^{-1}$  for the rhyolitic glass and  $\sim 27700\text{ cm}^{-1}$  and  $1200\text{ cm}^{-1}$  for the basaltic glass. For wavenumbers below about  $10000\text{ cm}^{-1}$ , we used a Nicolet iS50 FT-IR spectrometer with CaF<sub>2</sub>, KBr and SiO<sub>2</sub> beamsplitters and InGaAs and deuterated triglycine sulfate detectors. Above  $10000\text{ cm}^{-1}$ , we used a Si diode array spectrometer. The sample chamber of the Nicolet iS50 FT-IR spectrometer was purged to reduce atmospheric H<sub>2</sub>O and CO<sub>2</sub> in the infrared region. Spectra were averaged over approximately 1000-2000 scans in the UV/VIS region and 200-400 scans in the IR region.

Relevant hyperfine parameters for the silicate glasses were determined with Mössbauer spectroscopy [Mössbauer, 1962]. The isomer shift (IS) originates from the electron density at the nucleus and is indirectly influenced, via shielding effects, by the  $d$  electrons in the valence shell, thus allowing constraints on the oxidation state. A nuclear quadrupole splitting (QS) results from a non-vanishing electric field gradient at the

Mössbauer nucleus occupying a state with an angular momentum quantum number  $I > 1/2$ . The QS yields information on the local coordination environment and, complementary to the isomer shift, oxidation and spin states of the atom can be deduced.

Conventional energy-domain  $^{57}\text{Fe}$  Mössbauer spectroscopic experiments were conducted using a radioactive source at 1 bar and 298 K. The spectra for the basaltic and andesitic glasses were collected at the Advanced Photon Source (APS), and the spectra for rhyolitic and dacitic glasses were collected at the Unité Matériaux et Transformations (UMET) laboratory. High-pressure hyperfine parameters for the rhyolitic and basaltic glasses were determined with time-domain synchrotron Mössbauer spectroscopy (SMS). The SMS measurements were conducted at Sector 3-ID-B of the APS. The storage ring was operated in top-up mode with 24 bunches separated by 153 ns. A high-resolution monochromator was tuned to the 14.4125 keV nuclear transition energy of  $^{57}\text{Fe}$  with a FWHM of 1 meV [Toellner, 2000]. The beam was focused to an area of 10 by 11  $\mu\text{m}^2$  using a Kirkpatrick-Baez mirror system [Zhang *et al.*, 2015]. The time spectra were measured with an avalanche photodiode detector, positioned  $\sim 0.5$  m downstream from the sample in the forward direction. A time window of 21 to 128 ns after excitation was used to observe nuclear resonant scattering and fit the data.

A stainless steel (SS) foil was placed in the downstream direction as a reference absorber for isomer shift measurements. At each compression point, an SMS spectrum was collected for the sample with and without a naturally  $^{57}\text{Fe}$ -enriched SS foil. For the experiments on rhyolitic glass, a 25  $\mu\text{m}$  SS foil was used between 3.1 and 24.8 GPa, a 6  $\mu\text{m}$  SS foil was used between 30.5 and 94.0 GPa, and a 10  $\mu\text{m}$  SS foil was used between 102 and 119 GPa. For the experiments on basaltic glass, we used a 10  $\mu\text{m}$  SS foil for the entire pressure range. The isomer shifts between the SS foils and  $\alpha$ -iron metal were measured at the APS using a radioactive source and found to be -0.107(4), -0.100(3) and -0.094(3) mm/s with a corresponding FWHM (due to the combined effect of site distribution and source broadening) of 0.42(1), 0.445(9) and 0.50(1) mm/s for the 6, 10 and 25  $\mu\text{m}$  SS foils, respectively. Pressure was determined before and after the SMS data collection with ruby fluorescence at GSECARS of the APS using the ruby fluorescence pressure scale reported in Mao *et al.* [1986]. We select this particular pressure scale due to its use in previous high-pressure studies on silicate glasses [Gu *et al.*, 2012; Mao *et al.*, 2014; Prescher *et al.*, 2014; Dorfman *et al.*, 2016]. The average pressure drifts during the measurements were 0.3 GPa for the rhyolitic glass and 0.6 GPa for the basaltic glass. For the rhyolitic glass, pressure was measured with the first-order Raman band of the diamond anvils above 94 GPa. We assume a pressure error of 3 GPa above 94 GPa, accounting for the systematic difference between Raman band pressure and ruby pressure.

### 4.2.3 Fitting Procedure of Mössbauer Spectra

Synchrotron Mössbauer spectroscopy spectra were fitted with version 2.1.1 of the CONUSS software [Sturhahn, 2000], which uses a least-square algorithm to fit iron's hyperfine parameters (e.g., isomer shift, quadrupole splitting and distribution of the quadrupole splitting expressed as the full width at half maximum, and the correlation parameter for the distributions), sample thickness, and relative weights of the sites. We used the dual fit module within the CONUSS software (implemented in version 2.1.1), which fits the spectrum of the sample and sample with SS simultaneously, and permits the use of prior information (“priors”) in fitting of the data. It is important to use a well-defined reference foil with a uniform effective thickness that is similar to that of the sample. For evaluations of data of the rhyolitic glass sample between 3.1 and 24.8 GPa, the relatively large effective thickness of the 25  $\mu\text{m}$  stainless steel foil required a prior of 1.08 mm/s with a prior window of  $\pm 0.01$  mm/s for the isomer shift of site 1 (equivalent to the isomer shift of site 2) and a prior of 0.80 mm/s with a prior window of  $\pm 0.01$  mm/s for the isomer shift of site 3. Prior values correspond to the isomer shifts of the two sites fitted in the ambient pressure spectra that were collected using a radioactive source, adjusted relative to the 25- $\mu\text{m}$  thick stainless steel foil. No priors were used for pressures above 24.8 GPa, and no priors were used while fitting the spectra of the basaltic glass.

Energy-domain Mössbauer absorption spectra of silicate glasses are typically composed of asymmetrical doublets due to site distributions. To account for the spectral asymmetry, we model the distributions of the isomer shift and quadrupole splitting as linearly correlated. The use of correlated isomer shift and quadrupole splitting distributions results in a lower reduced  $\chi^2$  compared to models without the use of correlated distributions. In CONUSS, one-dimensional distributions are implemented with the possibility of attaching a second parameter corresponding to a pseudo two-dimensional distribution defined by the covariance matrix

$$\hat{\sigma} = \frac{\text{FWHM}^2}{8\ln 2} \begin{pmatrix} 1 & \Delta \\ \Delta & \Delta^2 \end{pmatrix} \quad (4.1)$$

where  $\Delta$  is the attachment parameter. The distribution width of the two lines is then

$$\text{FWHM}_{\pm} = \left| 1 \pm \frac{\Delta}{2} \right| \text{FWHM}. \quad (4.2)$$

Two values of  $\Delta$  and FWHM,

$$\Delta_1 = 2 \frac{\text{FWHM}_+ + \text{FWHM}_-}{\text{FWHM}_+ - \text{FWHM}_-}, \quad (4.3)$$

$$\Delta_2 = 2 \frac{\text{FWHM}_+ - \text{FWHM}_-}{\text{FWHM}_+ + \text{FWHM}_-}, \quad (4.4)$$

$$\text{FWHM}_1 = \frac{1}{2} |\text{FWHM}_+ - \text{FWHM}_-|, \quad (4.5)$$

$$\text{FWHM}_2 = \frac{1}{2} |\text{FWHM}_+ + \text{FWHM}_-| \quad (4.6)$$

lead to identical spectra. Thus, one may obtain alternative solutions using the relationship:  $\Delta_2=4/\Delta_1$  and  $\text{FWHM}_2=2\text{FWHM}_1/\Delta_2$ . For example, for site 1 in basaltic glass at 58.3 GPa, the FWHM is 0.68 mm/s and the attachment parameter is 0.27; the alternative solution is a FWHM of 0.09 mm/s and an attachment parameter of 14.65. We choose the FWHM similar to those reported in high-pressure energy-domain synchrotron Mössbauer studies on silicate glasses [Murakami *et al.*, 2014; Prescher *et al.*, 2014; Dorfman *et al.*, 2016].

## 4.3 Results

### 4.3.1 Optical Absorption Spectroscopy

The ultraviolet/visible/near-infrared (UV/VIS/NIR) absorption spectra of rhyolitic and basaltic glasses are shown in Figure 4.2. The dominant features of the spectrum of rhyolitic glass are two intense bands at  $\sim 9000 \text{ cm}^{-1}$  and  $12500 \text{ cm}^{-1}$  while the dominant feature of the spectrum of basaltic is an intense absorption band near  $\sim 9500 \text{ cm}^{-1}$ . The spectrum of the basaltic glass also has an absorption band at  $\sim 5000 \text{ cm}^{-1}$ , which appears as a shoulder in the spectrum of the rhyolitic glass. These absorption bands are consistent with electronic transitions in ferrous iron in fourfold, fivefold and/or sixfold coordination in silicate glasses [e.g., Boon and Fyfe, 1972; Iwamoto, 1978; Nolet, 1980; Jackson *et al.*, 2005; Kido *et al.*, 2006; Carl *et al.*, 2007; Rossano *et al.*, 2008; Klement *et al.*, 2009]. Distorted octahedral ferrous sites (e.g., the M2 crystallographic site in orthopyroxenes) result in absorption bands at about  $11000$ ,  $5400$  and  $2350 \text{ cm}^{-1}$  [Goldman and Rossman, 1977], fivefold ferrous iron sites in grandidierite and joaquinite result in two to three absorption bands between  $12550$  and  $9500 \text{ cm}^{-1}$  and one at around  $4500$ - $5000 \text{ cm}^{-1}$  [Rossman and Taran, 2001] and tetrahedral ferrous sites typically result in absorption bands between  $2500$  and  $6250 \text{ cm}^{-1}$  [Burns, 1985; Rossman and Taran, 2001]. In a glass, iron atoms most likely occupy a continuum of coordination environments. Nonetheless, a qualitative assessment of the optical spectra suggests that there is a low concentration of tetrahedrally-coordinated iron in these glasses. In the basaltic glass, the approximate fourfold ferrous iron concentration with respect to total ferrous iron is 0.6-14%, assuming that the  $5000$  and  $9500 \text{ cm}^{-1}$  bands are entirely due to fourfold and sixfold ferrous iron

with a molar extinction coefficient of 30-40 L/mol-cm and 1-16 L/mol-cm, respectively [Rossman and Taran, 2001; Klement *et al.*, 2009]. The rhyolitic glass contains about half the concentration of tetrahedrally-coordinated iron compared to the basaltic glass using the same assumptions. Thus, the majority of the iron in the rhyolitic and basaltic glasses most likely exist in fivefold and/or distorted sixfold coordination, similar to that reported in the Jackson *et al.* [2005] study for iron-bearing silicate glasses of a wide variety of compositions (see Table 4.1).

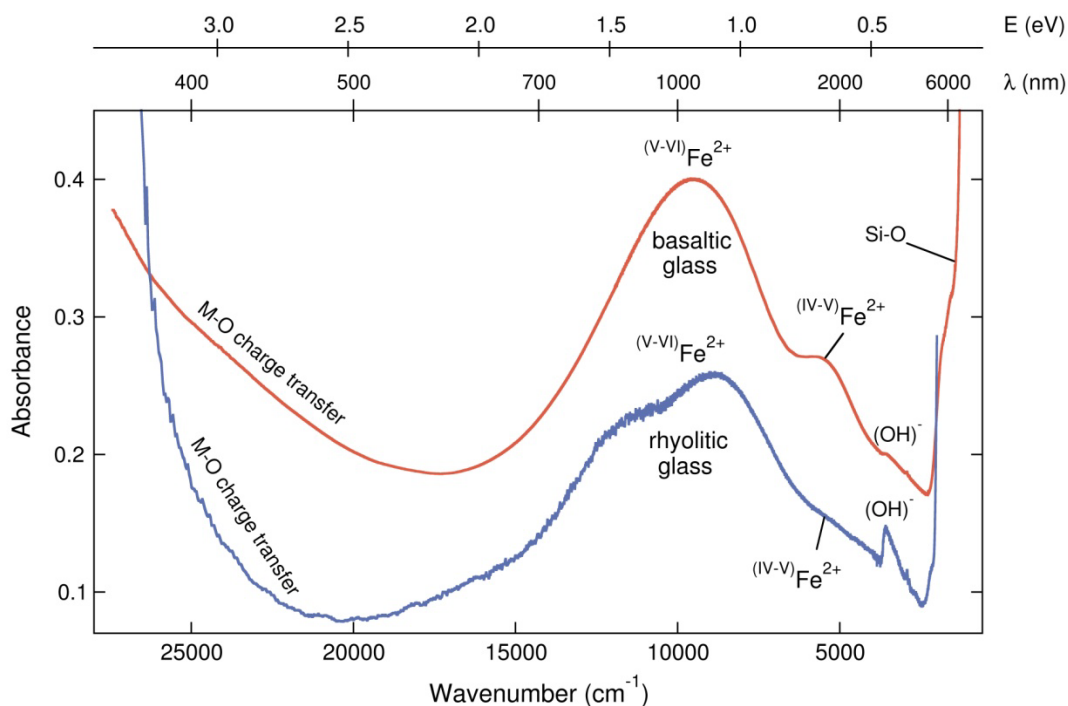


Figure 4.2: UV/VIS/NIR absorption spectra of rhyolitic glass (blue) and basaltic glass (red). The samples were polished to a thickness of 95 and 300  $\mu\text{m}$ , respectively. The spectra are plotted for an equivalent iron concentration, and offset for clarity.

There are no clearly identifiable  $\text{Fe}^{3+}$  features in the optical absorption spectra; however, small amounts of  $\text{Fe}^{3+}$  cannot be excluded based on these spectra due to the intense metal-oxygen charge transfer in the ultra-violet region above  $\sim 20000\text{ cm}^{-1}$  [ElBatal *et al.*, 2007; Carl *et al.*, 2007]. The very intense absorption band at  $\sim 950\text{-}1100\text{ cm}^{-1}$  is due to the Si-O fundamental stretching mode and the less intense absorption bands at about  $1600\text{-}1950\text{ cm}^{-1}$  evident in the basaltic glass are related to Si-O stretching overtones [Manghnani *et al.*, 1973; Costa *et al.*, 1997; Karakassides *et al.*, 1999; Madejova and Komadel, 2001]. In both glasses, the sharp features at about  $3500\text{ cm}^{-1}$  are due to structural  $\text{OH}^-$ . We fitted a Gaussian function to the dominant  $\text{OH}^-$  band at  $3583$  and  $3451\text{ cm}^{-1}$  in the rhyolitic and basaltic glasses, respectively. The molar extinction

coefficients for the OH<sup>-</sup> vibrational bands depend on the composition and the OH<sup>-</sup> content of the glasses. Using values of 60 to 100 Lmol<sup>-1</sup>cm<sup>-1</sup> as lower and upper bounds [Newman *et al.*, 1986; Pandya *et al.*, 1992; Behrens *et al.*, 2003], we find that the rhyolitic glass likely contains about 0.02 - 0.04 wt% (0.1 - 0.2 mol%) of OH<sup>-</sup> while the basaltic glass contains about 0.005 - 0.008 wt% (0.03 - 0.05 mol%) of OH<sup>-</sup>.

### 4.3.2 Mössbauer Spectroscopy

Conventional Mössbauer spectra for the rhyolitic and basaltic glasses used in this study were reported in *Dauphas et al.* [2014], but detailed fits of the hyperfine parameters were not reported. These spectra are shown in Figure 4.3 with our best fits. The rhyolitic glass required two Fe<sup>2+</sup>-like sites with weight fractions, 0.80(5) and 0.20 for the sites with a higher and lower QS, respectively, where the uncertainties are given in parentheses at the 68% confidence level (Table 4.2). The first site is characterized by a QS of 1.729(9) mm/s and an IS of 0.982(2) mm/s. The second site is characterized by a QS of 0.65(2) mm/s and an IS of 0.705(8) mm/s. The basaltic glass required two sites with weight fractions, 0.83(6) and 0.17 for the sites with a higher and lower QS, respectively. The first site is characterized by a QS of 1.995(7) mm/s and an isomer shift of 0.948(3) mm/s, whereas the second site is characterized by a QS of 0.96(5) mm/s and an IS of 0.69(2) mm/s. For both glasses, the site with the higher QS is likely a result of fivefold and/or sixfold coordination Fe<sup>2+</sup>, while the site with the lower QS can be attributed to fourfold or fivefold Fe<sup>2+</sup> (see Discussion for more details). The spectra of basaltic glass can also be fitted with a three-site model, but results in a slightly worse fit than the two-site model. Attempts were made to fit the low-pressure energy-domain and time-domain spectra with 5-10% Fe<sup>3+</sup> (i.e., isomer shift values below about 0.5 mm/s [Mysen, 1986; Burns, 1994]), however these models did not reproduce the shape of the spectra well and resulted in significantly higher  $\chi^2$  values. Thus, we conclude that the Fe<sup>3+</sup> content in our samples is below the detection limits of Mössbauer and optical absorption spectroscopy.

Typical high-pressure time-domain synchrotron Mössbauer spectra (SMS) for rhyolitic and basaltic glass are shown in Figure 4.4 together with their best-fit models. The hyperfine parameters of the best-fit models were then used to calculate the energy spectra shown in Figure 4.5. The spectra for rhyolitic glass required three sites with weight fractions, 0.34(2), 0.47 and 0.19 for site 1, site 2 and site 3, respectively (Figure 4.6). These values were determined from Monte Carlo searches and a careful analysis of  $\chi^2$ , because strong parameter correlations prevented unconstrained variation. The isomer shifts for site 1 and site 2 are very similar and are constrained to be equal. The steep increase at low pressures in the QS values for site 1 plateaus at ~3.1-3.3 mm/s above about 40 GPa. The shallow increase of the QS for site 2 up to ~50 GPa is followed by a

plateau at  $\sim 2.3$ - $2.4$  mm/s. The QS of site 3 increases slowly with pressure from 0.63 mm/s at 0 GPa to 1.18 mm/s at 119 GPa. The IS values are roughly constant at about 1 and 0.7 mm/s up to 81 GPa, after which they decrease to 0.85 and 0.63 mm/s at 119 GPa for the first two sites and the third site, respectively. Hyperfine parameters for rhyolitic glass are tabulated in Table 4.3 and the correlation matrix for the fitted parameters is reported in Table 4.4.

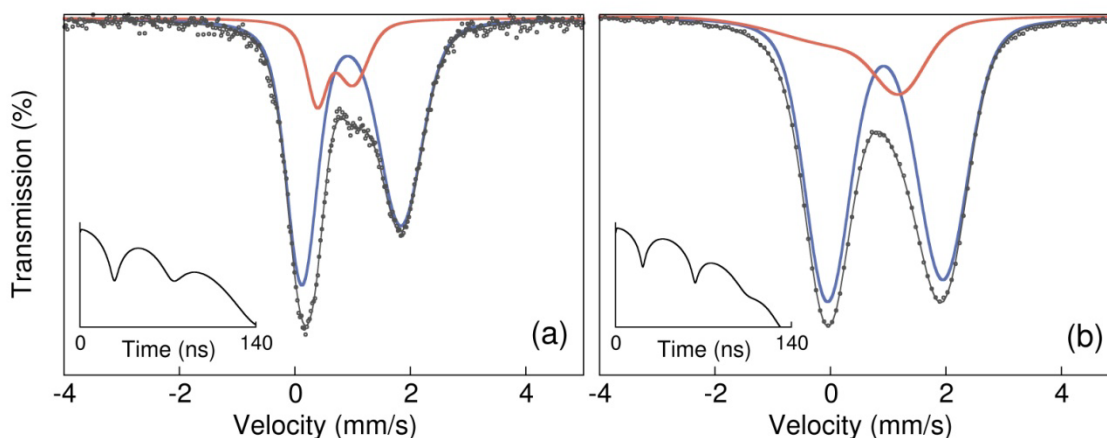


Figure 4.3: Conventional Mössbauer spectra for (a) rhyolitic glass and (b) basaltic glass at room pressure and temperature, and the corresponding best fits. Blue and red lines correspond to site 1 and site 2, respectively. Insets show modeled time-domain spectra of these best fits.

	Weight 1	QS site 1 (mm/s)	IS site 1 (mm/s)	FWHM site 1 (mm/s)	$\Delta$ site 1	QS site 2 (mm/s)	IS site 2 (mm/s)	FWHM site 2 (mm/s)	$\Delta$ site 2
Rhyolite	0.80(5)	1.729(9)	0.982(2)	0.571(9)	0.38(2)	0.65(2)	0.705(8)	0.37(2)	0.66(9)
Basalt	0.83(6)	1.995(7)	0.948(3)	0.804(6)	0.102(6)	0.96(5)	0.69(2)	1.72(6)	-1.09(7)
Andesite	0.77(4)	2.032(8)	1.001(3)	0.812(7)	0.086(2)	1.00(3)	0.922(2)	1.24(7)	-0.84(5)
Dacite	0.94(9)	1.859(3)	1.040(2)	0.632(5)	0.276(8)	0.70(8)	0.91(4)	0.80(8)	-1.18(9)

Table 4.2: Best-fit hyperfine parameters for rhyolitic, basaltic, andesitic and dacitic glasses from fitting the ambient conventional Mössbauer spectra with the CONUSS software. The uncertainties are given in parenthesis at the 68% confidence level for the last reported significant digit.

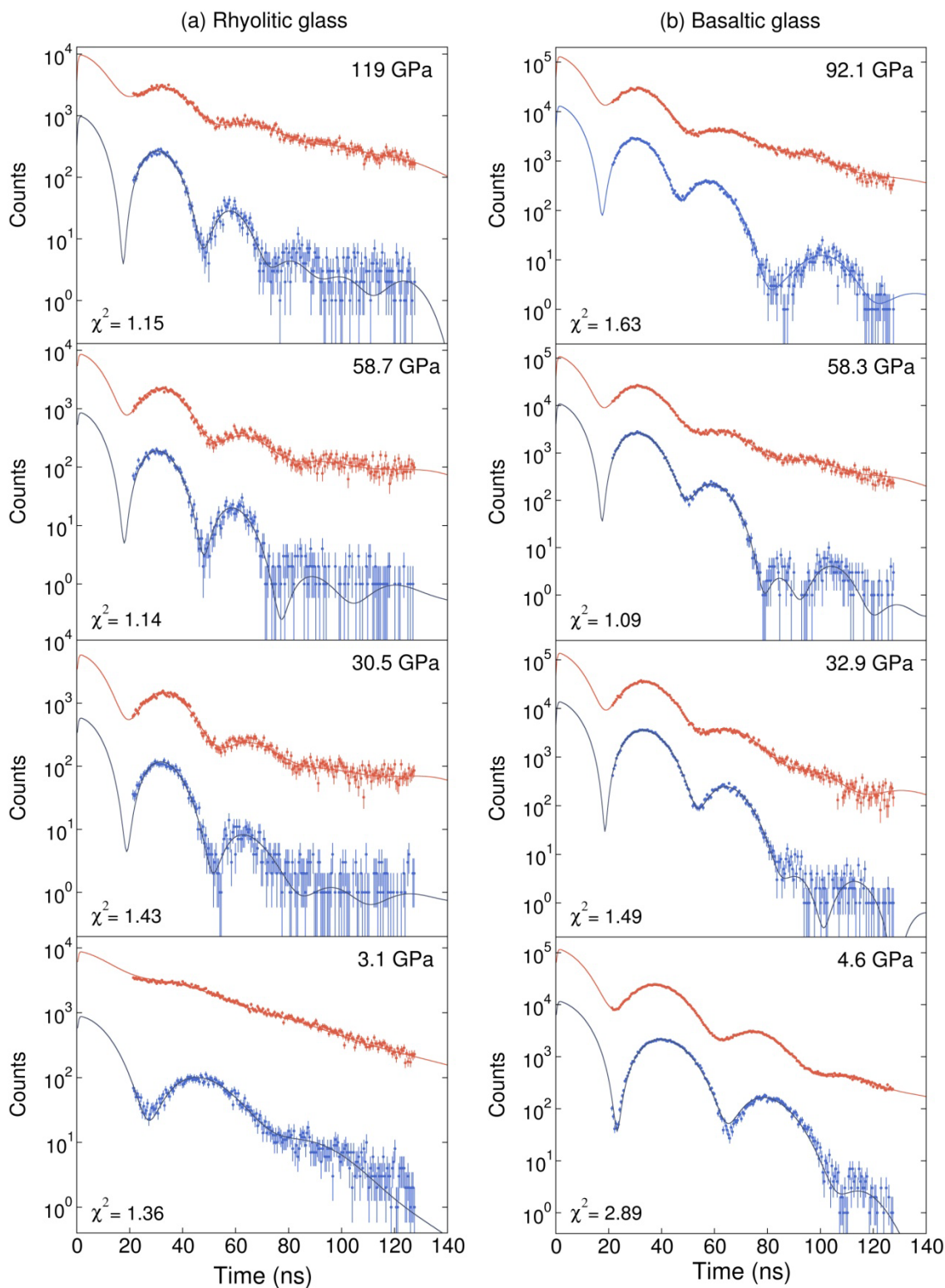


Figure 4.4: Select synchrotron Mössbauer spectra of (a) rhyolitic glass (Table 4.3) and (b) basaltic glass (Table 4.5) without stainless steel foil (blue) and with stainless steel foil (red) in the X-ray beam path. Their corresponding best fits with the reduced  $\chi^2$  for each dual fit are shown in the lower left corner.

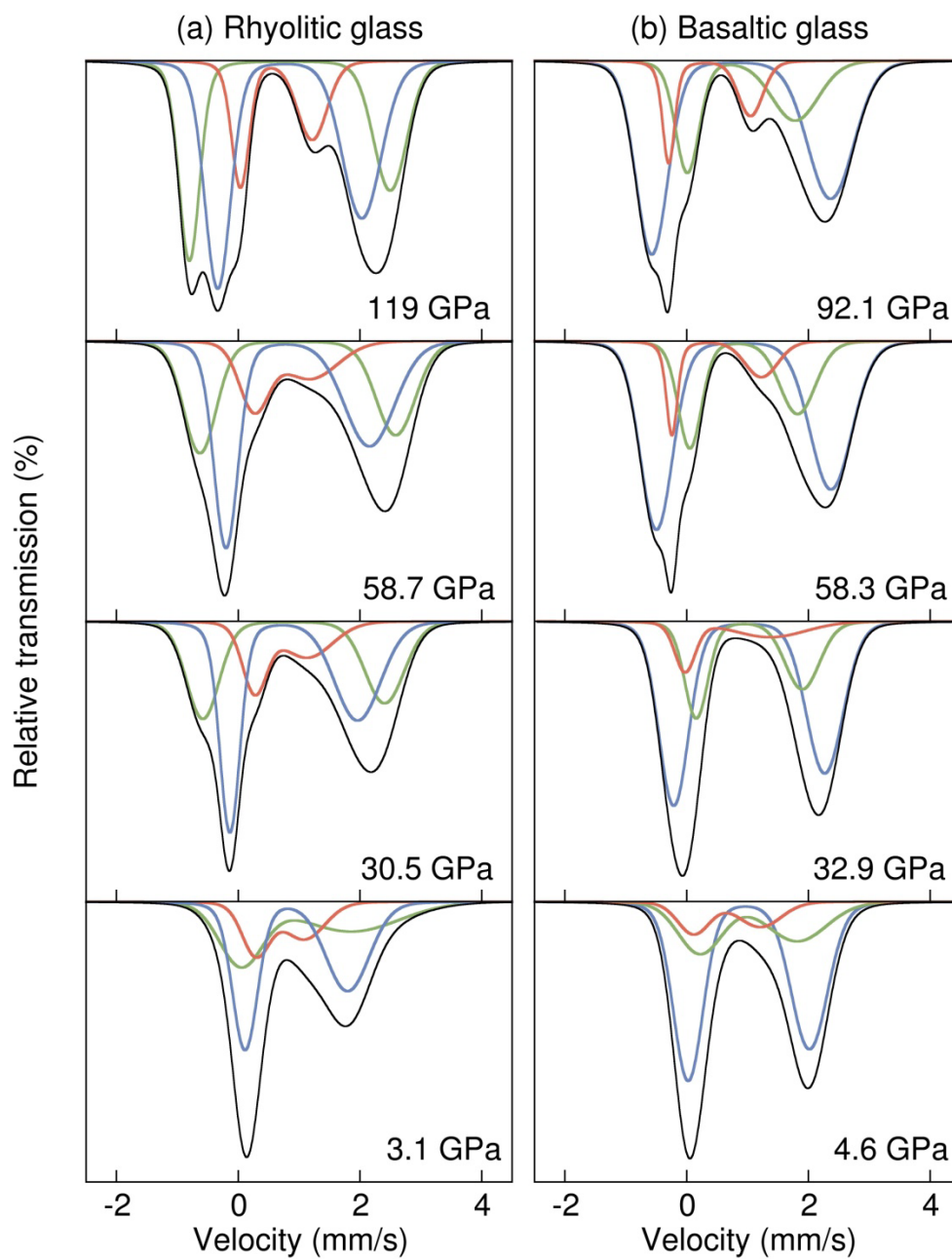
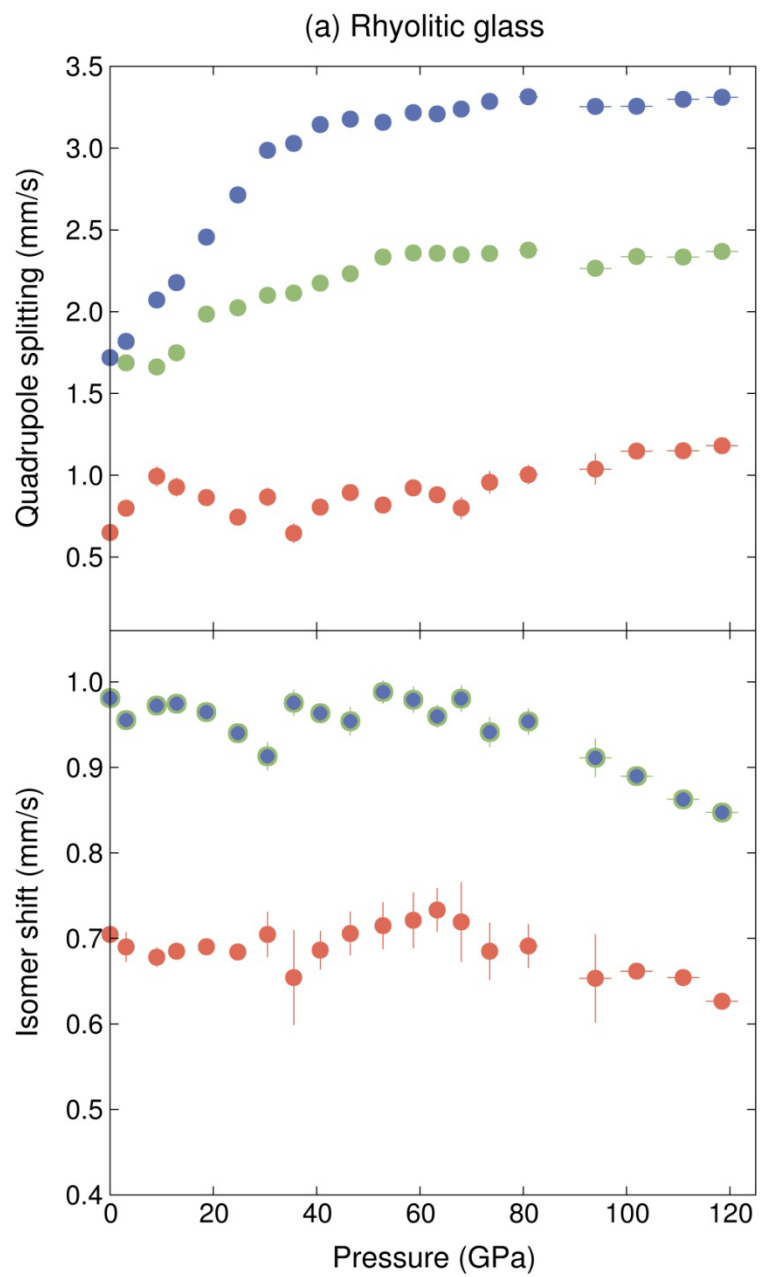


Figure 4.5: Modeled energy spectra of rhyolitic and basaltic glass using the best-fit parameters (Tables 4.3 and 4.5, respectively). Blue, green and red lines correspond to site 1, site 2 and site 3, depicted as blue, green and red circles in Figure 4.6. Source broadening is not modeled and isomer shifts are relative to  $\alpha$ -iron.



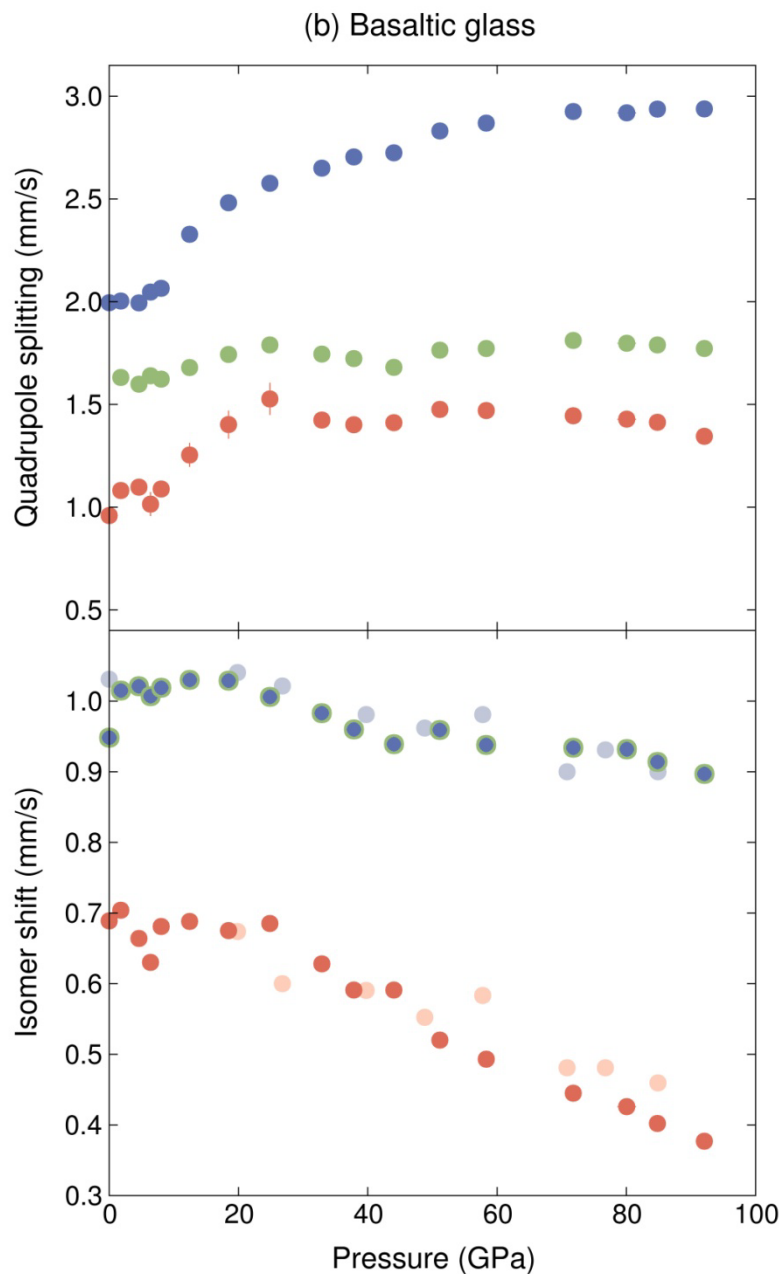


Figure 4.6: Quadrupole splitting and isomer shift (relative to  $\alpha$ -Fe) of (a) rhyolitic glass and (b) basaltic glass. Blue circles correspond to  $\text{Fe}^{2+}$  with a high quadrupole splitting (site 1), green circles are  $\text{Fe}^{2+}$  with an intermediate quadrupole splitting (site 2) and red circles are  $\text{Fe}^{2+}$  with a low quadrupole splitting (site 3). The isomer shifts of site 1 and site 2 are set to be equivalent (blue circles with green outline). (a) At 0 GPa, the relative weight fractions are 0.80 and 0.20 for site 1 and site 2, respectively. Above 0 GPa, the relative weights are 0.34, 0.47 and 0.19 for site 1, site 2 and site 3 respectively. (b) At 0 GPa, the relative weight fractions are 0.83 and 0.17 for the high and low QS sites, respectively. Between 1.8 and 80.1 GPa, the relative weights are 0.62, 0.26 and 0.12 for site 1, site 2 and site 3, respectively. At 84.8 and 92.4 GPa, the relative weights are 0.6, 0.26 and 0.14 for site 1, site 2 and site 3, respectively.

The SMS spectra for basaltic glass also required three sites (Figure 4.6). Between 1.8 and 80.1 GPa, the weight fractions were fixed at 0.62(3), 0.26 and 0.12 for site 1, site 2 and site 3, respectively. As in the case of the rhyolitic glass, variations of these values were accompanied by large errors caused by strong parameter correlations. Therefore they were determined from Monte Carlo searches and a careful analysis of  $\chi^2$  and correlations between fitted parameters. There was no need to vary the weights for spectra collected at pressures higher than 80.1 GPa due to excellent fits to both sample and sample with the stainless steel reference absorber. At higher pressures, we found that the best weight fractions are 0.60(2), 0.26 and 0.14 for site 1, site 2 and site 3, respectively. Between 0 and 8 GPa, the QS of site 1 is constant around 2 mm/s and increases with pressure from 12 to 58 GPa, after which it plateaus to  $\sim 2.9$  mm/s. The QS of site 2 is roughly constant around 1.7 mm/s while the QS of site 3 increases from 0.96 mm/s at 0 GPa to about 1.5 mm/s at 25 GPa, after which it plateaus at  $\sim 1.4$  mm/s. The IS of site 1 and site 2 are constant up to 25 GPa at  $\sim 1$  mm/s, after which they decrease to  $\sim 0.9$  mm/s at the highest pressure, while the isomer shift of site 3 remains constant at  $\sim 0.7$  mm/s up to 25 GPa after which it decreases to 0.37 mm/s at the highest pressure. The negative slope of the IS with pressure for the  $\text{Fe}^{2+}$  sites is consistent with previous studies on silicate glasses of similar composition [Murakami *et al.*, 2014; Prescher *et al.*, 2014]. Attempts were made to fit the high-pressure data with a fourth ferrous site with low-spin hyperfine parameters (QS=0-0.4 mm/s and IS=0.3-0.6 mm/s), but after extensive Monte Carlo searches, such a site in any proportion could not fit the data. Hyperfine parameters for basaltic glass are tabulated in Table 4.5 and the correlation matrix for the fitted parameters at 58.3 GPa is reported in Table 4.6.

## 4.4 Discussion

### 4.4.1 Coordination Environments at Room Pressure

In silicate minerals at ambient conditions, sixfold ferrous iron sites typically show QS values ranging from 1.5 to 3.2 mm/s and IS values of 1 to 1.2 mm/s. For eightfold ferrous iron sites, QS values of 3.2 to 3.5 mm/s and IS values of 1.2 to 1.3 mm/s have been observed [e.g., Burns 1994; Dyar *et al.*, 2006]. The range of QS values for sixfold ferrous iron has been correlated to the degree of distortion of the local site environment [Burns 1994; Victor *et al.*, 2001; Dyar *et al.*, 2006; Zhang *et al.*, 2011].

The range of reported QS and IS values of fourfold ferrous iron is shifted to lower values, with some overlap, relative to those of sixfold coordinated sites. QS values range from 0.7 to 2.3 mm/s with IS values of about 0.9 to 1.1 mm/s. In staurolite, the reported QS and IS values for fourfold iron are 1.3 to 1.6 mm/s and  $\sim 1$  mm/s, respectively [Dowty,

Pressure (GPa)	QS site 1 (mm/s)	IS site 1 (mm/s)	FWHM site 1 (mm/s)	$\Delta$ site 1	QS site 2 (mm/s)	FWHM site 2 (mm/s)	$\Delta$ site 2	QS site 3 (mm/s)	IS site 3 (mm/s)	FWHM site 3 (mm/s)	$\Delta$ site 3	reduced $\chi^2$
3.1(3)	1.818(8)	0.955(1)	0.51	5.13	1.69(2)	0.63	0.58	0.80(3)	0.69(2)	0.63	0.41	1.36(6)
9.0(4)	2.07(3)	0.972(6)	0.46	3.88	1.66(2)	0.77	0.21	0.99(6)	0.68(1)	0.77	0.33	1.38(6)
12.9(2)	2.18(3)	0.975(6)	0.55	3.46	1.75(2)	0.82	0.11	0.93(5)	0.685(7)	0.82	0.21	1.20(5)
18.7(6)	2.46(3)	0.965(7)	0.41	4.57	1.99(1)	0.61	0.31	0.86(3)	0.690(8)	0.61	1.74	1.71(6)
24.8(1)	2.71(5)	0.940(7)	0.65	0.20	2.02(5)	0.71	1.30	0.744(7)	0.684(7)	1.40	1.41	2.15(7)
30.5(4)	2.99(2)	0.91(2)	0.65	0.20	2.10(1)	0.59	0.84	0.87(5)	0.71(3)	0.68	0.74	1.43(6)
35.6(2)	3.03(2)	0.98(2)	0.65	0.20	2.11(1)	0.65	0.77	0.65(6)	0.65(6)	0.84	0.60	1.45(6)
40.7(4)	3.14(1)	0.96(1)	0.65	0.20	2.17(1)	0.61	0.82	0.80(4)	0.69(2)	0.64	0.78	1.10(5)
46.5(6)	3.18(1)	0.95(2)	0.65	0.20	2.23(1)	0.62	0.81	0.89(5)	0.71(3)	0.72	0.70	1.32(6)
52.8(1)	3.157(9)	0.99(1)	0.65	0.20	2.334(8)	0.69	0.73	0.82(4)	0.72(3)	0.77	0.65	1.17(5)
58.7(9)	3.22(2)	0.98(2)	0.65	0.20	2.36(1)	0.67	0.75	0.92(5)	0.72(3)	0.78	0.64	1.14(5)
63.3(7)	3.21(1)	0.96(1)	0.65	0.20	2.36(1)	0.69	0.75	0.88(4)	0.73(3)	0.73	0.66	1.18(5)
68.0(8)	3.24(1)	0.98(2)	0.65	0.20	2.35(1)	0.72	0.70	0.80(7)	0.72(5)	0.91	0.55	1.23(5)
73.5(9)	3.29(2)	0.94(2)	0.65	0.20	2.36(1)	0.66	0.76	0.96(7)	0.69(3)	0.80	0.62	1.36(6)
81.0(7)	3.31(1)	0.95(2)	0.65	0.20	2.38(1)	0.65	0.77	1.00(6)	0.69(3)	0.77	0.65	1.20(5)
94.0(5)	3.25(1)	0.91(2)	0.65	0.20	2.27(1)	0.68	0.74	1.04(9)	0.65(5)	1.00	0.50	1.69(6)
102(3)	3.256(6)	0.890(9)	0.49	0.51	2.337(6)	0.61	0.38	1.15(1)	0.662(9)	0.44	0.53	1.17(5)
111(3)	3.298(7)	0.863(5)	0.42	0.45	2.334(8)	0.54	0.51	1.15(2)	0.654(7)	0.41	0.67	1.47(6)
119(3)	3.310(8)	0.847(7)	0.47	0.51	2.369(8)	0.58	0.43	1.18(2)	0.627(8)	0.41	0.58	1.15(5)

Table 4.3: Best-fit hyperfine parameters for rhyolitic glass and the corresponding reduced  $\chi^2$  from fitting the time-domain synchrotron Mössbauer spectra with the CONUSS software. The relative weight of site 1, site 2 and site 3 were fixed to 34%, 47% and 19%, respectively. These values were found with Monte Carlo searches combined with  $\chi^2$  and parameter correlation analysis as a function of pressure, and cannot be fitted freely due to parameter correlations. The isomer shift for site 1 and site 2 are equivalent. Isomer shift values are with respect to  $\alpha$ -iron metal. The physical thickness was fixed to 10  $\mu\text{m}$  at all pressures ( $\eta \approx 1.6$ ). The uncertainties are given in parentheses at the 68% confidence level for the last reported significant digit.

	QS site 1	QS site 2	QS site 3	IS site 1	IS site 3
QS site 1	1.000	-0.212	0.314	-0.483	-0.448
QS site 2	-0.212	1.000	0.487	-0.044	0.385
QS site 3	0.314	0.487	1.000	-0.235	0.407
IS site 1	-0.483	-0.044	-0.235	1.000	0.608
IS site 3	-0.448	0.385	0.407	0.608	1.000

Table 4.4: Error correlation matrix for the fitted hyperfine parameters for rhyolitic glass at 58.7 GPa, acquired with CONUSS. Perfect correlation corresponds to  $\pm 1$  and a lack of correlation corresponds to 0. Thickness, thickness distribution, QS distribution, attachment parameter, and weight fractions of the different sites were fixed.

1972], whereas in chromite, the fourfold ferrous iron has QS values ranging from 0.5 to 1.6 mm/s and IS values of 0.9 to 1.1 mm/s [Chen *et al.*, 1992; Kuno *et al.*, 2000]. Fourfold ferric iron has slightly higher QS values and significantly lower IS values than fourfold ferrous iron. For example, melilite has two distinct tetrahedral ferric sites with QS values ranging from 1 to 1.9 mm/s and IS values of 0.1 to 0.3 mm/s [Hamada and Akasaka, 2013].

Fivefold ferrous iron has a larger spread of hyperfine parameters as reported in literature, with QS and IS values ranging from 0.4 to 2.7 mm/s and from about 0.2 to 1.1 mm/s, respectively, depending on the crystal structure and interpretation of hyperfine parameters [Burns, 1994]. Grandidierite and kornerupine each have a fivefold ferrous site with QS and IS values of  $\sim 1.7$  mm/s and  $\sim 1.1$  mm/s, respectively [Seifart and Olesch, 1977; Zhe *et al.*, 2000]. Also in vesuvianite, a site with QS and IS values of 0.6 mm/s and 0.33 to 0.37 mm/s was attributed to fivefold ferrous iron [Malczewski *et al.*, 2006]. For natural hibonite, Burns and Burns [1984] attribute a site with QS and IS values of 2.2 mm/s and 0.3 mm/s, respectively, to fivefold ferric iron and a site with QS and IS values of 2.2 mm/s and 1 mm/s, respectively, to fivefold ferrous iron. Unlike grandidierite and kornerupine, where the fivefold and sixfold sites are distinct, the three to five sites in the spectra for vesuvianite and hibonite have significant overlap, and alternative models may possibly fit the spectra as well. Thus, it is unclear if QS values of 0.4 to 2.7 mm/s establish a plausible strict range for fivefold ferrous iron in crystalline phases, because different types of fivefold iron geometries result in a wide variability of quadrupole splitting values. Optical spectra of grandidierite and joaquinite support the idea that fivefold iron geometries can be very dissimilar from each other [Rossmann and Taran, 2001].

Pressure (GPa)	QS site 1 (mm/s)	IS site 1 (mm/s)	FWHM site 1 (mm/s)	$\Delta$ site 1	QS site 2 (mm/s)	FWHM site 2 (mm/s)	$\Delta$ site 2	QS site 3 (mm/s)	IS site 3 (mm/s)	FWHM site 3 (mm/s)	$\Delta$ site 3	$\eta$	reduced $\chi^2$
1.8(3)	2.003(3)	1.015(4)	0.57	0.22	1.63(2)	1.02	0.53	1.08(4)	0.704(4)	0.75	0.46	6.87	1.48(6)
5(1)	1.994(5)	1.021(3)	0.59	0.23	1.60(1)	0.94	0.31	1.10(3)	0.664(3)	0.66	0.29	8.07	2.89(8)
6.4(4)	2.047(3)	1.007(4)	0.57	0.27	1.64(3)	0.69	0.45	1.02(6)	0.630(4)	0.90	0.70	8.08	1.56(6)
8.1(5)	2.065(3)	1.019(4)	0.59	0.19	1.62(2)	0.71	0.34	1.09(3)	0.681(4)	0.72	0.95	7.87	1.31(5)
12.4(6)	2.328(2)	1.030(4)	0.61	0.13	1.679(7)	0.52	0.41	1.25(6)	0.688(4)	0.75	1.30	8.92	1.30(6)
18.5(2)	2.481(2)	1.029(4)	0.60	0.22	1.743(7)	0.51	0.42	1.40(7)	0.675(4)	0.84	1.17	9.22	1.40(6)
24.9(1)	2.576(2)	1.006(5)	0.64	0.28	1.79(1)	0.57	0.39	1.53(8)	0.685(5)	0.93	1.09	9.19	1.26(5)
32.9(1)	2.650(2)	0.983(5)	0.62	0.23	1.745(9)	0.52	0.11	1.42(1)	0.628(5)	0.51	0.75	8.99	1.49(6)
37.9(0)	2.704(2)	0.960(5)	0.64	0.24	1.72(1)	0.55	0.14	1.40(2)	0.591(5)	0.49	1.00	8.87	1.21(5)
44.0(0)	2.724(2)	0.939(5)	0.64	0.19	1.680(9)	0.52	0.14	1.41(1)	0.591(5)	0.39	0.86	9.25	1.62(6)
51.2(3)	2.831(2)	0.959(4)	0.67	0.23	1.764(8)	0.52	0.29	1.48(1)	0.520(4)	0.40	1.07	9.28	1.16(5)
58.3(6)	2.869(2)	0.938(4)	0.68	0.27	1.772(7)	0.52	0.45	1.47(1)	0.493(4)	0.38	1.14	9.28	1.09(5)
71.8(7)	2.925(2)	0.934(4)	0.68	0.30	1.811(6)	0.52	0.49	1.45(1)	0.445(4)	0.36	1.00	7.91	1.39(6)
80(1)	2.919(2)	0.932(4)	0.68	0.30	1.798(6)	0.52	0.53	1.43(1)	0.426(4)	0.35	0.98	7.63	1.56(6)
84.8(6)	2.938(3)	0.912(4)	0.69	0.30	1.772(7)	0.56	0.58	1.40(1)	0.404(5)	0.34	0.86	7.45	1.90(7)
92.1(8)	2.938(2)	0.895(4)	0.71	0.38	1.756(6)	0.63	0.70	1.338(9)	0.378(4)	0.31	0.80	7.21	1.63(6)

Table 4.5: Best-fit hyperfine parameters for basaltic glass and the corresponding reduced  $\chi^2$  from fitting the time-domain synchrotron Mössbauer spectra with the CONUSS software. The relative weight of site 1, site 2 and site 3 were fixed to 62%, 26% and 12%, respectively between 1.8 and 80.1 GPa. At 84.8 and 92.1 GPa, the relative weights are 60%, 26% and 14%, respectively. The isomer shift for site 1 and site 2 are equivalent. Isomer shift values are with respect to  $\alpha$ -iron metal. The uncertainties are given in parentheses at the 68% confidence level for the last reported significant digit.

	QS site 1	QS site 2	QS site 3	IS site 1	IS site 3
QS site 1	1.000	0.553	0.393	0.195	0.413
QS site 2	0.553	1.000	0.724	0.165	0.480
QS site 3	0.393	0.724	1.000	-0.106	0.296
IS site 1	0.195	0.165	-0.106	1.000	0.746
IS site 3	0.413	0.480	0.296	0.746	1.000

Table 4.6: Error correlation matrix for the fitted hyperfine parameters for basaltic glass at 58.3 GPa, acquired with CONUSS. Thickness, thickness distribution, the QS distribution, attachment parameter, and weight fractions of the different sites were fixed.

At ambient pressure, the majority site in rhyolitic and basaltic glasses shows hyperfine parameters typical for sixfold and possibly fivefold ferrous iron in silicate minerals. The minority site has a QS value that falls between those associated to fourfold ferrous and ferric iron in minerals, and may represent a less distorted fivefold site. The presence of predominantly fivefold and distorted sixfold ferrous iron is consistent with the absorption spectra (see Results section for more details). The IS value for the minority site in both glasses is about 0.7 mm/s, which is higher than that reported for  $\text{Fe}^{3+}$  in minerals [Mysen, 1986; Burns, 1994; Dyar *et al.*, 2006]. The silicate glasses were synthesized under reducing conditions (see Experimental Methods). The rhyolitic glass remained optically colorless at all pressures, and is therefore unlikely that the minority site with a weight fraction of 20% is  $\text{Fe}^{3+}$ . Using the extended Voigt-based fitting method [Alberto *et al.*, 1996], Rossano *et al.* [1999] did not detect ferric iron in the tektites in their study, although the  $\text{Fe}^{3+}/\Sigma\text{Fe}_{\text{tot}}$  ranges from 5 to 9%, as determined from coulometric titration. The minority site in the tektites has QS and IS values of  $\sim 1$  mm/s and  $\sim 0.6$  mm/s, respectively, and is attributed to tetrahedral  $\text{Fe}^{2+}$  [Rossano *et al.*, 1999], consistent with the minority site in the rhyolitic and basaltic glasses in this study at room pressure-temperature conditions. One cannot rule out that the lower isomer shift value is a result of electron exchange between ferrous iron and small amounts of ferric iron in the glasses [Burns, 1991; Burns, 1994; Dyar *et al.*, 2006], but based upon the optical absorption spectra showing no detectable ferric iron features, the amount of ferric iron would indeed be very small.

#### 4.4.2 Coordination Environments at High Pressure

At high pressure, the increase of the QS values of site 1 with pressure up to about 30 GPa is likely associated with glass densification that results in an increase in the coordination number of that site from around four to eight, and perhaps higher than eight.

*Bajgain et al.* [2015] presented density functional theory-based results on the behavior of hydrous and anhydrous basaltic melts with pressure, noting steep gradients in the coordination increases of Ca-O, Na-O, and Si-O from ambient pressure to about 40 GPa. This particular densification does not appear to affect the electron density near the nucleus of iron, as evidenced by the relatively flat trend of the IS up to about 30 GPa for both glasses. The QS and IS values of site 2 in rhyolitic and basaltic glass are consistent with fivefold and sixfold ferrous iron in minerals. At elevated pressure, a third site is required to fit the glass spectra. Site 3 in the rhyolitic glass has a QS value that increases from about 0.7 to 1.2 mm/s and an IS value that plateaus at about 0.7 mm/s up to 80 GPa, likely remaining in a low-coordinated site environment to high pressure.

In the basaltic glass, the IS values start to decrease from 0.7 mm/s to 0.5 mm/s at about 25 GPa with a very similar trend to that reported by *Murakami et al.* [2014]. *Murakami et al.* [2014] propose that the decrease in IS values is due to a change in the spin state from high spin to intermediate spin. For Al-bearing enstatite glass, *Gu et al.* [2012] observe comparable IS values (0.5-0.7 mm/s relative to a stainless steel reference absorber) for the site with low QS values and attribute it to low-spin ferrous iron. We do not attribute site 3 to intermediate-spin or low-spin iron because of its existence even at low pressures with significant weight fractions, 19% for the rhyolitic glass and ~12% for the basaltic glass, without significant change at higher pressures. We attribute the decreasing trend of the isomer shift values to glass densification and near-neighbor coordination increases that start to have a stronger effect on the electron density near the nucleus.

#### 4.4.3 Comparison with Previous Studies

A comparison of our results to previous room-temperature studies is shown in Figure 4.7, where we plot QS against IS values for a variety of reduced and oxidized silicate glasses for pressures up to ~60 GPa. At ambient pressure, the hyperfine parameters for the dominant ferrous iron site are tightly constrained with QS and IS values ranging from 1.7 to 2 mm/s and from 0.9 to 1 mm/s, respectively. The QS values for all sites generally increase with pressure. At higher pressures, the increased scatter of hyperfine parameters is likely a result of compositional effects that become more prominent. At high pressure, the hyperfine parameters of the ferrous site with a low QS value are similar to those reported for ferric iron. Therefore, if there is a lack of constraint on the behavior of this site from low pressure data and/or complementary spectroscopic data, it can be difficult to interpret. The weights of such sites obtained from MB studies can also conceivably trade for each other making quantitative assignments uncertain. In

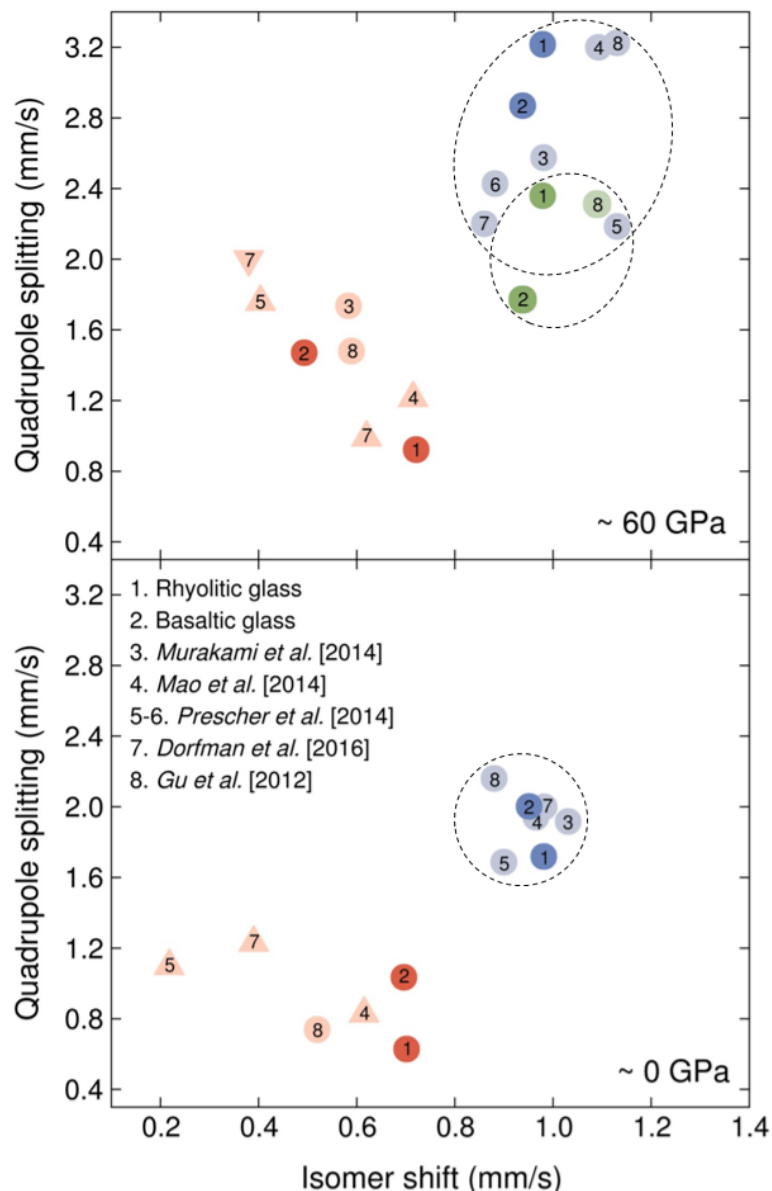


Figure 4.7: Quadrupole splitting versus isomer shift at about 0 GPa and 60 GPa for high-pressure synchrotron Mössbauer studies on silicate glasses. Our study is in bold, whereas previous studies are in pastel colors. Blue, green and red circles represent  $\text{Fe}^{2+}$  sites with relatively high, intermediate and low quadrupole splitting values, respectively. Triangles have been interpreted as  $\text{Fe}^{3+}$  sites; the inverted triangle denotes low-spin  $\text{Fe}^{3+}$  [Dorfman et al., 2016]. Isomer shifts are with respect to  $\alpha$ -iron, except for the Al-bearing silicate glass from Gu et al. [2012], which is with respect to a stainless steel foil. For the Al-free silicate glass, Gu et al. [2012] do not report isomer shifts. Murakami et al. [2014], Mao et al. [2014] and Prescher et al. [2014] fit their spectra with two sites; thus, there is no intermediate QS site for those studies. The bottom figure is at 1 bar for all studies, except for Prescher et al. [2014] where their lowest pressure is at 0.18 GPa for the  $\text{Fe}^{3+}$ -bearing glass in a Ne pressure medium. The high-pressure measurements for rhyolitic and basaltic glass were measured at 58.7 and 58.3 GPa, respectively. The high-pressure measurements for Murakami et al. [2014], Mao et al. [2014], Prescher et al. [2014] with  $\text{Fe}^{3+}$ , Prescher et al. [2014] without  $\text{Fe}^{3+}$ , Dorfman et al. [2016] and Gu et al. [2012] were conducted at 58, 55, 56, 61, 57 and 58 GPa, respectively.

our study of the rhyolitic glass, this site has a weight fraction of about 20% which clearly exceeds the possible  $\text{Fe}^{3+}$  content.

#### 4.4.4 Trends with Composition

QS values are affected by the coordination environment, which may be influenced by the type and number of cations in the vicinity of the iron atoms. Here we examine the effect of different cations on the QS values of ferrous iron in combination with the effect of the molar quantities of  $\text{Na}_2\text{O}$ ,  $\text{K}_2\text{O}$ ,  $\text{MgO}$ ,  $\text{CaO}$ ,  $\text{SiO}_2$ , and  $\text{Al}_2\text{O}_3$  with respect to  $\text{FeO}$ . Studies on glasses that reported a detectable amount of ferric iron ( $\text{Fe}^{3+}/\Sigma\text{Fe}_{\text{tot}} > 6\%$ ) were not included in this analysis due to the strong effect of ferric iron on the local coordination environment of ferrous sites [Alberto *et al.*, 1995; Wilke *et al.*, 2005]. Asymmetric peak shapes, characteristic of silicate glasses, require correlated distributions to fit the spectra and cannot be quantitatively compared to studies that do not use correlated distributions [Rossano *et al.*, 1999]. Thus, we do not include the results of those studies [e.g., Aramu *et al.*, 1994; Costa *et al.*, 2013; Gu *et al.*, 2012]. Although Dunlap *et al.* [1998] use correlated distributions, they do not report the compositions of the natural tektites in their study; thus, their results are not included in our compositional analysis. At high pressures, Gu *et al.* [2012] fit their data using FWHM values ranging from 1 to 2 mm/s, which are larger than have been used in previous studies on silicate glasses, in particular those studies using a radioactive source, and is likely a result of not implementing correlated distributions.

Large concentrations of  $\text{FeO}$  (above about 10 mol%) appear to result in iron-iron interactions that affect the quadrupole splitting of the minority site more than other oxides (Figure 4.8). There is a positive trend in the quadrupole splitting of the minority site with increasing  $\text{FeO}$  concentration, such that the effect of compositional differences on the minority site can only be resolved at low  $\text{FeO}$  concentrations. For this reason, we do not include the iron-rich silicate glasses of Jackson *et al.*, [2005] in our detailed compositional analysis. By including only reduced glasses with low  $\text{FeO}$  concentrations and comparing studies that use similar methods to fit their data, it becomes possible to examine the effect of composition on the QS of ferrous iron in a self-consistent manner.

At ambient pressure, we observe a negative correlation between QS values and  $\text{Na}_2\text{O}/\text{FeO}$ ,  $\text{K}_2\text{O}/\text{FeO}$  and  $(\text{Na}_2\text{O}+\text{K}_2\text{O})/\text{FeO}$ , and a positive correlation between QS values and  $\text{CaO}/\text{FeO}$  and  $(\text{MgO}+\text{CaO})/\text{FeO}$  for both the majority and minority sites (Figure 4.9). The Mg-free Ca-silicate glass of Alberto *et al.* [1996] has relatively large QS values for the majority site, which is likely affected by  $\text{CaO}$ . The result is a very weak correlation for  $\text{MgO}/\text{FeO}$  vs. QS and a strong correlation for  $(\text{MgO}+\text{CaO})/\text{FeO}$  vs. QS for the majority site. Ferrous iron in mafic melts, containing more  $\text{MgO}$  and  $\text{CaO}$ , is likely to

be more distorted and/or have a higher coordination than ferrous iron in felsic melts, containing more  $\text{Na}_2\text{O}$  and  $\text{K}_2\text{O}$ . One can interpret the effect of  $\text{SiO}_2$  with respect to  $\text{FeO}$  as having a weak negative correlation or a moderately strong quadratic relationship. With the amount of data available at present, it appears that the type of network-modifying cations in the glass have a stronger effect on the quadrupole splitting (and likely coordination environment) of iron than the silica or alumina content. As discussed earlier, IS values have also been used as an indicator for coordination [Mysen, 1987; Dyar *et al.*, 2006]. However, when plotted against compositional ratios or against absolute oxide content, the IS values are scattered with low  $R^2$  values (typically 0 to 0.2). It appears that IS values are not sensitive to composition in silicate glasses. In fact, an enstatite glass with the composition  $(\text{Mg}_{0.8}\text{Fe}_{0.2})\text{SiO}_3$  [Murakami *et al.*, 2014] shows very similar IS values, but different QS values than the compositionally-complex basaltic glass in this study (Figures 4.6 and 4.7).

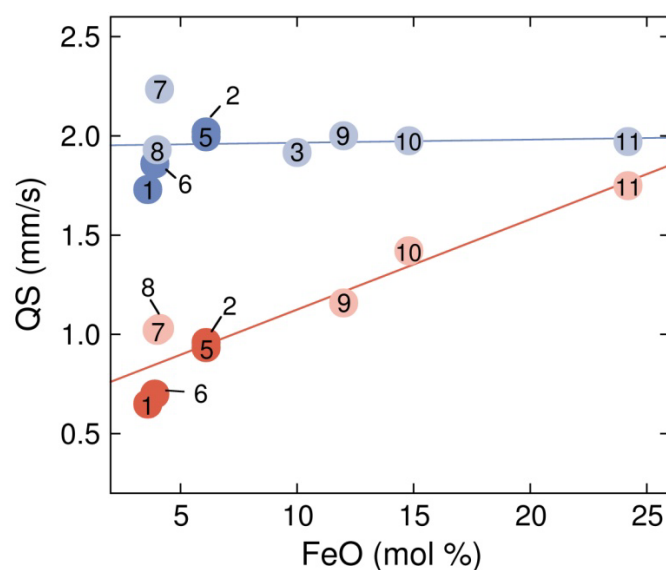


Figure 4.8: Quadrupole splitting as a function of  $\text{FeO}$  concentration at  $\sim 0$  GPa. Rhyolitic glass [this study] (1), basaltic glass [this study] (2), Murakami *et al.* [2014] (3), andesitic glass [this study] (5), dacitic glass [this study] (6), Alberto *et al.* [1995] (7), Rossano *et al.* [1999] (8), and Jackson *et al.* [2005] (9-11). Jackson *et al.* [2005] do not report the hyperfine parameters for the individual sites. Thus, the quadrupole splitting values are estimated from their fits. The total concentration of  $\text{FeO}$  in a glass affects the quadrupole splitting of the minor site more than the concentration of other cations above a certain threshold of  $\text{FeO}$ , likely due to iron-iron interactions. For this reason, the results of Jackson *et al.* [2005] are not included in Figure 4.9.

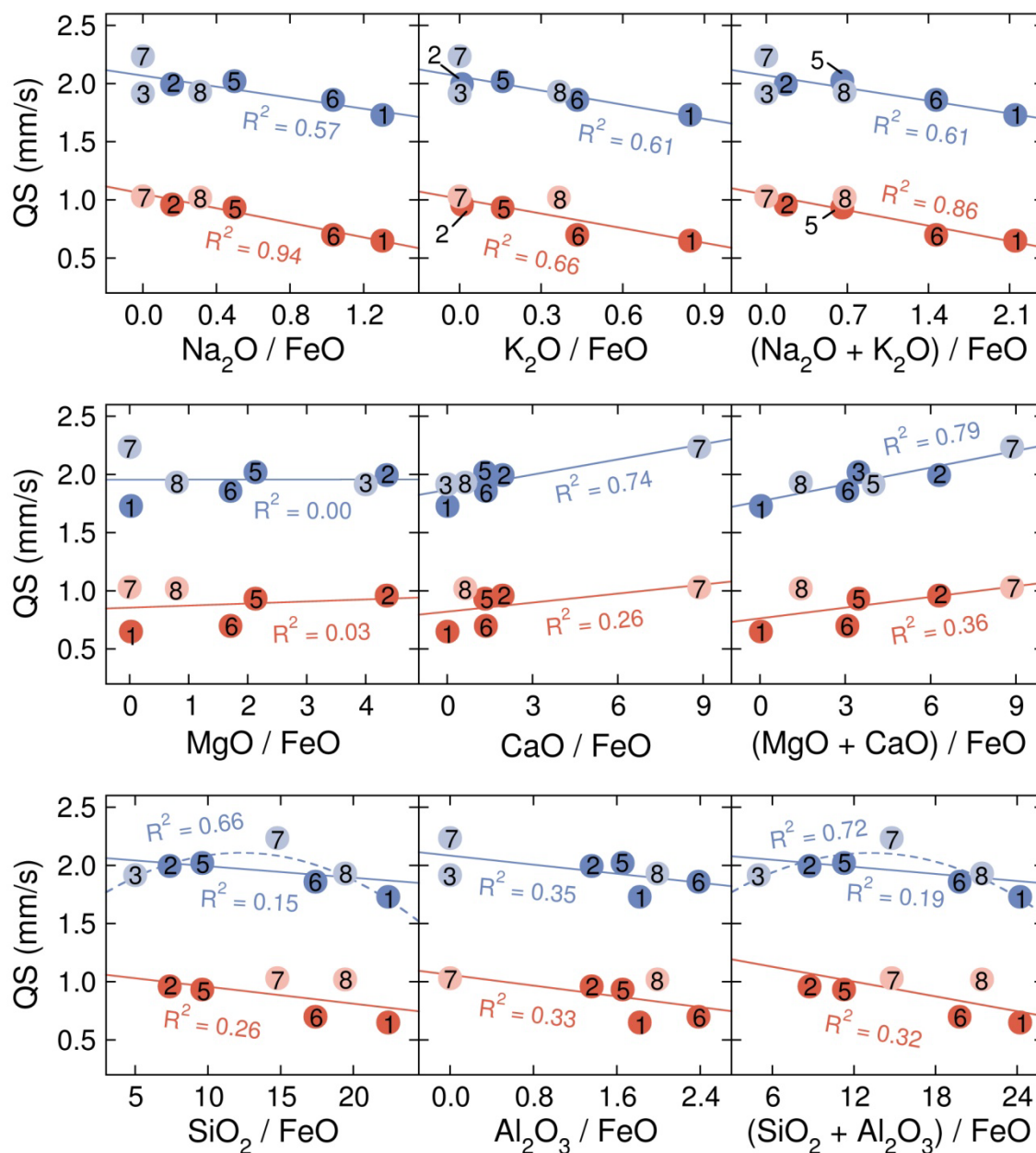


Figure 4.9: Quadrupole splitting as a function of the oxide mole ratios, Na<sub>2</sub>O/FeO, K<sub>2</sub>O/FeO, (Na<sub>2</sub>O+K<sub>2</sub>O)/FeO, MgO/FeO, CaO/FeO, (MgO+CaO)/FeO, SiO<sub>2</sub>/FeO, Al<sub>2</sub>O<sub>3</sub>/FeO and (SiO<sub>2</sub>+Al<sub>2</sub>O<sub>3</sub>)/FeO at ~0 GPa. Only reduced glasses ( $\text{Fe}^{3+}/\Sigma\text{Fe}_{\text{tot}}$  below 6%) are included in this figure due to the strong effect of ferric iron on the coordination environment of ferrous sites [Alberto *et al.*, 1995; Wilke *et al.*, 2005; Jackson *et al.*, 2005]. Rhyolitic glass [this study] (1), basaltic glass [this study] (2), Murakami *et al.* [2014] (3), Prescher *et al.* [2014] at 0.18 GPa (4), andesitic glass [this study] (5), dacitic glass [this study] (6), Alberto *et al.* [1995] (7) and Rossano *et al.* [1999] (8). Fitting quadratic trends to the majority sites in the plots of QS vs. SiO<sub>2</sub>/FeO and QS vs. (SiO<sub>2</sub>+Al<sub>2</sub>O<sub>3</sub>)/FeO leads to better  $R^2$  values.

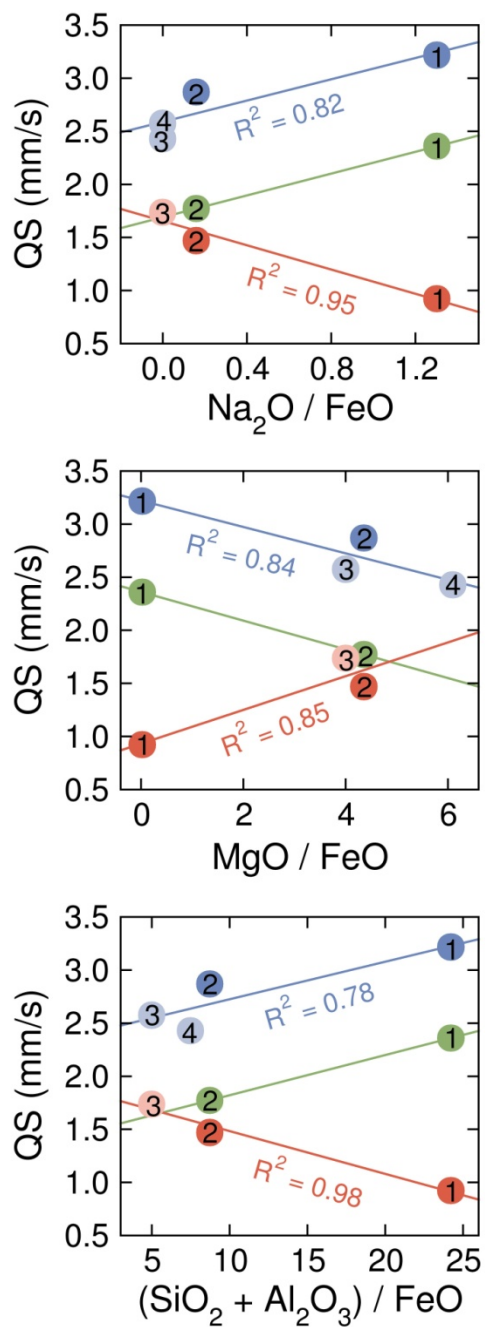


Figure 4.10: Quadrupole splitting as a function of the oxide mole ratios,  $\text{Na}_2\text{O}/\text{FeO}$ ,  $\text{MgO}/\text{FeO}$  and  $(\text{SiO}_2 + \text{Al}_2\text{O}_3)/\text{FeO}$  at  $\sim 60$  GPa. The high-pressure measurements for rhyolitic glass (1) and basaltic glass (2) were conducted at 58.7 and 58.3 GPa, respectively, and the high pressure measurements for *Murakami et al.* [2014] (3) and *Prescher et al.* [2014] (4) were conducted at 58 and 61 GPa, respectively. See text for discussion.

At high pressure, only three studies on reduced glasses use correlated hyperfine parameter distributions to fit the spectra [Murakami *et al.*, 2014; Prescher *et al.*, 2014; this study]. We restrict the figures to ones with the most spread in compositional space: Na<sub>2</sub>O/FeO, MgO/FeO and (SiO<sub>2</sub>+Al<sub>2</sub>O<sub>3</sub>)/FeO. At ~60 GPa, the trend for the majority site is reversed, such that QS values are now positively correlated with Na<sub>2</sub>O/FeO and negatively correlated with MgO/FeO (Figure 4.10). The rhyolitic glass has a much larger distribution of site environments compared to the other glasses, indicating that felsic melts may be expected to have a larger distribution of ferrous iron sites than mafic melts at high pressures.

## 4.5 Conclusions

Our results indicate that ferrous iron in rhyolitic and basaltic glass experiences an increase in coordination with increasing pressure. The increase in coordination is likely accompanied by variable distortions in the environments. A decreasing trend of the isomer shift values at high pressures can be associated with glass densification and steep gradients of coordination changes in the different glasses, noting that this trend occurs at lower pressures in basaltic glass compared to rhyolitic glass. Over the pressure range studied, these local environmental changes occur without the iron atoms undergoing high-spin to low-spin transitions, but would nevertheless affect physical and transport properties. With the assumption that silicate glasses can be used to model some of the behavior in silicate melts, our study predicts that ferrous iron in chemically-complex silicate-rich melts in the lower mantle likely exists in a high-spin state. We compare the results of studies that used similar methods in fitting their Mössbauer spectra of reduced glasses, and observe a negative relationship between quadrupole splitting and the concentration of Na<sub>2</sub>O and K<sub>2</sub>O with respect to FeO at ambient pressure. At high pressure, this relationship turns into a positive trend of quadrupole splitting for the majority site and a negative trend for the minority site. Our results indicate that at high pressure, felsic melts may have a larger distribution in ferrous iron site geometries while mafic melts have ferrous iron site geometries that are more similar to each other. To the extent that the distribution of available coordination environments affects element partitioning between the solid and the melt, more silica-poor melts would accommodate a smaller variety of cations compared to more silica-rich melts at lower mantle pressures.

# Chapter 5

## Theory

### 5.1 Introduction

To simulate systems, such as crystalline solids, on an atomic level, one can use either classical or quantum mechanical methods. Classical methods require empirically-derived potentials to describe interatomic forces while quantum mechanical methods are *ab initio*; that is, they simulate the electronic structure of a system without the use of empirical potentials or other experimental input. Empirically-derived potentials are often system-dependent, sometimes fail to describe the system accurately at high pressures (if potentials are produced at low pressure), and require large amounts of experimental data. Thus, a quantum mechanical approach is necessary to examine novel carbonate phases at extreme pressures.

The Schrödinger equation is a partial differential equation that describes how a wavefunction of a quantum particle will evolve over time under an external potential:

$$i\hbar \frac{\delta\Psi}{\delta t} = -\frac{\hbar^2}{2m_e} \frac{\delta^2\Psi}{\delta x^2} + V\Psi, \quad (5.1)$$

where  $\hbar$  is Planck's constant,  $m_e$  is the mass of an electron,  $V$  is the potential that is independent of time, and  $\Psi$  is the wavefunction, which is a function of space ( $x$ ) and time ( $t$ ). The equation can be solved by separation of variables, resulting in two ordinary differential equations, one a function of only time and the other a function of only position. To calculate the electronic structure of a system, one must solve the time-independent Schrödinger equation:

$$-\frac{\hbar^2}{2m_e} \frac{d^2\psi}{dx^2} + V\psi = E\psi, \quad (5.2)$$

where  $\psi$  is now the time-independent wavefunction. However, for a many-body system, the time-independent Schrödinger equation cannot be solved exactly. Approximate methods must be used to reduce the number of spatial variables.

The Born-Oppenheimer approximation allows for the separation of the wavefunction into the electronic and nuclear components:

$$\Psi_{\text{total}} = \Psi_{\text{electronic}} \times \Psi_{\text{nuclear}}. \quad (5.3)$$

The mass of the atomic nucleus is more than  $10^3$  times the mass of an electron, and so, the nuclei move much more slowly than the electrons. Consequently, one can make the assumption that, at any moment, the electrons are in their ground state with respect to an instantaneous nuclear configuration, allowing one to solve only for the electronic part of the wavefunction. Even with this simplification, the many-body problem is still too complex to solve.

## 5.2 Density Functional Formalism

*Hohenberg and Kohn* [1964] formulated two theorems to simplify the N-body problem further. The first Hohenberg-Kohn theorem demonstrates that the electron density fully and uniquely determines the external potential and thus, the ground state properties of a many-body system. According to this theorem, the total energy can be expressed as:

$$E[n(\mathbf{r})] = \int V_{ext}(\mathbf{r})n(\mathbf{r})dr + F_{HK}[n(\mathbf{r})], \quad (5.4)$$

where  $n(\mathbf{r})$  is a scalar electron density,  $V_{ext}(\mathbf{r})$  is an external potential and  $F_{HK}[n(\mathbf{r})]$ , the Hohenberg-Kohn functional, is known as a universal functional because it does not depend on the external potential.  $F_{HK}[n(\mathbf{r})]$  is composed of the kinetic energy functional of the interacting electrons,  $T[n(\mathbf{r})]$ , and the Coulomb potential functional for the interacting system,  $J[n(\mathbf{r})]$ . The second Hohenberg-Kohn theorem demonstrates that the electron density corresponding to the lowest total energy is the exact ground state density. Thus, if one could calculate  $F_{HK}[n(\mathbf{r})]$ , the ground state density for a given  $V_{ext}(\mathbf{r})$  could be determined by minimizing the energy. The Hohenberg-Kohn theorems reduce the N-body problem to a 3-dimensional scalar field, but they do not produce a way to solve the Schrödinger equation because  $F_{HK}[n(\mathbf{r})]$  is unknown. In 1965, Kohn and Sham proposed to rewrite  $F_{HK}[n(\mathbf{r})]$  as:

$$F_{HK}[n(\mathbf{r})] = T_0[n(\mathbf{r})] + V_H[n(\mathbf{r})] + V_{xc}[n(\mathbf{r})], \quad (5.5)$$

where  $T_0[n(\mathbf{r})]$  is the kinetic energy functional for non-interacting electrons,  $V_H[n(\mathbf{r})]$  is the classical Hartree potential and  $V_{xc}[n(\mathbf{r})]$  is the exchange-correlation potential (i.e., everything that is omitted in the first two terms). This way, the easily computable terms are extracted. Now the energy functional for the independent-particle (non-interacting) system can be written as:

$$E[n(\mathbf{r})] = T_0[n(\mathbf{r})] + V_H[n(\mathbf{r})] + V_{xc}[n(\mathbf{r})] + V_{ext}[n(\mathbf{r})], \quad (5.6)$$

with a corresponding Hamiltonian that results in the same ground state electron density as the original system:

$$\left[ -\frac{\hbar^2}{2m_e} \nabla^2 + V_{KS}(\mathbf{r}) \right] \psi_i(\mathbf{r}) = \varepsilon_i \psi_i(\mathbf{r}), \quad (5.7)$$

where  $m_e$  is the mass of an electron,  $\psi_i(\mathbf{r})$  are the one-electron Kohn-Sham orbitals with  $i$  ranging from 1 to  $N/2$  (assuming double occupancy for all the states) and  $V_{KS}(\mathbf{r})$  is a unique potential with a ground state electron density of  $n(\mathbf{r})$ , as demonstrated by the first theorem of Hohenberg and Kohn. The only unknown term is the exchange-correlation functional, which can be approximated in several ways.

The most commonly used approximations to the exchange-correlation functional are the local density approximation (LDA) [Kohn and Sham, 1965; Perdew, 1979] and the generalized gradient approximation (GGA) [Perdew, 1986; Perdew et al., 1996]. In the LDA, the exchange-correlation is defined as:

$$V_{xc}^{LDA}[n(\mathbf{r})] = \int n(\mathbf{r}) \varepsilon_{xc}[n(\mathbf{r})] \, d\mathbf{r}. \quad (5.8)$$

The exchange correlation functional is approximated as a function of the local density of a homogeneous electron gas, determined through highly accurate Monte-Carlo calculations. LDA assumes that the density distribution is uniform over all space. The GGA includes the local gradient in the electron density and is defined as:

$$V_{xc}^{GGA}[n(\mathbf{r})] = \int n(\mathbf{r}) \varepsilon_{xc}[n(\mathbf{r}), |\nabla n(\mathbf{r})|] \, d\mathbf{r}. \quad (5.9)$$

The cohesive energy is generally underestimated with LDA and overestimated with GGA, resulting in an underestimated and overestimated volume, respectively.

With an approximation for the exchange-correlation functional, it is now possible to solve the Kohn-Sham equations. The Kohn-Sham Hamiltonian depends on the electron density  $n(\mathbf{r})$ , which depends on the  $\psi_i(\mathbf{r})$  that is being calculated. We do not know  $\psi_i(\mathbf{r})$  until we solve the Kohn-Sham equations. Thus, an iterative process is required starting with an initial guess  $n(\mathbf{r})$  to calculate the  $\psi_i(\mathbf{r})$  and a new  $n(\mathbf{r})$  from  $\psi_i(\mathbf{r})$ , and then using each subsequent new  $n(\mathbf{r})$  in the next set of calculations until convergence of  $n(\mathbf{r})$  is achieved.

### 5.3 Periodicity and Plane Waves

It is convenient to define a crystal's lattice in reciprocal space (often referred to as  $k$ -space) by applying a Fourier transform to the real space lattice. The uniquely defined primitive cell in reciprocal space is known as the first Brillouin zone, which is computationally sampled with a uniform mesh of  $k$ -points. The wavefunction can be completely characterized in the first Brillouin zone with periodic conditions.

Periodic boundary conditions allow the approximation of an infinite system with a finite number of atoms, such that the atoms in each unit cell move identically to the atoms in all other unit cells. Bloch's theorem demonstrates that the wavefunction of an electron within a perfectly periodic potential may be written as the product of a wave-like term and a term with the periodicity of the unit cell. The electronic wavefunction at each  $k$ -point can then be expanded in terms of a discrete plane wave basis set according to Bloch's theorem. The plane wave basis set is truncated to include plane waves with kinetic energies that are smaller than some specified energy, which should be determined through convergence of the calculated total energy to a desired accuracy. If one is considering several compositions (e.g., chemical reactions), then the largest cutoff energy should be used, and should be kept constant throughout all calculations in the study.

Valence wavefunctions oscillate rapidly near the atomic nucleus due to the orthogonalization of valence and core states, which require many Fourier components to represent exactly. Although the wavefunctions of core electrons change only slightly during the formation of bonds (and may be regarded as essentially spherical), inaccurate descriptions of the rapid oscillations will result in an improper description of the valence orbitals. To mediate this problem, core electrons are commonly treated with a basis set different from that used for the valence electrons, for example by using augmented planewaves (APW), pseudopotentials (PP) or projector-augmented waves (PAW).

In the APW approach [Slater, 1937], a sphere is defined around the atom, approximately the size of the covalent radius. Within the sphere, the radial Schrödinger's equation is solved for the spherically-averaged effective potential whereas in the interstitial region between spheres, plane waves are solved. The basis functions and their derivatives are made continuous with the linear augmented plane wave method (LAPW) [Andersen, 1975; Soler, 1989]. In the LAPW method, the core electrons are explicitly included in the calculations.

To avoid describing the core electrons explicitly, the core potential can be replaced with a smoothly varying pseudopotential and simpler pseudo-wavefunctions [Phillips and Kleinman, 1959; Antoncik, 1959]. In the pseudopotential approach, the orthogonality condition in the orthogonalized plane-wave method [Herring, 1940] is replaced with an effective potential. Two of the most common forms of pseudopotentials are norm-conserving [Hamann *et al.*, 1979] and ultrasoft [Vanderbilt, 1990]. In the norm-conserving method, the norm of the pseudo-wavefunctions within the core radius is constrained to be the same as the true wavefunctions. In the ultrasoft method, the norm-conserving constraint is relaxed to create softer pseudo-wavefunctions within the core radius. The softness of a pseudopotential refers to the ability to use as few planewaves as possible in the expansion of the valence pseudo-wavefunctions. Localized atom-centered

augmentation charges are introduced to correct for the charge deficit resulting from non-conservation of norms. Because the augmentation charges may depend on a number of factors, ultrasoft pseudopotentials are less transferable than norm-conserving pseudopotentials.

A more transferable approach is the projector-augmented wave (PAW) method [Blöchl, 1994], which is a combination of the APW and PP methods where a linear and invertible transformation is used to connect the true wavefunctions with soft pseudo-wavefunctions.

### 5.3 Implementation of Density Functional Theory

The two software packages based on density functional theory that are used in this thesis are the Vienna Ab-initio Simulation Package (VASP) [Kresse and Furthmüller, 1996; Kresse and Joubert, 1999] and PWscf (Plane-Wave Self-Consistent Field) in Quantum ESPRESSO (QE; ESPRESSO is an acronym for opEn-Source Package for Research in Electronic Structure, Simulation and Optimization) [Giannozzi *et al.*, 2009]. For materials without transition elements, VASP and QE will produce identical results; any differences are likely a result of differences in the choice or generation of the basis sets. QE is slower than VASP and is more likely to get trapped in local energy minima or not achieve convergence. However, the ability to use linear response theory to calculate the Hubbard  $U$  potential, a key part of the modeling described in Chapter 7, is not officially implemented or documented in the VASP software at the time of writing this thesis. In this section, I briefly discuss some pertinent aspects of both software packages; a detailed description of the input parameters can be found in their respective manuals.

	VASP	QE
Most energies	eV	Ry
Fermi energy	eV	eV
Hubbard $U$	eV	eV
Smearing width	eV	Ry
Distance	Å	Å, bohr
Pressure	Pa	kbar
Forces on atoms	eV/Å	Ry/Bohr
Pulay stress and external pressure	kbar	Ry/Bohr <sup>3</sup> , kbar
Unit-cell volume	Å <sup>3</sup>	Å <sup>3</sup> , bohr <sup>3</sup>

Table 5.1: A comparison of the units used in the VASP and QE packages. More than one unit implies that both are output or accepted within QE.

VASP requires five input files: INCAR (input parameters that control how the code runs), POSCAR (lattice parameters and atomic positions), POTCAR (atomic basis sets concatenated into one file), KPOINTS (k-points), and the submission script. In QE, the minimum required files are: the input file containing all the information about the phase, the submission script that includes parallelization details, and the atomic basis sets as individual files. Table 5.1 compares the units that are used by VASP and QE.

The lattice parameters are necessarily specified as a matrix in VASP and optionally in QE. Three lattice vectors define the unit cell and are written as a matrix whose three rows correspond to the three lattice vectors:

$$\begin{array}{ccc} a_x & a_y & a_z \\ b_x & b_y & b_z \\ c_x & c_y & c_z \end{array} \quad (5.10)$$

where the lattice parameters and angles are consequently defined as, for example,

$$a = \sqrt{a_x^2 + a_y^2 + a_z^2}, \quad (5.11)$$

$$\alpha = \cos^{-1} \frac{b_x c_x + b_y c_y + b_z c_z}{\sqrt{b_x^2 + b_y^2 + b_z^2} \sqrt{c_x^2 + c_y^2 + c_z^2}}. \quad (5.12)$$

The remaining parameters,  $b$ ,  $c$ ,  $\beta$ , and  $\gamma$  follow by deduction. The unit cell can be relaxed in multiple ways. In VASP, the parameter ‘ISIF’ determines how the cell is relaxed. For example, the volume and cell shape can be fixed while the ionic positions are relaxed, the volume can be fixed while the ionic positions and cell shape are relaxed, the cell shape and volume can be relaxed without changing the relative atomic positions, the volume can be relaxed without changing the shape or atomic positions or everything can be relaxed. In QE, one can choose to relax everything (‘variable-cell’) or only the atomic positions (‘relax’), after which one can choose various ways in which the cell parameters are relaxed via ‘cell\_dofree’. For example, all axes and angles are relaxed, only one or two of the axes are relaxed, or all axes and angles are relaxed while the volume is fixed. Thus, either QE or VASP may be better suited for certain relaxation requirements. The convergence threshold for the electronic self-consistency, ionic minimization loop and interatomic forces are specified in the input. Nonetheless, the structure may be relaxed two to three times with the previous step’s relaxed structure as the starting structure until convergence in energy is achieved. Forces acting on the atoms are checked at the end of each calculation and the calculated pressure should be identical to the dictated pressure in the input file.

The magnetic behavior of the atoms is specified differently in the two packages. In QE, one specifies the starting magnetization (values range between -1 and 1 for all spin down and all spin up, respectively) and may choose to fix the total magnetization or allow the self-consistent cycle to determine the magnetization (typically, the desired method). Thus, for the antiferromagnetic case, one site will have a positive starting magnetization while the other site will have a negative starting magnetization. Constrained magnetization calculations may be performed where the total or atomic magnetization or direction are constrained by adding a penalty functional to the total energy. In VASP, the user specifies the initial magnetic moment per atom in units of Bohr magneton. In either case, it may be difficult to obtain a magnetic spin state, particularly an antiferromagnetic state. Possible solutions are: (1) start with a different initial structure, relaxed with different parameters or at a different pressure, (2) start with higher magnetic moments in VASP or different magnetization in QE, (3) remove the symmetry constraint on k-points, (4) relax the structure with fixed total magnetization to get the correct structure for unconstrained calculations in QE, (5) relax the structure with correct magnetic charge densities to get the correct structure, and (6) specify starting eigenvalues of the occupation matrix in QE, perhaps holding it constant for several iterations (see ‘starting\_ns\_eigenvalue(m,ispin,l)’ and ‘mixing\_fixed\_ns’).

For metals, semi-conductors and materials with transition elements, one should smear the occupations using Fermi-Dirac, Gaussian, Methfessel-Paxton, Marzari-Vanderbilt (QE only) smearing or the linear tetrahedron method. The smearing width must be converged for a given k-point resolution with respect to the Fermi energy. For detailed density of states calculations, a small smearing width and dense k-point resolution is required to determine an accurate Fermi energy and precise electronic structure. The difference in free energy and the energy with the smearing width extrapolated back to 0 should be smaller than the accuracy of the convergence of the k-point resolution and cutoff energy.

In VASP, one can effectively parallelize the calculations with input parameters in the INCAR file, ‘NCORE’ and ‘NSIM’. NCORE specifies the number of cores that work on each orbital and NSIM determines how many bands are optimized in parallel. In QE, the parallelization is specified in the submission script with five types of tags corresponding to five levels of parallelization: images in NEB calculations (-ni), k-points or “pools” (-nk), Kohn-Sham orbitals or “band groups” (-nb), task groups for plane waves and charge density (-nt) and linear algebra operations (-nd). For VASP and QE these parallelization parameters, along with the number of nodes and processors per node on which the job is distributed, must be uniquely determined for each type of calculation, mostly by trial and error.

## 5.4 The Hubbard $U$ Method

For transition elements, it is important to accurately describe the strongly correlated nature of their  $d$  and  $f$  electrons, which are poorly treated by LDA and GGA alone. Conventional DFT does not remove the fictitious electron self-interaction, resulting in an overestimate in the electron-electron repulsion, and thus, incorrectly delocalizes electrons to give a metallic ground state for ferromagnetic and antiferromagnetic insulators. It has been shown that DFT with a Hubbard  $U$  parameter, which characterizes the intra-atomic Coulomb repulsions, treats the correlation effects well with the proper selection of  $U$ , and accurately predicts magnetic insulators.  $U$  is an intrinsic response property that corrects for the fact that DFT without  $U$  calculates an unphysical smooth quadratic energy profile as a function of integer occupations. The addition of  $U$  creates a linear piecewise energy curve (Figure 5.1). Thus, the Hubbard  $U$  parameter is a physical property (i.e., not an empirical fitting parameter) that can be experimentally determined through X-ray photoelectron spectroscopy experiments or self-consistently calculated using the linear response approach within density functional theory.

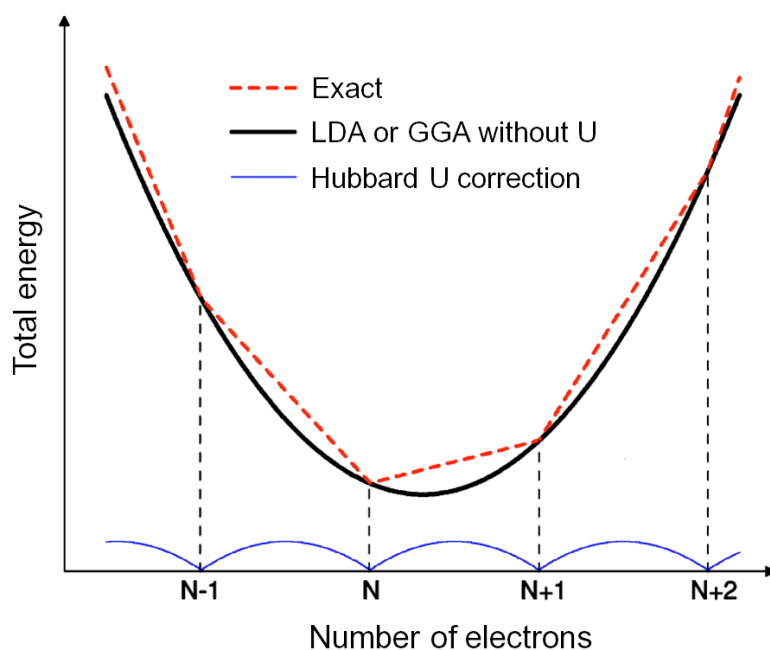


Figure 5.1. Schematic of the total energy as a function of electronic occupations. The black curve is the calculated energy curve with DFT without the Hubbard  $U$  correction, the red dashed curve is the correct linear piecewise energy curve and the blue curve is the Hubbard  $U$  correction, or the difference between the black and red curves. Modified from *Coccocioni et al.* [2005].

In many studies, the Hubbard  $U$  parameter is tuned semi-empirically through the agreement of physical or electronic properties with experimentally-measured values [e.g., *Bengone et al.*, 2000; *Shi et al.*, 2008; *Yang et al.*, 2009]. However,  $U$  is strongly dependent of the structure and spin state, and thus, when examining enthalpy differences between multiple phases and/or spin states, dedicated calculation of the Hubbard  $U$  parameter for each case is essential.  $J$  is the screened exchange energy, describing the effects associated with higher-multipolar terms in the Coulomb interaction.

Quantum Espresso (v6.0) currently has two types of DFT+ $U$  calculations: the fully rotationally invariant scheme by *Liechtenstein et al.* [1995] and the simplified rotationally-invariant scheme by *Cococcioni and Gironcoli* [2005]. In the fully rotationally-invariant approach,  $U$  and  $J$  are specified independently, whereas in the simplified rotationally-invariant scheme,  $J$  is set to 0 (using only lower-order Slater integrals).  $J$  is particularly important in non-collinear magnetic systems, multiband metals, superconductors and heavy-fermion systems [*Jeong and Pickett*, 2006; *Bultmark et al.*, 2009; *Bousquet and Spaldin*, 2010; *de'Medici*, 2011]. For most other materials, the simplified rotationally-invariant method produces similar results to the fully rotationally-invariant method.  $U$  can be calculated using linear response theory within the Quantum Espresso package based on the simplified rotationally invariant method of *Cococcioni and Gironcoli* [2005]. The  $U$  resulting from this method is often referred to as an internally consistent  $U$  ( $U_0$ ).

An internally consistent  $U$  is calculated from the difference between the non-interacting (bare) and interacting (self-consistent) response functions obtained by applying rigid potential shifts on the  $\text{Fe}^{2+}$  sites (Figure 5.2). A perturbation is added to the Kohn-Sham potential:

$$V_{tot}|\psi_{\sigma}^{kv}\rangle = V_{KS}|\psi_{\sigma}^{kv}\rangle + \alpha_I \sum_m |\phi_I^m\rangle \langle \phi_I^m | \psi_{\sigma}^{kv}\rangle, \quad (5.13)$$

where  $\phi_I^m$  is the localized states of atom  $I$  and  $\alpha_I$  is the strength of the perturbation (typically -0.1 to +0.1 eV). The modified total energy is a function of  $\alpha$ :

$$E(\alpha_I) = \min_{n(\mathbf{r})} \{E_{DFT}[n(\mathbf{r})] + \alpha_I n_I\}, \quad (5.14)$$

where  $n(\mathbf{r})$  is the one-body density matrix,  $E_{DFT}[n(\mathbf{r})]$  is the total DFT energy based on the total electron density  $n(\mathbf{r})$  and  $n_I$  is the value of the on-site occupation. The localized potential shift of strength,  $\alpha_I$ , on each Hubbard atom is changed from values typically ranging from -0.1 to +0.1 eV while  $U$  itself is kept at 0 eV. Solving for  $E(\alpha_I)$  for each perturbation value, one can get the response function,  $\chi_{IJ} = \frac{\delta n_I}{\delta \alpha_J}$ , which is the inverse of

the second derivative of the energy,  $\frac{\delta^2 E}{\delta n_I^2} = -\frac{\delta \alpha_I}{\delta n_I}$  computed from  $E[\{n_I\}] = E(\alpha_I) - \alpha_I n_I$ .  $U$  is defined as:

$$U = (\chi_0^{-1} - \chi^{-1})_{II}, \quad (5.15)$$

where  $\chi_0$  is the response function that is not related to the electron-electron interactions and must be subtracted from the interacting response function,  $\chi$ . It is due to the re-hybridization of the orbitals before electron-electron interactions can screen the perturbation.

In Quantum Espresso, one performs a self-consistent calculation to calculate the charge densities without a perturbation. Using these charge densities, self-consistent calculations are performed with varying values of  $\alpha$ . The occupation matrices calculated without readjusting self-consistently to screen the perturbation (printed before the electronic minimization) are used to calculate the non-interacting response functions while the occupation matrices calculated after adjusting self-consistently to screen the perturbation (printed at the end of the electronic minimization) are used to calculate the interacting response functions. The  $U$  calculated from the LDA or GGA ground state from these response functions is the internally consistent Hubbard  $U$  (sometimes denoted as  $U_0$ ).

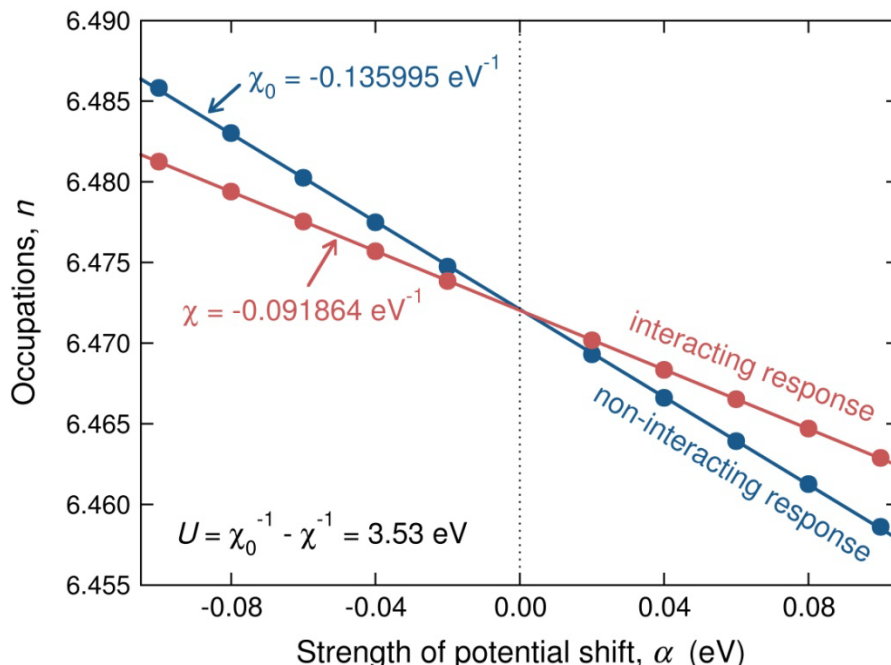


Figure 5.2. Occupations of iron's  $d$  electrons in  $(\text{Mg}_{0.875}\text{Fe}_{0.125})\text{CO}_3$  at 0 GPa plotted against the strength of the applied potential shift. The resulting non-interacting and interacting response functions,  $\chi_0$  and  $\chi$ , are  $-0.135995 \text{ eV}^{-1}$  and  $-0.091864 \text{ eV}^{-1}$ , respectively, producing an internally consistent Hubbard  $U$  of 3.53 eV.

Additional steps may be taken to achieve a self-consistent  $U$  through the methods described in *Kulik et al.* [2006] or *Hsu et al.* [2011]. The latter two provide essentially identical results [*Hsu et al.* 2011], as they both calculate  $U$  from the LDA+ $U$  or GGA+ $U$  ground states. In the *Kulik et al.* [2006] method, the linear response calculations are performed with different values of  $U$  (referred to as  $U_{in}$ ) and are plotted against the resulting  $U$  values (referred to as  $U_{out}$ ) (Figure 5.3). The result is a linear relationship close to where  $U_{in} = U_{sc}$  of  $U_{in}$ :

$$U_{out} = \frac{d^2E}{d(n(\mathbf{r}))^2} = U_{sc} - \frac{U_{in}}{m}, \quad (5.16)$$

where the slope,  $1/m$ , is related to the effective degeneracy of the orbitals. At smaller  $U_{in}$  values,  $U_0$  deviates from linearity. This effect is phase dependent (e.g., for some phases  $U_0$  may be essentially equivalent to  $U_{sc}$ ).

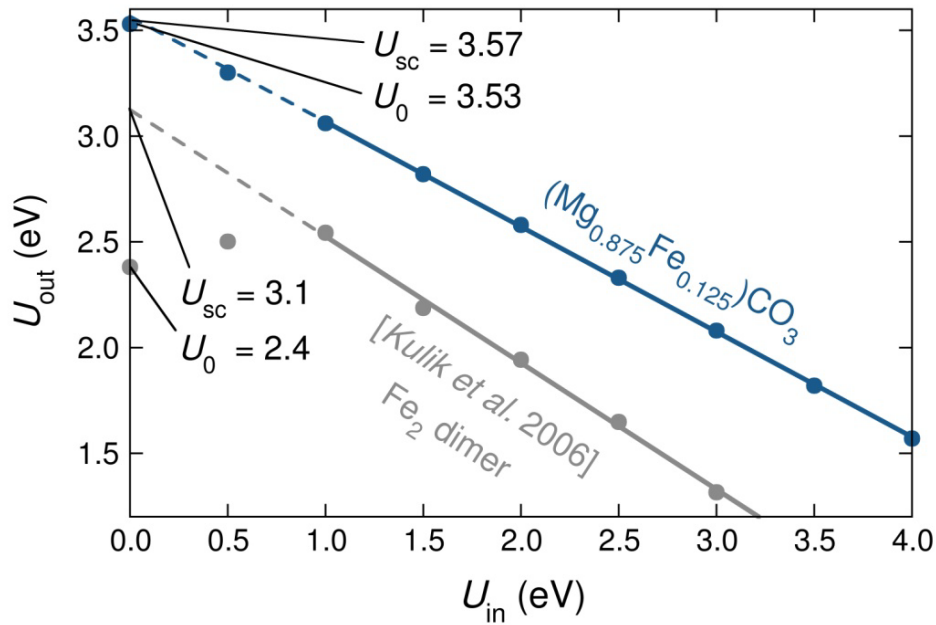


Figure 5.3.  $U_{out}$  as a function of  $U_{in}$  for a  $\text{Fe}_2$  dimer [*Kulik et al.* 2006] and ferromagnetic high-spin ferromagnesite,  $(\text{Mg}_{0.875}\text{Fe}_{0.125})\text{CO}_3$ .

In the method described in *Hsu et al.* [2011],  $U$  is calculated with an iteratively-determined  $U_{in}$ . The first linear-response calculation is performed with a guess  $U_{in}$ . During the perturbed calculation, the Hubbard potential is fixed so that the second derivative of the energy,  $\frac{d^2E}{d(n(\mathbf{r}))^2}$ , is contributed solely by  $\frac{d^2E_{DFT}}{d(n(\mathbf{r}))^2}$  (i.e.,  $U_{sc}$ ). In each iteration, the  $U_{out}$  is used as the new  $U_{in}$  until convergence is achieved to the desired

accuracy. The final  $U_{out}$  is equivalent to  $U_{sc}$  described in *Kulik et al.* [2006] without the need to test for linearity of  $U_{in}$  vs.  $U_{out}$ , and is thus more computationally efficient. Nonetheless,  $U_0$  is far more efficient than either of the methods described above.  $U_0$  only requires one linear response calculation per volume, while  $U_{sc}$  either requires four to six calculations until linearity around  $U_{in}=U_{sc}$  is established [*Kulik et al.*, 2006] or three to five iterations until convergence of  $U_{sc}$  to the desired precision is achieved [*Hsu et al.*, 2011]. An additional step to the methods described thus far is the convergence of  $U$  with respect to the local structure of the Hubbard site, which is affected by the value of  $U$ . Typically, one additional iteration of the linear response calculation is required, with an updated  $U$  value to achieve convergence to 0.01 eV.

## 5.5 Crystal Structure Prediction

USPEX (Universal Structure Predictor: Evolutionary Xtallography) [*Oganov and Glass*, 2006; *Oganov and Glass*, 2006; *Glass et al.*, 2006] is an evolutionary algorithm that can be interfaced with density functional theory codes, such as the Vienna *Ab initio* Simulation Package (VASP) and Quantum Espresso (QE). It has been shown to successfully predict stable phases without experimental input [*Oganov and Glass*, 2006]. The minimal amount of information that the user must input is: the number of atoms of each type (newer versions of USPEX allow for variable-composition calculations), an initial guess of the unit cell volume, physical constraints, parameters that control how the structures evolve and the stopping criteria. USPEX creates a user-defined number of structures (typically 20-80) within each generation. The first generation is created randomly with some minimal physical restrictions, such as atomic distances and minimum length of a cell parameter. The user also has the choice to input any number of non-random structures into the first generation. Using the negative of the enthalpy (equivalent to free energy at 0 K) as a fitness parameter, a user-defined fraction (typically 40-60%) of each generation is chosen to compete in the following generation through the following operations:

(1) Heredity. Two parent structures are combined to produce a child structure by randomly selecting a slab from each parent structure and fitting them together. The  $a_{ij}$  matrices are averaged to create the new lattice parameters. If there are too many or too few atoms of one type, they are removed or inserted randomly. Typically, 70-90% of offspring are generated through heredity.

(2) Lattice mutations. A symmetric strain matrix, composed of zero-mean Gaussian random variables, is applied to the cell shape to create a structure with different lattice parameters. Typically, 0-20% of offspring evolve through lattice mutations.

(3) Atomic permutations. Two atomic identities are switched a random number of times within the unit cell. This operation is only applicable if the system is composed of more than one type of atom. If the system has more than one type of atom, about 10-20% of the offspring evolve through atomic permutations.

The few best structures of each generation compete in the next generation without evolution. The simulation terminates if the best structure is chosen for a user-defined number of generations or when the maximum number of generations that the user has specified is complete. Version 9.4.4 of USPEX is capable of minimizing a variety of parameters, including the enthalpy (discussed above), volume, hardness, band gap, magnetization, elastic moduli and sound velocities.

## Chapter 6

# *Ab initio* Study of the Structure and Stability of $\text{CaMg}(\text{CO}_3)_2$ \*

\* This chapter has been reformatted from what was previously published as: Solomatova, N. V. and Asimow, P. D. (2017): *Ab initio* study of the structure and stability of  $\text{CaMg}(\text{CO}_3)_2$  at high pressure, *American Mineralogist*, 102, 201-215, doi:10.2138/am-2017-5830.

### 6.1 Introduction

Carbon is exchanged between the surface and Earth's interior through ingassing by subduction and through both passive and volcanic outgassing [Kelemen and Manning, 2015]. Carbon is subducted into the mantle primarily in the form of carbonate ( $\text{CO}_3^{2-}$ -bearing) minerals as metasomatically calcium-enriched basaltic rock (rodingite), calcified serpentinites (ophicarbonates) and sedimentary carbonaceous ooze [Brenker *et al.*, 2006]. Evidence of carbon-bearing phases in the Earth's mantle includes: the release of  $\text{CO}_2$  in volcanic eruptions, dissolved  $\text{CO}_2$  in magmatic glasses and glass inclusions [Mörner and Etiope, 2002], diamonds and carbonate minerals in mantle xenoliths [Eggler, 1978; Sobolev and Shatsky, 1990], and the existence of carbonatite and kimberlite magmas [Wyllie *et al.*, 1990]. Carbon has low solubility in mantle silicates [Shcheka *et al.*, 2006], such that significant carbon storage or transport in the mantle requires formation of carbon-rich phases. Decomposition of carbonates can produce free  $\text{CO}_2$ , which lowers the viscosity and melting temperature of the surrounding mantle [Eggler *et al.*, 1976] and enables rapid recycling of carbon through subduction-related volcanism rather than deep subduction and long-term storage. Identifying and characterizing the stability of carbonate phases is therefore a necessary step towards understanding the transport and storage of carbon through the Earth's deep carbon cycle [Hazen *et al.*, 2013]. The identification of a new, more stable, carbonate phase that is able to host carbon under conditions where known carbonates may decompose has the potential to substantially change estimates of the geochemical fluxes of carbon.

It has been suggested that magnesite is the dominant carbonate phase in relatively oxidized regions of the mantle [Brenker *et al.*, 2006; Isshiki *et al.*, 2004]. Skorodumova *et al.* [2005], reasoning by analogy to silicates, examined the stability of magnesite in selected pyroxene and perovskite structures, finding that magnesite could transform into a  $\text{C}2/c$  pyroxene structure with 4-fold coordination of carbon by oxygen at 113 GPa. Using

USPEX, however, *Oganov et al.* [2008] searched a vastly larger space of possible structures and found that magnesite undergoes a phase transition at 84 GPa to a monoclinic phase (“phase II”) with space group  $C2/m$ , containing rings of  $(C_3O_9)^{6-}$ , and subsequently at 138 GPa transitions to an orthorhombic phase (“phase III”) with space group  $P2_1$ , containing chains of  $CO_4^{4-}$  tetrahedra. Their calculations show that the  $C2/c$  pyroxene structure has a higher energy than either phase II or phase III at all relevant pressures. Calcite, on the other hand, transitions to aragonite at 2 GPa, which transitions to the post-aragonite phase (space group  $Pm\bar{m}n$ ) at 42 GPa, persisting up to core-mantle boundary pressures [*Ono et al.*, 2005; *Oganov et al.*, 2006].

End-member  $CaMg(CO_3)_2$  dolomite typically breaks down into two carbonates at about 5-6 GPa in the temperature range of 800-1200 K [*Shirasaka et al.*, 2002]. However, X-ray diffraction experiments have proposed that dense high-pressure phases of dolomite may be more stable or comparable in stability to single-cation carbonates above 35 GPa. High-pressure dolomite may be resistant to decomposition into single-cation carbonates prior to the transformation of trigonal magnesite to monoclinic phase II. *Santillan et al.* [2003] observed a phase transition of  $CaMg(CO_3)_2$  dolomite to a new phase (“dolomite II”) at about 20 GPa. Experiments on two iron-bearing compositions,  $Ca_{0.988}Mg_{0.918}Fe_{0.078}Mn_{0.016}(CO_3)_2$  [*Mao et al.*, 2011] and  $CaMg_{0.6}Fe_{0.4}(CO_3)_2$  [*Merlini et al.*, 2012], led to observations of two phase transitions in dolomite at 17 and 35 GPa. Both studies refer to the high-pressure phases as “dolomite II” and “dolomite III,” and find that dolomite II decomposes upon heating while dolomite III is resistant to decomposition into single-cation carbonates at high pressure and temperature. However, they report different high-pressure dolomite phases. *Mao et al.* [2011] characterize their observed dolomite II with orthorhombic symmetry and dolomite III with monoclinic symmetry, but do not refine atomic coordinates or identify the space groups. *Merlini et al.* [2012] characterize their high-pressure dolomite phases with triclinic symmetry, refining both the crystal structures and atomic coordinates. The X-ray diffraction patterns for the dolomite II structures are consistent with each other (see supplementary materials for *Merlini et al.* [2012]), whereas the dolomite III structures have distinct X-ray diffraction patterns resulting from nonequivalent crystal structures. The difference in symmetry reflects the complex nature of dolomite polymorphs, whose stability and transformation kinetics may be strongly affected by variations in composition and experimental conditions. As already seen in comprehensive structure searches for  $MgCO_3$ , it is likely that Fe-Mn-bearing  $CaMg(CO_3)_2$  has a complex energy landscape, resulting in many polymorphs with similar energies. Even after sample annealing, it may be that the most stable phase is never achieved experimentally or that slight variations in composition result in different ground states.

In addition to a difference in symmetry, the two studies report different unit-cell volumes for dolomite II and dolomite III, with discrepancies larger than can be explained simply by the difference in composition. *Mao et al.* [2011] report a 15% unit-cell volume drop upon the phase transition from dolomite I to dolomite II, whereas *Merlini et al.* [2012] do not observe a detectable change in volume. For the phase transition from dolomite II to dolomite III, *Mao et al.* [2011] report an 8% volume drop and *Merlini et al.* [2012] report a 3% volume drop. Although it is possible that the difference in unit cell volumes for the high-pressure phases is a result of the combined effect of different compositions, crystal structures and experimental conditions, *Merlini et al.* [2012] propose that a different choice of formula units per unit cell is required to correctly index the structure of *Mao et al.* [2011]. In any case, the differing experimental observations create a need for a theoretical study to confirm which high-pressure dolomite phases are the most thermodynamically stable.

## 6.2 Computational Methods

USPEX (Universal Structure Predictor: Evolutionary Xtallography), an evolutionary algorithm that can be interfaced with a variety of density functional theory codes, has been shown to successfully predict stable phases without experimental input [*Oganov and Glass, 2006*]. USPEX compares the energies of structures that continuously evolve through operations of (1) heredity – a combination of two parent structures, (2) lattice mutations – a distortion of the cell shape through a symmetric strain matrix, and (3) atomic permutations – switching of atoms within the cell. We ran USPEX interfaced with the *ab initio* code VASP [*Kresse and Furthmüller, 1996*] for  $\text{CaMg}(\text{CO}_3)_2$  with 20 or 30 atoms/cell at 25-40 GPa pressure, with population sizes between 30 and 50 structures per generation. *Ab initio* calculations were performed at 0 K using the projector-augmented wave (PAW) method [*Bloch, 1994*] implemented in VASP. The generalized gradient approximation (GGA) [*Perdew et al., 1996*] was used to approximate the exchange correlation terms. In structure prediction calculations, GGA produces results better than LDA in terms of agreement with experiments for phase transition pressures and chemical reactions [*Oganov et al., 2013*]. The following PAW pseudo-potentials were used in VASP for structure prediction: core radius of 3.7 a.u. for Ca ( $1s^2 2s^2 2p^6$  core,  $3s^2 3p^6 4s^2$  valence), 2.0 a.u. for Mg ( $1s^2 2s^2 2p^6$  core,  $3s^2$  valence), 1.5 a.u. for C ( $1s^2$  core,  $2s^2 2p^2$  valence), and 1.52 a.u. for O ( $1s^2$  core,  $2s^2 2p^4$  valence).

These calculations were run several times both with and without prescribed seed structures. The first generation was created either entirely randomly or with one to three seeded structures with standard physical constraints on the minimum ion distance of 0.7 Å and minimum lattice vector of 2-2.5 Å. For subsequent generations, 40-50% of the

structures were created through heredity using the lowest energy structures from the previous generation, 10-20% were produced through lattice mutations, 10% were produced through atomic permutations and 20% were randomly generated. The best five structures in each generation were left unchanged and competed in subsequent generations. Generated structures were relaxed at constant pressure in four stages with incrementally increasing precision, where the final plane-wave energy cut off, k-point resolution and convergence criteria for electronic self-consistency were 550 eV,  $0.08 \text{ \AA}^{-1}$  and  $10^{-5}$  eV, respectively. Through this procedure, we were able to find a 20-atom monoclinic dolomite with  $P2/c$  symmetry and a 20-atom primitive  $C2/c$  cell to which we applied a crystallographic transformation matrix to obtain the conventional 40-atom monoclinic  $C2/c$  structure. Due to the complex nature of the free energy landscape for double carbonates, it is possible that a global minimum was never achieved.

A  $C2/c$  structure with 4-fold C was created by substituting the dolomitic composition into the diopside structure and relaxing it at high pressure. We also examined the triclinic dolomite II and dolomite III structures from *Merlini et al.* [2012], and we substituted the dolomitic composition into several previously published carbonate structures: the post-aragonite structure ( $Pm\bar{m}n$ ) [*Oganov et al.*, 2006];  $\text{MgCO}_3$  phase II ( $C2/m$ ), phase III ( $P2_1$ ), structure  $P2_1-10$  and structure  $Pna2_1-20$  [*Oganov et al.*, 2008]; calcite III ( $C2$ ) [*Smyth and Ahrens*, 1997]; and  $\text{MnCO}_3$  phase II ( $P\bar{1}$ ) [*Merlini et al.*, 2015]. Appropriate supercells with the dolomite stoichiometry were created with various choices of cation site ordering (i.e., layers of Ca/Mg atoms and checkered Ca/Mg arrangement). The  $P2_1-10$  structure has the space group  $C2$  after relaxing it at high pressures with the dolomite stoichiometry. The resulting structure was crystallographically transformed to a conventional  $C2$  unit cell, and resembles the  $P2/c$  structure. The relaxed calcite III structure extended to a  $1 \times 1 \times 2$  supercell with layers of Ca and Mg atoms are equivalent to the  $C2$  structure with a different unit cell. These structures from the literature and several competitive structures found with USPEX are not considered further in this study due to their relatively high energies. However, it is possible that, with certain cation substitutions, these phases may be observed experimentally. Hence, all of these structures are provided in the supplementary crystallographic information file.

Finally, the short list of low-energy candidate dolomite structures remaining after USPEX and literature search were relaxed using more accurate PAW pseudo-potentials for the 3<sup>rd</sup>-row elements: core radius of 2.3 a.u. for Ca ( $1s^2 2s^2 2p^6$  core,  $3s^2 3p^6 4s^2$  valence) and 2.0 a.u. for Mg ( $1s^2 2s^2$  core,  $2p^6 3s^2$  valence). C and O pseudo-potentials remained the same. A plane-wave energy cut off of 600 eV was used and a fine k-point grid of  $0.02-0.03 \text{ \AA}^{-1}$  was required to refine the transition pressures between phases with similar

energies. We carried out all the requisite convergence tests to ensure these parameters were adequate. The convergence criteria for electronic self-consistency and ionic relaxation loop are  $10^{-5}$  eV and  $10^{-4}$  eV, respectively. We ensured that forces acting on all relaxed atoms were  $<0.01$  eV/Å.

The pressure-volume data were fitted with third-order Birch-Murnaghan equations of state using MINUTI 1.1.2 [Sturhahn, 2015]. For dolomite III and *P2/c* dolomite, equations of states were fitted above 10 GPa; at lower pressures, these structures transform into lower-pressure polymorphs with coplanar  $\text{CO}_3^{2-}$  groups during structural relaxation. Similarly, in *C2/c* dolomite with 4-fold C, the carbonate tetrahedra transform to triangular coordination environments below 60 GPa. Thus, for the *C2/c* structure with 4-fold C, equation of state parameters  $V_0$ ,  $K_0$  and  $K_0'$ , though defined at 0 pressure, are fitted to data in the range from 60 to 140 GPa. Conversely, the dolomite II structure is not stable above 30 GPa; thus, an equation of state was fitted to the pressure range between 0 and 30 GPa. Structures *C2/c* with 3-fold C and dolomite I were fitted with equations of state at pressures between 0 and 80 GPa.

### 6.3 High-Pressure Dolomite Structures

We found two competitive  $\text{CaMg}(\text{CO}_3)_2$  structures with *C2/c* and *P2/c* symmetry using USPEX (Table 6.1; Figure 6.1). Simulated X-ray diffraction patterns are shown in Figure 6.2. The enthalpy difference between candidate high-pressure dolomite polymorphs and  $R\bar{3}$  dolomite I are shown in Figure 6.3. For static *ab initio* calculations, the enthalpy is equivalent to Gibbs free energy; the structure with the lowest enthalpy is the most stable structure. Dolomite II is energetically similar to dolomite I and was not successfully relaxed above 30 GPa without the rotation of its  $\text{CO}_3$  groups (i.e., a second order phase transition). The *P2/c* structure is less stable than the *C2/c* structure at all pressures examined in this study but more stable than the dolomite III structure above 32 GPa. Above 15 GPa, the *C2/c* structure is more favorable than all other structures discovered by USPEX in this study and all previously reported structures. There is a shift from  $\text{sp}^2$  bonding (triangular coordination) to  $\text{sp}^3$  bonding (tetrahedral coordination) in the *C2/c* structure at 127.5 GPa (Figure 6.3 inset).

The pressure-volume relationship for the candidate dolomite phases and their corresponding third-order Birch-Murnaghan equations of state (EOS) are shown in Figure 6.4. The zero-pressure volume per  $\text{CO}_3^{2-}$  group ( $V_0$ ), bulk modulus ( $K_0$ ) and the bulk modulus derivative ( $K_0'$ ) for these structures are compared in Table 6.2. The fitted  $K_0$  and  $K_0'$  for dolomite I are 86.8(3) GPa and 4.20(2) with a  $V_0$  of  $55.1 \text{ \AA}^3$ , in reasonable

<i>C2/c</i> (3-fold C) ( $Z = 4$ )			
a=8.0127, b=7.6005, c=4.8652, $\alpha=90$ , $\beta=106.43$ , $\gamma=90$ , V=284.20			
atom	x	y	z
Ca	0.00000	0.67015	0.75000
Mg	0.50000	0.40958	0.25000
C	0.21854	0.36747	0.81476
O1	0.37765	0.40733	0.85578
O2	0.33535	0.73448	0.83822
O3	0.13315	0.44102	0.96001

<i>C2/c</i> (4-fold C) ( $Z = 4$ )			
a=8.3072, b=7.8089, c=4.3586, $\alpha=90$ , $\beta=103.53$ , $\gamma=90$ , V=274.89			
atom	x	y	z
Ca	0.00000	0.68472	0.75000
Mg	0.50000	0.39288	0.25000
C	0.21954	0.40787	0.76878
O1	0.37742	0.42091	0.83232
O2	0.33653	0.75551	0.80211
O3	0.14558	0.47281	0.00112

<i>P2/c</i> ( $Z = 2$ )			
a=6.4089, b= 2.8246, c=7.7595, $\alpha=90$ , $\beta=92.54$ , $\gamma=90$ , V=140.32			
atom	x	y	z
Ca	0.00000	0.19756	0.25000
Mg	0.50000	0.80172	0.25000
C	0.73864	0.56617	0.99292
O1	0.75561	0.29761	0.64840
O2	0.59086	0.71271	0.89469
O3	0.86966	0.27650	0.94243

Table 6.1: Fractional coordinates, lattice parameters and unit-cell volume for calculated high-pressure  $\text{CaMg}(\text{CO}_3)_2$  polymorphs at 80 GPa.

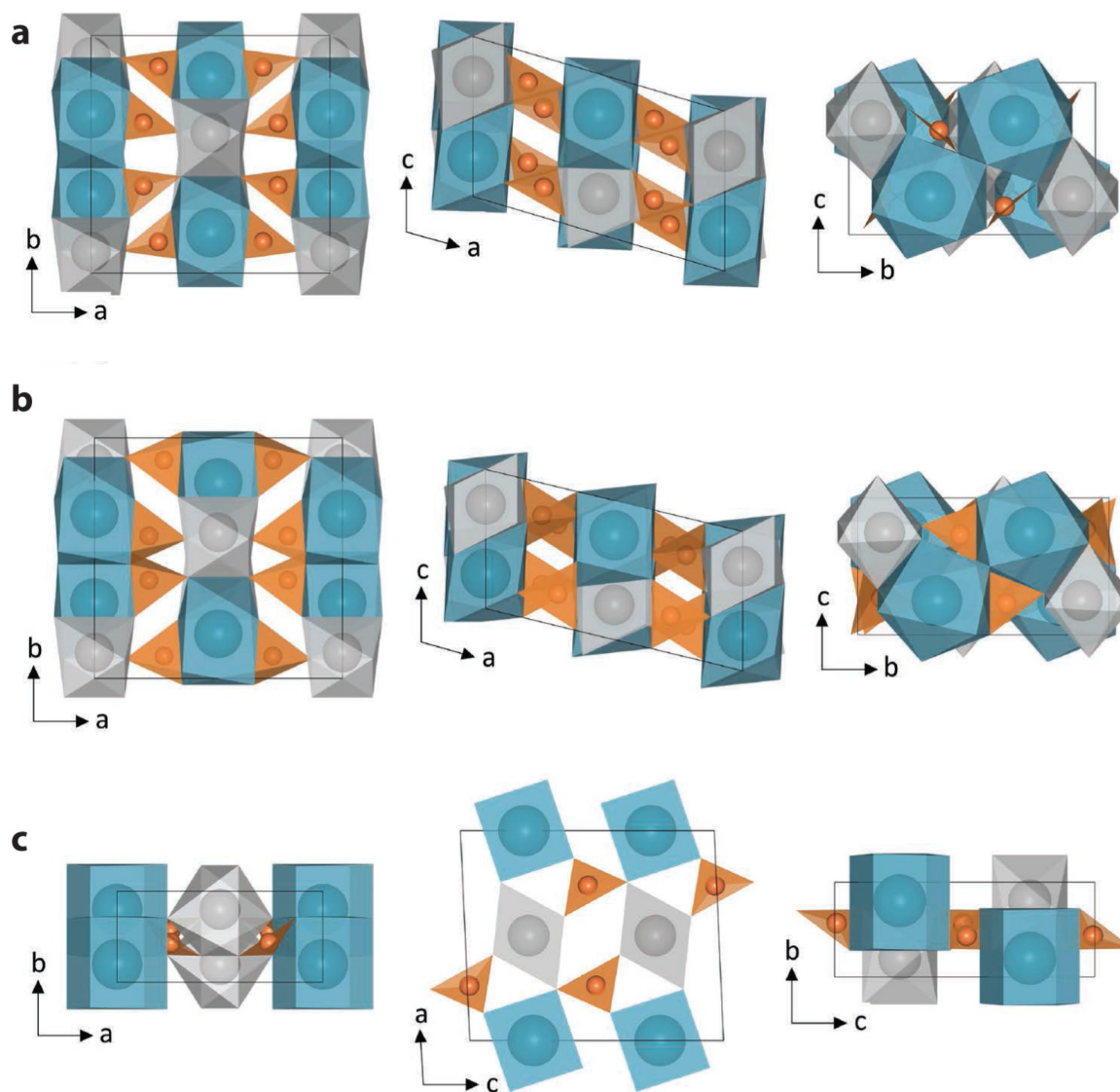


Figure 6.1: Novel high-pressure dolomite polymorphs at 80 GPa: (a)  $C2/c$  dolomite with 3-fold C, (b)  $C2/c$  dolomite with 4-fold C and (c)  $P2/c$  dolomite. Figures were produced with the VESTA software [Momma and Izumi, 2008]. Ca polyhedra are blue, Mg polyhedra are grey and C polyhedra are orange.

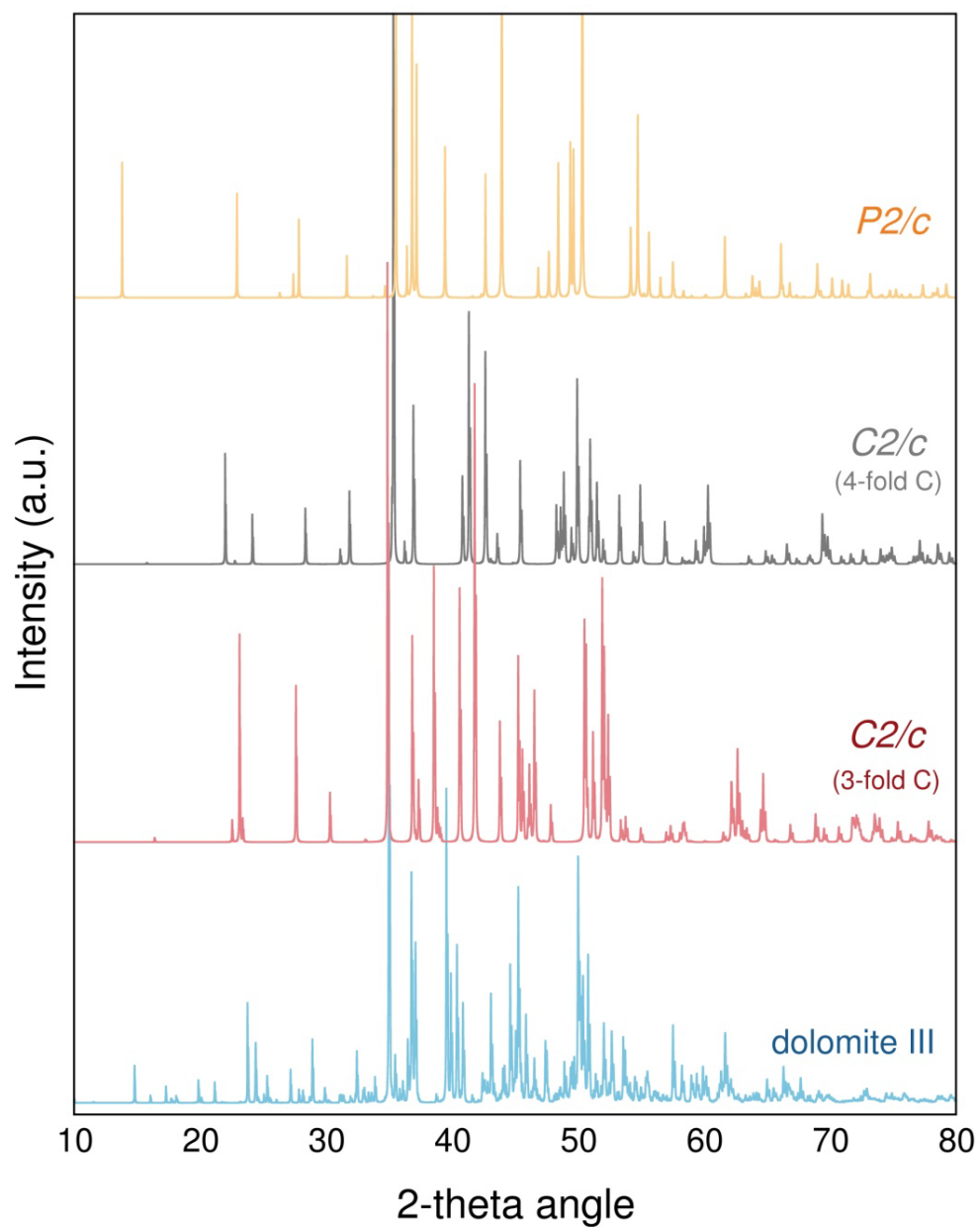


Figure 6.2: Synthetic X-ray diffraction patterns for high-pressure dolomite phases at 80 GPa ( $\lambda=1.54 \text{ \AA}$ ). Dolomite III is blue, *C2/c* dolomite with 3-fold C is red, *C2/c* dolomite with 4-fold C is grey and *P2/c* dolomite is orange.

Table 6.2: Equation of state parameters for the calculated  $\text{CaMg}(\text{CO}_3)_2$  and experimental  $\text{Ca}(\text{Mg,Fe})(\text{CO}_3)_2$  polymorphs. We fitted the pressure-volume data using a third-order Birch-Murnaghan equation of state with the MINUTI software, applying a 1% error to pressure and volume.  $V_0$  is the zero-pressure volume per  $\text{CO}_3^{2-}$  group. Dolomite III and structures  $P2/c$  and  $C2/c$  with 4-fold C were not successfully relaxed at 0 GPa without a second-order phase transition to a lower-pressure structure. Thus, their zero-pressure volumes were fitted.

Phase	$V_0$ ( $\text{\AA}^3$ )	$K_0$ (GPa)	$K_0'$
dolomite I	55.1	86.8(3)	4.20(2)
dolomite II <sup>a</sup>	55.0	94.0(8)	2.80(7)
dolomite III <sup>b</sup>	52.2(1)	94.1(9)	3.89(3)
dolomite III <sup>c</sup> [ <i>Mao et al.</i> , 2011]	39.9(3)	164(8)	4
dolomite III <sup>d</sup> [ <i>Merlini et al.</i> , 2012]	51.8(1.6)	92.7(20.0)	3.92(4)
$C2/c$ (3-fold C)	51.9	84.8(6)	4.78(5)
$C2/c$ (4-fold C)	45.1(3)	178.4(8.1)	3.69(9)
$P2/c$	51.2(1)	85.4(1.4)	4.76(6)

<sup>a</sup> We fitted an equation of state to our calculated pressure-volume data for the triclinic dolomite II structure reported in *Merlini et al.* [2012].

<sup>b</sup> We fitted an equation of state to our calculated pressure-volume data for the triclinic dolomite III structure reported in *Merlini et al.* [2012].

<sup>c</sup> Equation of state parameters as reported in *Mao et al.* [2011] for their observed monoclinic dolomite III structure.  $K_0'$  was fixed to 4. The full composition as determined from microprobe analysis is  $\text{Ca}_{0.988}\text{Mg}_{0.918}\text{Fe}_{0.078}\text{Mn}_{0.016}(\text{CO}_3)_2$ . It is possible that the volume of dolomite III is underestimated due to an incorrect assumption of the number of formula units per unit cell [*Merlini et al.*, 2012].

<sup>d</sup> We fitted an equation of state to the published experimental pressure-volume data for triclinic dolomite III, with the chemical formula  $\text{CaMg}_{0.6}\text{Fe}_{0.4}(\text{CO}_3)_2$  [*Merlini et al.*, 2012]. We used a prior estimate of 4 and prior window of  $\pm 1$  for  $K_0'$ .

agreement with reported equation of state parameters determined from fitting a Birch-Murnaghan EOS to pressure-volume data from X-ray diffraction experiments:  $V_0=53.4(1) \text{ \AA}^3$ ,  $K_0=94.1(7)$ , with a fixed  $K_0'$  of 4 [*Ross and Reeder*, 1992]. The volume of dolomite I is overestimated by 3.3%, which is typical for the GGA method. We fitted the experimental pressure-volume data for  $\text{Ca}(\text{Mg}_{0.6}\text{Fe}_{0.4})(\text{CO}_3)_2$  dolomite III [*Merlini et al.*, 2012] with a third-order Birch Murnaghan EOS using a prior estimate of 4 and prior window of  $\pm 1$  for  $K_0'$ , resulting in  $V_0=51.8(1.6) \text{ \AA}^3$ ,  $K_0=92.7(20.0)$  GPa and  $K_0'=3.92(4)$ . These results are in good agreement with the equation of state parameters fitted to the calculated dolomite III compression data where  $V_0=52.2(1) \text{ \AA}^3$ ,  $K_0=94.1(9)$  GPa and  $K_0'=3.89(3)$ . For high-spin  $\text{Ca}(\text{Mg}_{0.92}\text{Fe}_{0.08})(\text{CO}_3)_2$  dolomite III, *Mao et al.*, [2008] report

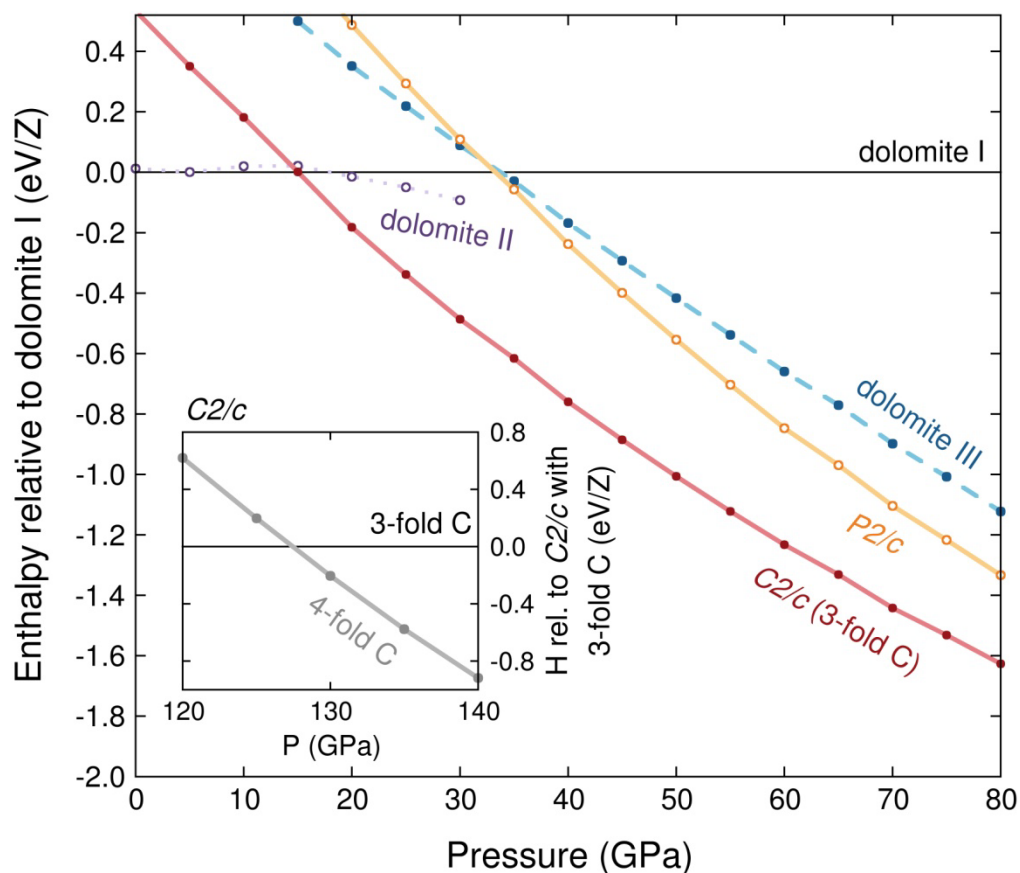


Figure 6.3: Enthalpies per formula unit of candidate dolomite structures relative to dolomite I (horizontal line at zero). *C2/c* dolomite is energetically more stable than all other phases examined in this study for the  $\text{CaMg}(\text{CO}_3)_2$  composition. Inset shows the enthalpy ( $H$ ) per formula unit of *C2/c* dolomite 4-fold C relative to *C2/c* dolomite with 3-fold C. The transition from  $\text{sp}^2$  bonding (triangular coordination) to  $\text{sp}^3$  bonding (tetrahedral coordination) of C in the *C2/c* structure occurs at 127.5 GPa.

a  $K_0=164(4)$  with a  $K_0'=4$  (fixed), resembling the compression behavior of our calculated *C2/c* dolomite with 4-fold coordination. The zero-pressure bulk moduli for all phases with triangular  $(\text{CO}_3)^{2-}$  groups range from 80 to 90 GPa, whereas the  $K_0$  for the *C2/c* structure with 4-fold C is 180 GPa, more than twice as large as for the *C2/c* structure with 3-fold C. By 80 GPa, however, the difference in bulk moduli decreases to 30 GPa (Figure 6.4 inset). Nevertheless, a high bulk modulus for high-pressure carbonates may be an indication of 4-fold coordinated C.

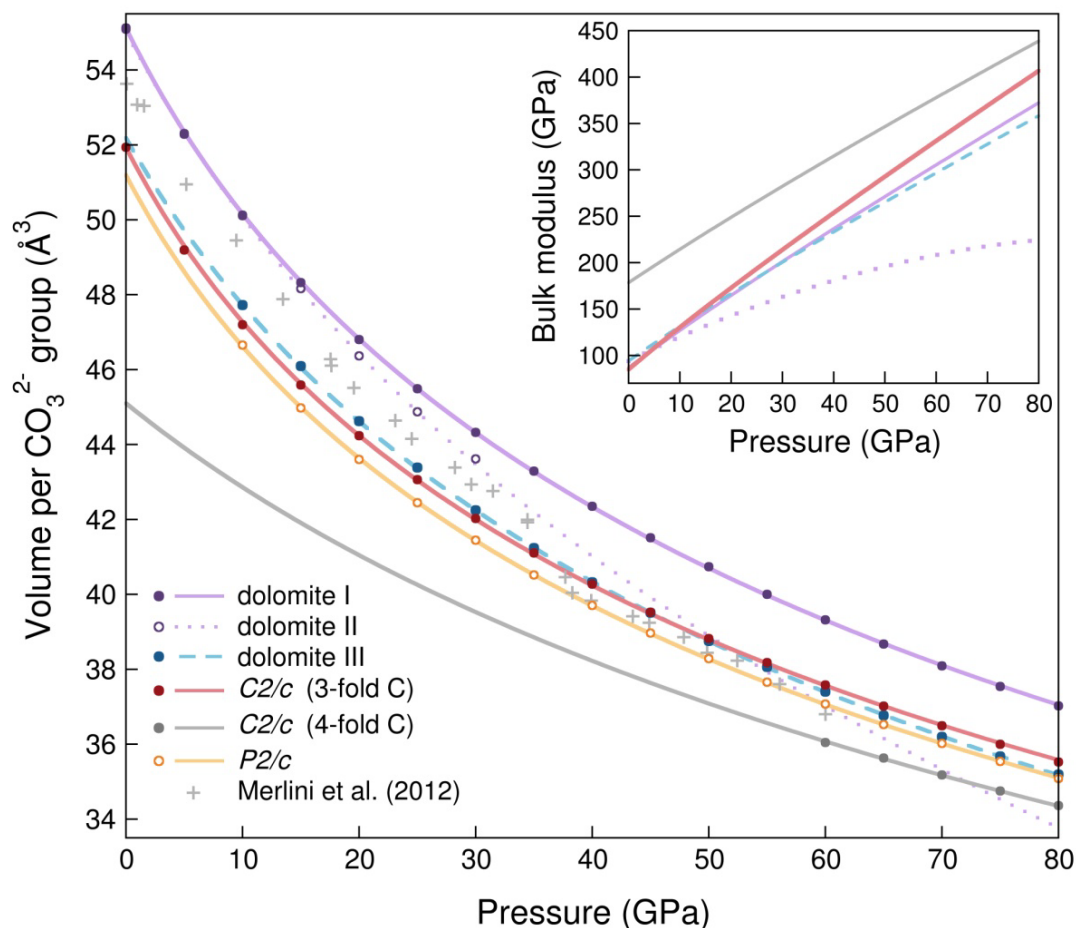


Figure 6.4: Pressure-volume data and the fitted third-order Birch Murnaghan equations of state for candidate dolomite phases. Experimental pressure-volume data for  $\text{CaMg}_{0.6}\text{Fe}_{0.4}(\text{CO}_3)_2$  are shown in grey “+” symbols, with a second-order phase transition to dolomite II at 17 GPa and a first-order phase transition to dolomite III at 35 GPa [Merlino *et al.*, 2012]. The equation of state for  $C2/c$  dolomite with 4-fold C was calculated from data at 60–140 GPa in intervals of 5 GPa. Inset shows the fitted bulk modulus as a function of pressure. Structures  $C2/c$  and  $P2/c$  have indistinguishable bulk moduli.

## 6.4 Discussion

In mantle silicates, Si changes from 4-fold to 6-fold coordination at the decomposition of ringwoodite to bridgmanite and periclase. In  $\text{MgCO}_3$ , C forms tetrahedra above 82 GPa, whereas in  $\text{CaCO}_3$ , C remains 3-fold coordinated up to core-mantle boundary pressures, only forming tetrahedra above 137 GPa [Oganov *et al.*, 2008; Boulard *et al.*, 2015]. In  $C2/c$  dolomite, C tetrahedra become stable at 127.5 GPa, an intermediate pressure compared to the tetrahedra-forming pressures for the single-carbonate end members,  $\text{MgCO}_3$  and  $\text{CaCO}_3$ . Prior to these calculations, there have been no reports in the literature addressing whether C in double carbonates, such as dolomite, would become tetrahedrally coordinated at lower mantle pressures.

With increasing pressure, Mg, Fe<sup>2+</sup> and Ca in mantle silicates transition from 6-fold coordination in olivine and pyroxenes to 6- and 8-fold coordination in garnets and then to 6- and 12-fold coordination in bridgmanite [Murakami *et al.*, 2004; Oganov and Ono, 2004]. In CaCO<sub>3</sub>, Ca increases in coordination number from 6 in calcite to 9 in aragonite to 12 in post-aragonite while, in MgCO<sub>3</sub>, Mg atoms increase in coordination from 6 in magnesite to 8-10 in phases II and III to 9 in *Pna2<sub>1</sub>-20* [Oganov *et al.*, 2008]. In the dolomite III structure [Merlini *et al.*, 2012], the coordination numbers are variable, ranging from 7 to 10, with Ca occupying the larger sites. In *C2/c* dolomite, Mg is 6-fold coordinated and Ca is 8-fold coordinated up to at least 140 GPa. Although, at high pressure, *C2/c* dolomite is the least dense CaMg(CO<sub>3</sub>)<sub>2</sub> candidate, it is stiffer than all the other considered phases in this study, a result of the persistence of relatively low coordination values for its metal cations.

Our simulations show that dolomite has many energetically competitive polymorphs at high pressure with similar enthalpies to the *P2/c* and dolomite III structures; however, above 15 GPa, the *C2/c* structure with 3-fold C has a lower energy than all other phases found with USPEX and reported structures in literature. It is possible that the *C2/c* structure has not been observed experimentally due to a high activation barrier and/or a high sensitivity of the crystal symmetry to iron concentration. Additionally, it is very likely that the stability of high-pressure dolomite with respect to decomposition into single-cation carbonates is related to its composition.

Pure high-pressure dolomite phases will likely decompose into single-cation carbonates at high pressures. The rapid decrease of the enthalpy of high-density post-aragonite beyond 42 GPa is the main driver of the predicted breakdown of all dolomites into single-cation carbonates, including the most stable *C2/c* polymorph (Figure 6.5). However, the addition of Fe and Mn is likely to stabilize dolomite with respect to decomposition. A careful treatment of iron is necessary to accurately describe the strongly correlated nature of the *d* electrons using self-consistently calculated Hubbard *U* parameters, which are a function of iron concentration, spin state, crystal symmetry and unit-cell volume. Additionally, the effect of temperature on high-pressure dolomite phases is unknown. The stability field of pure dolomite I increases with increasing temperature, decomposing at about 4 GPa at 400 K and 6 GPa at 1200 K [Martinez *et al.*, 1996]. It is possible that a similar trend is true for high-pressure dolomite polymorphs. Additional calculations and experiments on iron-bearing dolomites at high temperatures and pressures are needed.

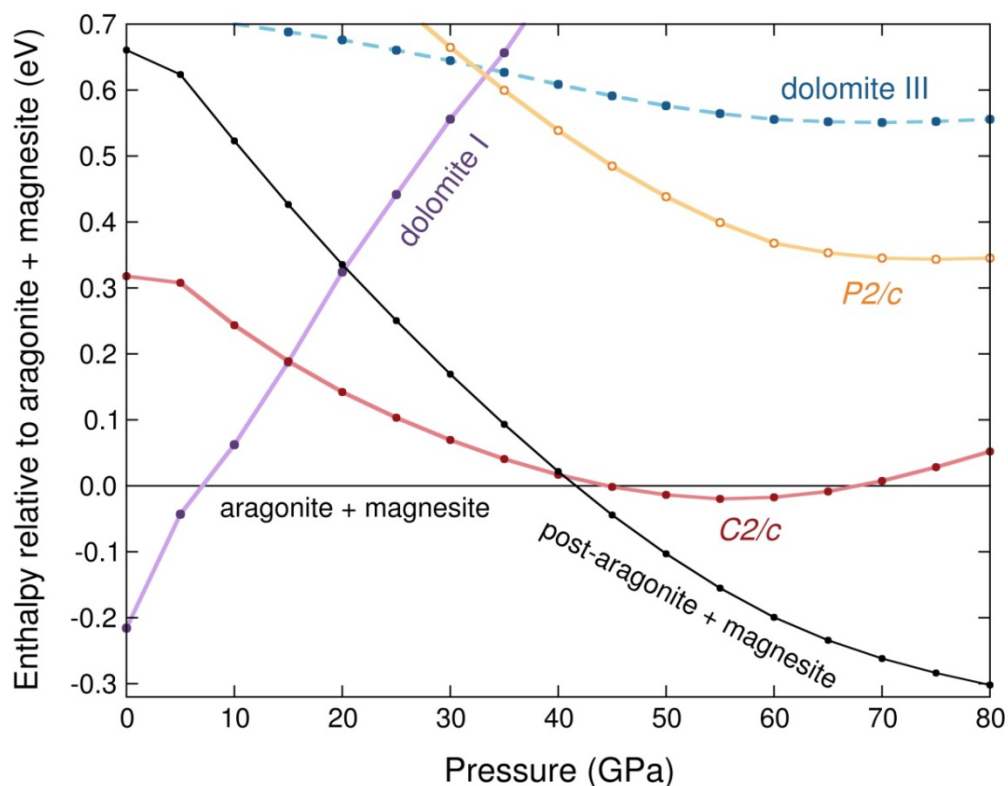


Figure 6.5: The enthalpy difference between dolomite polymorphs and aragonite + magnesite. The rapid decrease of the enthalpy of the post-aragonite + magnesite assemblage is the main driver of the breakdown of all dolomites into single-cation carbonates. However, the substitution of Fe for Mg is likely to stabilize *C2/c* dolomite with respect to decomposition.

## 6.5 Implications

The behavior of high-pressure carbonates influences the global carbon cycle and, subsequently, global climate over geologic time scales. The feedbacks inherent in the formation and destruction of carbonate and the role of carbonate in storage of the potent greenhouse gas  $\text{CO}_2$  are central to maintaining the habitability of our planet. It has been suggested that Ca-Mg-Fe carbonates play a leading role in transporting and storing carbon in the deep earth [Brenker *et al.*, 2007; Boulard *et al.*, 2012]. Although the present study of pure  $\text{CaMg}(\text{CO}_3)_2$  dolomite has identified new, more stable high pressure phases than those previously known, it has not yet changed our understanding of the ultimate stability of double carbonates relative to their decomposition products. However, when Fe is considered in future calculations, we may find that high-pressure polymorphs of iron-bearing dolomite could in fact represent the main reservoir for carbon storage within sections of the Earth's mantle. Combined with thermodynamic, geochemical and tectonic models, these results will help us understand the effect of the global carbon cycle on long-term climate change.

## Chapter 7

# *Ab initio* Study of Iron-bearing Carbonates\*

\* This chapter has been reformatted from what was submitted to *Physics and Chemistry of Minerals: Solomatova, N. V., and Asimow, P. D. (2017), First-principles calculations of high-pressure iron-bearing monoclinic dolomite and single-cation carbonates with internally consistent Hubbard U, Physics and Chemistry of Minerals.*

### 7.1 Introduction

Earth's global carbon cycle is influenced by the behavior of carbonates upon subduction into the mantle. In colder subducting slabs, carbonates resist decarbonation and penetrate into the lower mantle. It has been demonstrated that high-pressure Ca-Mg-Fe carbonates may play a leading role in transporting and storing carbon in the deep earth [Gillet, 1993; Isshiki *et al.*, 2004; Fiquet *et al.*, 2002; Santillán and Williams, 2004; Oganov *et al.*, 2006; Mao *et al.*, 2011; Nagai *et al.*, 2010; Boulard, 2011; Merlini *et al.*, 2012; Liu *et al.*, 2015]. The subduction of carbon into the lower mantle may explain the observation that Earth's surface contains a significantly lower abundance of carbon than would be expected based on cosmochemical analysis [Anders and Owen, 1977; Katsura *et al.*, 1991; Isshiki *et al.*, 2004; Hirschmann and Dasgupta, 2009]. The presence of carbon in the mantle is demonstrated by the existence of ultra-high-pressure marbles [Becker and Altherr, 1992; Kato *et al.*, 1997; Wang and Liou, 1993], carbonate minerals in mantle xenoliths [Eggler, 1987; Sobolev and Shatsky, 1990] and superdeep diamonds [Kaminsky *et al.*, 2001; Wirth *et al.*, 2007; Walter *et al.*, 2011]. Due to carbon's low solubility in mantle silicates [Shcheka *et al.*, 2006], significant carbon storage or transport in the mantle requires the formation of carbon-rich phases. The existence of oxidized forms of carbon-bearing phases in the mantle is evidenced by the discovery of carbonate inclusions in superdeep diamonds [Wang *et al.*, 1996; Brenker *et al.*, 2007].

Although high-pressure magnesite is considered the dominant lower-mantle carbonate phase [Isshiki *et al.*, 2004; Brenker *et al.*, 2006; Oganov *et al.*, 2008; Lavina *et al.*, 2009; Hsu *et al.*, 2016], it has been suggested that a high-pressure iron-bearing dolomite phase may be more stable than single-cation carbonates [Mao *et al.*, 2011; Merlini *et al.*, 2012]. X-ray diffraction experiments have shown that dolomite undergoes phase transitions to denser lower symmetry structures above about 15-20 GPa [Santillan *et al.*, 2003; Mao *et al.*, 2011; Merlini *et al.*, 2012; Zucchini *et al.*, 2014]. Using density

functional theory interfaced with a genetic algorithm that predicts crystal structures (USPEX), a monoclinic phase with space group  $C2/c$  was found to have lower energy at pressures above 15 GPa than all previously reported dolomite structures [Solomatova and Asimow, 2017]. Although calculations have shown that high-pressure iron-free dolomite polymorphs are expected to decompose into single-cation carbonates [Efthimiopoulos *et al.*, 2017; Solomatova and Asimow, 2017], the effect of iron has not been previously investigated with *ab initio* methods. Characterizing the effect of iron on the stability of monoclinic  $\text{Ca}(\text{Mg,Fe})(\text{CO}_3)_2$  is a necessary step towards understanding the transport and storage of carbonate phases in the mantle. Dolomite,  $\text{CaMg}(\text{CO}_3)_2$  and ankerite,  $\text{CaFe}(\text{CO}_3)_2$ , form a solid solution similar to magnesite,  $\text{MgCO}_3$  and siderite,  $\text{FeCO}_3$ . Hereafter,  $\text{CaMg}(\text{CO}_3)_2$  with 12.5% and 50% Fe substitution for Mg will be referred to as ferrodolomite, while  $\text{MgCO}_3$  with 12.5% and 50% Fe substitution for Mg will be referred to as ferromagnesite.

## 7.2 Computational Methods

*Ab initio* calculations were performed using the PWscf (Plane-Wave Self-Consistent Field) module of Quantum Espresso (QE) [Giannozzi *et al.*, 2009]. The projector-augmented wave (PAW) method [Blochl, 1994] was used to represent the core electrons with a core radius of 1.5 a.u. for Ca ( $1s^2 2s^2 2p^6$  core,  $3s^2 3p^6 4s^2$  valence), 1.0 a.u. for Mg ( $1s^2$  core,  $2s^2 2p^6 3s^2$  valence), 1.5 a.u. for Fe ( $1s^2 2s^2 2p^6$  core,  $3s^2 3p^6 3d^6 4s^2$  valence), 0.9 a.u. for C ( $1s^2$  core,  $2s^2 2p^2$  valence), and 1.1 a.u. for O ( $1s^2$  core,  $2s^2 2p^4$  valence). Electron exchange and correlation are treated with the generalized gradient approximation (GGA) in the Perdew-Burke-Ernzerhof (PBE) form [Perdew *et al.*, 1996]. The basis sets used in this study are part of the publicly-available PSLibrary 1.0.0. The advantage of GGA over the local density approximation (LDA) for this study is that GGA reproduces experimental phase transition pressures and chemical reactions better than LDA [Oganov *et al.*, 2013]. Additionally, GGA PAW potentials have excellent transferability and relatively fast electronic and geometric convergence. Energy cutoffs of 70 and 600 Ry were used for the plane-wave expansion of the wavefunctions and charge density, respectively. The Brillouin zone was sampled using a  $\sim 0.03 \text{ \AA}^{-1}$  k-point grid density according to the Monkhorst–Pack scheme [Monkhorst and Pack, 1976]. An electronic temperature, or smearing of the density of states, is required to achieve partial occupancies. Gaussian smearing was applied with a width of 0.01 Ry for all calculations. For detailed density of states calculations, a smaller smearing width and denser k-point resolution would be required to determine an accurate Fermi energy and more precise electronic structure. For the purposes of this study, a smearing width of 0.01 Ry is appropriate for the chosen k-point resolution and results in a smearing contribution to the

total energy of less than  $10^{-8}$  Ry. The total magnetization was not fixed or constrained in any of the calculations. Structures were fully relaxed at constant pressure with a convergence threshold for the electronic self-consistency and ionic minimization loops of  $10^{-7}$  and  $10^{-6}$  Ry/Bohr, respectively. No symmetry or magnetic constraints were applied, allowing the structures to relax to their true energetic minima. We ensured that forces acting on all atoms were less than  $10^{-3}$  Ry/Bohr. We relaxed iron-free dolomite (space group  $C2/c$ ), magnesite (space group  $R\bar{3}$ ), aragonite (space group  $Pm\bar{c}n$ ) and post-aragonite (space group  $Pm\bar{m}n$ ) to 80 GPa.

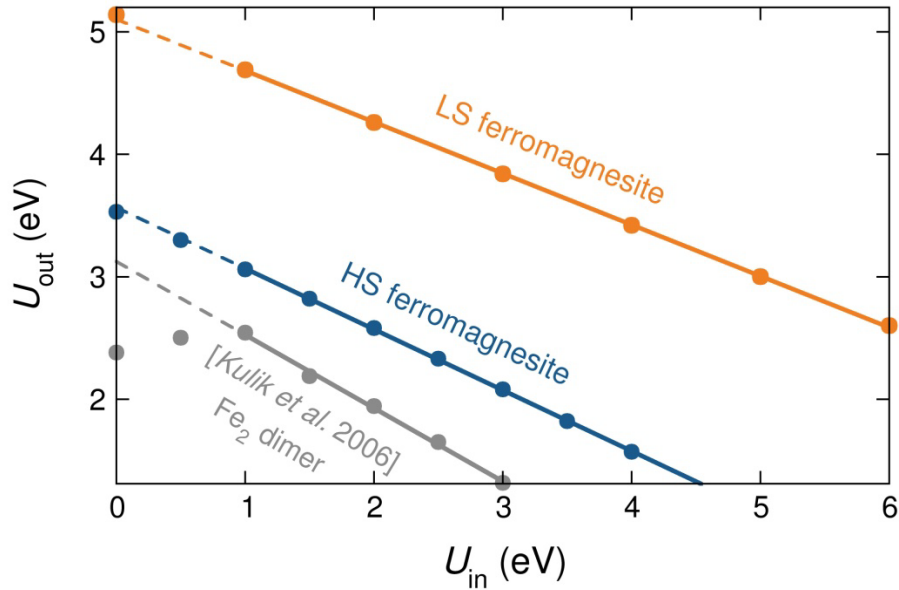


Figure 7.1:  $U_{in}$  plotted against  $U_{out}$ . For HS and LS ferromagnesite,  $(Mg_{0.875}Fe_{0.125})CO_3$ ,  $U_0$  ( $U$  calculated with  $U_{in}=0$ ) is nearly equivalent to  $U_{sc}$  ( $U$  determined from a linear extrapolation). For HS ferromagnesite,  $U_0=3.53$  while  $U_{sc}=3.57$  and for LS ferromagnesite,  $U_0=5.14$  and  $U_{sc}=5.12$ . Thus,  $U_0$  is a good approximation to  $U_{sc}$  for our system. In comparison,  $U_0$  for an  $Fe_2$  dimer is 2.4 while  $U_{sc}$  is 3.1 due to poor linearity at small values of  $U_{in}$  [Kulik *et al.*, 2006].

Dolomite,  $CaMg(CO_3)_2$ , and ankerite,  $CaFe(CO_3)_2$ , form a solid solution similar to magnesite,  $MgCO_3$ , and siderite,  $FeCO_3$ . Hereafter,  $CaMg(CO_3)_2$  with 12.5 and 50 mol%  $CaFe(CO_3)_2$  will be referred to as ferrodolomite, while  $MgCO_3$  with 12.5 and 50 mol%  $FeCO_3$  will be referred to as ferromagnesite. For iron-bearing phases, it is important to accurately describe the strongly correlated nature of iron's  $d$  electrons, which is poorly treated by LDA and GGA alone. It has been shown that DFT with a Hubbard  $U$  parameter, which characterizes the intra-atomic Coulomb repulsions, treats the correlation effects well with the proper selection of  $U$ , and accurately predicts ferromagnetic and antiferromagnetic insulators.  $U$  is an intrinsic response property that corrects for the fact that DFT without  $U$  calculates an unphysical smooth energy profile

as a function of occupations, whereas the addition of  $U$  creates a linear piecewise energy curve.  $U$  was calculated in Quantum Espresso from the non-interacting (bare) and interacting (self-consistent) response functions obtained by applying rigid potential shifts on the  $\text{Fe}^{2+}$  sites, according to the simplified rotationally invariant method of *Cococcioni and Gironcoli* [2005].

Based on this approach,  $U$  may be calculated in several ways. An internally consistent  $U$  ( $U_0$ ) may be calculated from the electronic GGA or LDA ground state according to the method described in *Cococcioni and Gironcoli* [2005]. For a self-consistent  $U$  ( $U_{sc}$ ), one needs to implement the method of *Kulik et al.* [2006], where an iterative approach is implemented to determine the linear dependence of  $U$  on  $U_{in}$  (the  $U$  applied in the linear response calculations) or the method described in *Hsu et al.* [2011], where  $U$  is calculated with an iteratively-determined  $U_{in}$  and a fixed Hubbard potential during the perturbed calculations.  $U_0$  only requires one linear response calculation per volume, while  $U_{sc}$  either requires four to six calculations until linearity around  $U_{in}=U_{sc}$  is established or three to five iterations until convergence of  $U_{sc}$  to the desired precision is achieved. For some phases, such as an  $\text{Fe}_2$  dimer,  $U_{in}$  vs.  $U_{out}$  does not demonstrate a linear behavior close to  $U_0$ , resulting in a significant discrepancy between  $U_0$  and  $U_{sc}$ . In this study, however,  $U_0 \approx U_{sc}$  (Figure 7.1) and so, for computational efficiency, we calculate  $U_0$  instead of  $U_{sc}$ .

For  $U$  calculations, the convergence threshold for self-consistency and iterative diagonalization were set to  $10^{-10}$  and  $10^{-12}$  Ry for energy and eigenvalue convergence, respectively.  $U$  was calculated for structures that were fully relaxed with an initial  $U$  value, and iteratively relaxed with newly calculated  $U$  values until convergence of  $U$  was achieved (one to two iterations).  $U$  was calculated for the ferromagnetic high-spin (HS) and low-spin (LS) states of 40-atom  $(\text{Mg,Fe})\text{CO}_3$  and 80-atom monoclinic  $\text{Ca}(\text{Mg,Fe})(\text{CO}_3)_2$  with 12.5% Fe substitution for Mg.  $U$  was calculated in 20 GPa steps between 0 and 120 GPa, after which a smooth polynomial was fitted to extrapolate to finer pressure steps of 10 GPa. For higher iron concentrations, we use the  $U$  calculated for 12.5% Fe substitution, similar to the procedure of *Hsu et al.* [2011]. For 12.5% and 50% Fe substitution in  $(\text{Mg,Fe})\text{CO}_3$  and  $\text{Ca}(\text{Mg,Fe})(\text{CO}_3)_2$ , the ferromagnetic (FM) spin state is preferred, whereas for the iron endmembers  $\text{CaFe}(\text{CO}_3)_2$  and  $\text{FeCO}_3$ , the anti-ferromagnetic (AFM) spin state is marginally preferred, in agreement with magnetic susceptibility and neutron diffraction experiments on siderite [*Bizette*, 1951; *Jacobs*, 1963]. Hereafter, we refer to FM and AFM simply as high-spin (HS). At about 80 GPa,  $(\text{Mg,Fe})\text{CO}_3$  undergoes a phase transition; however, there is disagreement in the literature about the phase transition pressure and high-pressure structure [*Isshiki et al.*, 2004; *Oganov et al.*, 2008; *Boulard et al.*, 2012; *Boulard et al.*, 2015; *Liu et al.*, 2015], which

may be dependent on iron concentration. Thus, we do not consider high-pressure polymorphs of  $(\text{Mg,Fe})\text{CO}_3$ .

The calculated Hubbard  $U$  values for rhombohedral ferromagnesite and monoclinic ferrodolomite  $C2/c$  are almost identical at low pressures while, at 120 GPa, ferrodolomite  $C2/c$  has a larger  $U$  by about 0.4 and 0.2 eV for the HS and LS states, respectively (Figure 7.2). In ferromagnesite,  $U$  increases from 3.53 to 4.93 eV and 5.14 to 6.44 eV for the HS and LS states, respectively, while in ferrodolomite,  $U$  increases from 3.58 to 4.51 eV and 5.17 to 6.26 eV for the HS and LS states, respectively.  $U$  is negatively correlated with the unit-cell volume (increasing with decreasing volume), and so is sensitive to the plane-wave energy cutoff, which is positively correlated with the unit-cell volume. Although  $U$  increases with increasing pressure, the correlation strength most likely decreases. The correlation strength is characterized by  $U/\Delta$ , where  $\Delta$  is the  $d$  electron bandwidth and ratios much greater than unity correspond to strong correlations. The bandwidth generally increases more steeply than  $U$  with increasing pressure; thus,  $U$  can have a positive trend with increasing pressure despite a decreasing correlation strength.

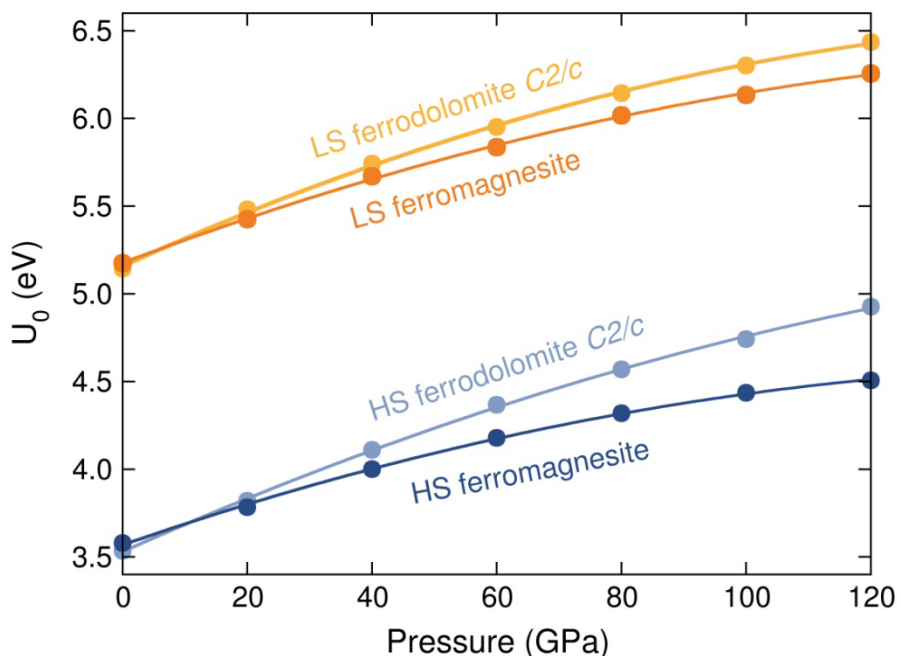


Figure 7.2: Calculated Hubbard  $U$  as a function of pressure for high-spin and low-spin  $\text{Fe}^{2+}$  in ferrodolomite  $C2/c$  and ferromagnesite with 12.5% substitution of Fe for Mg.

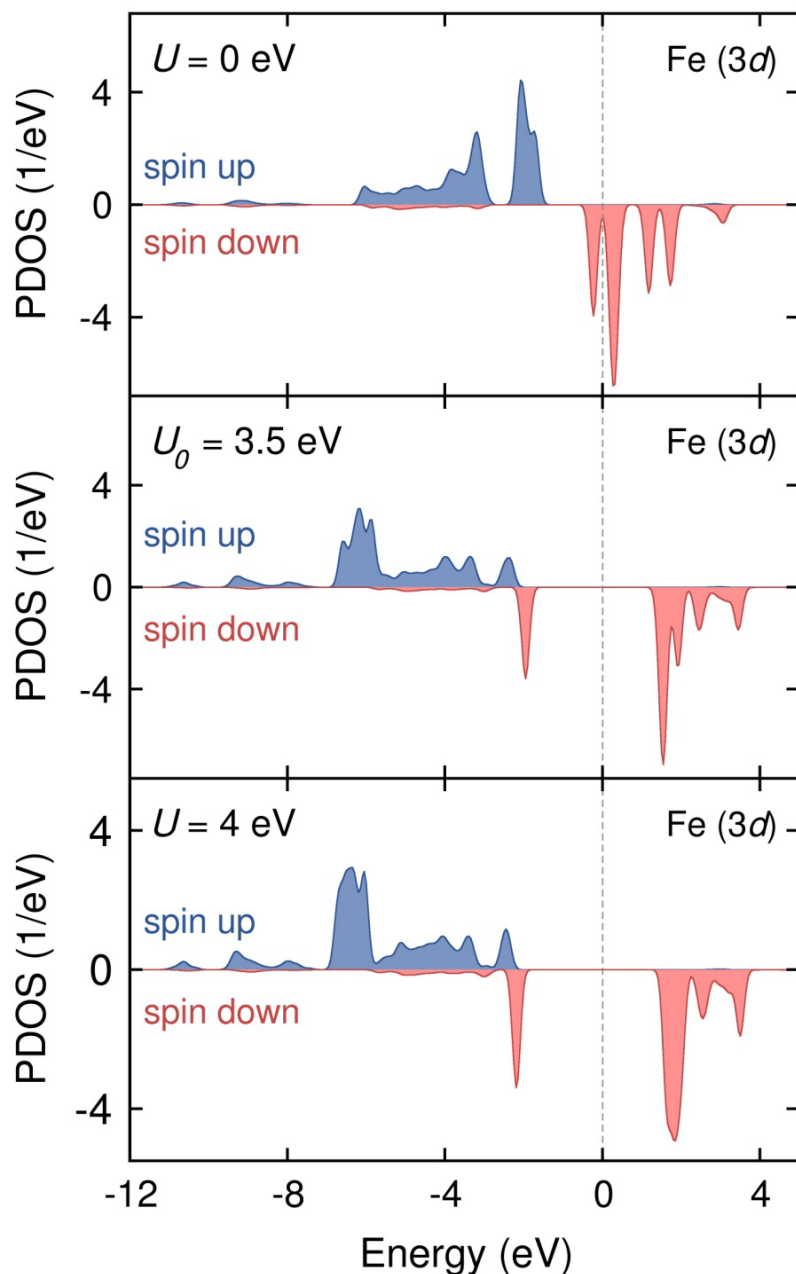


Figure 7.3: Partial density of states for iron's 3d electrons in high-spin  $(\text{Mg}_{0.875}\text{Fe}_{0.125})\text{CO}_3$  at 0 GPa. With  $U = 0$ , there is no band gap at the Fermi level, whereas with an internally consistent  $U$  ( $U_0 = 3.5$  eV) and with  $U = 4$  eV, there are  $\sim 2.7$  and 3 eV band gaps, respectively.

To compare the results of our calculations with an internally consistent  $U$  to those of a constant value of  $U$ , we also relax all iron-bearing phases with a constant  $U$  of 4 eV, a value commonly chosen in the literature [e.g., *Panchmati et al.*, 2008; *Shi et al.*, 2008; *Hsu et al.*, 2011; *Hsu et al.*, 2016]. The effect of  $U$  on the partial density of states of iron's 3d electrons is shown in Figure 7.3. Without  $U$ , GGA predicts  $(\text{Mg}_{0.875}\text{Fe}_{0.125})\text{CO}_3$  to be in the metallic ground state, evidenced by the occupied electronic orbitals at the

Fermi level; however, GGA with an internally consistent  $U$  or a fixed  $U$  of 4 eV predicts a Mott insulating ground state, evidenced by a 2.7-3 eV band gap at the Fermi level.

## 7.3 Results

### 7.3.1 Spin Transition

Iron-bearing phases undergo a high-spin (HS) to low-spin (LS) transition at high pressures due to the decreasing volume of iron's local site geometry, resulting in an increase in the crystal-field splitting energy. When the crystal-field splitting energy becomes larger than the spin-pairing energy, the electrons pair up to fully occupy the  $t_{2g}$  orbitals. Raman, X-ray emission, and X-ray diffraction studies have observed a HS to LS transition in  $(\text{Mg,Fe})\text{CO}_3$  at 42-56 GPa [Mattila *et al.*, 2007; Lavina *et al.*, 2010; Lin *et al.*, 2012; Liu *et al.*, 2015]. In this study, GGA PAW with a constant  $U$  of 4 eV for both spin states results in a spin transition pressure of 52-56 GPa for  $(\text{Mg,Fe})\text{CO}_3$  with 12.5-100 mol%  $\text{FeCO}_3$ , agreeing with the upper bound of the experimental results. The spin transition in  $\text{Ca}(\text{Mg,Fe})\text{CO}_3$  occurs at 65-68 GPa, higher than in  $(\text{Mg,Fe})\text{CO}_3$ . Using an internally consistent  $U$  shifts the spin transition in both phases to higher pressures:  $\sim 100$  GPa in  $(\text{Mg,Fe})\text{CO}_3$  and  $>140$  GPa in  $\text{Ca}(\text{Mg,Fe})\text{CO}_3$  (Figure 7.4).

The spin transition pressure is strongly affected by the choice of functional (e.g., local density approximation or generalized gradient approximation), the method of representing core electrons (e.g., projector-augmented wave method, norm-conserving pseudopotentials or ultrasoft pseudopotentials) and the method of determining  $U$  (e.g., arbitrarily selected, empirically derived or calculated with internally consistent methods).  $U$  increases the enthalpy of a given phase, such that the spin transition pressure is positively correlated with the difference in  $U$  between the HS and LS states ( $\Delta U_{\text{LS-HS}}$ ), as well as with the absolute value of  $U$ .

Previous computational studies on  $\text{FeCO}_3$  calculate a spin transition pressure ranging from 15 to 50 GPa, depending on the choice of basis set and Hubbard  $U$  parameter. Shi *et al.* [2008] used the PAW potentials with the GGA functional of PW91 type [Burke *et al.*, 1998] using the VASP software [Kresse and Furthmüller, 1996; Kresse and Joubert, 1999]. They sampled  $U$  values of 0, 4, 5 and 6 eV, which were fixed as a function of pressure and set to be equivalent for AFM and LS siderite, resulting in a spin transition at 15 and 28 GPa with  $U$  of 0 and 5 eV, respectively. Badaut *et al.* [2010] used ultrasoft (US) pseudopotentials with the GGA functional of PBE type using the CASTEP software [Segall *et al.*, 2002] without a Hubbard  $U$  parameter, resulting in a FM to LS transition in siderite at about 20 GPa. Ming *et al.* [2012] used the same basis set and software as Badaut *et al.* [2010], also without  $U$ , and found an AFM to LS transition at 40-50 GPa. Hsu *et al.* [2016] used the PAW potentials with the LDA functional using

the QE software. They calculated a spin transition pressure of 22 GPa with a constant  $U$  of 4 eV for both the AFM and LS states, and a spin transition pressure of 47 GPa with a self-consistent  $U$  of 4 and 5.3 eV for the AFM and LS states, respectively. The self-consistent  $U$  was determined from a linear interpolation between values calculated at 0 and 100 GPa.

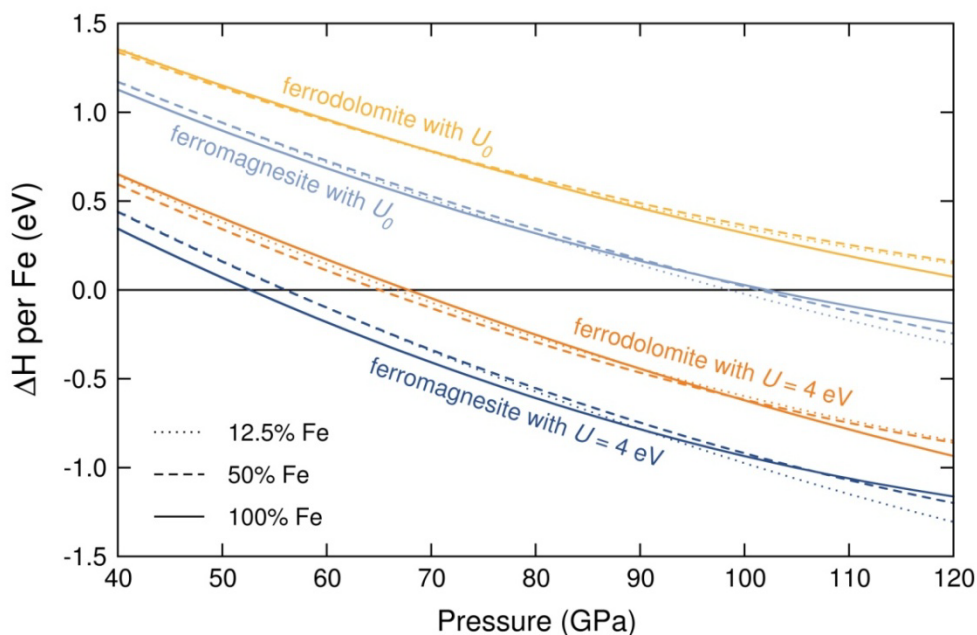


Figure 7.4: Spin transition pressures in  $(\text{Mg,Fe})\text{CO}_3$  and  $(\text{Mg,Fe})\text{Ca}(\text{CO}_3)_2$ . 12.5%, 50% and 100% Fe substitution for Mg are indicated by dotted, dashed and solid lines, respectively.  $(\text{Mg,Fe})\text{CO}_3$  with a constant  $U$  of 4 eV and with an internally consistent  $U$  are dark blue and light blue, respectively.  $(\text{Mg,Fe})\text{Ca}(\text{CO}_3)_2$  with a constant  $U$  of 4 eV and with an internally consistent  $U$  are dark orange and yellow, respectively.

Although often considered identical, GGA functionals of the PW91 and PBE type sometimes produce different results [Mattsson *et al.*, 2006] and this may explain the discrepancies observed in the calculated spin transition pressures. The strong dependence of the spin transition pressure in ferrous iron on the basis set and Hubbard  $U$  parameter has been observed in other phases as well. In  $(\text{Mg}_{0.9375}\text{Fe}_{0.0625})\text{SiO}_3$ , ferrous iron undergoes a spin transition at 95 GPa with the LDA approximation and 195 GPa with the GGA approximation of the PBE form [Bengtson *et al.*, 2008]. Persson *et al.* [2006] calculate that  $(\text{Mg}_{0.75}\text{Fe}_{0.25})\text{O}$  undergoes a spin transition at 69 GPa with  $U=3$  eV and at 106 GPa with  $U=5$  eV, both with the GGA approximation of the PBE form and PAW potentials. Our choice of the GGA approximation is justified in Computational Methods, and our use of an internally consistent  $U$  and a constant  $U$  of 4 eV allows for a comparison of the relative stability of iron-bearing carbonate phases with both choices of  $U$ .

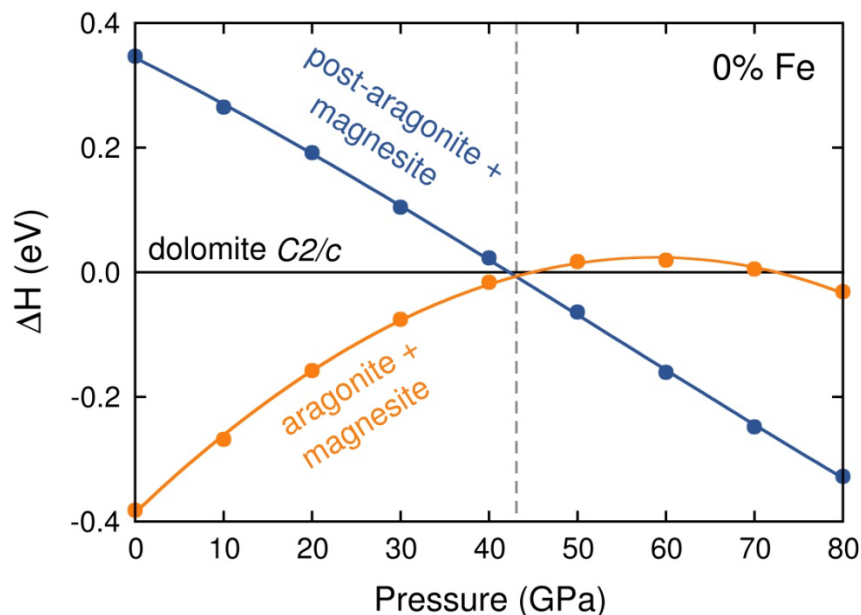


Figure 7.5: Enthalpy difference between dolomite  $C2/c$  and single-cation carbonate assemblages: aragonite + magnesite (orange) and post-aragonite + magnesite (blue). Iron-free dolomite  $C2/c$  has a higher enthalpy than single-cation carbonates at all pressures, although it is nearly competitive close to 42 GPa. Energy units are per formula unit of the species in the decomposition reaction,  $\text{CaMg}(\text{CO}_3)_2 \rightarrow \text{CaCO}_3 + \text{MgCO}_3$ .

### 7.3.2 Monoclinic Dolomite

Iron-free dolomite  $C2/c$  has a larger enthalpy than single-cation carbonate phases at all relevant pressures (Figure 7.5). The rapid decrease of the enthalpy of high-density post-aragonite beyond 43 GPa is the main driver of the predicted breakdown of iron-free dolomite  $C2/c$ . Our prediction of the phase transition of aragonite (space group  $Pm\bar{c}n$ ) to post-aragonite (space group  $Pmmn$ ) is in excellent agreement with the experimentally-observed phase transition pressure of 35-40 GPa [Santillán and Williams, 2004; Ono *et al.*, 2005] and with the previously calculated phase transition pressure of 42 GPa [Oganov *et al.*, 2006; Solomatova and Asimow, 2017]. Thus, in an iron-free system, aragonite + magnesite is preferred up to 43 GPa, at which point, post-aragonite + magnesite become the preferred assemblage. However, the addition of iron to the system lowers the enthalpy of dolomite  $C2/c$  with respect to decomposition products.

We consider the decomposition of monoclinic ferrodolomite into two or three phases: (post-)aragonite + ferromagnesite and (post-)aragonite + magnesite + siderite (Figure 7.6). Although an internally consistent  $U$  overestimates the spin transition pressures, it is possible that the phase transition pressures are more accurate with an internally consistent  $U$ . Thus, we compare the enthalpy differences resulting from the use of an internally consistent  $U$  to a constant  $U$  of 4 eV. With a constant  $U$  of 4 eV, dolomite

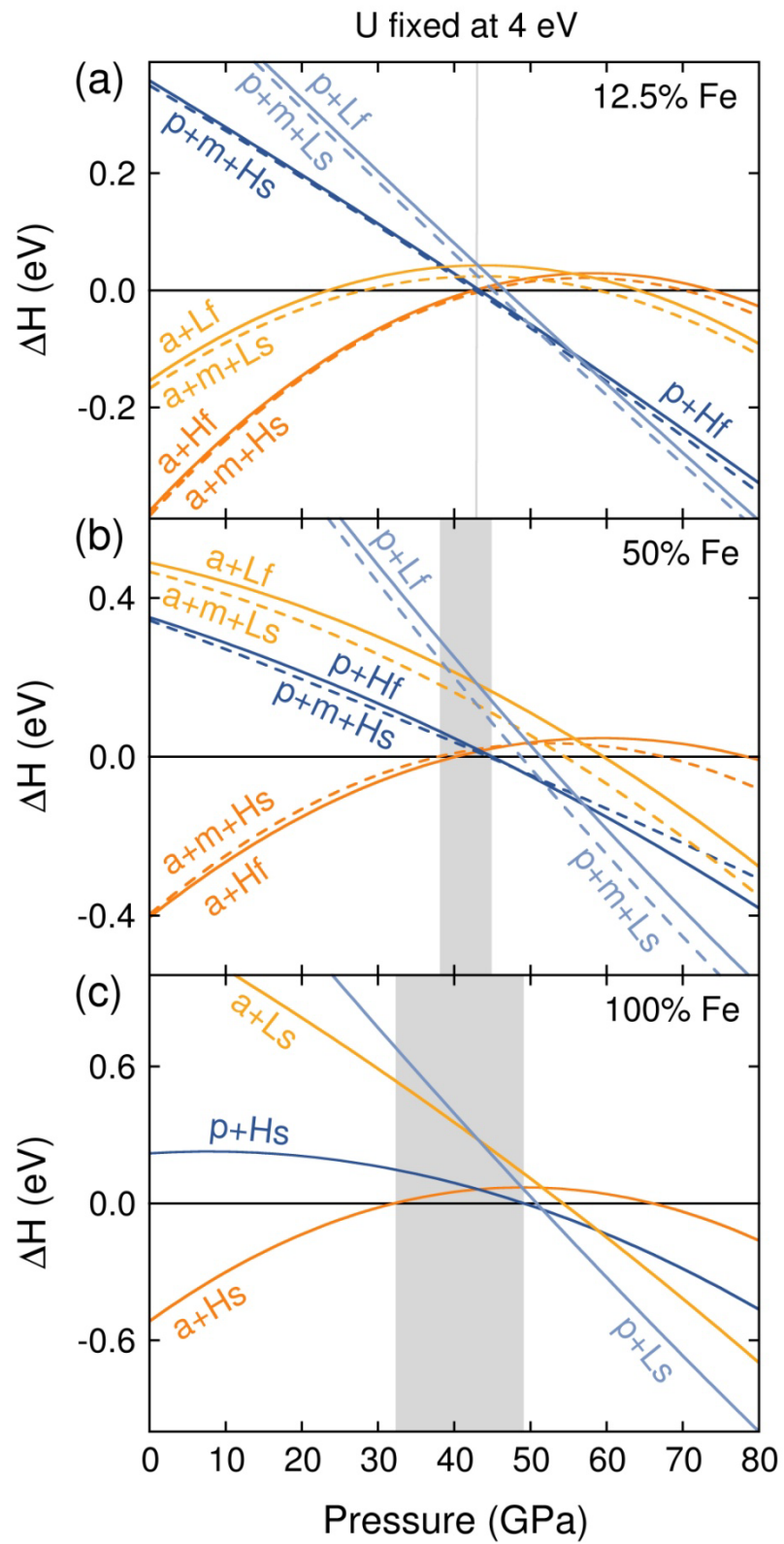
$C2/c$  is not preferred over single cation carbonates with 12.5% Fe substitution at any pressure, and is preferred over single cation carbonates at about 38-45 and 33-49 GPa for 50 and 100% Fe substitution, respectively. With an internally consistent  $U$ , ferrodolomite  $C2/c$  is preferred over single-cation carbonates at about 41-44, 35-48, and 31-53 GPa for 12.5, 50 and 100% Fe substitution. With either choice of  $U$ , a higher iron concentration decreases the enthalpy of dolomite  $C2/c$  with respect to decomposition products, effectively increasing its stability field.

## 7.4 Discussion

### 7.4.1 Spin Transition

We find that the spin transition pressure is insensitive to the iron concentration for both rhombohedral  $(\text{Mg,Fe})\text{CO}_3$  and monoclinic  $(\text{Mg,Fe})\text{Ca}(\text{CO}_3)_2$ . In  $(\text{Mg,Fe})\text{O}$ , on the other hand, experiments have demonstrated that the spin transition pressure is sensitive to the iron concentration, increasing from about 50 to 80 GPa between 10 and 60 mol% FeO [e.g., *Lin et al.*, 2005; *Speziale et al.*, 2005; *Solomatova et al.*, 2016]. This trend has been confirmed by *ab initio* calculations [*Persson et al.*, 2006]. One explanation for this trend is the effect of magnesium concentration on the  $\text{FeO}_6$  octahedra [*Speziale et al.*, 2005; *Persson et al.*, 2006]. It is thought that the relatively smaller size of the magnesium cations results in an increase in the local stress on the high-spin iron atoms, which increases the crystal field splitting energy. Consequently, a higher magnesium concentration (lower iron concentration) results in a notably lower spin transition pressure in the oxide series. Another possibility, not mutually exclusive with the first scenario, is the effect of iron-iron interactions. When the iron concentration increases, iron atoms become closer to each other, and the  $3d$  electrons of the  $d_{x^2-y^2}$  and  $d_{z^2}$  orbitals of one iron atom may begin to interact with the  $3d$  electrons of the  $d_{xy}$ ,  $d_{xz}$  and  $d_{zy}$  orbitals of a neighboring iron atom, resulting in the lowering of the  $t_{2g}$  orbitals with respect to the  $e_{2g}$  orbitals. This leads to an increase in the crystal field splitting energy, and thus, an increase in the spin transition pressure.

It has been proposed that the spin transition pressure in  $(\text{Mg,Fe})\text{CO}_3$ , by contrast, is insensitive to iron concentration due to the greater distance between  $\text{FeO}_6$  octahedra in this phase; the octahedra are isolated in ferromagnesite and corner-sharing in siderite, compared to the face-sharing octahedra in ferroperricline. The greater distance would presumably decrease the effect of iron-iron interactions [*Lin et al.* 2012; *Hsu et al.* 2016]. However, in monoclinic  $\text{CaFe}(\text{CO}_3)_2$ , the  $\text{FeO}_6$  octahedra share edges along the  $c$ -axis, and presumably iron-iron interactions should shift the spin transition to higher pressures with respect to  $(\text{Mg,Fe})\text{Ca}(\text{CO}_3)_2$ , an effect we do not observe. Thus, an alternative or modified explanation is required.



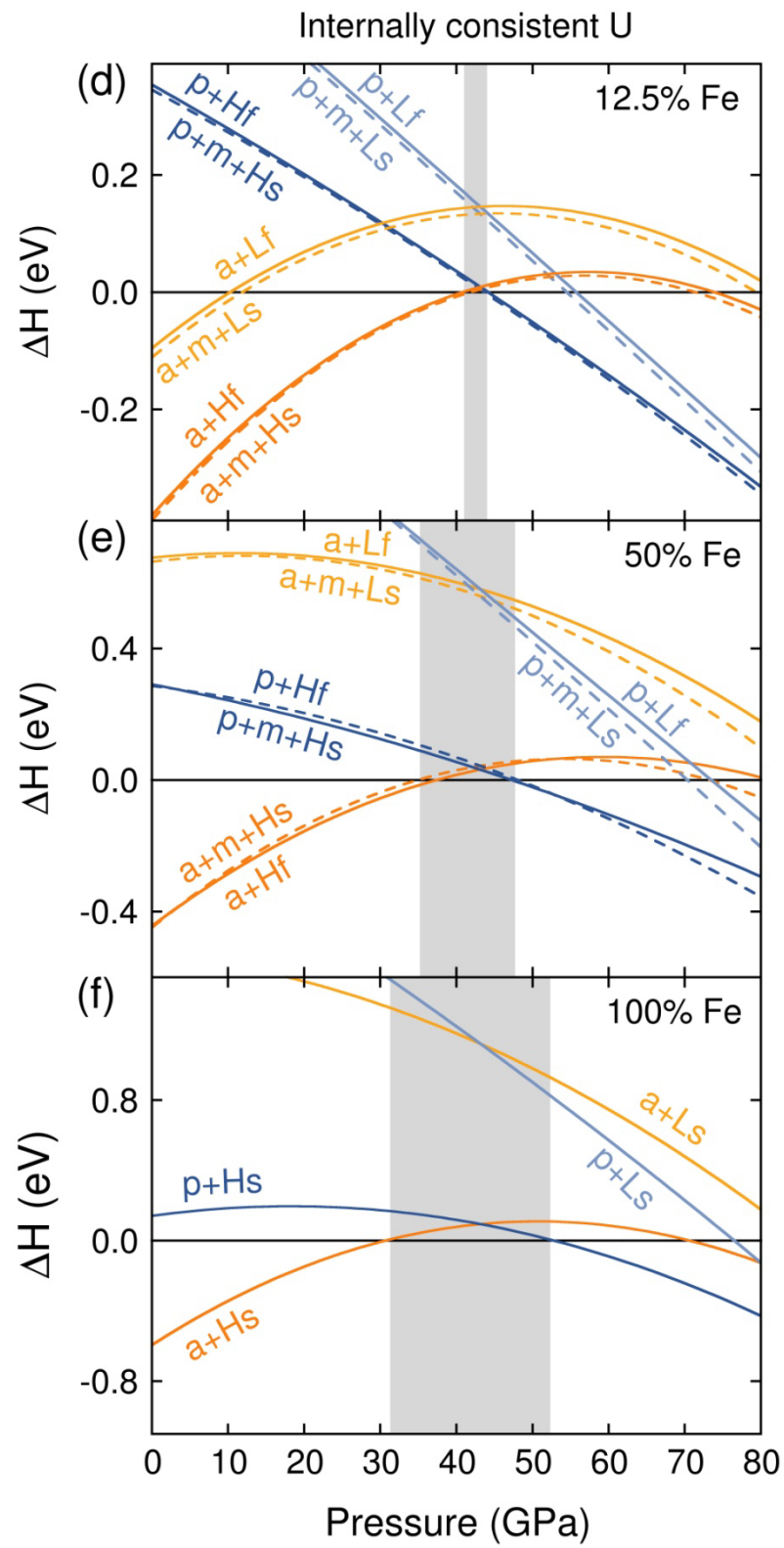


Figure 7.6: Enthalpy differences with respect to high-spin  $(\text{Mg,Fe})\text{Ca}(\text{CO}_3)_2$  with the  $C2/c$  space group with varying concentrations of iron, calculated using a fixed  $U$  of 4 eV in (a) to (c) and an internally consistent  $U$  in (d) to (e). In (a) and (d), 12.5% of the Mg sites are replaced with Fe; in (b) and (e), 50% of the Mg sites are replaced with Fe; and in (c) and (f), 100% of the Mg sites are replaced with Fe. Two-phase assemblages are indicated by solid lines and three-phase assemblages are indicated by dashed lines. Enthalpy difference between HS and LS  $(\text{Mg,Fe})\text{Ca}(\text{CO}_3)_2$  is not shown for clarity (see Figure 7.4 for spin transition pressures). The phases are abbreviated as follows: aragonite – a, post-aragonite – p, magnesite – m, HS ferromagnesite – Hf, LS ferromagnesite – Lf, HS siderite – Hs, and LS siderite – Ls. Grey regions indicate pressure ranges where high-spin  $(\text{Mg,Fe})\text{Ca}(\text{CO}_3)_2$  has a lower enthalpy than decomposition products.

In  $(\text{Mg,Fe})\text{SiO}_3$  perovskite, theory predicts a compositional dependence opposite to that observed in  $(\text{Mg,Fe})\text{O}$ : that the spin transition pressure of ferrous iron *decreases* with increasing iron concentration [*Bengtson et al.*, 2008; *Umemoto et al.*, 2008]. The interpretation has been that larger site distortions are allowed in the perovskite structure compared to the  $B1$  structure of ferroperricline, demonstrated by the remarkable difference in the spin transition pressure between a fully relaxed  $\text{FeSiO}_3$  perovskite (77 GPa) and a perfectly cubic  $\text{FeSiO}_3$  perovskite (900 GPa) [*Bengtson et al.*, 2008]. In this context, we note that the  $\text{FeO}_6$  octahedra in the carbonates are *less* distorted than in  $\text{FeSiO}_3$  perovskite and, at the same time, *more* distorted than in  $(\text{Mg,Fe})\text{O}$ . It may be that chemical pressure on iron induced by magnesium is negligible in carbonates due to the ability to distort the iron site to accommodate the stresses. On the other hand, the octahedra are not able to distort to the extent possible in the perovskite structure, and so the effect of site distortion with increasing iron concentration is not observed. Thus, the crystal field splitting energy remains essentially unchanged, resulting in an insensitivity of the carbonate spin transition pressure to the iron concentration.

#### 7.4.2 Monoclinic Dolomite

We find that monoclinic ferrodolomite with space group  $C2/c$  is preferred over single-cation carbonates at a maximum pressure width of about 32-52 GPa, which corresponds to an approximate depth of 850-1300 km within Earth's lower mantle. Although the spin transition is overestimated with an internally consistent  $U$ , the relative enthalpies may be more accurate. Experiments have annealed high-pressure polymorphs of dolomite (referred to as “dolomite III”) and did not observe decomposition into single-cation carbonates. *Mao et al.* [2011] annealed dolomite III with 8 mol%  $\text{FeCa}(\text{CO}_3)_2$  at 36 to 83 GPa at 1500 K and found that it did not decompose into single-cation carbonates. Similarly, *Merlini et al.* [2012] annealed dolomite III with 40 mol%  $\text{FeCa}(\text{CO}_3)_2$  at 46, 55 and 72 GPa at 2100-2200 K and also did not observe decomposition. The dolomite III structure observed in *Merlini et al.* [2012] is not the

same structure as dolomite  $C2/c$ , but it has a higher enthalpy (less stable) at all pressures than dolomite  $C2/c$  [Solomatova and Asimow, 2017] and therefore the stability field of dolomite  $C2/c$  should be even larger than that for dolomite III. Thus, the experimental results suggest that our calculations underestimate the stability field of iron-bearing dolomite  $C2/c$ .

Given that the stability field of endmember rhombohedral dolomite increases with increasing temperature at constant pressure [Martinez *et al.*, 1996; Buob *et al.*, 2006], it may be that a similar trend is true for high-pressure iron-bearing dolomite polymorphs. Although the effect of cation ordering and temperature on the behavior of iron-free rhombohedral dolomite I and triclinic dolomite II has been investigated up to about 30 GPa [Hammouda *et al.*, 2011; Zucchini *et al.*, 2017], additional experiments and calculations are needed on iron-bearing dolomite polymorphs at high temperatures and pressures.

So far, we have only discussed the stability of various carbonates with respect to one another. However, other decomposition routes are possible, for example to oxides or silicates and diamond or  $\text{CO}_2$ . Dorogokupets *et al.* [2007] calculated that  $\text{MgCO}_3$  will not decompose into  $\text{MgO} + \text{CO}_2$  up to at least 130 GPa and 3000 K based on the extrapolation of thermodynamic functions of  $\text{MgCO}_3$ ,  $\text{MgO}$  and  $\text{CO}_2$ . Likewise, Oganov *et al.* [2008] calculated that high-pressure polymorphs of  $\text{MgCO}_3$  and  $\text{CaCO}_3$  are energetically favorable over oxides and will not react with  $\text{SiO}_2$  to produce  $\text{CO}_2$  up to core-mantle-boundary pressures. In reduced regions of the mantle, Oganov *et al.* [2008] calculated that  $\text{MgCO}_3$  should decompose only above 50 GPa. Given that  $(\text{Mg,Fe})\text{CO}_3$  and  $\text{CaCO}_3$  are energetically favorable with respect to oxides [Dorogokupets *et al.*, 2007; Oganov *et al.*, 2008; Lin *et al.*, 2014], monoclinic  $(\text{Mg,Fe})\text{Ca}(\text{CO}_3)_2$  is expected to be stable with respect to simple oxides in at least the same pressure range for which it is energetically favorable over  $(\text{Mg,Fe})\text{CO}_3$  and  $\text{CaCO}_3$ .

## 7.5 Concluding Remarks

Iron substitution for magnesium in monoclinic dolomite with the  $C2/c$  space group is likely to stabilize this phase with respect to decomposition at certain depths within Earth's lower mantle. Although  $(\text{Mg,Fe})\text{CO}_3 + \text{CaCO}_3$  are expected to be favorable with respect to  $(\text{Mg,Fe})\text{Ca}(\text{CO}_3)_2$  at both lower and higher pressures, our results confirm the experimental observations that an iron-bearing polymorph of dolomite may resist decomposition at certain pressures and is certainly a viable competitor to single-cation carbonate phases. Thus, our study demonstrates that a high-pressure polymorph of iron-bearing dolomite could represent an important carrier of carbon within sections of the deep earth, and should be considered in future thermodynamic studies. We emphasize

that reaching this conclusion with confidence required careful evaluation of many computational details, including the choice of functional and basis set and method of computing the Hubbard  $U$  potential. Much of the conflict among published results about spin transition pressures in high-pressure iron-bearing phases is attributable to different choices about these computational details, often without justification or exploration. Although our computational results, other computational results and experiments show divergent behaviors in the compositional dependence of the high-spin to low-spin transition of octahedral  $\text{Fe}^{2+}$  in different phases, we propose a common explanation that can explain the compositional dependence of spin transition behaviors in perovskite, carbonate and oxide phases.

## Chapter 8

# Conclusions

Iron has an effect on the physical properties of periclase, silicate glasses and carbonates. In this thesis, I have demonstrated that the concentration of iron affects the spin transition pressure of oxides, does not affect the spin transition pressure of carbonates and likely does not occur in silicate glasses up to core-mantle boundary pressures.

The spin crossover behavior of (Mg,Fe)O with 48 mol% FeO was examined using X-ray diffraction and time-domain Mössbauer spectroscopy. Previous experimental and theoretical research has demonstrated a large scatter in spin transition pressures. For example, a spin transition was observed in (Mg<sub>0.8</sub>Fe<sub>0.2</sub>)O between 35-45 GPa with X-ray diffraction [*Fei et al.*, 2007] and 55-105 GPa with energy-domain Mössbauer spectroscopy [*Kantor et al.*, 2006], whereas using density functional theory, *Tsuchiya et al.* [2006] and *Holmström and Stixrude* [2015] predict a spin transition of 36 and 65 GPa with a spin transition width of 4 and 50 GPa for (Mg<sub>0.8125</sub>Fe<sub>0.1875</sub>)O and (Mg<sub>0.75</sub>Fe<sub>0.25</sub>)O at 300 K using ideal and non-ideal solid solutions of the two spin states, respectively. In my experiments, the X-ray diffraction results agree excellently with the time-domain Mössbauer spectroscopy results collected on (Mg,Fe)O with 48 mol% FeO, yielding a spin transition pressure of about 69 GPa with a width of 18 GPa. After systematically fitting a spin-crossover equation of state to the pressure-volume data from previous experiments on (Mg,Fe)O with 10 to 60 mol% FeO, I observed a trend in the spin-crossover behavior in (Mg,Fe)O as a function of iron concentration: the spin transition pressure increases from about 50 to 80 GPa and the width of the spin transition increases from 2 to 25 GPa for (Mg,Fe)O, in disagreement with previous density functional theory calculations. Thus, additional calculations are needed to better model the experiments, as determined in this thesis. Iron concentration plays an important role in stabilizing ultra-low velocity zones at the core-mantle boundary and an improved understanding of the effect of iron concentration on the spin-crossover behavior of (Mg,Fe)O presented in this thesis will help constrain the range of plausible compositions of ultra-low velocity zones.

In my research on double-cation carbonates, I used an evolutionary algorithm to predict the existence of a monoclinic dolomite phase with the *C2/c* space group, which is preferred over previously reported dolomite structures and single-cation carbonate structures with a dolomite stoichiometry. I found that the substitution of iron for

magnesium stabilizes monoclinic ferrodolomite,  $\text{Ca}(\text{Mg,Fe})(\text{CO}_3)_2$ , with respect to decomposition in the pressure range of about 32-52 GPa, demonstrating that a high-pressure polymorph of ferrodolomite could represent an important carrier of carbon at a depth of approximately 850-1300 km within Earth's lower mantle. Unlike in  $(\text{Mg,Fe})\text{O}$ , I found that the spin transition pressure in  $(\text{Mg,Fe})\text{CO}_3$  and  $\text{Ca}(\text{Mg,Fe})(\text{CO}_3)_2$  is weakly dependent on the iron concentration, possibly due to the ability of the iron octahedra to distort with pressure more than in  $(\text{Mg,Fe})\text{O}$  to accommodate the stresses caused by the coexistence of magnesium and iron atoms. Nonetheless, the amount of iron in both  $(\text{Mg,Fe})\text{O}$  and  $\text{Ca}(\text{Mg,Fe})(\text{CO}_3)_2$  dictates the dynamic and thermodynamic stabilities of those phases within Earth's lower mantle.

In iron-bearing rhyolitic and basaltic glasses, I found that ferrous iron will likely remain in the high-spin state throughout the entirety of Earth's lower mantle. Unlike in the crystalline phases I have studied, the iron atoms occupy a distribution of coordination geometries, increasing in coordination number with increasing pressure. The low-density structure of silicate glasses at low pressure undergoes rapid densification with increasing pressure, a phenomenon not observed in crystalline phases. I find that the total concentration of ferrous iron in silicate glasses has a significant effect on the coordination environment of the low-coordinated iron sites above a certain threshold of iron concentration, likely related to iron-iron interactions. The local environments of all ferrous iron sites are affected by the type of cations present in the glasses. In this thesis, I compared the quadrupole splitting of iron in silicate glasses from previous experiments using similar fitting methods. I observed a negative relationship between quadrupole splitting and the concentration of  $\text{Na}_2\text{O}$  and  $\text{K}_2\text{O}$  with respect to  $\text{FeO}$  at ambient pressure, whereas at high pressure this relationship turns into a positive trend of quadrupole splitting for the majority site and a negative trend for the minority site. Thus, I have demonstrated that the change in iron's coordination environments with pressure depends on the composition of the glasses.

# Bibliography

- Alberto, H. V., da Cunha, J. P., Mysen, B. O., Gil, J. M., and de Campos, N. A. (1996), Analysis of Mössbauer spectra of silicate glasses using a two-dimensional Gaussian distribution of hyperfine parameters, *Journal of Non-Crystalline Solids*, 194(1), 48-57, doi:10.1016/0022-3093(95)00463-7.
- Alp, E. E., and Mini, S. M. (1994), Chemical doping and charge balance in high temperature superconductors, *Physical and Material Properties of High Temperature Superconductors*, 4, 181.
- Anders, E., and Owen, T. (1977), Mars and Earth: Origin and abundance of volatiles, *Science*, 198(4316), 453-465, doi:10.1126/science.198.4316.453.
- Andersen, O. K. (1975), Linear methods in band theory, *Physical Review B*, 12(8), doi:3060.10.1103/PhysRevB.12.3060
- Antonangeli, D., Siebert, J., Aracne, C. M., Farber, D. F., Bosak, A., Hoesch, M., Krisch, M., Ryerson, F. J., Fiquet, G., and Badro, J. (2011), Spin crossover in ferropericlase at high pressure: A seismologically transparent transition? *Science*, 331, 64-67, doi: 10.1126/science.1198429.
- Antončík, E. (1959), Approximate formulation of the orthogonalized plane-wave method, *Journal of Physics and Chemistry of Solids*, 10(4), 314-320, doi: /10.1016/0022-3697 (59)90007-1.
- Auzende, A. L., Badro, J., Ryerson, F. J., Weber, P. K., Fallon, S. J., Addad, A., Siebert, J., and Fiquet, G. (2008), Element partitioning between magnesium silicate perovskite and ferropericlase: New insights into bulk lower-mantle geochemistry, *Earth and Planetary Science Letters*, 269, 164–174, doi: 10.1016/j.epsl.2008.02.001.
- Badro, J., Fiquet, G., Guyot, F., Rueff, J. P., Struzhkin, V. V., Vanko, G., and Monaco, G. (2003), Iron partitioning in Earth's mantle: toward a deep lower mantle discontinuity, *Science*, 300, 789–791, doi:10.1126/science.1081311.
- Bajgain, S., Ghosh, D. B., and Karki, B. B. (2015), Structure and density of basaltic melts at mantle conditions from first-principles simulations, *Nature Communications*, 6, doi:10.1038/ncomms9578.
- Becker, H., and Altherr, R. (1992), Evidence from ultra-high-pressure marbles for recycling of sediments into the mantle, *Nature*, 358(6389), 745-748, doi:10.1038/358745a0.

- Behrens, H., and Stuke, A. (2003), Quantification of H<sub>2</sub>O contents in silicate glasses using IR spectroscopy: a calibration based on hydrous glasses analyzed by Karl-Fischer titration, *Glass Science and Technology*, 76(4), 176-189.
- Bengone, O., Alouani, M., Blöchl, P., and Hugel, J. (2000), Implementation of the projector augmented-wave LDA+U method: Application to the electronic structure of NiO, *Physical Review B*, 62(24), 16392, doi:10.1103/PhysRevB.62.16392.
- Bengtson, A., Persson, K., and Morgan, D. (2008), *Ab initio* study of the composition dependence of the pressure-induced spin crossover in perovskite (Mg<sub>1-x</sub>Fe<sub>x</sub>)SiO<sub>3</sub>. *Earth and Planetary Science Letters*, 265(3), 535-545, doi:10.1016/j.epsl.2007.10.049.
- Bizette, H. (1951), État expérimental de la question de l'antiferromagnétisme, *Journal de Physique et Le Radium*, 12, 161-169, doi:10.1051/jphysrad:01951001203016100.
- Blöchl, P. E. (1994), Projector augmented-wave method, *Physical Review B*, 50(24), 17953, doi:10.1103/PhysRevB.50.17953.
- Boon, J. A., and Fyfe, W. S. (1972), The coordination number of ferrous ions in silicate glasses, *Chemical Geology*, 10(4), 287-298, doi:10.1016/0009-2541(72)90023-X.
- Boulard, E., Gloter, A., Corgne, A., Antonangeli, D., Auzende, A. L., Perrillat, J. P., Guyot, F., and Fiquet, G. (2011), New host for carbon in the deep Earth, *Proceedings of the National Academy of Sciences*, 108(13), 5184-5187, doi:10.1073/pnas.1016934108.
- Boulard, E., Menguy, N., Auzende, A. L., Benzerara, K., Bureau, H., Antonangeli, D., Corgne, A., Morard, G., Siebert, J., Perrillat, J. P. and Guyot, F. (2012), Experimental investigation of the stability of Fe-rich carbonates in the lower mantle, *Journal of Geophysical Research: Solid Earth*, 117, doi:10.1029/2011JB008733.
- Boulard, E., Pan, D., Galli, G., Liu, Z., and Mao, W. L. (2015), Tetrahedrally coordinated carbonates in Earth's lower mantle, *Nature Communications*, 6, doi:10.1038/ncomms7311.
- Bousquet, E., and Spaldin, N. (2010), J dependence in the LSDA+U treatment of noncollinear magnets, *Physical Review B*, 82(22), 220402, doi:10.1103/PhysRevB.82.220402.
- Bower, D. J., Gurnis, M., Jackson, J. M., and Sturhahn, W. (2009), Enhanced convection and fast plumes in the lower mantle induced by the spin transition in ferropericlase, *Geophysical Research Letters*, 36, L10306, doi:10.1029/2009GL037706.

- Bower, D. J., Wicks, J. K., Gurnis, M., and Jackson, J. M. (2011), A geodynamic and mineral physics model of a solid-state ultralow-velocity zone, *Earth and Planetary Science Letters*, 303, 193–202, doi:10.1016/j.epsl.2010.12.035.
- Brenker, F. E., Vollmer, C., Vincze, L., Vekemans, B., Szymanski, A., Janssens, K., and Kaminsky, F. (2006), CO<sub>2</sub>-recycling to the deep convecting mantle, *Geochimica et Cosmochimica Acta*, 70, A66, doi:10.1016/j.gca.2006.06.236.
- Brenker, F. E., Vollmer, C., Vincze, L., Vekemans, B., Szymanski, A., Janssens, K., Szaloki, I., Nasdala, L., Joswig, W., and Kaminsky, F. (2007), Carbonates from the lower part of transition zone or even the lower mantle, *Earth and Planetary Science Letters*, 260, 1-9, doi:10.1016/j.epsl.2007.02.038.
- Brown, S. P., Thorne, M. S., Miyagi, L., and Rost, S. (2015), A compositional origin to ultralow-velocity zones, *Geophysical Research Letters*, 42, 1039-1045, doi: 10.1002/2014GL062097.
- Bultmark, F., Cricchio, F., Grånäs, O., and Nordström, L. (2009), Multipole decomposition of LDA+U energy and its application to actinide compounds, *Physical Review B*, 80(3), 035121, doi:10.1103/PhysRevB.80.035121.
- Buob, A., Luth, R. W., Schmidt, M. W., and Ulmer, P. (2006), Experiments on CaCO<sub>3</sub>-MgCO<sub>3</sub> solid solutions at high pressure and temperature. *American Mineralogist*, 91(2-3), 435-440, doi:10.2138/am.2006.1910.
- Burns, R. G., and Burns, V. M. (1984), Optical and Mössbauer spectra of transition-metal-doped corundum and periclase, *Advances in Ceramics*, 10, 46.
- Burns, R. G. (1985), Thermodynamic data from crystal field spectra, *Reviews in Mineralogy and Geochemistry*, 14(1), 277-316.
- Burns, R. G. (1991), Mixed valency minerals: Influences of crystal structures on optical and Mössbauer spectra, *Mixed Valency Systems: Applications in Chemistry, Physics and Biology*, 175-199, Springer Netherlands.
- Burns, R. G. (1994), Mineral Mössbauer spectroscopy: correlations between chemical shift and quadrupole splitting parameters, *Hyperfine Interactions*, 91(1), 739-745, doi:10.1007/BF02064600.
- Carl, R., Gerlach, S., and Rüssel, C. (2007), The effect of composition on UV–vis–NIR spectra of iron doped glasses in the systems Na<sub>2</sub>O/MgO/SiO<sub>2</sub> and Na<sub>2</sub>O/MgO/Al<sub>2</sub>O<sub>3</sub>/SiO<sub>2</sub>, *Journal of Non-Crystalline Solids*, 353(3), 244-249, doi:10.1016/j.jnoncrysol.2006.11.010.
- Chen, Y. L., Xu, B. F., Chen, J. G., and Ge, Y. Y. (1992), Fe<sup>2+</sup>–Fe<sup>3+</sup> ordered distribution in chromite spinels, *Physics and Chemistry of Minerals*, 19(4), 255-259, doi:10.1007/BF00202316.

- Chen, B., Jackson, J. M., Sturhahn, W., Zhang, D., Zhao, J., Wicks, J. K., and Murphy, C. A. (2012), Spin crossover equation of state and sound velocities of  $(\text{Mg}_{0.65}\text{Fe}_{0.35})\text{O}$  ferropericlase to 140 GPa, *Journal of Geophysical Research*, 117, B08208, doi: 10.1029/2012JB009162.
- Cococcioni, M., and De Gironcoli, S. (2005), Linear response approach to the calculation of the effective interaction parameters in the LDA+U method, *Physical Review B*, 71(3), 035105, doi:10.1103/PhysRevB.71.035105.
- Costa, T. M. H., Gallas, M. R., Benvenuti, E. V., and Da Jornada, J. A. H. (1997), Infrared and thermogravimetric study of high pressure consolidation in alkoxide silica gel powders, *Journal of Non-Crystalline Solids*, 220(2-3), 195-201.
- Cottrell, E., and Kelley, K. A. (2011), The oxidation state of Fe in MORB glasses and the oxygen fugacity of the upper mantle, *Earth and Planetary Science Letters*, 305(3), 270-282, doi:10.1016/j.epsl.2011.03.014.
- Dauphas, N., Roskosz, M., Alp, E. E., Neuville, D. R., Hu, M. Y., Sio, C. K., Tissot, F. L. H., Zhao, J., Tissandler, L., Médard, E., and Cordier, C. (2014), Magma redox and structural controls on iron isotope variations in Earth's mantle and crust, *Earth and Planetary Science Letters*, 398, 127-140, doi:10.1016/j.epsl.2014.04.033.
- Dasgupta, R., and Hirschmann, M. M. (2010), The deep carbon cycle and melting in Earth's interior, *Earth and Planetary Science Letters*, 298(1), 1-13, doi: 10.1016/j.epsl.2010.06.039.
- de'Medici, L. (2011), Hund's coupling and its key role in tuning multiorbital correlations. *Physical Review B*, 83(20), 205112, doi:10.1103/PhysRevB.83.205112.
- Dewaele, A., Torrent, M., Loubeyre, P., and Mezouar, M. (2008), Compression curves of transition metals in the Mbar range: Experiments and projector augmented-wave calculations, *Physical Review B*, 78(10), 104102, doi:10.1103/PhysRevB.78.104102.
- Dobson, D. P., and Brodholt, J. P. (2005), Subducted banded iron formations as a source of ultralow-velocity zones at the core-mantle boundary, *Nature*, 434, 371-374, doi: 10.1038/nature03430.
- Dorfman S. M., Dutton S. E., Potapkin V., Chumakov A. I., Rueff J. P., Chow P., Xiao Y., Cava R. J., Duffy T. S., McCammon C. A., Gillet P. (2016), Electronic transitions of iron in almandine-composition glass to 91 GPa, *American Mineralogist*, 101(7), 1659-67.
- Dorogokupets, P. I. (2007), Equation of state of magnesite for the conditions of the Earth's lower mantle, *Geochemistry International*, 45(6), 561-568, doi:10.1134/S0016702907060043.

- Dowty, E. (1972), Site distribution of iron in staurolite, *Earth and Planetary Science Letters*, 15, 72-74, doi:10.1016/0012-821X(72)90031-3.
- Duffy, T. S., and Ahrens, T. K. (1993), Thermal expansion of mantle and core materials at very high pressures, *Geophysical Research Letters*, 20, 1103–1106, doi: 10.1029/ 93GL00479.
- Dunlap, R. A., Eelman, D. A., and MacKay, G. R. (1998), A Mössbauer effect investigation of correlated hyperfine parameters in natural glasses (tektites), *Journal of Non-Crystalline Solids*, 223(1-2), 141-146, doi:10.1016/S0022-3093(97)00364-5.
- Dyar, M. D., Agresti, D. G., Schaefer, M. W., Grant, C. A., and Sklute, E. C. (2006), Mössbauer spectroscopy of earth and planetary materials, *Annual Review of Earth and Planetary Sciences*, 34, 83-125, doi:10.1146/annurev.earth.34.031405.125049.
- Dziewonski, A. M., and Anderson, D. L. (1981), Preliminary reference Earth model, *Physics of the Earth and Planetary Interiors*, 25, 297-356, doi: 10.1016/0031-9201 (81)90046-7
- Efthimiopoulos, I., Jahn, S., Kuras, A., Schade, U., and Koch-Müller, M. (2017), Combined high-pressure and high-temperature vibrational studies of dolomite: phase diagram and evidence of a new distorted modification, *Physics and Chemistry of Minerals*, 1-12, doi:10.1007/s00269-017-0874-5.
- Eggler, D. H. (1976), Does CO<sub>2</sub> cause partial melting in the low-velocity layer of the mantle? *Geology*, 4, 69-72, doi:10.1130/0091-7613.
- Eggler, D. H. (1987), Solubility of major and trace elements in mantle metasomatic fluids: experimental constraints, *Mantle Metasomatism*, 21-41.
- Fei, Y., and Mao, H. K. (1994), In situ determination of the NiAs phase of FeO at high pressure and temperature, *Science*, 266, 1678–1680, doi:10.1126/science.266.5191.1678.
- Fei Y., Zhang, L., Corgne, A., Watson, H., Ricolleau, A., Meng, Y., and Prakapenka, V. (2007), Spin transition and equations of state of (Mg,Fe)O solid solutions, *Geophysical Research Letters*, 34(17), doi:10.1029/2007GL030712.
- Fiquet, G., Guyot, F., Kunz, M., Matas, J., Andrault, D., and Hanfland, M. (2002), Structural refinements of magnesite at very high pressure, *American Mineralogist*, 87(8-9), 1261-1265, doi:10.2138/am-2002-8-927.
- Fischer, R. A., Campbell, A. J., Shofner, G. A., Lord, O. T., Dera, P., and Prakapenka, V. B. (2011), Equation of state and phase diagram of FeO, *Earth and Planetary Science Letters*, 304, 496–502, doi:10.1016/j.epsl.2011.02.025.

- Fujii, A., Kondo, T., Taniguchi, T., and Sakaiya, T. (2011), Néel transition in (Mg,Fe)O: A possible change of magnetic structure, *American Mineralogist*, 96, 329–332, doi: 10.2138/am.2011.3534.
- Frost, D. J., Liebske, C., Langenhorst, F., McCammon, C. A., Trønnes, R. G., and Rubie, D. C. (2004), Experimental evidence for the existence of iron-rich metal in the Earth's lower mantle, *Nature*, 428(6981), 409-412, doi:10.1038/nature02413.
- Garnero, E. J., and Helmberger, D. V. (1996), Seismic detection of a thin laterally varying boundary layer at the base of the mantle beneath the central Pacific, *Geophysical Research Letters*, 23, 977–980, doi:10.1029/95GL03603.
- Garnero, E. J., Revenaugh, J., Williams, Q., Lay, T., and Kellogg, L. H. (1998), Ultralow velocity zone at the core-mantle boundary, *The Core-Mantle Boundary Region*, 319-334.
- Gerdau, E., Ruffer, R., Winkler, H., Tolksdorf, W., Klages, C. P., and Hannon, J. P. (1985), Nuclear Bragg diffraction of synchrotron radiation in yttrium iron garnet. *Physical Review Letters*, 54(8), 835, doi:10.1103/PhysRevLett.54.835.
- Giannozzi, P., Baroni, S., Bonini, N., Calandra, M., Car, R., Cavazzoni, C., Ceresoli, D., Chiarotti, G. L., Cococcioni, M., Dabo, I., Dal Corso, A., Fabris, S., Fratesi, G., de Gironcoli, S., Gebauer, R., Gerstmann, U., Gougoussis, C., Kokalj, A., Lazzeri, M., Martin-Samos, L., Marzari, N., Mauri, F., Mazzarello, R., Paolini, S., Pasquarello, A., Paulatto, L., Sbraccia, C., Scandolo, S., Sclauzero, G., Seitsonen, A. P., Smogunov, A., Umari, P., and Wentzcovitch, R. M. (2009), QUANTUM ESPRESSO: a modular and open-source software project for quantum simulations of materials, *Journal of physics: Condensed matter*, 21(39), 395502, doi:10.1088/0953-8984/21/39/395502.
- Gillet, P., Biellmann, C., Reynard, B., and McMillan, P. (1993), Raman spectroscopic studies of carbonates Part I: High-pressure and high-temperature behaviour of calcite, magnesite, dolomite and aragonite, *Physics and Chemistry of Minerals*, 20(1), 1-18, doi:10.1007/BF00202245.
- Glass, C. W., Oganov, A. R., and Hansen, N. (2006), USPEX—evolutionary crystal structure prediction, *Computer Physics Communications*, 175(11), 713-720, doi: 10.1016/j.cpc.2006.07.020.
- Goldman, D. S., and Rossman, G. R. (1977), The spectra of iron in orthopyroxene revisited: the splitting of the ground state, *American Mineralogist*, 62, 151-157.
- Goncharov, A. F., Struzhkin, V. V., and Jacobsen, S. D. (2006), Reduced radiative conductivity of low-spin (Mg,Fe)O in the lower mantle, *Science*, 312, 1205–1208, doi:10.1126/science.1125622.

- Gu, C., Catalli, K., Grocholski, B., Gao, L., Alp, E., Chow, P., Xiao, Y., Cynn, H., Evans, W. J., and Shim, S. H. (2012), Electronic structure of iron in magnesium silicate glasses at high pressure, *Geophysical Research Letters*, 39(24), doi:10.1029/2012GL053950.
- Hamada, M., and Akasaka, M. (2013), Distribution of cations at two tetrahedral sites in  $\text{Ca}_2\text{MgSi}_2\text{O}_7\text{-Ca}_2\text{Fe}^{3+}\text{AlSiO}_7$  series synthetic melilite and its relation to incommensurate structure, *Physics and Chemistry of Minerals*, 40, 259-270, doi:10.1007/s00269-013-0566-8.
- Hamann, D. R., Schlüter, M., and Chiang, C. (1979), Norm-conserving pseudopotentials, *Physical Review Letters*, 43(20), 1494, doi:10.1103/PhysRevLett.43.1494
- Hammersley, A. O., Svensson, S. O., Hanfland, M., Fitch, A. N., and Hausermann, D. (1996), Two-dimensional detector software: from real detector to idealized image or two-theta scan, *High Pressure Research*, 14, 235–248, doi: 10.1080/08957959608201408.
- Hammouda, T., Andrault, D., Koga, K., Katsura, T., and Martin, A. M. (2011), Ordering in double carbonates and implications for processes at subduction zones, *Contributions to Mineralogy and Petrology*, 161(3), 439-450, doi:10.1007/s00410-010-0541-z.
- Hazen, R. M., Jones, A. P. and Baross, J. A. (eds) (2013), Carbon in Earth. Mineralogical Society of America and Geochemical Society, *Reviews in Mineralogy and Geochemistry*, 75.
- Herring, C. (1940), A new method for calculating wave functions in crystals, *Physical Review*, 57(12), 1169, doi:10.1103/PhysRev.57.1169.
- Hirschmann, M. M., and Dasgupta, R. (2009), The H/C ratios of Earth's near-surface and deep reservoirs, and consequences for deep Earth volatile cycles, *Chemical Geology*, 262(1), 4-16, doi:10.1016/j.chemgeo.2009.02.008.
- Hohenberg, P., and Kohn, W. (1964), Inhomogeneous electron gas, *Physical review*, 136(3B), B864, doi:10.1103/PhysRev.136.B864.
- Holmström, E., and Stixrude, L. (2015), Spin crossover in ferropericlase from first-principles molecular dynamics, *Physical Review Letters*, 114, 117202, doi:10.1103/PhysRevLett.114.117202.
- Hsu, H., and Huang, S. C. (2016), Spin crossover and hyperfine interactions of iron in  $(\text{Mg,Fe})\text{CO}_3$  ferromagnesite, *Physical Review B*, 94(6), 060404, doi:10.1103/PhysRevB.94.060404.
- Hsu, H., Blaha, P., Cococcioni, M., and Wentzcovitch, R. M. (2011), Spin-state crossover and hyperfine interactions of ferric iron in  $\text{MgSiO}_3$  perovskite, *Physical Review Letters*, 106(11), 118501, doi:10.1103/PhysRevLett.106.118501.

- Isshiki, M., Irifune, T., Hirose, K., Ono, S., Ohishi, Y., Watanuki, T., Nishibori, E., Takata, M., and Sakata, M. (2004), Stability of magnesite and its high-pressure form in the lowermost mantle, *Nature*, 427, 60-63, doi:10.1038/nature02181.
- Iwamoto, N., Tsunawaki, Y., Nakagawa, H., Yoshimura, T., and Wakabayashi, N. (1978), Investigation of calcium-iron-silicate glasses by the Mössbauer method, *Journal of Non-Crystalline Solids*, 29(3), 347-356, doi:10.1016/0022-3093(78)90155-2.
- Jackson, W. E., Farges, F., Yeager, M., Mabrouk, P. A., Rossano, S., Waychunas, G. A., Solomon, E., and Brown, G. E. (2005), Multi-spectroscopic study of Fe(II) in silicate glasses: Implications for the coordination environment of Fe(II) in silicate melts, *Geochimica et Cosmochimica Acta*, 69(17), 4315-4332, doi:10.1016/j.gca.2005.01.008.
- Jackson, J. M., Sinogeikin, S. V., Jacobsen, S. D., Reichmann, H. J., Mackwell, S. J., and Bass, J. D. (2006), Single-crystal elasticity and sound velocities of  $(\text{Mg}_{0.94}\text{Fe}_{0.06})\text{O}$  ferropericlase to 20 GPa, *Journal of Geophysical Research*, 111, B09203, doi:10.1029/2005JB004052.
- Jacobs, I. S. (1963), Metamagnetism of siderite ( $\text{FeCO}_3$ ), *Journal of Applied Physics*, 34, 1106-1107, doi:10.1063/1.1729389.
- Jacobsen, S. D., Reichmann, H. J., Spetzler, H., Mackwell, S. J., Smyth, J. R., Angel, R. J., and McCammon, C. A. (2002), Structure and elasticity of single-crystal  $(\text{Mg,Fe})\text{O}$  and a new method of generating shear waves for gigahertz ultrasonic interferometry, *Journal of Geophysical Research*, 107, 5867-5871, doi:10.1029/2001JB000490.
- Jacobsen, S. D., Holl, C. M., Adams, K. A., Fischer, R. A., Martin, E. S., Bina, C. R., Lin, J., Prakapenka, V. B., Kubo, A., and Dera, P. (2008), Compression of single-crystal magnesium oxide to 118 GPa and a ruby pressure gauge for helium pressure media, *American Mineralogist*, 93, 1823-1828, doi:10.2138/am.2008.2988.
- Jeong, T., and Pickett, W. E. (2006), First-principles study of the electronic structure of heavy fermion  $\text{YbRh}_2\text{Si}_2$ , *Journal of Physics: Condensed Matter*, 18(27), 6289, doi:10.1088/0953-8984/18/27/012.
- Kaminsky, F., Zakharchenko, O., Davies, R., Griffin, W., Khachatryan-Blinova, G., and Shiryaev, A. (2001), Superdeep diamonds from the Juina area, Mato Grosso State, Brazil, *Contributions to Mineralogy and Petrology*, 140(6), 734-753, doi:10.1007/s004100000221.
- Kantor, I., Dubrovinsky, L., McCammon, C., Kantor, A., Pascarelli, S., Aquilanti, G., Crichton, W., Mattesini, M., Ahuja, R., Almeida, J., and Urusov, V. (2006),

- Pressure-induced phase transition in  $(\text{Mg}_{0.8}\text{Fe}_{0.2})\text{O}$  ferropericlyase, *Physics and Chemistry of Minerals*, 33, 35–44, doi:10.1007/s00269-005-0052-z.
- Karakassides, M. A., Gournis, D., and Petridis, D. (1999), An infrared reflectance study of Si–O vibrations in thermally treated alkali-saturated montmorillonites, *Clay Minerals*, 34(3), 429–429, doi:10.1180/000985599546334.
- Kato, T., Enami, M., and Zhai, M. (1997), Ultra-high-pressure (UHP) marble and eclogite in the Su-Lu UHP terrane, eastern China, *Journal of Metamorphic Geology*, 15(2), 169–182, doi:10.1111/j.1525-1314.1997.00013.x.
- Katsura, T., Tsuchida, Y., Ito, E., Yagi, T., Utsumi, W., and Akimoto, S. I. (1991), Stability of magnesite under the lower mantle conditions, *Proceedings of the Japan Academy, Series B*, 67(4), 57–60, doi:10.2183/pjab.67.57.
- Kelemen, P. B., and Manning, C. E. (2015), Reevaluating carbon fluxes in subduction zones, what goes down, mostly comes up, *Proceedings of the National Academy of Sciences*, 112, E3997–E4006, doi:10.1073/pnas.1507889112.
- Keppler, H., Kantor, I. Y., and Dubrovinsky, L. S. (2007), Optical absorption spectra of ferropericlyase to 84 GPa, *American Mineralogist*, 92, 433–436, doi:10.2138/am.2007.2454, doi:10.2138/am.2007.2454.
- Kesson, S. E., and Ringwood, A. E. (1989), Slab-mantle interactions: 2. The formation of diamonds, *Chemical Geology*, 78(2), 97–118, doi:10.1016/0009-2541(89)90110-1.
- Kido, L., Müller, M., and Rüssel, C. (2006), Redox reactions during temperature change in soda-lime–silicate melts doped with copper and iron or copper and manganese, *Journal of Non-Crystalline Solids*, 352(38), 4062–4068, doi:10.1016/j.jnoncrysol.2006.06.027.
- Klement, R., Kraxner, J., and Liška, M. (2009), Spectroscopic analysis of iron doped glasses with composition close to the E-glass: a preliminary study, *Ceramics – Silikáty*, 53, 180–183.
- Klotz, S., Chervin, J. C., Munsch, P., and Marchand, G. L. (2009), Hydrostatic limits of 11 pressure transmitting media, *Journal of Physics D: Applied Physics*, 42, doi:10.1088/0022-3727/42/7/075413.
- Kobayashi, Y., Kondo, T., Ohtani, E., Hirao, N., Miyajima, N., Yagi, T., Nagase, T., and Kikegawa, T. (2005), Fe-Mg partitioning between  $(\text{Mg,Fe})\text{SiO}_3$  post-perovskite, perovskite, and magnesiowüstite in the Earth's lower mantle, *Geophysical Research Letters*, 32, L19301, doi:10.1029/2005GL023257.
- Kohn, W., and Sham, L. J. (1965), Self-consistent equations including exchange and correlation effects, *Physical Review*, 140(4A), A1133, doi:10.1103/PhysRev.140.A1133.

- Kobayashi, Y., Kondo, T., Ohtani, E., Hirao, N., Miyajima, N., Yagi, T., Nagase, T. and Kikegawa, T. (2005), Fe-Mg partitioning between (Mg, Fe) SiO<sub>3</sub> post-perovskite, perovskite, and magnesiowüstite in the Earth's lower mantle, *Geophysical Research Letters*, 32(19), doi:10.1029/2005GL023257.
- Komabayashi, T., Hirose, K., Nagaya, Y., Sugimura, E., and Ohishi, Y. (2010), High-temperature compression of ferroperricite and the effect of temperature on iron spin transition, *Earth and Planetary Science Letters*, 297, 691–699, doi: 10.1016/j.epsl.2010.07.025.
- Kresse, G., and Furthmüller, J. (1996), Efficient iterative schemes for *ab initio* total-energy calculations using a plane-wave basis set, *Physical Review B*, 54(16), 11169, doi: 10.1103/PhysRevB.54.11169.
- Kresse, G., and Joubert, D. (1999), From ultrasoft pseudopotentials to the projector augmented-wave method, *Physical Review B*, 59(3), 1758, doi: 10.1103/PhysRevB.59.1758.
- Kuno, A., Santos, R., Matsuo, M., and Takano, B. (2000), Characterization of natural chromite samples from ophiolite complexes in the Philippines by <sup>57</sup>Fe Mössbauer spectroscopy, *Journal of Radioanalytical and Nuclear Chemistry*, 246, 79-83, doi:10.1023/A:1006724913427.
- Labrosse, S., Hernlund, J. W., and Coltice, N. (2007), A crystallizing dense magma ocean at the base of the Earth's mantle, *Nature*, 450, 866–869, doi:10.1038/nature06355.
- Langer K., Platonov A. N., and Rossman G. R. (1996), Optical Absorption Spectroscopy, *Advanced Mineralogy*, 2, doi:10.1007/978-3-642-78526-9\_3.
- Lavina, B., Dera, P., Downs, R. T., Prakapenka, V., Rivers, M., Sutton, S., and Nicol, M. (2009), Siderite at lower mantle conditions and the effects of the pressure-induced spin-pairing transition, *Geophysical Research Letters*, 36(23), doi:10.1029/2009GL039652.
- Liechtenstein, A. I., Anisimov, V. I., and Zaanen, J. (1995), Density-functional theory and strong interactions: Orbital ordering in Mott-Hubbard insulators, *Physical Review B*, 52(8), R5467, doi:10.1103/PhysRevB.52.R5467.
- Lin, J. F., Heinz, D. L., Mao, H. K., Hemley, R. J., Devine, J. M., Li, J., and Shen, G. (2003), Stability of magnesiowüstite in Earth's lower mantle, *Proceedings of the National Academy of Sciences*, 100, 4405-4408, doi:10.1073/pnas.252782399.
- Lin, J. F., Struzhkin, V. V., Jacobsen, S., Hu, M. Y., Chow, P., Kung, J., Liu, H., Mao, H., and Hemley, R. J. (2005), Spin transition of iron in magnesiowüstite in the Earth's lower mantle, *Nature*, 436, 377–380, doi:10.1038/nature03825.
- Lin, J. F., Gavriluk, A. G., Struzhkin, V. V., Jacobsen, S. D., Sturhahn, W., Hu, M. Y., and Chow, P., Yoo, C. S. (2006a), Pressure-induced electronic spin transition of

- iron in magnesiowüstite-(Mg,Fe)O, *Physical Review B*, 73, 113107, doi:10.1103/PhysRevB.73.113107.
- Lin, J. F., Jacobsen, S. D., Sturhahn, W., Jackson, J. M., Zhao, J., and Yoo, C. S. (2006b), Sound velocities of ferropericlase in the Earth's lower mantle, *Geophysical Research Letters*, 33, L22304, doi:10.1029/2006GL028099.
- Lin, J. F., Struzhkin, V. V., Gavriliuk, A. G., and Lyubutin, I. (2007), Comment on "Spin crossover in (Mg,Fe)O: a Mössbauer effect study with an alternative interpretation of X-ray emission spectroscopy data", *Physics Review*, 75, 177102, doi:10.1103/PhysRevB.73.100101.
- Lin, J. F., Liu, J., Jacobs, C., and Prakapenka, V. B. (2012), Vibrational and elastic properties of ferromagnesite across the electronic spin-pairing transition of iron, *American Mineralogist*, 97(4), 583-591, doi:10.2138/am.2012.3961.
- Liu, J., Lin, J. F., and Prakapenka, V. B. (2015), High-pressure orthorhombic ferromagnesite as a potential deep-mantle carbon carrier, *Scientific Reports*, 5, doi:10.1038/srep07640.
- Madejová, J., and Komadel, P. (2001), Baseline studies of the clay minerals society source clays: infrared methods, *Clays and clay minerals*, 49(5), 410-432.
- Malczewski, D., Frąckowiak, J. E., and Galuskin, E.V. (2006), <sup>57</sup>Fe Mössbauer spectroscopy and X-ray diffraction study of some complex metamict minerals, In ICAME 2005 (pp. 529-536), *Springer Berlin Heidelberg*, doi:10.1007/978-3-540-49850-6\_83.
- Manga, M., and Jeanloz, R. (1996), Implications of a metal-bearing chemical boundary layer in D'' for mantle dynamics, *Geophysical Research Letters*, 23, 3091–3094, doi: 10.1029/96GL03021.
- Manghnani, M. H., Ferraro, J. R., and Basile, L. J. (1974), A Study of Na<sub>2</sub>O-TiO<sub>2</sub>-SiO<sub>2</sub> Glasses by Infrared Spectroscopy, *Applied Spectroscopy*, 28(3), 256-259, doi:10.1366/000370274774332542.
- Mao, H. K., Xu, J., and Bell, P. M. (1986), Calibration of the ruby pressure gauge to 800 kbar under quasi-hydrostatic conditions, *Journal of Geophysical Research*, 91, 4673–4676, doi:10.1029/JB091iB05p04673.
- Mao, H. K., Shu, J., Fei, Y., Hu, J., and Hemley, R. J. (1996), The wüstite enigma, *Physics of the Earth and Planetary Interiors*, 96, 135–145, doi:10.1016/0031-9201(96)03146-9.
- Mao, W., Shu, J., Hu, J., Hemley, R., and Mao, H. K. (2002), Displacive transition in magnesiowüstite, *Journal of Physics: Condensed Matter*, 14, 11349, doi:10.1088/0953-8984/14/44/480.

- Mao, W. L., Shen, G., Prakapenka, V.B., Meng, Y., Campbell, A. J., Heinz, D. L., Shu, J., Hemley, R. J., and Mao, H. (2004), Ferromagnesian postperovskite silicates in the D'' layer of the Earth, *Proceedings of the National Academy of Sciences*, 101, 15867–15869, doi:10.1073/pnas.0407135101.
- Mao, Z., Armentrout, M., Rainey, E., Manning, C. E., Dera, P., Prakapenka, V. B., and Kavner, A. (2011), Dolomite III: A new candidate lower mantle carbonate, *Geophysical Research Letters*, 38, doi:10.1029/2011GL049519.
- Mao, Z., Lin, J. F., Liu, J., and Prakapenka, V. B. (2011), Thermal equation of state of lower-mantle ferropericlase across the spin crossover, *Geophysical Research Letters*, 38, L23308, doi:10.1029/2011GL049915.
- Mao, Z., Lin, J. F., Yang, J., Wu, J., Watson, H. C., Xiao, Y., Chow, P. and Zhao, J. (2014), Spin and valence states of iron in Al-bearing silicate glass at high pressures studied by synchrotron Mössbauer and X-ray emission spectroscopy, *American Mineralogist*, 99(2-3), 415-423, doi:10.2138/am.2014.4490.
- Marquardt, H., Speziale, S., Reichmann, H. J., Frost, D. J., Schilling, F. R., and Garnero, E. J. (2009a), Elastic shear anisotropy of ferropericlase in Earth's lower mantle, *Science*, 324, 224–226, doi:10.1126/science.1169365.
- Marquardt, H., Speziale, S., Reichmann, H. J., Frost, D. J., and Schilling, F. R. (2009b), Single-crystal elasticity of  $(\text{Mg}_{0.9}\text{Fe}_{0.1})\text{O}$  to 81 GPa, *Earth and Planetary Science Letters*, 287, 345-352, doi:10.1016/j.epsl.2009.08.017.
- Martinez, I., Zhang, J., and Reeder, R. J. (1996), In situ X-ray diffraction of aragonite and dolomite at high pressure and high temperature; evidence for dolomite breakdown to aragonite and magnesite, *American Mineralogist*, 81, 611-624, doi:10.2138/am-1996-5-608.
- Maruyama, S., Santosh, M. and Zhao, D. (2007), Superplume, supercontinent, and post-perovskite: mantle dynamics and anti-plate tectonics on the core–mantle boundary, *Gondwana Research*, 11(1), 7-37, doi:10.1016/j.gr.2006.06.003.
- Mattila, A., Pylkkanen, T., Rueff, J.P., Huotari, S., Vanko, G., Hanfland, M., Lehtinen, M. and Hamalainen, K. (2007), Pressure induced magnetic transition in siderite  $\text{FeCO}_3$  studied by X-ray emission spectroscopy, *Journal of Physics: Condensed Matter*, 19, 386206, doi:10.1088/0953-8984/19/38/386206.
- Mattson, S. M., and Rossman, G. R. (1984), Ferric iron in tourmaline, *Physics and Chemistry of Minerals*, 11(5), 225-234, doi:10.1007/BF00308137.
- McCammon, C. A. (2005), Mantle oxidation state and oxygen fugacity: constraints on mantle chemistry, structure, and dynamics, *Earth's Deep Mantle: Structure, Composition, and Evolution*, 219-240, doi:10.1029/160GM14.

- McNamara, A. K., Garnero, E. J., and Rost, S. (2010), Tracking deep mantle reservoirs with ultra-low velocity zones, *Earth and Planetary Science Letters*, 299, 1–9, doi:10.1016/j.epsl.2010.07.042.
- Merlini, M., Crichton, W. A., Hanfland, M., Gemmi, M., Müller, H., Kuppenko, I., and Dubrovinsky, L. (2012), Structures of dolomite at ultrahigh pressure and their influence on the deep carbon cycle, *Proceedings of the National Academy of Sciences*, 109, 13509-13514, doi:10.1073/pnas.1201336109.
- Ming, X., Wang, X. L., Du, F., Yin, J. W., Wang, C. Z., and Chen, G. (2012), First-principles study of pressure-induced magnetic transition in siderite  $\text{FeCO}_3$ , *Journal of Alloys and Compounds*, 510(1), L1-L4, doi:10.1016/j.jallcom.2011.08.079.
- Momma, K., and Izumi, F. (2008), VESTA: a three-dimensional visualization system for electronic and structural analysis, *Journal of Applied Crystallography*, 41, 653-658, doi:10.1107/S0021889808012016.
- Monkhorst, H. J., and Pack, J. D. (1976), Special points for Brillouin-zone integrations. *Physical review B*, 13(12), 5188, doi:10.1103/PhysRevB.13.5188.
- Mörner, N. A., and Etiope, G. (2002), Carbon degassing from the lithosphere, *Global and Planetary Change*, 33, 185-203, doi:10.1016/S0921-8181(02)00070-X.
- Mosenfelder, J. L., Asimow, P. D., Frost, D. J., Rubie, D. C., and Ahrens, T. J. (2009), The  $\text{MgSiO}_3$  system at high pressure: Thermodynamic properties of perovskite, postperovskite, and melt from global inversion of shock and static compression data, *Journal of Geophysical Research*, 114, B01203, doi:10.1029/2008JB005900.
- Mössbauer, R. L. (1962), Recoilless nuclear resonance absorption, *Annual Review of Nuclear Science*, 12(1), 123-152, doi:10.1146/annurev.ns.12.120162.001011.
- Murakami, M., Goncharov, A. F., Hirao, N., Masuda, R., Mitsui, T., Thomas, S. M., and Bina, C. R. (2014), High-pressure radiative conductivity of dense silicate glasses with potential implications for dark magmas, *Nature communications*, 5, 5428.
- Murakami, M., Hirose, K., Kawamura, K., Sata, N. and Ohishi, Y. (2004), Post-perovskite phase transition in  $\text{MgSiO}_3$ , *Science*, 304, 855-858, doi:10.1126/science.1095932.
- Mysen, B. O. (1987), Redox equilibria and coordination of  $\text{Fe}^{2+}$  and  $\text{Fe}^{3+}$  in silicate glasses from  $^{57}\text{Fe}$  Mössbauer spectroscopy, *Journal of Non-Crystalline Solids*, 95, 247-254, doi:10.1016/S0022-3093(87)80117-5.
- Nagai, T., Ishido, T., Seto, Y., Nishio-Hamane, D., Sata, N., and Fujino, K. (2010), Pressure-induced spin transition in  $\text{FeCO}_3$ -siderite studied by X-ray diffraction

- measurements, *Journal of Physics: Conference Series*, 215(1), 012002, doi:10.1088/1742-6596/215/1/012002.
- Newman, S., Stolper, E. M., and Epstein, S. (1986), Measurement of water in rhyolitic glasses; calibration of an infrared spectroscopic technique, *American Mineralogist*, 71(11-12), 1527-1541.
- Nolet, D. A. (1980), Optical absorption and Mössbauer spectra of Fe, Ti silicate glasses, *Journal of Non-Crystalline Solids*, 37(1), 99-110, doi:10.1016/0022-3093(80)90482-2.
- Nomura, R., Ozawa, H., Tateno, S., Hirose, K., Hernlund, J., Muto, S., Ishii, H., and Hiraoka, N. (2011), Spin crossover and iron-rich silicate melt in the Earth's deep mantle, *Nature*, 473(7346), 199-202, doi:10.1038/nature09940.
- Oganov, A. R., and Ono, S. (2004), Theoretical and experimental evidence for a post-perovskite phase of MgSiO<sub>3</sub> in Earth's D'' layer, *Nature*, 430, 445-448, doi:10.1038/nature02701.
- Ono, S., Kikegawa, T., Ohishi, Y., and Tsuchiya, J. (2005), Post-aragonite phase transformation in CaCO<sub>3</sub> at 40 GPa, *American Mineralogist*, 90, 667-671, doi:10.2138/am.2005.1610.
- Oganov, A. R., and Glass, C. W. (2006), Crystal structure prediction using *ab initio* evolutionary techniques: Principles and applications, *The Journal of chemical physics*, 124, 244704, doi:10.1063/1.2210932.
- Oganov, A. R., Glass, C. W., and Ono, S. (2006), High-pressure phases of CaCO<sub>3</sub>: crystal structure prediction and experiment, *Earth and Planetary Science Letters*, 241, 95-103, doi:10.1016/j.epsl.2005.10.014.
- Oganov, A. R., Ono, S., Ma, Y., Glass, C. W., and Garcia, A. (2008), Novel high-pressure structures of MgCO<sub>3</sub>, CaCO<sub>3</sub> and CO<sub>2</sub> and their role in Earth's lower mantle, *Earth and Planetary Science Letters*, 273, 38-47, doi:10.1016/j.epsl.2008.06.005.
- Oganov, A. R., Hemley, R. J., Hazen, R. M. and Jones, A. P. (2013), Structure, bonding, and mineralogy of carbon at extreme conditions, *Reviews in Mineralogy and Geochemistry*, 75, 47-77, doi:10.2138/rmg.2013.75.3.
- Panchmatia, P. M., Sanyal, B., and Oppeneer, P. M. (2008), GGA+U modeling of structural, electronic, and magnetic properties of iron porphyrin-type molecules, *Chemical Physics*, 343(1), 47-60, doi:10.1016/j.chemphys.2007.10.030.
- Pandya, N., Muenow, D. W., and Sharma, S. K. (1992), The effect of bulk composition on the speciation of water in submarine volcanic glasses, *Geochimica et Cosmochimica Acta*, 56(5), 1875-1883, doi:10.1016/0016-7037(92)90317-C.

- Pasternak, M. P., Taylor, R. D., Jeanloz, R., Li, X., Nguyen, J. H., and McCammon, C.A. (1997), High pressure collapse of magnetism in  $\text{Fe}_{0.94}\text{O}$ : Mössbauer spectroscopy beyond 100 GPa, *Physical Review Letters*, 79, 5046–5049, doi:10.1103/PhysRevLett.79.5046.
- Perdew, J. P. (1979), Orbital functional for exchange and correlation: self-interaction correction to the local density approximation, *Chemical Physics Letters*, 64(1), 127-130, doi:10.1016/0009-2614(79)87292-9.
- Perdew, J. P. (1986), Density-functional approximation for the correlation energy of the inhomogeneous electron gas, *Physical Review B*, 33(12), 8822, doi: 10.1103/PhysRevB.33.8822.
- Perdew, J. P., Burke, K., and Ernzerhof, M. (1996), Generalized gradient approximation made simple, *Physical review letters*, 77(18), 3865, doi:10.1103/PhysRevLett.77.3865.
- Persson, K., Bengtson, A., Ceder, G., and Morgan, D. (2006), *Ab initio* study of the composition dependence of the pressure induced spin transition in the  $(\text{Mg}_{1-x}\text{Fe}_x)$ , *Geophysical Research Letters*, 33, L16306, doi:10.1029/2006GL026621.
- Phillips, J. C., and Kleinman, L. (1959), New method for calculating wave functions in crystals and molecules, *Physical Review*, 116(2), 287, doi:10.1103/PhysRev.116.287.
- Prescher, C., Weigel, C., McCammon, C., Narygina, O., Potapkin, V., Kuppenko, I., Sinmyo, R., Chumakov, A. I., and Dubrovinsky, L. (2014), Iron spin state in silicate glass at high pressure: Implications for melts in the Earth's lower mantle, *Earth and Planetary Science Letters*, 385, 130-136, doi:10.1016/j.epsl.2013.10.040.
- Gudfinnsson, G. H., and Presnall, D. C. (2005), Continuous gradations among primary carbonatitic, kimberlitic, melilititic, basaltic, picritic, and komatiitic melts in equilibrium with garnet lherzolite at 3–8 GPa, *Journal of Petrology*, 46(8), 1645-1660. doi:10.1093/petrology/egi029.
- Rivers, M., Prakapenka, V. B., Kubo, A., Pullins, C., Holl, C. M., and Jacobsen, S. D. (2008), The COMPRES/GSECARS gas-loading system for diamond anvil cells at the Advanced Photon Source, *High Pressure Research*, 28(3), 273-292, doi:10.1080/08957950802333593.
- Ross, N. L. and Reeder, R. J. (1992), High-pressure structural study of dolomite and ankerite, *American Mineralogist*, 77, 412-421.

- Rossano, S., Balan, E., Morin, G., Bauer, J. P., Calas, G., and Brouder, C. (1999),  $^{57}\text{Fe}$  Mössbauer spectroscopy of tektites, *Physics and Chemistry of Minerals*, 26(6), 530-538, doi:10.1007/s002690050216.
- Rossano, S., Behrens, H., and Wilke, M. (2008), Advanced analyses of  $^{57}\text{Fe}$  Mössbauer data of aluminosilicate glasses, *Physics and Chemistry of Minerals*, 35(2), 77-93, doi:10.1007/s00269-007-0200-8.
- Rossman, G. R. (1988), Optical spectroscopy, *Reviews in Mineralogy*, 18, 207-254.
- Rossman, G. R., and Taran, M. N. (2001), Spectroscopic standards for four- and fivefold-coordinated  $\text{Fe}^{2+}$  in oxygen-based minerals, *American Mineralogist*, 86(7-8), 896-903, doi:10.2138/am-2001-0713.
- Rossman, G. R. (2014), Optical spectroscopy, *Reviews in Mineralogy and Geochemistry*, 78(1), 371-398, doi:10.2138/rmg.2014.78.9.
- Rost, S., Garnero, E. J., Williams, Q., and Manga, M. (2005), Seismological constraints on a possible plume root at the core-mantle boundary, *Nature*, 435, 666-669, doi:10.1038/nature03620.
- Rost, S. (2013), Core-mantle boundary landscapes, *Nature*, 6, 89-90, doi:10.1038/ngeo1715.
- Sakai, T., Ohtani, E., Terasaki, H., Sawada, N., Kobayashi, Y., Miyahara, M., Nishijima, M., Hirao, N., Ohishi, Y., and Kikegawa, T. (2009), Fe-Mg partitioning between perovskite and ferropericlasite in the lower mantle, *American Mineralogist*, 94, 921-925, doi:10.2138/am.2009.3123.
- Sano, Y., and Williams, S. N. (1996), Fluxes of mantle and subducted carbon along convergent plate boundaries, *Geophysical Research Letters*, 23(20), 2749-2752, doi:10.1029/96GL02260.
- Santillán, J., Williams, Q., and Knittle, E. (2003), Dolomite-II: A high-pressure polymorph of  $\text{CaMg}(\text{CO}_3)_2$ , *Geophysical Research Letters*, 30, doi:10.1029/2002GL016018.
- Santillán, J., and Williams, Q. (2004), A high pressure X-ray diffraction study of aragonite and the post-aragonite phase transition in  $\text{CaCO}_3$ , *American Mineralogist*, 89(8-9), 1348-1352, doi:10.2138/am-2004-8-925.
- Santillán, J., and Williams, Q. (2004), A high-pressure infrared and X-ray study of  $\text{FeCO}_3$  and  $\text{MnCO}_3$ : comparison with  $\text{CaMg}(\text{CO}_3)_2$ -dolomite, *Physics of the Earth and Planetary Interiors*, 143, 291-304, doi:10.1016/j.pepi.2003.06.007.
- Segall, M. D., Lindan, P. J., Probert, M. A., Pickard, C. J., Hasnip, P. J., Clark, S. J., and Payne, M. C. (2002), First-principles simulation: ideas, illustrations and the CASTEP code, *Journal of Physics: Condensed Matter*, 14(11), 2717, doi:10.1088/0953-8984/14/11/301.

- Seifert, F., and Olesch, M. (1977), Mössbauer spectroscopy of grandidierite, (Mg, Fe)Al<sub>3</sub>SiO<sub>9</sub>, *American Mineralogist*, 62, 547-553.
- Shatskiy, A. F., Litasov, K. D., and Palyanov, Y. N. (2015), Phase relations in carbonate systems at pressures and temperatures of lithospheric mantle: review of experimental data, *Russian Geology and Geophysics*, 56(1-2), 113-142, doi:10.1016/j.rgg.2015.01.007.
- Shcheka, S. S., Wiedenbeck, M., Frost, D. J., and Keppler, H. (2006), Carbon solubility in mantle minerals, *Earth and Planetary Science Letters*, 245, 730-742, doi:10.1016/j.epsl.2006.03.036.
- Shi, H., Luo, W., Johansson, B., and Ahuja, R. (2008), First-principles calculations of the electronic structure and pressure-induced magnetic transition in siderite FeCO<sub>3</sub>, *Physical Review B*, 78(15), 155119, doi:10.1103/PhysRevB.78.155119.
- Shirasaka, M., Takahashi, E., Nishihara, Y., Matsukage, K., and Kikegawa, T. (2002), In situ X-ray observation of the reaction dolomite = aragonite + magnesite at 900–1300 K, *American Mineralogist*, 87, 922-930, doi:10.2138/am-2002-0715.
- Sinmyo, R., Hirose, K., Nishio-Hamane, D., Seto, Y., Fujino, K., Sata, N., and Ohishi, Y. (2008), Partitioning of iron between perovskite/postperovskite and ferropericlae in the lower mantle, *Journal of Geophysical Research*, 113, B11204, doi:10.1029/2008JB005730.
- Skorodumova, N. V., Belonoshko, A. B., Huang, L., Ahuja, R., and Johansson, B. (2005), Stability of the MgCO<sub>3</sub> structures under lower mantle conditions, *American mineralogist*, 90, 1008-1011, doi:10.2138/am.2005.1685.
- Slater, J. (1937), Wave functions in a periodic potential, *Physical Review*, 51(10), 846, doi:10.1103/PhysRev.51.846.
- Smyth, J. R., and Ahrens, T. J. (1997), The crystal structure of calcite III. *Geophysical Research Letters*, 24, 1595-1598, doi:10.1029/97GL01603.
- Sobolev, N. V., and Shatsky, V. S. (1990), Diamond inclusions in garnets from metamorphic rocks: a new environment for diamond formation, *Nature*, 343, 742-746, doi:10.1038/343742a0.
- Soler, J. M., and Williams, A. R. (1989), Simple formula for the atomic forces in the augmented-plane-wave method, *Physical Review B*, 40(3), 1560, 10.1103/PhysRevB.40.1560.
- Solomatova, N. V., and Asimow, P. D. (2017), *Ab initio* study of the structure and stability of CaMg(CO<sub>3</sub>)<sub>2</sub> at high pressure, *American Mineralogist*, 102(1), 210-215, doi:10.2138/am-2017-5830.
- Solomatova, N. V., Jackson, J. M., Sturhahn, W., Wicks, J. K., Zhao, J., Toellner, T. S., Kalkan, B., and Steinhardt, W. M. (2016), Equation of state and spin crossover of

- (Mg,Fe)O at high pressure, with implications for explaining topographic relief at the core-mantle boundary, *American Mineralogist*, 101(5), 1084-1093, doi:10.2138/am-2016-5510.
- Speziale, S., Milner, A., Lee, V. E., Clark, S. M., Pasternak, M. P., and Jeanloz, R. (2005), Iron spin transition in Earth's mantle, *Proceedings of the National Academy of Sciences*, 102, 17918–17922, doi:10.1073/pnas.0508919102.
- Stagno, V., Tange, Y., Miyajima, N., McCammon, C. A., Irifune, T., and Frost, D. J. (2011), The stability of magnesite in the transition zone and the lower mantle as function of oxygen fugacity, *Geophysical Research Letters*, 38(19), doi:10.1029/2011GL049560.
- Struzhkin, V. V., Mao, H., Hu, J., Schwoerer-Böhning, M., Shu, J., Hemley, R.J., Sturhahn, W., Hu, M. Y., Alp, E. E., Eng, P., and Shen, G. (2001), Nuclear inelastic X-ray scattering of FeO to 48 GPa, *Earth-Science Reviews*, 110, 1–25, doi:10.1103/PhysRevLett.87.255501.
- Sturhahn, W., Quast, K. W., Toellner, T. S., Alp, E. E., Metge, J., and Gerdau, E. (1996), Electron emission from Fe<sup>57</sup> nuclei excited with synchrotron radiation, *Physical Review B*, 53(1), 171, doi:10.1103/PhysRevB.53.171.
- Sturhahn, W. (2000), CONUSS and PHOENIX: Evaluation of nuclear resonant scattering data, *Hyperfine Interactions*, 125(1-4), 149-172, doi:10.1088/0953-8984/16/5/009.
- Sturhahn, W., Jackson, J. M., and Lin, J. F. (2005), The spin state of iron in minerals of Earth's lower mantle, *Geophysical Research Letters*, 32, L12307, doi:10.1029/2005GL022802.
- Sturhahn, W. (2015), MINUTI open source software, version 1.1.2, www.nrixs.com.
- Sun, D., Helmberger, D. V., Jackson, J. M., Clayton, R. W., and Bower, D. J. (2013), Rolling hills on the core–mantle boundary, *Earth and Planetary Science Letters*, 361, 333–342, doi:10.1016/j.epsl.2012.10.027.
- Tange, Y., Takahashi, E., Nishihara, Y., Funakoshi, K. I., and Sata, N. (2009), Phase relations in the system MgO-FeO-SiO<sub>2</sub> to 50 GPa and 2000 C: An application of experimental techniques using multianvil apparatus with sintered diamond anvils, *Journal of Geophysical Research: Solid Earth*, 114(B2), doi:10.1029/2008JB005891.
- Thomas, C. W., Liu, Q., Agee, C. B., Asimow, P. D., and Lange, R. A. (2012), Multi-technique equation of state for Fe<sub>2</sub>SiO<sub>4</sub> melt and the density of Fe-bearing silicate melts from 0 to 161 GPa, *Journal of Geophysical Research*, 117, B10206, doi:10.1029/2012JB009403.

- Toellner, T. S. (2000), Monochromatization of synchrotron radiation for nuclear resonant scattering experiments, *Hyperfine Interactions*, 125, 3–28, doi:10.1023/A:1012621317798.
- Tsuchiya, T., Wentzcovitch, R. M., da Silva, C. R. S., and de Gironcoli, S. (2006), Spin transition in magnesiowüstite in Earth's lower mantle, *Physical Review Letters*, 96, 198501, doi:0.1103/PhysRevLett.96.198501.
- Umemoto, K., Wentzcovitch, R. M., Yonggang, G. Y., and Requist, R. (2008), Spin transition in (Mg,Fe)SiO<sub>3</sub> perovskite under pressure, *Earth and Planetary Science Letters*, 276(1), 198-206, doi:10.1016/j.epsl.2008.09.025.
- van Bürck, U., Siddons, D. P., Hastings, J. B., Bergmann, U., and Hollatz, R. (1992), Nuclear forward scattering of synchrotron radiation, *Physical Review B*, 46(10), 6207, doi: 10.1103/PhysRevB.46.6207.
- Vanderbilt, D. (1990), Soft self-consistent pseudopotentials in a generalized eigenvalue formalism, *Physical Review B*, 41(11), 7892, 10.1103/PhysRevB.41.7892.
- Victor, G. Y. V., Ghosh, D., and Ghose, S. (2001), Ligand-field splitting of Fe<sup>2+</sup> in distorted octahedral sites of the magnesium-rich orthopyroxenes Fe<sub>x</sub>Mg<sub>1-x</sub>SiO<sub>3</sub>: Correlation of magnetic susceptibility, Mössbauer, and optical absorption spectra, *Physical Review B*, 64(14), 144413, doi: 10.1103/PhysRevB.64.144413.
- Vidale, J. E., and Hedlin, M. A. (1998), Evidence for partial melt at the core–mantle boundary north of Tonga from the strong scattering of seismic waves, *Nature*, 391(6668), 682-685, doi:10.1038/35601.
- Walter, M. J., Kohn S. C., Araujo D., Bulanova G. P., Smith C. B., Gaillou E., Wang J., Steele A., and Shirey S. B. (2011), Deep mantle cycling of oceanic crust: evidence from diamonds and their mineral inclusions, *Science*, 334(6052), 54-57, doi:10.1126/science.1209300.
- Wang, X., and Liou, J. G. (1993), Ultra-high-pressure metamorphism of carbonate rocks in the Dabie Mountains, central China, *Journal of Metamorphic Geology*, 11(4), 575-588, doi:10.1111/j.1525-1314.1993.tb00173.x.
- Wang, A., Pasteris, J. D., Meyer, H. O., and Dele-Duboi, M. L. (1996), Magnesite-bearing inclusion assemblage in natural diamond, *Earth and Planetary Science Letters*, 141(1-4), 293-306, doi:10.1016/0012-821X(96)00053-2.
- Waychunas, G. A., and Rossman, G. R. (1983), Spectroscopic standard for tetrahedrally coordinated ferric iron:  $\gamma$  LiAlO<sub>2</sub>: Fe<sup>3+</sup>, *Physics and Chemistry of Minerals*, 9(5), 212-215, doi:10.1007/BF00311957.
- Wicks, J. K., Jackson, J. M., Sturhahn, W. (2010), Very low sound velocities in iron-rich (Mg,Fe)O: Implications for the core-mantle boundary region, *Geophysical Research Letters*, 37, L15304, doi:10.1029/2010GL043689.

- Wicks, J. K., Jackson, J. M., Sturhahn, W., Zhuravlev, K. K., Tkachev, S. N., and Prakapenka, V. B. (2015), Thermal equation of state and stability of  $(\text{Mg}_{0.06}\text{Fe}_{0.94})\text{O}$ , *Physics of the Earth and Planetary Interiors*, 249, 28–42, doi:10.1016/j.pepi.2015.09.003.
- Wicks, J.K., Jackson, J. M., Sturhahn, W. and Zhang, D. (2017), Sound velocity and density of magnesiowüstites: Implications for ultralow-velocity zone topography, *Geophysical Research Letters*, 44, doi: 10.1002/2016GL071225.
- Wilke, M., Partzsch, G. M., Bernhardt, R., and Lattard, D. (2005), Determination of the iron oxidation state in basaltic glasses using XANES at the K-edge, *Chemical Geology*, 220(1), 143-161, doi:10.1016/j.chemgeo.2005.03.004.
- Williams, Q., and Garnero, E. J. (1996), Seismic evidence for partial melt at the base of Earth's mantle, *Science*, 273, 1528-1530, doi:10.1126/science.273.5281.1528.
- Williams, Q., Revenaugh, J., and Garnero, E. (1998), A correlation between ultra-low basal velocities in the mantle and hot spots, *Science*, 281, 546-549, doi:10.1126/science.281.5376.546.
- Wirth, R., Vollmer, C., Brenker, F., Matsyuk, S., and Kaminsky, F. (2007), Inclusions of nanocrystalline hydrous aluminium silicate “Phase Egg” in superdeep diamonds from Juina (Mato Grosso State, Brazil), *Earth and Planetary Science Letters*, 259(3), 384-399, doi:10.1016/j.epsl.2007.04.041.
- Wojdyr, M. (2010), Fityk: a general-purpose peak fitting program, *Journal of Applied Crystallography*, 43, 1126–1128, doi:10.1107/S0021889810030499.
- Wood, B. J., Bryndzia, L. T., and Johnson, K. E. (1990), Mantle oxidation state and its relationship to tectonic environment and fluid speciation, *Science*, 248(4953), 337-346, doi:10.1126/science.248.4953.337.
- Wyllie, P. J., Baker, M. B., and White, B. S. (1990), Experimental boundaries for the origin and evolution of carbonatites, *Lithos*, 26, 3-19, doi:10.1016/0024-4937(90)90037-2.
- Yagi, T., Suzuki, T., and Akimoto, S. I. (1985), Static compression of wüstite ( $\text{Fe}_{0.98}\text{O}$ ) to 120 GPa. *Journal of Geophysical Research*, 90, 8784–8788, doi:10.1029/JB090iB10p08784.
- Yang, W. L., Sorini, A. P., Chen, C. C., Moritz, B., Lee, W. S., Vernay, F., Olalde-Velasco, P., Denlinger, J. D., Delley, B., Chu, J. H. and Analytis, J. G. (2009), Evidence for weak electronic correlations in iron pnictides, *Physical Review B*, 80(1), 014508, doi:10.1103/PhysRevB.80.014508.
- Zhang, D., Jackson, J. M., Sturhahn, W., and Xiao, Y. (2011), Local structure variations observed in orthoenstatite at high pressures, *American Mineralogist*, 96(10), 1585-1592, doi:10.2138/am.2011.3721.

- Zhang, D., Jackson, J. M., Zhao, J., Sturhahn, W., Alp, E. E., Toellner, T. S., and Hu, M. (2015), Fast temperature spectrometer for samples under extreme conditions, *Review of Scientific Instruments*, 86, 013105, doi:10.1063/1.4905431.
- Zhang, Z., Church, N., Lappe, S. C., Reinecker, M., Fuith, A., Saines, P. J., Harrison, R. J., Schranz, W., and Carpenter, M. A. (2012), Elastic and anelastic anomalies associated with the antiferromagnetic ordering transition in wüstite,  $\text{Fe}_x\text{O}$ , *Journal of Physics: Condensed Matter*, 24, 215404, doi:10.1088/0953-8984/24/21/215404.
- Zhe, L., Laixi, T., Xiaohan, L., Liudong, R., Mingzhi, J., and Milan, L. (2000), Quadrupole splitting distributions in grandidierite and kornorupine from Antarctica, *Hyperfine Interactions*, 131(1), 91-102, doi: 10.1023/A:1010901706882.
- Zhuravlev, K. K., Jackson, J. M., Wolf, A. S., Wicks, J. K., Yan, J., and Clark, S. M. (2010), Isothermal compression behavior of (Mg,Fe)O using neon as a pressure medium, *Physics and Chemistry of Minerals*, 37, 465–474, doi:10.1007/s00269-009-0347-6.
- Zucchini, A., Comodi, P., Nazzareni, S., and Hanfland, M. (2014), The effect of cation ordering and temperature on the high-pressure behaviour of dolomite, *Physics and Chemistry of Minerals*, 41(10), 783-793, doi:10.1007/s00269-014-0691-z.
- Zucchini, A., Prencipe, M., Belmonte, D., and Comodi, P. (2017), *Ab initio* study of the dolomite to dolomite-II high-pressure phase transition, *European Journal of Mineralogy*, 29(1), doi:10.1127/ejm/2017/0029-260.

